Development, Characterization, and Application of Flowing Atmospheric-Pressure Afterglow Ionization for Mass Spectrometric Analysis of Ambient Organic Aerosols

Dissertation

for Attaining the Academic Degree of
"Doktor rerum naturalium" (Dr. rer. nat.)
of the Departments
08 – Physics, Mathematics, and Computer Science,
09 – Chemistry, Pharmaceutics, and Geosciences,
10 – Biology,
and University Medicine
of the Johannes Gutenberg University

by

Martin Brüggemann

born in Attendorn, Germany

JG|U
JOHANNES GUTENBERG UNIVERSITÄT MAINZ

Max Planck Graduate Center
mit der Johannes Gutenberg-Universität Mainz

Mainz, September 2015

Faculty director: [redacted]

1st supervisor: [redacted]

2nd supervisor: [redacted]

Date of Examination: November 6th, 2015

D77 – Dissertation of the Johannes Gutenberg University, Mainz

I hereby declare that I wrote the dissertation submitted without any unauthorized external assistance and used only sources acknowledged in the work. All textual passages which are appropriated verbatim or para-phrased from published and unpublished texts as well as all information obtained from oral sources are duly indicated and listed in accordance with bibliographical rules. In carrying out this research, I complied with the rules of standard scientific practice as formulated in the statutes of Johannes Gutenberg-University Mainz to insure standard scientific practice.

Mainz, September 2015

Zusammenfassung

Atmosphärische Aerosole haben große Auswirkungen auf die Luftqualität, die Sichtweite, das Klima und die menschliche Gesundheit. In Abhängigkeit von ihren chemischen und physikalischen Eigenschaften können Aerosolpartikel Strahlung streuen oder absorbieren, die Anzahl von Wolken und deren Lebensdauer beeinflussen und schädliche Wirkungen auf die menschlichen Atem- und Herz-Kreislauf-Systeme haben. Insbesondere der organische Anteil dieser Suspension macht atmosphärische Aerosole zu einem sehr komplexen und dynamischen Gemisch, welches üblicherweise aus einer Vielzahl von verschiedenen Verbindungen mit großer zeitlicher sowie räumlicher Variabilität besteht. Aufgrund dieser Komplexität stellen chemische Analysen von atmosphärischen organischen Aerosolen (OA) in der Regel eine ernsthafte Herausforderung für aktuelle Analyseinstrumente dar. Aufgrund ihrer Fähigkeit Verbindungen in Spuren-konzentrationen in komplexen Gemischen nachzuweisen, sind Verfahren unter Verwendung von Massenspektrometrie (MS) im Allgemeinen gut geeignet für diese Aufgabe. Übliche Methoden weisen allerdings eine eher geringe Zeitauflösung auf oder sind nicht in der Lage einzelne organische Spezies zu identifizieren.

Mit Bezug auf aktuelle Einschränkungen üblicher Instrumente in der Aerosolforschung waren die Ziele dieser Arbeit die Erforschung und Bewertung der Anwendbarkeit einer neuen sanften Ionisierungstechnik, der sogenannten *flowing atmospheric-pressure afterglow* (FAPA) Technik, für die massenspektrometrische Analyse von luftgetragenen organischen Partikeln. Die FAPA Ionisationstechnik wurde, neben anderen sanften Ionisierungsmethoden, in den letzten zehn Jahren während des Aufkommens der *ambient desorption/ionization* Massenspektrometrie (ADI–MS) entwickelt. Basierend auf einem Helium-Glimmentladungsplasma bei Atmosphärendruck werden angeregte Helium-Spezies sowie Primärionen erzeugt, welche den Entladungsbereich über eine Kapillar-Elektrode verlassen und die sogenannte *afterglow*-Region bilden, in welcher die Desorption und Ionisation des Analyten erfolgt. Bisherigen Studien zufolge werden Fragmentierungen von Analyten während der Ionisation üblicherweise nur in einem minimalen Ausmaß beobachtet und es werden überwiegend Quasimolekülionen, das heißt $[M+H]^+$ im positiven und $[M–H]^–$ im negativen Modus, gebildet und detektiert. Dadurch wird die Identifizierung und Detektion von Signalen und den zugehörigen Verbindungen in aufgenommenen Massenspektren erleichtert.

Der Schwerpunkt des ersten Teils dieser Arbeit liegt auf der Anwendung, Charakterisierung und Beurteilung von FAPA–MS im *offline*-Modus, das heißt auf der Anwendung von Desorption und Ionisation der Analyten von Oberflächen. Es wurden Ionisierungsmuster im positiven sowie im negativen Modus für eine Vielzahl von Verbindungsklassen, bestehend aus Alkanen, Alkoholen, Aldehyden, Ketonen, Carbonsäuren, organischen Peroxiden und Alkaloiden, gemessen. Außer der häufig betonten Detektion von Quasimolekülionen wurde ein breites Spektrum an Signalen für Addukte und Verluste gefunden. Zusätzlich wurden die Möglichkeiten und Grenzen der Technik in drei Machbarkeits-Studien untersucht. Im Allgemeinen zeigte sich, dass das Verfahren am besten für polare Analyten mit hoher Volatilität und niedrigen Molekulargewichten geeignet ist, welche idealerweise Stickstoff- und/oder Sauerstoff-Funktionalitäten aufweisen. Für Verbindungen mit niedrigen Dampfdrücken, langen Kohlenstoffketten und/oder hohen Molekulargewichten stehen Desorption und Ionisation jedoch in direktem Wettbewerb mit der Oxidation des Analyten, welche zur Bildung von Addukten und Oxidationsprodukten führen und eine klare Zuordnung der Signale in den aufgenommen Massenspektren verhindern. Ungeachtet dessen konnte gezeigt werden, dass FAPA–MS die Detektion und Identifizierung von bekannten Limonen-Oxidationsprodukten in sekundärem OA (SOA) von Filteroberflächen erlaubt. Somit wird FAPA–MS als geeignetes Verfahren für die *offline*-Analyse von OA-Partikeln angesehen.

Im zweiten und auch den nachfolgenden Teilen dieser Arbeit wurde FAPA–MS im *online*-Modus verwendet, das heißt für die Echtzeitanalyse von luftgetragenen OA-Partikeln. Daher wurde die Abkürzung AeroFAPA–MS (abgekürzt für Aerosol FAPA–MS) ausgewählt, um auf dieses Verfahren zu verweisen. Nach Optimierung und Charakterisierung der Methode wurde diese verwendet um eine Reihe von Modellverbindungen zu messen und typische Ionisationsmuster im positiven sowie negativen Ionenmodus zu untersuchen. Darüber hinaus werden Ergebnisse von Laborstudien sowie einer Feldmesskampagne in Mitteleuropa (F–BEACh 2014) vorgestellt und diskutiert. Während der F–BEACh-Kampagne wurde AeroFAPA–MS in Kombination mit komplementären MS-Techniken verwendet, um eine umfassende Charakterisierung der untersuchten OA-Partikel zu erhalten. So wurden mehrere bekannte SOA-Markerverbindungen in Echtzeit durch MS^n-Experimente identifiziert, welche auf die Anwesenheit photochemisch gealterter SOA-Partikel während des Messzeitraums hinweisen. Außerdem war es mithilfe von AeroFAPA–MS möglich hochoxidierte schwefelhaltige Verbindungen in der Partikelphase erstmalig in Echtzeit zu detektieren. Vergleiche mit Daten von anderen Aerosol- und Gasphasenmessungen deuten zudem darauf hin, dass sowohl partikuläres Sulfat als auch hochoxidierte Peroxyradikale in der Gasphase eine Rolle bei der Bildung dieser Substanzen spielen könnten.

Neben der Anwendung von AeroFAPA–MS für die Analyse von Aerosolpartikeln wurden außerdem die Desorptionsprozesse von Partikeln im *afterglow*-Bereich untersucht, um ein detaillierteres Verständnis der angewendeten Methode zu erlangen. Während in den vorangegangenen Messungen Aerosolpartikel vor der Analyse durch AeroFAPA–MS vorverdampft wurden, wurde in diesem Teil auf eine externe Wärmequelle verzichtet. Messungen der Partikelgrößenverteilungen vor und nach der AeroFAPA-Ionenquelle zeigten, dass nur eine Grenzflächenschicht der OA-Partikel desorbiert und somit chemisch charakterisiert wird. In diesen Messungen wurden für Partikel mit Anfangsdurchmessern von 112 nm Desorption-Radien von 2,5 bis 36,6 nm bei Entladungsströmen von 15 bis 55 mA bestimmt. Darüber hinaus wurde die Methode für die Analyse von laborgenerierten Kern-Schale-Partikeln in einer Machbarkeits-Studie angewendet. Wie erwartet, wurden vorwiegend Verbindungen, die in der Hülle der Partikel vorlagen, desorbiert und mit zunehmenden Sondiertiefen ionisiert. Die Ergebnisse deuten darauf hin, dass AeroFAPA–MS eine vielversprechende Technik für die Tiefenprofilierung von OA-Partikeln in zukünftigen Studien darstellen kann.

Abstract

Atmospheric aerosols have major implications for air quality, visibility, climate, and human health. Depending on their chemical and physical properties, aerosol particles can scatter or absorb radiation, affect cloud abundances and lifetimes, and can have hazardous effects to the human respiratory and cardiovascular systems. In particular, the organic fraction of this suspension makes it a highly complex and dynamic mixture, commonly comprising myriads of different compounds with a huge temporal as well as spatial variability. Due to this complexity, the chemical analysis of ambient organic aerosols (OAs) typically represents a serious challenge to current analytical instrumentation. In general, methods utilizing mass spectrometry (MS) are well suited to face this task due to their ability of detecting compounds at trace concentrations in complex mixtures. However, common approaches are either exhibiting a rather low time resolution or are not able to identify single organic species.

Addressing current limitations of state-of-the-art instrumentation in aerosol research, the aim of this work was to explore and assess the applicability of a novel soft ionization technique, namely flowing atmospheric-pressure afterglow (FAPA), for the mass spectrometric analysis of airborne particulate organic matter. Among other soft ionization methods, the FAPA ionization technique was developed in the last decade during the advent of ambient desorption/ionization mass spectrometry (ADI–MS). Based on a helium glow discharge plasma at atmospheric-pressure, excited helium species and primary reagent ions are generated which exit the discharge region through a capillary electrode, forming the so-called afterglow region where desorption and ionization of the analytes occurs. Commonly, fragmentation of the analytes during ionization is reported to occur only to a minimum extent, predominantly resulting in the formation of quasimolecular ions, i.e. $[M+H]^+$ and $[M–H]^–$ in the positive and the negative ion mode, respectively. Thus, identification and detection of signals and their corresponding compounds is facilitated in the acquired mass spectra.

The focus of the first part of this study lies on the application, characterization and assessment of FAPA–MS in the offline mode, i.e. desorption and ionization of the analytes from surfaces. Experiments in both positive and negative ion mode revealed ionization patterns for a variety of compound classes comprising alkanes, alcohols, aldehydes, ketones, carboxylic acids, organic peroxides, and alkaloids. Besides the always emphasized detection of quasimolecular ions, a broad range of signals for adducts and losses was found. Additionally, the capabilities and limitations of the technique were studied in three proof-of-principle applications. In general, the method showed to be best suited for polar analytes with high volatilities and low molecular weights, ideally containing nitrogen- and/or oxygen functionalities. However, for compounds with low vapor pressures, containing long carbon chains and/or high molecular weights, desorption and ionization is in direct competition with oxidation of the analytes, leading to the formation of adducts and oxidation products which impede a clear signal assignment in the acquired mass spectra. Nonetheless, FAPA–MS showed to be capable of detecting and identifying common limonene oxidation products in secondary OA (SOA) particles on a filter sample and, thus, is considered a suitable method for offline analysis of OA particles.

In the second as well as the subsequent parts, FAPA–MS was applied online, i.e. for real time analysis of OA particles suspended in air. Therefore, the acronym AeroFAPA–MS (i.e. Aerosol FAPA–MS) was chosen to refer to this method. After optimization and characterization, the method was used to measure a range of model compounds and to evaluate typical ionization patterns in the positive and the negative ion mode. In addition, results from laboratory studies as well as from a field campaign in Central Europe (F–BEACh 2014) are presented and discussed. During the F–BEACh campaign AeroFAPA–MS was used in combination with complementary

MS techniques, giving a comprehensive characterization of the sampled OA particles. For example, several common SOA marker compounds were identified in real time by MS^n experiments, indicating that photochemically aged SOA particles were present during the campaign period. Moreover, AeroFAPA–MS was capable of detecting highly oxidized sulfur-containing compounds in the particle phase, presenting the first real-time measurements of this compound class. Further comparisons with data from other aerosol and gas-phase measurements suggest that both particulate sulfate as well as highly oxidized peroxyradicals in the gas phase might play a role during formation of these species.

Besides applying AeroFAPA–MS for the analysis of aerosol particles, desorption processes of particles in the afterglow region were investigated in order to gain a more detailed understanding of the method. While during the previous measurements aerosol particles were pre-evaporated prior to AeroFAPA–MS analysis, in this part no external heat source was applied. Particle size distribution measurements before and after the AeroFAPA source revealed that only an interfacial layer of OA particles is desorbed and, thus, chemically characterized. For particles with initial diameters of 112 nm, desorption radii of 2.5–36.6 nm were found at discharge currents of 15–55 mA from these measurements. In addition, the method was applied for the analysis of laboratory-generated core-shell particles in a proof-of-principle study. As expected, predominantly compounds residing in the shell of the particles were desorbed and ionized with increasing probing depths, suggesting that AeroFAPA–MS might represent a promising technique for depth profiling of OA particles in future studies.

Table of Contents

1 Introduction

1.1 Atmospheric Aerosols

> *"The outlines of distant objects appear undetermined and confused* [...]*: between the eye and the distant objects there is so much air interposed, that it becomes thick; and, like a veil, tinges the shadows with its own whiteness* [...]*."*
>
> Leonardo da Vinci
> A Treatise on Painting (1651)

Atmospheric aerosols, defined as solid or liquid particles suspended in air, are ubiquitously found on Earth and play a key role in many environmental processes (Seinfeld and Pandis, 2006). Their existence was probably first discovered and described around 1500 by painters and polymaths like Leonardo da Vinci or Leon Battista Alberti, who recognized the influence of aerosol particles on visibility by scattering sunlight. Today, in arts this effect is known as aerial perspective (Carlson, 2013). In fact, aerosol particles do not only scatter but also absorb solar as well as terrestrial radiation. Moreover, they affect cloud formation and lifetime by acting as cloud condensation nuclei (CCN) or ice nuclei (IN) and have major effects on distribution and abundance of atmospheric trace gases by participating in heterogeneous chemical reactions and other multiphase processes (Barbara J. Finlayson-Pitts, 2000; Pöschl, 2005; Seinfeld and Pandis, 2006; Hallquist *et al.*, 2009). As a result, atmospheric aerosols have major implications for the Earth's radiation balance and climate (IPCC, 2014; Schneidemesser *et al.*, 2015). In addition, ambient aerosol particles can have severe impacts on human health by entering and damaging the respiratory and cardiovascular system or causing infectious and allergic diseases (Pöschl, 2005; Hallquist *et al.*, 2009; Schneidemesser *et al.*, 2015; Pöschl and Shiraiwa, 2015).

Although the term airborne particulate matter would be more accurate, the term aerosol is often used to refer only to the particle phase of this suspension (Seinfeld and Pandis, 2006). Furthermore, in atmospheric science the term is traditionally connected to airborne particles that are mainly made of condensed matter other than water since clouds, which are the most prominent example of atmospheric aerosols, are typically considered as separate phenomena (Pöschl, 2005). The size of these airborne particles can span several

orders of magnitude from 10^{-9}–10^{-4} m, with a lower limit given by molecular cluster size and an upper limit determined by rapid sedimentation (Seinfeld and Pandis, 2006; Kulkarni *et al.*, 2011).

Atmospheric aerosol represents a highly dynamic and complex system with a huge temporal and spatial variability regarding chemical composition, concentration and size distribution. This complexity can be explained to a large extent by continuous changes in particle size and composition by condensation of vapors or by evaporation, by coagulation, by chemical reactions, or by activation in the presence of water supersaturation to become fog and cloud droplets (Seinfeld and Pandis, 2006). In addition, atmospheric particles can have a wide variety of natural as well as anthropogenic sources. Particles emitted directly as liquids or solids into the atmosphere from sources such as sea spray, volcanic eruptions, biomass burning, combustion of fossil fuels, or suspension of soil and dust, are referred to as primary aerosols. Prominent examples of primary aerosols also include biological aerosols such as pollen, fungal spores, bacteria or viruses. In contrast, particles which are formed in the atmosphere by gas–particle conversion processes, i.e. nucleation, condensation and heterogeneous and multiphase chemical reactions, of gaseous precursor compounds are called secondary aerosols (Pöschl, 2005; Seinfeld and Pandis, 2006). The corresponding precursor compounds can either be inorganic or organic compounds. For example, the conversion of inorganic precursors such as sulfur dioxide (SO_2), nitrogen dioxide (NO_2) and ammonia (NH_3) leads to formation of particulate sulfate, nitrate, and ammonium (Hallquist *et al.*, 2009). On the other hand, the oxidation of volatile organic compounds (VOCs) by atmospheric oxidants, such as ozone (O_3), hydroxyl radicals ($^{\bullet}OH$), nitrate radicals ($NO_3^{\bullet}$), or even reactive halogen species, results in the formation of organic compounds with low volatility, eventually yielding secondary organic aerosol (SOA) particles, which will be discussed in more detail in section 1.2 (Pöschl, 2005; Fuzzi *et al.*, 2006; Seinfeld and Pandis, 2006; Hallquist *et al.*, 2009; Pöschl and Shiraiwa, 2015).

Besides their chemical composition, formation mechanisms largely determine the size and, thereby, transport properties and lifetime of aerosol particles in the atmosphere. Particles larger than 1 µm in diameter, also referred to as the coarse mode, are typically primary in nature. They contribute largely to the mass of aerosol populations, however, exhibit rather short atmospheric lifetimes due to fast gravitational settling. Long-range transport of these particles is therefore rather limited and only occurs by large-scale convective processes, e.g. dust storms. Despite their large size and low number concentration, primary particle in the coarse mode are essential for the formation of clouds

and precipitation due to their ability to act as IN (Barbara J. Finlayson-Pitts, 2000; Seinfeld and Pandis, 2006; Pöschl and Shiraiwa, 2015). Particles with diameters smaller than 1 µm are generally defined as the fine mode, which is commonly divided into accumulation mode (0.1–1 µm), Aitken mode (0.01–0.1 µm), and nucleation mode (<0.01 µm). These particles are typically secondary in nature and contribute largely to number and surface area of atmospheric particle populations. Particles of the nucleation mode and the Aitken mode exhibit fast growing rates due to condensation of vapors and coagulation with other particles and, thus, rapidly enter the accumulation mode. Since dry deposition plays a minor role for particles in the fine mode, the accumulation mode comprises aerosol particles with the longest atmospheric lifetime (Barbara J. Finlayson-Pitts, 2000; Seinfeld and Pandis, 2006). Figure 1.1.1 gives examples and an overview of common atmospheric aerosol particles, corresponding size ranges and composition as well as chemical reactions and transformations in the course of aerosol–cloud–droplet–precipitation interactions in the atmosphere.

Atmospheric aerosols influence the Earth's climate by affecting the global radiation budget either directly via aerosol–radiation effects or indirectly via aerosol–cloud effects. The direct effects result from the absorption or scattering of radiation by aerosol particles, whereby absorbed radiation, e.g. by black carbon particles, contributes to warming of the atmosphere. In contrast, solar radiation scattered back into space, e.g. by sulfate particles, tends to cool the Earth's surface. Absorption as well as scattering of incident radiation is most efficient for particle sizes in the range of the incident wavelength and, therefore, particles in the accumulation mode (Schwartz, 1996; Seinfeld and Pandis, 2006; Schneidemesser *et al.*, 2015). The indirect effects are based on the capability of aerosol particles in the size range of 50–100 nm to act as CCN, which are activated to form cloud droplets in rising air masses. Since a larger number concentration of cloud droplets leads to an increased cloud albedo, i.e. scattering of solar radiation back into space, and longer cloud lifetimes, the concentration of CCN sized particles is a main driver for cooling the Earth's atmosphere by shading the planet from solar radiation (Seinfeld and Pandis, 2006; Schneidemesser *et al.*, 2015). In addition, aerosol–cloud effects can have severe impacts on the Earth's hydrological cycle since a larger number of CCN increases the formation of small cloud droplets, eventually suppressing precipitation (Ramanathan, 2001; Rosenfeld *et al.*, 2008).

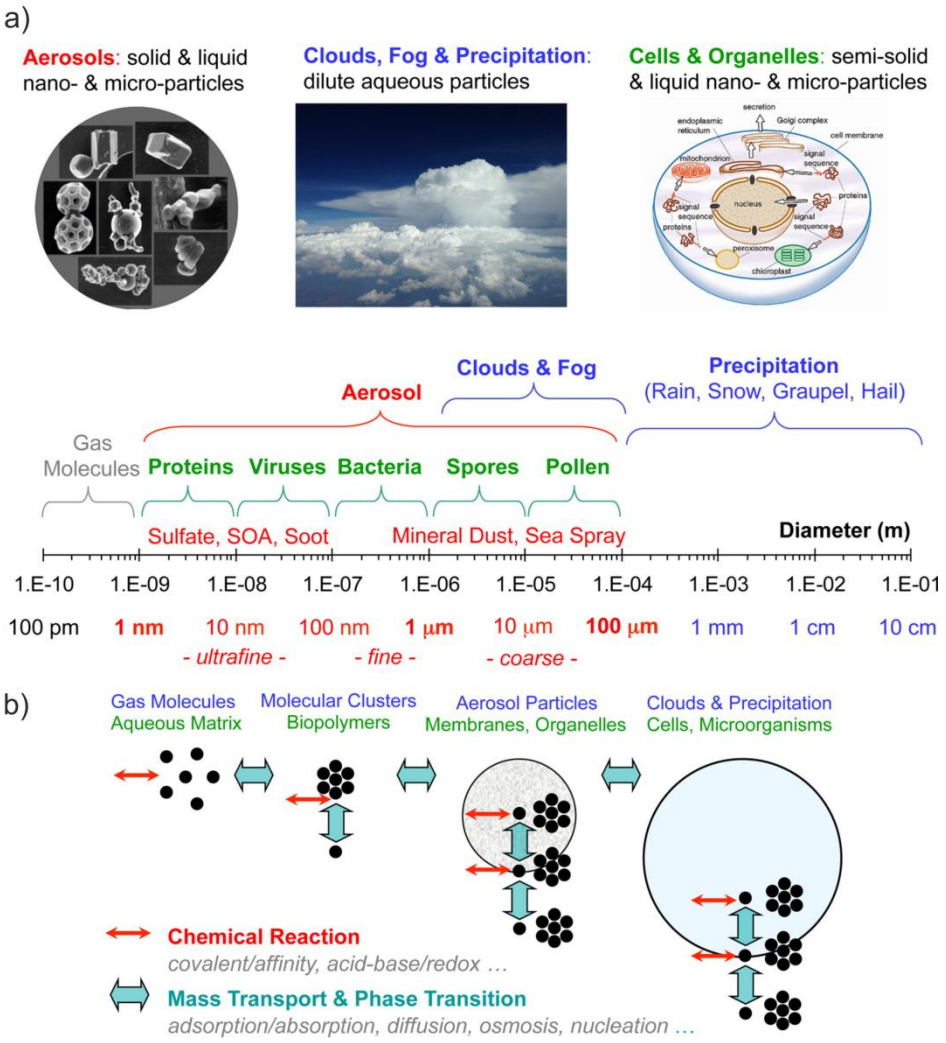

Figure 1.1.1: Overview of atmospheric aerosol particles. (a) Size range of aerosols, hydrometeors, cells, and organelles. (b) Formation and transformation of atmospheric aerosols: mass transport and phase transitions in and between gas phase, clusters, aerosol, cloud, and precipitation particles; chemical reactions in the gas phase, at the interface, and in the particle bulk (Pöschl and Shiraiwa, 2015).

Since industrialization the emissions of aerosol particles and their precursors to the atmosphere by human activities have increased significantly. In the lower troposphere, number and mass concentrations of aerosol particles in polluted urban areas are nowadays often 1–2 orders of magnitude higher than in pristine air of remote continental regions. Among other increasing concentrations of air contaminants such as greenhouse gases and reactive nitrogen species, this increase in anthropogenic aerosol concentrations is considered a characteristic feature of global environmental change in the Anthropocene, i.e. the present era of globally pervasive and steeply increasing human influence on Earth (Crutzen and Stoermer, 2000; Crutzen, 2002; Pöschl and Shiraiwa, 2015). Overall, according to the latest Intergovernmental Panel on Climate Change (IPCC) report anthropogenic aerosols are generally believed to cool the atmosphere. The cooling effect

due to aerosol–cloud interactions and scattering is believed to exceed the warming effect due to absorbed radiation by black and brown carbon. As a result, the increase in aerosol concentrations might have masked global warming in the past to a certain extent (IPCC, 2014; Schneidemesser *et al.*, 2015). However, aerosol particles continue to contribute the largest uncertainty in the estimations of global radiative forcing. In contrast to the relatively long-lived greenhouse gases, the short lifetime and corresponding highly variable temporal and spatial distribution impede accurate model calculations. Figure 1.1.2 gives an overview of the variation in aerosol abundance and chemical composition in the northern hemisphere, retrieved from aerosol mass spectrometer (AMS) measurements.

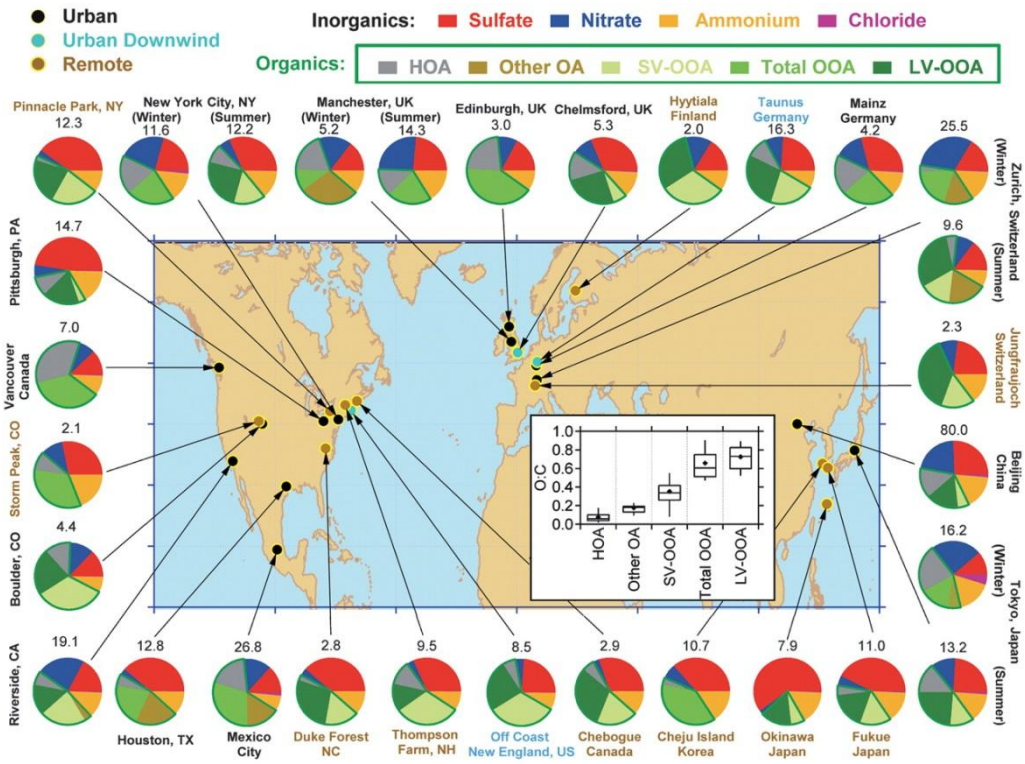

Figure 1.1.2: Total mass concentration (in $\mu g \cdot m^{-3}$) and mass fractions of nonrefractory inorganic species and organic components in submicrometer aerosols at multiple surface locations in the Northern Hemisphere. Organic aerosol is divided into hydrocarbon-like OA (HOA), semi-volatile oxygenated OA (SV-OOA) and low-volatile oxygenated OA (LV-OOA) (Jimenez *et al.*, 2009).

Besides climatic effects, several epidemiological studies have shown a clear correlation between exposure to particulate matter and adverse health effects including but not restricted to cardiovascular, respiratory, and allergic diseases (Pope and Dockery, 2013; Dominici *et al.*, 2014). These health effects largely depend on chemical composition, number concentration and particle size distribution of the aerosol. For example, the penetration and penetration efficiency of aerosol particles into human lungs is greatly

affect by particle size, whereas the chemical composition determines the toxicity. By now, air pollution by ozone and airborne particulate matter are recognized as one of the most prominent leading risk factors for the global burden of disease (Schneidemesser *et al.*, 2015; Pöschl and Shiraiwa, 2015).

1.2 Secondary Organic Aerosols in the Troposphere

1.2.1 Formation Mechanisms

Numerous studies indicate that organic aerosol (OA), i.e. carbonaceous particulate matter other than black carbon, is a major component of tropospheric aerosol, representing 20–90% of the total dry fine particulate mass in the atmosphere. Furthermore, it was shown that commonly 64–95% of these OA particles are secondary in nature (Kanakidou *et al.*, 2005; Murphy *et al.*, 2006; Zhang *et al.*, 2007; Jimenez *et al.*, 2009). In general, SOA is formed when condensable organic vapors form particulate matter by phase-transition, which is either the result of condensation on pre-existing particles or nucleation processes. In both cases, the required condensable vapors are generated by oxidation of VOCs, causing a significant decrease in volatility, as already outlined in section 1.1. (Seinfeld and Pandis, 2006; Pöschl and Shiraiwa, 2015). Figure 1.2.1 depicts a simplified scheme of initial oxidation processes and mechanisms of VOCs in the gas phase. While traditionally oxidation processes were assumed to occur on an intermolecular level, recent studies by Ehn and co-workers revealed that extremely low-volatile organic compounds (ELVOCs) are formed by rapid intramolecular auto-oxidation processes of VOCs (Ehn *et al.*, 2012; Ehn *et al.*, 2014). It was found that after an initial oxidation step by ozone or OH-radicals VOCs are further oxidized by subsequent H-shifts and O_2 addition, yielding highly oxidized ELVOCs in the time scale of seconds from the oxidation reaction (Jokinen *et al.*, 2014; Ehn *et al.*, 2014; Mentel *et al.*, 2015; Jokinen *et al.*, 2015).

Globally, the dominant precursors for SOA are biogenic VOCs, such as isoprene, monoterpenes ($C_{10}H_{16}$), and sesquiterpenes ($C_{15}H_{24}$), which are emitted in tremendous amounts from terrestrial ecosystems. Total emission estimates are in the range of ~410 $Tg \cdot a^{-1}$ of isoprene and ~160 $Tg \cdot a^{-1}$ of monoterpenes (Guenther *et al.*, 1995; Kesselmeier and Staudt, 1999). Although less relevant on a global scale, anthropogenic VOCs, e.g. alkanes and aromatic compounds, can play a key role on local to regional scales, as it was shown by studies downwind of megacities and major conurbations (Gouw, 2005; Bahreini *et al.*, 2009; DeCarlo *et al.*, 2010). Moreover, recent studies suggest that

SOA formation might be enhanced when biogenic VOCs encounter anthropogenically perturbed air masses (Weber *et al.*, 2007; Goldstein *et al.*, 2009).

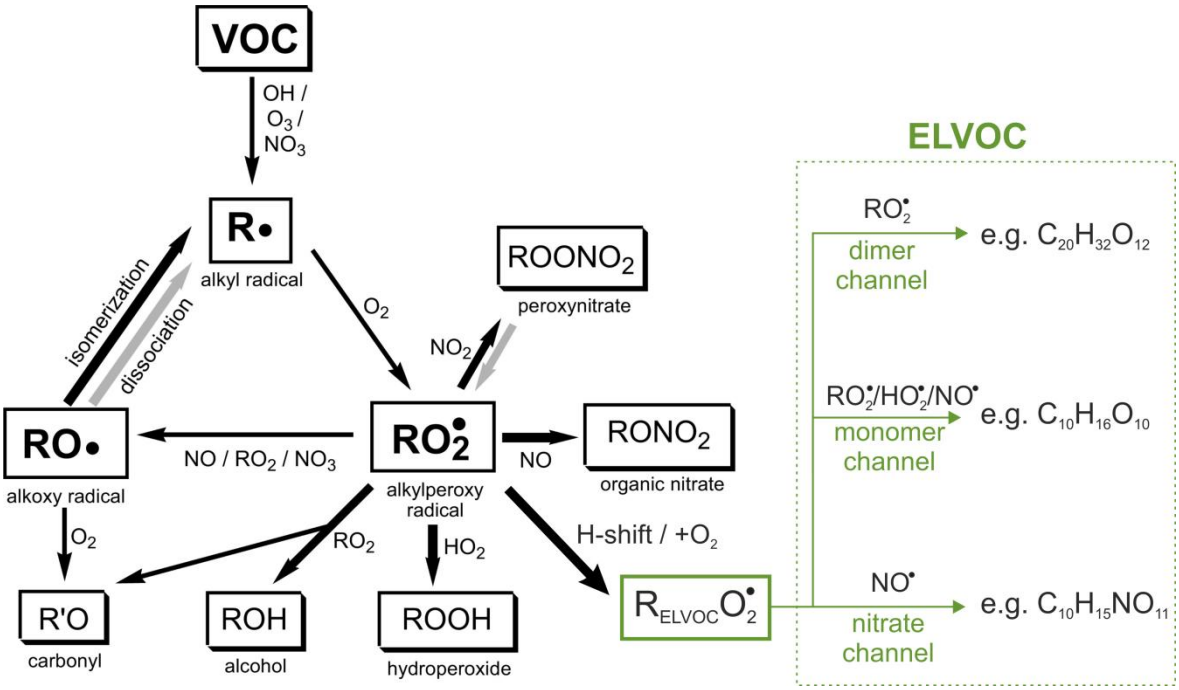

Figure 1.2.1: Initial gas-phase oxidation mechanisms of VOCs. Thick black arrows denote reactions that can lead to a substantial decrease in volatility; gray arrows denote reactions that can lead to a substantial volatility increase (adapted from Kroll and Seinfeld, 2008 and Ehn *et al.*, 2014).

In general, condensational growth due to SOA formation is commonly assumed to be the main player in the atmospheric growth of aerosol particles (Riipinen *et al.*, 2011; Donahue *et al.*, 2011; Riccobono *et al.*, 2012). Nucleation occurs only when vapor molecules form small molecular clusters of a few nanometers (<2 nm), subsequently growing via condensation and coagulation processes to form CCN-sized particles (>50−100 nm). In particular, it was shown that ELVOCs play a crucial role in the initial nucleation process together with sulfuric acid (and other) molecules in a number of environments, e.g. pristine boreal forests (Schobesberger *et al.*, 2013; Kulmala *et al.*, 2013; Ehn *et al.*, 2014; Riccobono *et al.*, 2014). However, also in this case only a small portion of SOA is participating in the actual nucleation process while the majority is a driving factor of particle growth via condensation on the formed condensation nuclei. Figure 1.2.2 gives an overview of the path from emissions of volatile compounds to the formation of SOA and their corresponding climate effects.

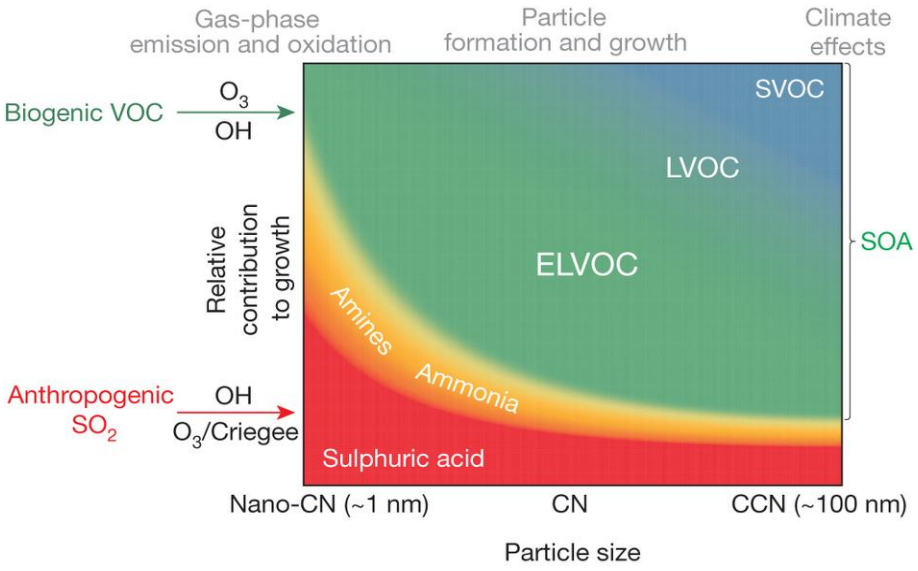

Figure 1.2.2: Overview of the path from emissions of volatile compounds, via aerosol particles, to their climate effects (gray labels at top). ELVOCs are probably major contributors to condensational growth at all sizes, ranging from newly formed particles through to CCN. The relative roles of different vapors, described by corresponding colors (H_2SO_4, red; bases, orange; organics, varying shades of green), will vary depending on location and prevailing meteorological conditions, but this figure provides an estimate of the average contribution of the most important precursor vapors to particle growth in boreal forest-type environments. Both biogenic VOCs (green arrow on vertical axis) and anthropogenic SO_2 emissions (red arrow on vertical axis) can enhance the formation and growth of particles to climate-relevant sizes (Ehn *et al.*, 2014).

1.2.2 Gas–Particle Partitioning, Phase-State and Multiphase Chemistry

In contrast to ELVOCs, which represent the lower end in volatility of SOA components, the majority of oxidation products found in SOA have considerably higher vapor pressures. These compounds typically partition between the gas phase and the particle phase. Theoretical descriptions on OA phase partitioning were first described by Pankow (Pankow, 1994a, 1994b) and later extended by Odum *et al*. to SOA formation (Odum *et al.*, 1996). The gas–particle partitioning of semi-volatile organic compounds (SVOCs) is expressed herein by an equilibrium partitioning coefficient $K_{p,i}$ (in $m^3 \cdot \mu g^{-1}$) or the inverse proportional saturation vapor concentration C_i^* (in $\mu g \cdot m^{-3}$) (Donahue *et al.*, 2006), as depicted in the following equation:

$$\frac{C_i^p}{C_i^g} = K_{p,i} \cdot C_{OA} = \frac{C_{OA}}{C_i^*} \tag{1.1}$$

where C_i^g and C_i^p represent the mass concentrations of species *i* per unit volume of air (in $\mu g \cdot m^{-3}$) in the gas phase and the particle phase, respectively. C_{OA} is the mass concentration per unit volume of air (in $\mu g \cdot m^{-3}$) of the total absorbing particle phase. This hypothesis implies that a fraction of each SVOC will partition into the particle phase, even if its gas-

phase concentration is below its saturation concentration, C_i^*. As an example, when $C_{OA} = C_i^*$ partitioning will lead to a 50:50 distribution between particle and gas phase. In contrast, when $C_{OA} >> C_i^*$ the corresponding compound will reside almost completely in the particle phase. Using equation 1.1, the exact fraction F_i of a semivolatile compound in the particle phase can be retrieved via equation 1.2 (Hallquist *et al.*, 2009):

$$F_i = \frac{C_i^p}{C_i^p + C_i^g} = \frac{C_{OA} \cdot K_{p,i}}{1 + C_{OA} \cdot K_{p,i}} = \frac{1}{1 + C_i^*/C_{OA}} \quad (1.2)$$

Because a comprehensive theoretical description of SOA partitioning using this approach is, however, impeded by the wide range of C_{OA} in the atmosphere and the ongoing oxidation of SVOCs in the gas phase as well as in the particle phase, Donahue and co-workers suggested the use of a volatility basis set (VBS) (Donahue *et al.*, 2006). In the VBS semivolatile compounds are binned to predefined values for C_i^*, which are separated by one order of magnitude. Measurements of C_{OA} then allow the calculation of partitioning for a compound, using equation 1.2.

Inferred from equilibrium gas–particle partitioning theory, atmospheric models commonly treat SOA as well-mixed liquid in which the gas-phase oxidation products are assumed to quickly adopt gas–particle equilibrium (Pankow, 1994b; Odum *et al.*, 1996; Donahue *et al.*, 2006). Nonetheless, recent studies found that, depending on temperature and relative humidity, SOA rather behaves as a highly viscous, amorphous solid or semisolid (Virtanen *et al.*, 2010; Saukko *et al.*, 2012; Renbaum-Wolff *et al.*, 2013). Diffusion within such particles is significantly decreased due to the higher viscosities, impeding mixing of compounds within the particle phase. As depicted in Figure 1.2.3 (panel a), molecular diffusion for particles in the size range of the accumulation mode (~100 nm) varies from microseconds to milliseconds for liquids, however, from seconds to years for semisolids, and up to many years for solids (Shiraiwa *et al.*, 2011). As a result, longer equilibration timescales of SOA partitioning are assumed, questioning the hypothesis of equilibrium partitioning (Shiraiwa and Seinfeld, 2012).

Moreover, it was demonstrated that, besides molecular diffusion, evaporation kinetics and volatility of particle components are affected by the phase-state of the particles. In particular, studies showed that coatings of solid or semisolid OA and SOA particles led to significantly reduced evaporation and reaction rates (Cappa and Wilson, 2011; Vaden *et al.*, 2011). It was demonstrated that oxidation of compounds in the core of particles can be completely suppressed by shielding the core with layers of rather inert compounds (Vaden *et al.*, 2010; Zhou *et al.*, 2012; Zhou *et al.*, 2013). As illustrated in Figure 1.2.3 (panel b),

oxidation of particle components at the surface of solid or semisolid particles eventually lead to the formation of particles with core-shell morphology. Due to limited bulk diffusion in such particles, degradation of compounds occurs solely in the interfacial layer of the particles, resulting in steep concentration gradients from shell to core.

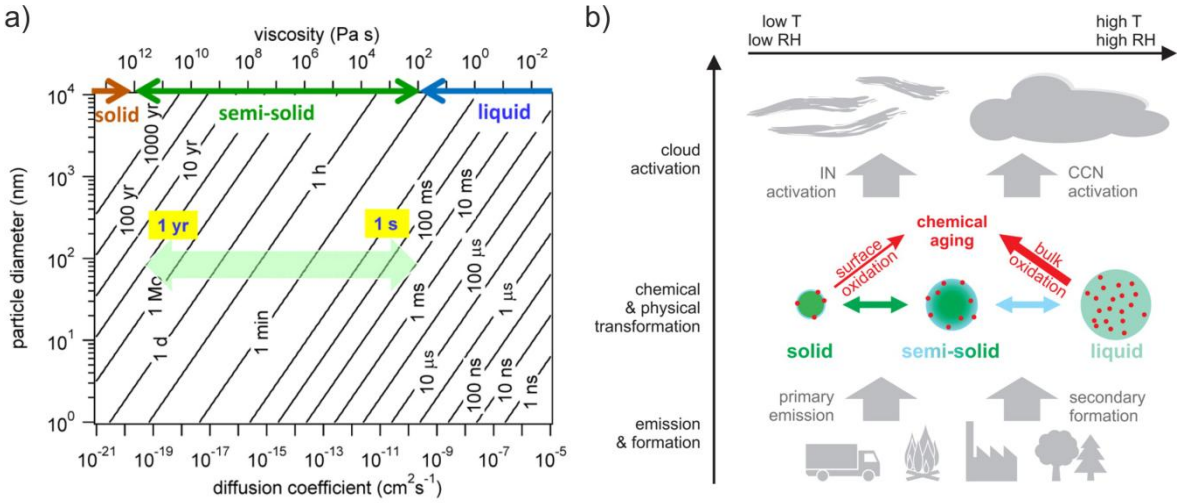

Figure 1.2.3: (a) Characteristic time of bulk diffusion in liquid, semisolid, and solid particles as a function of diffusion coefficient and particle diameter. In the size range of the atmospheric aerosol accumulation mode (particle diameters around ~100 nm), diffusion in semisolid particles varies from seconds to years (light green arrow). (b) Organic particulate matter in the atmosphere is usually amorphous, and its phase state can vary between liquid, semisolid, and solid (glassy), depending on ambient relative humidity and temperature. Particle phase state, viscosity, and diffusivity play an important role in most aerosol interactions like uptake and partitioning of reactive and condensable gases, chemical transformation and aging, and activation as CCN or IN (Shiraiwa *et al.*, 2011).

1.3 Mass Spectrometry in Aerosol Research

> *"I feel sure that there are many problems in Chemistry which could be solved with far greater ease by this than by any other method. The method is surprisingly sensitive* [...]*, requires an infinitesimal amount of material, and does not require this to be specially purified* [...]*."*
>
> Joseph John Thomson
> Rays of Positive Electricity (1913)

Since its development in the late 19th and early 20th century mass spectrometry (MS) has become a powerful and versatile tool, not only in analytical chemistry but also in aerosol research. Due to its high sensitivity as well as response time, many of the significant advances in our understanding of atmospheric aerosols can be attributed to the application

of MS. Nowadays, MS is the most commonly applied technique for the chemical analysis of airborne particulate matter (Farmer and Jimenez, 2010).

In general, the applied MS techniques can be separated in online and offline techniques: Online techniques commonly operate in or near real time, i.e. with a time-resolution of 0.1 s to 1 h, and, thus, allow capturing even processes on rather short timescales. However, the obtained data are typically less specific than those acquired by offline techniques, which collect samples over several hours to days on filters or by impaction prior to analysis (Farmer and Jimenez, 2010; Pratt and Prather, 2012b, 2012a). In the following a brief overview will be given about recent advances in online as well as offline MS techniques, including recent advances in the field of ambient desorption MS techniques. A more detailed description of the current status of analytical techniques used for the chemical analysis of atmospheric aerosol can be found in recently published reviews by Parshintev and Hyötyläinen (2014), Laskin *et al*. (2013), or Pratt and Prather (2012a, 2012b).

1.3.1 Offline Mass Spectrometry and Ambient Desorption Techniques

Commonly, offline MS methods have sampling times ranging from hours to days, sometimes even up to weeks. In case of filtration, sampling substrates are often quartz or polytetrafluoroethylene-coated fiber filters, depending on the analytes. Alternatively, particles can also be sampled by inertial impaction which is commonly conducted using inert metal surfaces. Prior to the actual analysis, the sampled aerosol particles are processed in a laboratory, for example, by extraction, sonification, or derivatization. Subsequent analysis is often conducted by separation techniques followed by MS detection such as liquid chromatography– (LC) or gas chromatography–MS (GC–MS). Due to the possibility to separate single or even multiple organic species, the chemical complexity of the aerosol particles is drastically reduced, and quantification of specific marker compounds is possible (Pratt and Prather, 2012a).

With regard to the analysis of OA and SOA particles, in particular LC–MS techniques in combination with electrospray ionization (ESI) became increasingly popular during the last decades. In most cases reversed-phase C18 or C8 columns are employed for separation of the analytes since they offer a wide range of both suitable analytes and pH stability (Hallquist *et al.*, 2009). For example, using LC–MS methods, a number of SOA marker compounds was identified during the last years (Claeys *et al.*, 2009; Yasmeen *et al.*, 2010; Yasmeen *et al.*, 2011). Moreover, several groups showed that sulfate as well as nitrate

groups can be incorporated in SOA components (Surratt *et al.*, 2007; Iinuma *et al.*, 2007; Surratt *et al.*, 2008; Mutzel *et al.*, 2015). Typically, identification and structural elucidation of the compounds is either conducted by MS^n experiments, e.g. using ion trap or triple quadrupole mass spectrometers, or by using high resolution MS instrumentation, such as Fourier transform ion cyclotron resonance–MS or Orbitrap–MS (Hoffmann *et al.*, 2011).

The Orbitrap mass spectrometer is a modification of the Kingdon trap which was already developed in the early 1920s (Kingdon, 1923; Makarov, 2000; Zubarev and Makarov, 2013). However, in contrast to the Kingdon trap, Orbitrap–MS is capable of producing mass spectra with a mass resolution of up to $R = 10^6$ at $m/z < 300$–400 and, thus, is often referred to as high resolution MS (HRMS) or even ultrahigh resolution MS (UHRMS). In addition, the technique typically exhibits mass accuracies in the range of 1–5 ppm (Nizkorodov *et al.*, 2011; Nozière *et al.*, 2015). The combination with separation techniques, typically reversed-phase LC followed by ESI, allows unambiguous detection of certain compounds by determination of the corresponding elemental composition, as can be seen in Figure 1.3.1. Recent studies applied Orbitrap–MS for the detection of organosulfates in ambient aerosols (Gómez-González *et al.*, 2008), the determination of elemental compositions of nitrogen-containing compounds in rain water (Altieri *et al.*, 2009), and the analysis of photolytic processing of SOA in cloud droplets (Bateman *et al.*, 2011).

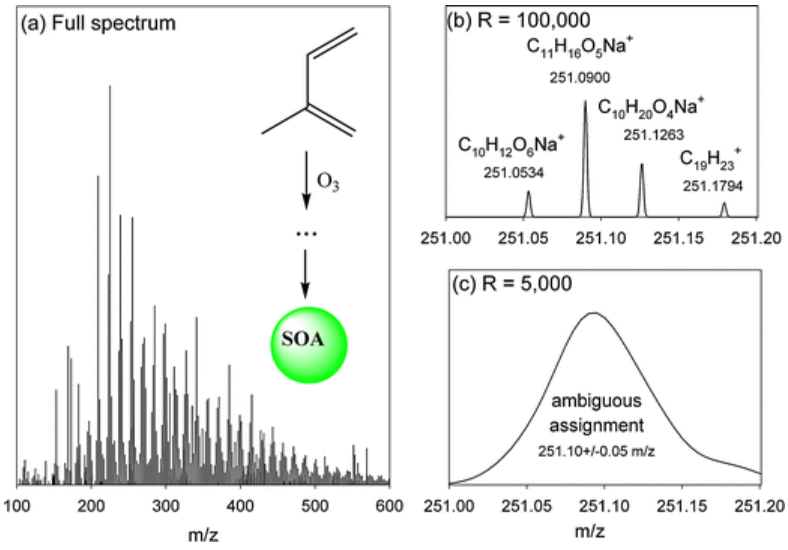

Figure 1.3.1: (a) Positive ion mode ESI–MS spectrum of isoprene/O_3 SOA. Panel (b) zooms in on peaks near m/z 251 recorded at the Orbitrap resolving power of $R = 10^5$. Panel (c) shows how the same mass range would look like if recorded at a typical resolving power of a reflection-TOF instrument R = 5000 (Nizkorodov *et al.*, 2011).

In contrast to established ionization methods, such as ESI or atmospheric-pressure chemical ionization (APCI), the latest developments in soft ionization techniques that have been made during the advent of ambient desorption/ionization mass spectrometry (ADI–MS) are rather unexplored in aerosol research. Ionization techniques developed under the concept of ADI–MS comprise ion sources such as the low temperature plasma probe (LTP) (Albert and Engelhard, 2012), the DART source (Cody *et al.*, 2005), the flowing atmospheric-pressure afterglow (FAPA) source (Andrade *et al.*, 2008) or the desorption electrospray ionization (DESI) source (Takats, 2004). All these techniques have in common to operate under ambient conditions without the need of preprocessing the sampled material prior to analysis. A typical setup of DESI–MS for the analysis of OA from filter material is depicted in Figure 1.3.2, giving a representative example of ADI–MS experiments.

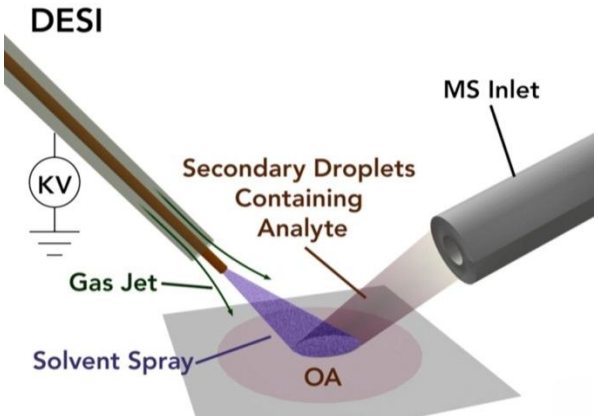

Figure 1.3.2: Schematic drawing of ambient surface desorption/ionization using DESI–MS for the analysis of OA samples (Nizkorodov *et al.*, 2011).

Although these techniques are still playing a minor role in chemical analyses of OA, the number of studies using ADI–MS techniques is steadily growing. For example, recent studies applied DESI–MS (Laskin *et al.*, 2010), near-infrared laser desorption/ionization MS (Geddes *et al.*, 2010), nano-DESI–MS (Roach *et al.*, 2010; Boone *et al.*, 2015), and DART–MS (Ewing *et al.*, 2013) for the identification of oxidation products in ambient and laboratory-generated OA particles on filter surfaces.

However, since quantification of compounds still represents a major challenge when using ADI–MS techniques, these methods are mainly applied for detection of new compounds and elucidation of underlying reaction mechanisms. In addition, the large sampling times, which are necessary for all offline methods, often impede studies on

reactive or (semi)volatile compounds since further reactions or evaporation on the time scale of minutes or even seconds cannot be excluded for such species.

1.3.2 Online Mass Spectrometry Techniques

Online MS techniques can generally be divided into two subgroups: methods for the analysis of bulk aerosol and methods for the analysis of single particles. Commonly, bulk aerosol methods are used to obtain statistical information on the average composition of a large ensemble of aerosol particles, whereas in single particle measurements pulsed laser ionization techniques are typically used to analyze single particles successively. Since the results of this study are based on bulk measurements, the reader is guided to recent reviews and textbooks for more information on single particle measurements (Kulkarni *et al.*, 2011; Pratt and Prather, 2012b; Laskin *et al.*, 2013).

By now, the AMS is probably the most established MS method for real time chemical characterization of bulk aerosol particles in the submicrometer range (~50–1000 nm) (Canagaratna *et al.*, 2007). Briefly, an aerodynamic lens is utilized to transfer aerosol particles into the vacuum region, focusing the sampled particles to a linear beam which is directed onto a heated evaporation unit (~600 °C). After flash evaporation of the aerosol components, the resulting gas-phase species are ionized by electron ionization (EI), commonly operating at 70 eV. Subsequently, the ions are detected by MS. In addition, particles are typically size separated by passing a particle time-of-flight region (Canagaratna *et al.*, 2007; Pratt and Prather, 2012b). A schematic of the AMS illustrating the essential components is given in Figure 1.3.3.

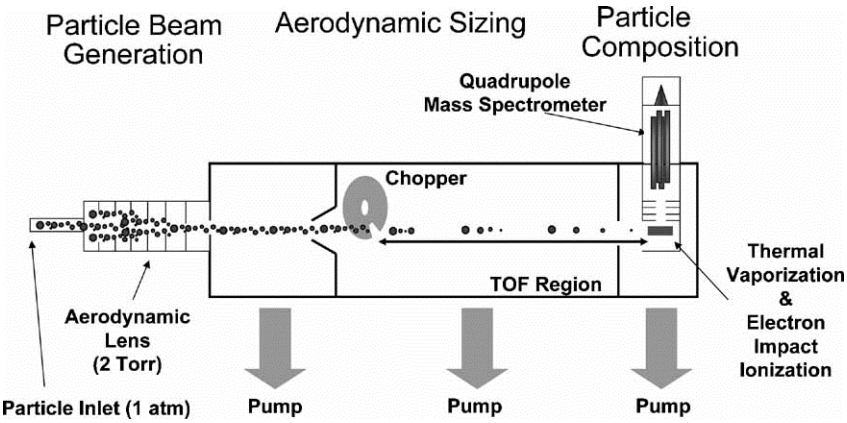

Figure 1.3.3: Schematic of an AMS showing the most essential components. The depicted quadrupole mass spectrometer can be replaced by other MS types, e.g. time-of-flight MS (Canagaratna *et al.*, 2007).

Due to the application of EI, a wide range of chemical species can efficiently be ionized. Solely, refractory compounds, such as black carbon, which cannot be volatilized at ~600 °C in the vacuum region (~10^{-5} Pa) are eluding analysis by AMS. However, EI also results in a high degree of fragmentation of organic species, because of excess internal energy conveyed during the ionization processes. Therefore, identification and quantification of individual particle phase organics is commonly not possible, leading to a relatively low level of chemical information (Hoffmann *et al.*, 2011).

Addressing this drawback of the AMS, recent instrumental developments focus on softer ionization techniques, which preserve structural information during the ionization process. For example, recent approaches utilized online APCI–MS for the analysis of ambient SOA particles (Vogel *et al.*, 2013a; Brüggemann *et al.*, 2014). Other approaches apply extractive electrospray ionization (EESI–MS) (Gallimore and Kalberer, 2013), near-infrared laser desorption ionization (Geddes *et al.*, 2010), or the aforementioned DART–MS technique (Chan *et al.*, 2013; Nah *et al.*, 2013). Furthermore, it was shown that such approaches allow retrieving structural information on OA species in real time by MS^n experiments using a quadrupole ion trap (QIT) mass spectrometer (Vogel *et al.*, 2013b). Since a QIT mass spectrometer was utilized within this study as well, a brief description of the working principle will be given in the following.

As depicted in Figure 1.3.4 (panel a), the QIT mass analyzer basically consists of two hyperbolic electrodes, resembling the end-cap electrodes, and a ring electrode. Ions enter the QIT through one of the end-cap electrodes and are stored inside by a three-dimensional electric field, keeping the ions on stable trajectories. Commonly, the end-cap electrodes are held at ground potential, whereas the electrical potential Φ, consisting of a direct current (DC) voltage U and a radio frequency (RF) voltage $V \cdot \cos\Omega t$, is applied to the ring electrode. In the RF term, V is the amplitude and Ω represents $2\pi f$, with f equaling the fixed frequency of the RF (commonly ~1 MHz) (equation 1.3).

$$\Phi = U + V cos\Omega t \tag{1.3}$$

By solving differential equations of the Mathieu type, stable trajectories within the quadrupole field can be calculated. As depicted in equations 1.4 and 1.5, the motion of ions in radial (r) and axial (z) direction can be described by the Mathieu parameters a and q, where z^* is the number of elementary charges e.

$$a_z = -2a_r = \frac{-16z^* eU}{m(r_0^2 + 2z_0^2)\Omega^2} \tag{1.4}$$

$$q_z = -2q_r = \frac{8z^* eV}{m(r_0^2 + 2z_0^2)\Omega^2} \tag{1.5}$$

The solutions of equation 1.4 and 1.5 can be visualized in the a_z/q_z space, giving a stability diagram as shown in Figure 1.3.4 (panel b). Typically a_z equals zero since no DC voltage is applied ($U = 0$) in most commercial QITs. Therefore, the mass stability is solely determined by q_z, which is confined to a maximum value of $q_z = 0.908$. For q_z values exceeding this threshold, the corresponding ion trajectories are unstable in z direction, leading to ejection of the ions to the detector. During operation this behavior of the ions is used in the mass selective instability mode: Ions with increasing m/z values are successively destabilized by increasing the RF amplitude V. Commonly, combinations of conversion dynodes and secondary electron multipliers are utilized for detection of the ejected ions (Edmond Hoffmann, 2007; Gross, 2013).

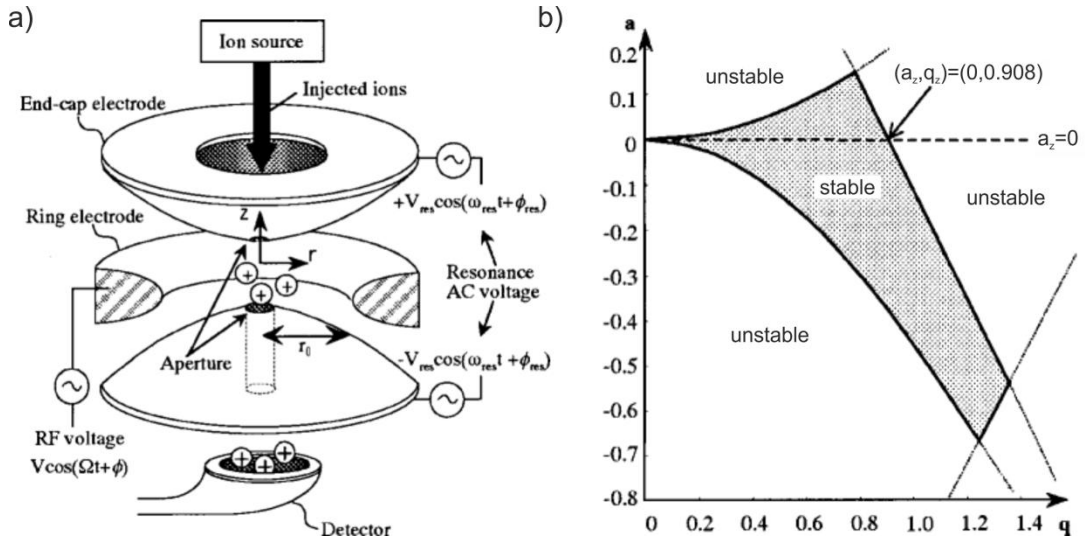

Figure 1.3.4: (a) Schematic of a QIT. (b) Stability diagram of ion trajectories (Yoshinari, 2000).

Mass resolution and sensitivity of QITs can significantly be improved by adding a damping gas at low pressures (~0.1 Pa) to the ion trap, which in most cases is carried out using helium. Collisions between the damping gas and ions in the trap are reducing kinetic energies of the ions, and are thereby focusing these in the center of the trap. The resulting spatially uniform trajectories of the stored ions serve two advantages: Firstly, ions are kept away from inhomogeneities of the electric field in the QIT, which are induced by the entrance and exit apertures. And secondly, ions of a given m/z value exhibit uniform starting points during the ejection procedure.

Additionally, the damping gas can also be used for collision-induced dissociation (CID) of the stored ions and, therefore, allows structural elucidation of ions by MS^n studies. To

perform CID, ions with one *m*/*z* ratio are isolated in the QIT by combining forward and backward scans in the mass selective instability mode and the resonant ejection mode, i.e. an additional RF is applied to the end-cap electrodes and brought into resonance with the *m*/*z* ratios that need to be ejected. After isolation the selected ions are stored at $q_z = 0.25$ and accelerated by resonance excitation. Collisions between the damping gas and the excited ions now result in fragmentation. The resulting fragment ions are ejected successively in the mass selective instability mode towards the detector, revealing structural information (Edmond Hoffmann, 2007; Gross, 2013).

1.4 Thesis Objectives and Outline

The chemical analysis of ambient aerosols represents an enormous challenge due to its high complexity and dynamic behavior. In particular, a comprehensive characterization of OA particles, mostly comprising myriads of different compounds, is often impeded by a lack of suitable instrumentation. Although mass spectrometry has proven a suitable and versatile tool in aerosol research, current approaches are typically either time-consuming and tedious or not capable of identifying and monitoring single organic substances. However, the advent of ADI–MS has led to promising developments in soft ionization techniques during the last years which might aid in overcoming these barriers in the future.

The aim of this work was to explore and assess the applicability of the FAPA ionization technique, which represents a common ADI source, to the offline as well as online analysis of OA particles and substances found therein. In addition, ionization pathways and desorption characteristics in the afterglow region were investigated to gain a more detailed understanding of the underlying processes. Based on the pin-to-capillary design, first described by Shelley *et al*. (2011), a prototype was developed and constructed which allowed operation in both offline and online mode. A description of this prototype including circuit layouts and technical drawings can be found in the appendix (section D).

The first part of this study focusses on the application, characterization and assessment of FAPA–MS in the offline mode. Ionization patterns in the positive as well as the negative ion mode were investigated for a variety of compound classes comprising alkanes, alcohols, aldehydes, ketones, carboxylic acids, organic peroxides, and alkaloids. In addition, the capabilities and limitations of the technique were studied in three proof-of-principle applications.

In the second and also the following parts FAPA–MS was applied for the real time analysis of OA particles. Therefore, the acronym AeroFAPA–MS (i.e. Aerosol FAPA–MS) was chosen to describe this method. After optimization and characterization, a range of model compounds was analyzed using AeroFAPA–MS to evaluate typical ionization patterns in the positive and the negative ion mode. Additionally, results from laboratory studies as well as from a field campaign in Central Europe (F–BEACh 2014) are presented and discussed.

The third part is a more in-depth analysis of the results obtained during the F–BEACh 2014 campaign. In addition to the AeroFAPA–MS measurements, data from a variety of complementary MS methods are presented and discussed, giving a comprehensive characterization of the sampled OA particles. Moreover, in this section AeroFAPA–MS is shown to be capable of detecting compounds of a recently described class of highly oxidized sulfur-containing compounds in the particle phase.

While in the previous sections aerosol particles were pre-evaporated prior to AeroFAPA–MS analysis, in the last part of this study particle desorption characteristics in the afterglow region were investigated without additional heating, indicating that only an interfacial layer of OA particles is desorbed and, thus, chemically characterized. This finding suggests that AeroFAPA–MS might represent a promising technique for depth profiling of OA particles in real time. Therefore, the method was applied for the analysis of laboratory-generated core-shell particles in a proof-of-principle study.

2 Ambient Desorption/Ionization Mass Spectrometry Using FAPA–MS

This chapter is a reprint of the manuscript:

Martin Brüggemann, Einar Karu, Thorsten Hoffmann

Critical Assessment of Ionization Patterns and Applications of Ambient Desorption/Ionization Mass Spectrometry Using FAPA–MS

In preparation for Journal of Mass Spectrometry

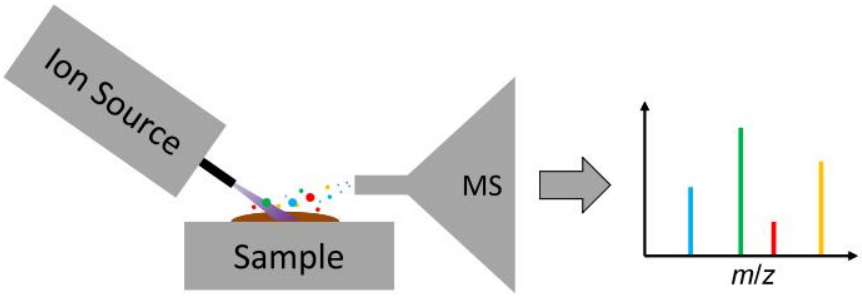

Abstract

Ambient Desorption/Ionization Mass Spectrometry (ADI–MS) has gained a lot of interest during the last decade due to its high analytical performance and yet simplicity. Here, one of the developed ADI–MS sources, the flowing atmospheric-pressure afterglow (FAPA) source, was investigated regarding typical ionization patterns in the positive and the negative ion mode for a variety of compound classes, comprising alkanes, alcohols, aldehydes, ketones, carboxylic acids, organic peroxides, and alkaloids. A broad range of signals for adducts and losses was found, besides the always emphasized detection of quasimolecular ions, i.e. $[M+H]^+$ and $[M–H]^-$ in the positive and the negative mode, respectively. Additionally, the source was used in three different fields of analytical chemistry: Firstly, the detection and identification of cocaine on Euro banknotes, suggesting a correlation between cocaine abundance and age of the banknote. Secondly, the identification of acidic marker compound in organic aerosol samples, possibly revealing yet undiscovered matrix and sample surface effects of FAPA–MS ionization pathways. And thirdly, the analysis of stalagmite samples which demonstrated that the method is capable of detecting sample contamination.

2.1 Introduction

In his book from 1913 “Rays of Positive Electricity and Their Application to Chemical Analyses”, J. J. Thompson already notes that mass spectrometry (MS) is a “surprisingly sensitive [method]… [which] requires an infinitesimal amount of material, and does not require this to be specially purified…”(Thomson, 1913). Since then, MS has become a powerful and versatile tool for chemical analyses, yet, mostly in combination with separation and purification techniques such as chromatography. Only since the last decade, the rise of Ambient Desorption/Ionization MS (ADI–MS) has led to a quickly growing number of techniques and methods that not only allow but also facilitate the analysis of samples under ambient conditions without the need for purification. Numerous ion sources were developed under this concept and used for applications such as the analysis of biological tissues (Eberlin *et al.*, 2011), the screening of gunshot residues (Morelato *et al.*, 2012), or the detection of pesticides on fruits (Shelley and Hieftje, 2011).

In general, these ADI–MS ion sources can be divided into two main classes: spray-based sources and plasma-based sources. Spray-based sources, e.g. desorption electrospray ionization (DESI) (Takats, 2004), apply electrospray-like ionization processes, whereas

plasma-based sources, e.g. direct analysis in real time (DART) (Cody *et al.*, 2005), rely on ionization mechanisms that are similar to atmospheric-pressure chemical ionization (APCI). However in contrast to common APCI sources, ADI sources typically use helium as discharge gas to create reagent ions. The prevalence of helium is due to the high excitation energies of 19.6 and 20.4 eV of its metastables, which lie above the ionization energy of nearly every molecule. In addition, the nonradiative lifetimes of these species are in the range of seconds, supporting a rich ion chemistry and effective chemi-ionization in the ionization region (Andrade *et al.*, 2008; Raizer *et al.*, 2011). One prerequisite of all plasma-based ADI–MS sources is to have the analyte present in the gas phase. Although a few alternative routes have been hypothesized, it is generally believed that this is achieved by thermal desorption. In most cases, however, it is already sufficient to have a quite low amount of molecules present in the gas phase above the sample, thus, also compounds with rather low vapor-pressures and high molecular weights can be analyzed (Jecklin *et al.*, 2008; Monge *et al.*, 2013).

One of these plasma-based ADI–MS sources is the flowing atmospheric-pressure afterglow (FAPA) source, which will be focused in this study. The sources utilizes an atmospheric pressure glow discharge (APGD) to generate excited helium species and reagent ions, which form the so-called afterglow region in front of the source. In positive ion mode, ionization of the analytes occurs mainly by charge transfer from protonated water clusters ($[(H_2O)_n+H]^+$ with n=1,2,3,…), which are eventually formed from reactions between exited helium metastables, nitrogen and water vapors, typically present under ambient conditions (Andrade *et al.*, 2008; Shelley *et al.*, 2009). Although the negative ion mode for this source is less characterized in the literature, it is assumed that ionization mainly occurs via oxygen species such as O_2^-, which can deprotonate the analyte molecules (Schilling *et al.*, 2010). In contrast to ion sources such as DART, no additional heat source is necessary for thermal desorption in the afterglow region due to the inherent heating of the APGD, leading to afterglow temperatures of ~50–250 °C (Shelley *et al.*, 2009; Shelley *et al.*, 2011).

So far, the FAPA source has been used for applications such as the detection of explosives and pesticides (Jecklin *et al.*, 2008; Shelley *et al.*, 2011), the analysis of human urine (Schaper *et al.*, 2012), or the identification of compounds in airborne particulate matter (Brüggemann *et al.*, 2015). Commonly, the source is described as a soft ionization technique which favors the formation of quasimolecular ions, yielding $[M+H]^+$ and $[M–H]^-$ in the positive and the negative mode, respectively. However, adduct formation and/or

fragmentation processes occurring in the afterglow region are rarely discussed. Nevertheless, to apply FAPA–MS to appropriate analytical tasks it is essential to know not only the capabilities but also the limitations of this method. Therefore, this study tries to give a critical view on typical ionization patterns for a variety of compound classes analyzed by ambient desorption FAPA–MS. At first, background mass spectra in positive and negative ion mode were measured and common contaminants as well as reagent ions could be identified. Then, typical ionization characteristics of FAPA–MS were investigated for a variety of compound classes. Furthermore, the method was used in proof-of-principle studies to detect and identify traces of cocaine on Euro banknotes, acidic marker compounds in organic aerosol (OA) samples, and organic compounds on stalagmite samples, demonstrating possible fields of application.

2.2 Experimental

2.2.1 Reagents and Materials

All reagents were analytical-grade. A comprehensive list of all substances used is given in the Supplemental Material.

2.2.2 Design and Setup of the Ion Source

The design of the ion source is similar to the pin-to-capillary FAPA described by Shelley *et al.* (Shelley *et al.*, 2011), thus, only a brief description will be given here (Figure 2.2.1). The ion source is made of a ceramic discharge chamber (Marcor, MCI UG, Neumünster, Germany) in which an APGD is sustained between two stainless steel electrodes. A pin electrode (outer diameter 3.00 mm) serves as the cathode, whereas a capillary electrode (outer diameter 3.18 mm, inner diameter 1.40 mm) functions as anode. The distance between the tip of the cathode and the anode is set to 7 mm. A port in the back of the source body serves as an inlet for helium (5.0, Westfalen AG, Münster, Germany) which is used as discharge gas. The helium flow was typically set to 0.6 $L \cdot min^{-1}$. A dc high voltage power supply (PTV-3N200, Spellman High Voltage Electronics Corporation, Hauppauge, NY, USA) was used to apply a negative potential to the cathode through a 5 kΩ ballast resistor in order to create and maintain the discharge. All experiments were carried out under current controlled conditions with I = 55 mA, resulting in discharge voltages of ~450 V. The exit capillary electrode was held at potentials of +15

V in the positive mode and –15 V in the negative mode to maintain a field-free region between the ion source and the MS inlet.

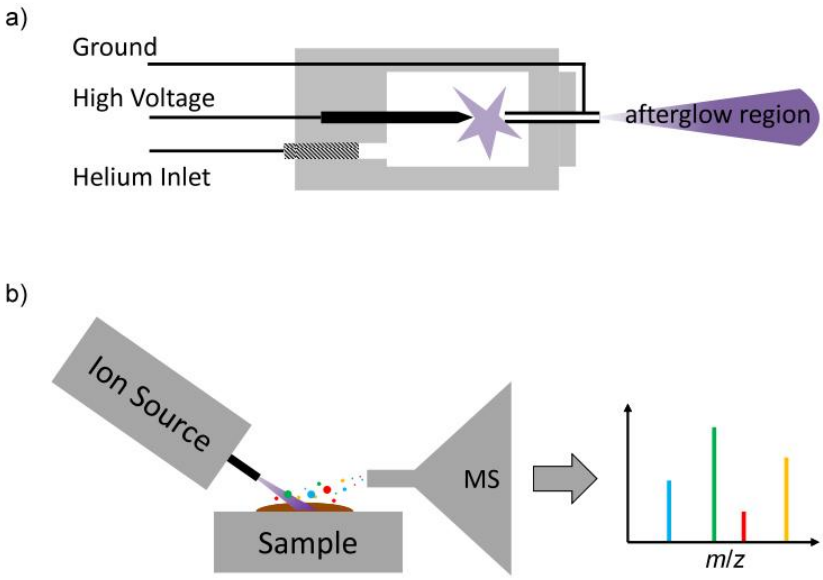

Figure 2.2.1: (a) Cross sectional drawing of the FAPA ion source. A helium APGD is maintained between the pin and the capillary electrode. Exited helium species exiting the ion source and primary reagent ions form the afterglow region in front of the FAPA. (b) Setup for ambient desorption FAPA–MS. The afterglow is directed towards the sample to desorb and ionize the analytes which are subsequently detected by MS.

Ambient desorption experiments were carried out by placing the sample directly in front of the MS inlet and directing the afterglow towards the sample surface with a desorption angle of 90°. The distance between the sample and the MS inlet was set to <5 mm using a xyz-stage. The distance between the ion source and the sample was set to ~5 mm. For the analysis of pure compounds 10 µL of a methanolic solution ($c = 10^{-2}$ mol·L^{-1}) were applied on a glass slide. For compounds that were not soluble in methanol dichloromethane was used as solvent instead.

2.2.3 Mass Spectrometric Analyses

Mass spectra were recorded using an LCQ Deca XP Plus ion trap MS (Thermo, San José, CA, USA). The MS inlet was heated to 200 °C and a potential of +15 V was applied in the positive mode, whereas –15 V were used in the negative mode. In both polarities no potentials were applied to the tube lens. Automatic gain control was used for recording mass spectra with five microscans per spectrum and a maximum injection time of 200 ms. Structural elucidation of the tested compounds was performed by collision-induced

dissociation (CID) and the subsequent recording of MS^n spectra. All mass spectra were recorded and processed using XCalibur 2.0.7 (Thermo, San José, CA, USA).

2.2.4 Aerosol Particle Generation and Sampling

A detailed description of the method that was used to generate secondary OAs via terpene oxidation can be found elsewhere (Müller *et al.*, 2008; Brüggemann *et al.*, 2014). Briefly, secondary OA particles were generated by limonene oxidation under dark and dry conditions (RH <30%) using a 100 L continuous-flow reaction vessel. Gaseous limonene was introduced into the chamber using a thermally controlled diffusion source (Thorenz *et al.*, 2012), leading to a gas-phase concentration of 290 ppb. Ozone was generated by an ozone generator (1008-RS, Dasibi Environmental Corp., Glendale, CA, USA) and introduced into the chamber to give a concentration of roughly 1 ppm. Moreover, gaseous tetramethylethylene (TME) was added as a source for OH radicals with a concentration of 1500 ppb. The average residence time of the particles in the chamber was ~15 min. A condensational particle counter was used to measure the formation of aerosol particles. Temperature and humidity in the chamber were monitored by a built-in sensor. After the reaction reached a steady-state inside the chamber, aerosol particles were collected on tetrafluorethylene(TFE)-coated borosilicate fiber filters (Pallflex T60A20, Pall Life Sciences, USA) for four hours using a flow rate of 2.0 $L \cdot min^{-1}$.

2.2.5 Stalagmite Sample Analysis

The stalagmite sample was taken from Herbstlabyrinth-Adventhöhle cave system, Germany. A few pieces of the stalagmite were taken and cleaned by sonification in a solution of dichloromethane/methanol (9:1). Afterwards, the samples were dried under ambient conditions and stored in polyethylene (PE) bags until analysis. Sample manipulation was solely conducted using stainless steel tweezer to avoid contamination. For the analysis, the samples were taken out of the storage bag and placed directly in the afterglow region on a glass slide without further treatment.

2.3 Results and Discussion

2.3.1 Ionization Mechanisms and Background Mass Spectra of the FAPA source

In order to characterize the FAPA source and to evaluate its analytical performance, background mass spectra in the positive and the negative mode were acquired. Figure 2.3.1 shows a typical background mass spectrum that was obtained in the positive ion mode when a clean glass slide was positioned in the afterglow of the FAPA source. In the mass range from *m*/*z* 50 to 500 (top panel) intense signals can be seen for common plasticizers and their degradation products such as Phthalic Anhydride (*m*/*z* 149, $[M+H]^+$), Dibutylphthalate (*m*/*z* 279, $[M+H]^+$), or Diisooctylphthalate (*m*/*z* 391, $[M+H]^+$). These compounds are typical MS contaminants and are also reported for other ion sources operating under ambient conditions, e.g. ESI–MS (Keller *et al.*, 2008). Other well-known and detected contaminants are Polyethyleneglycols (e.g. *m*/*z* 327, $[M+H]^+$), flame retardants (e.g. *m*/*z* 344, $[M+H]^+$), and Polysiloxanes (e.g. *m*/*z* 371, $[M+H]^+$) (Keller *et al.*, 2008). The ubiquity of these substances in indoor environments impedes a clear source identification. However, since these signals were even visible when no glass slide was present in the afterglow it is very likely that these compounds were rather present in the ambient laboratory air during the measurements than being desorbed from the glass slide.

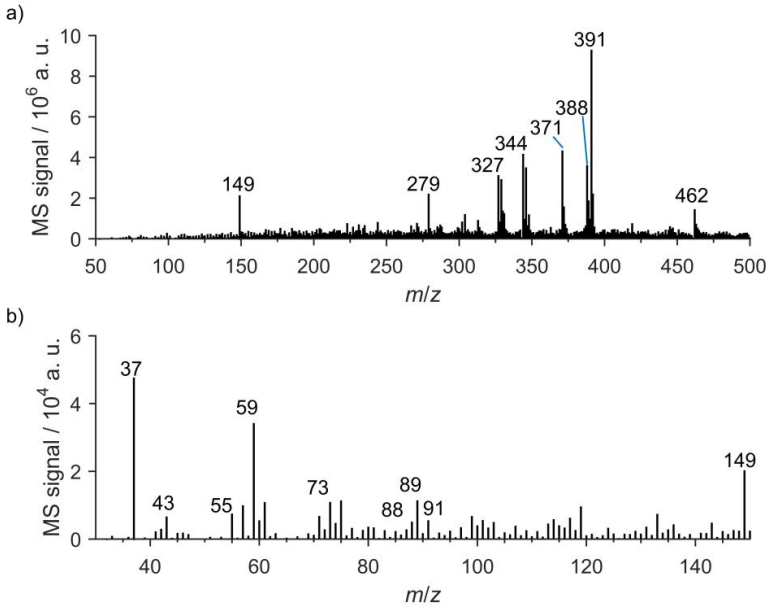

Figure 2.3.1: Background mass spectrum in the positive ion mode of FAPA–MS when measuring a clean glass slide. Panel (a) shows the mass range from *m*/*z* 50 to 500. Panel (b) exhibits the low mass range from *m*/*z* 30 to 150. The annotated *m*/*z* values correspond to typical compounds that are present in ambient laboratory air (Table 2.3.1).

Table 2.3.1: Background ions in positive ion mode which were observed for ambient desorption FAPA–MS.

m/z	Corresponding Ion	Comment / Reference
19	H_3O^+	Schilling *et al.* (2010)
28	N_2^+	Shelley *et al.* (2009)
30	NO^+	Shelley *et al.* (2009)
32	O_2^+	Shelley *et al.* (2009)
37	$[(H_2O)_2H]^+$	Shelley *et al.* (2009)
42	$[(ACN)H]^+$	HPLC solvent
43	$C_2H_3O^+$	Fragment of Acetone or Ethyl Acetate
44	CO_2^+	Andrade *et al.* (2008)
46	NO_2^+	Schilling *et al.* (2010)
48	$[(H_2O)NO]^+$	
55	$[(H_2O)_3H]^+$	Shelley *et al.* (2009)
59	$[(Acetone)H]^+$	Solvent
60	$[(ACN)H_3O]^+$	HPLC Solvent
73	$[(H_2O)_4H]^+$	
74	$[(ACN)(MeOH)H]^+$	HPLC solvent
88	$[(ACN)(Formic\ Acid)H]^+$	HPLC solvent
89	$[(Ethyl\ Acetate)H]^+$	Solvent
91	$[(H_2O)_5H]^+$	
109	$[(H_2O)_6H]^+$	
149	$[(Phthalic\ Anhydride)H]^+$	Fragment of phthalate esters
279	$[(Dibutylphthalate)H]^+$	Plasticizer
327	$[(Triphenylphosphate)H]^+$	Flame retardant in plastics
	$[(Polyethyleneglycol)H]^+$	PEG, ubiquitous polyether
344	$[(Triphenylphosphate)NH_4]^+$	Flame retardant in plastics
371	$[(Polyethyleneglycol)H]^+$	PEG, ubiquitous polyether
	$[(Polysiloxane)NH_4]^+$	Polysiloxane, followed by *m/z* 388
388	$[(Polysiloxane)NH_4]^+$	Polysiloxane, (see *m/z* 371)
391	$[(Diisooctylphthalate)H]^+$	Plasticizer
445	$[(Polysiloxane)NH_4]^+$	Polysiloxane, followed by *m/z* 462
462	$[(Polysiloxane)NH_4]^+$	Polysiloxane, (see *m/z* 445)

In the lower mass range (*m/z* 30–150) several primary reagent ions can be observed (Figure 2.3.1 bottom panel). The most abundant signal was found for the reagent ion $[(H_2O)_2H]^+$ at *m/z* 37. Due to the extremely high gas-phase acidity of this protonated water-cluster, this reagent ion is a very efficient proton-transfer agent and allows even the ionization of compounds with low gas-phase basicity, yielding $[M+H]^+$ quasimolecular ions (Shelley *et al.*, 2009). In addition, reagent ions like NO^+, O_2^+, NO_2^+, and CO_2^+ were reported, and also observed here, for the FAPA source (Andrade *et al.*, 2008; Shelley *et al.*, 2009; Schilling *et al.*, 2010). These additional reagent ions are capable of ionizing compounds via charge-transfer processes, and thus, offer alternative routes of ionization besides proton-transfer, leading to a broader range of suitable analytes. Nevertheless, these

ionization mechanisms may also lead to the formation of adducts and oxidation of the original analyte compounds, as it will be discussed below. Besides primary reagent ions, the mass spectrum also exhibits signals for solvents that are typically used in laboratory environments, such as Acetonitrile (*m*/*z* 42, $[M+H]^+$), Acetone (*m*/*z* 59, $[M+H]^+$), or Ethylacetate (*m*/*z* 89, $[M+H]^+$). These compounds were probably present in the ambient air during the analysis, and thus, contributed to the background mass spectrum. A complete list of detected and identified ions in background spectra of FAPA–MS for the positive ion mode is given in Table 2.3.1.

In the negative ion mode the background mass spectra appear much cleaner, as can be seen in Figure 2.3.2. In the mass range of *m*/*z* 50–400 (top panel), solely two signals, at *m*/*z* 62 and 125, are dominating the mass spectrum. These signals correspond to the formation of nitrate ions in the afterglow region (*m*/*z* 62 = NO_3^-, *m*/*z* 125 = $H(NO_3)_2^-$). Additional signals were measured in this mass range but exhibit intensities which are lower by two orders of magnitude, as depicted in the inset. In negative mode the main ionization mechanism is deprotonation by O_2^- ions, which leads to a high selectivity towards carboxylic acids since these compounds show high gas-phase acidities. Therefore, the background signals of the negative mode can be correlated to a large extent to ubiquitous acids like oxalic acid (*m*/*z* 89 = $[M–H]^-$) or fatty acids, e.g. *m*/*z* 255 = $[(\text{Palmitic Acid})–H]^-$.

The high abundance of NO_3^- ions is the result of the production of O_3 and NO_2 in the afterglow region. N_2 and O_2 are dissociated by electron capture giving atomic N and O, eventually leading to generation of O_3 and NO_2 (Sekimoto and Takayama, 2011). Similar to corona discharges in air, NO_3^- is formed due to the presence of O^- and O_2^- ions via the following pathways (Nagato *et al.*, 2006):

$$O^- + NO_2 \rightarrow NO_2^- + O \qquad (1)$$
$$O_2^- + NO_2 \rightarrow NO_2^- + O_2 \qquad (2)$$
$$NO_2^- + O_3 \rightarrow NO_3^- + O_2 \qquad (3)$$

Furthermore, O_3 can react with O^- and O_2^- to give O_3^-, which can then form NO_3^- by the reaction with NO_2 (Nagato *et al.*, 2006):

$$O^- + O_3 \rightarrow O_3^- + O \qquad (4)$$
$$O_2^- + O_3 \rightarrow O_3^- + O_2 \qquad (5)$$
$$O_3^- + NO_2 \rightarrow NO_3^- + O_2 \qquad (6)$$

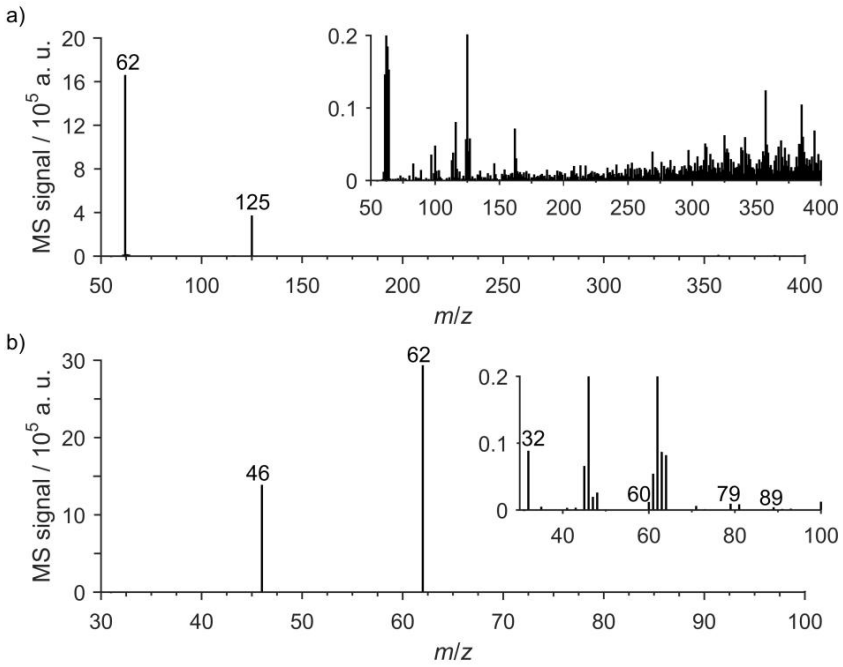

Figure 2.3.2: Background mass spectrum in the negative ion mode of FAPA–MS when measuring a clean glass slide. Panel (a) shows the mass range from *m*/*z* 50 to 400. The inset shows the same spectrum magnified by factor 100. Panel (b) exhibits the low mass range from *m*/*z* 40 to 150. The annotated *m*/*z* values correspond to the ions discussed in Table 2.3.2.

In the lower mass range (*m*/*z* 30–100, Figure 2.3.2 bottom panel), additional primary ions besides NO_3^- (*m*/*z* 62) and $(HNO_3)NO_3^-$ (*m*/*z* 125) can be observed. The signal at *m*/*z* 46 correlates to the formation of NO_2^- ions which are generated via reaction pathways (1) and (2). Additionally, the reaction of OH^- with NO_2 represents an alternative route towards the formation of NO_2^- (Nagato *et al.*, 2006). Significantly lower signals were measured for reagent ions such as O_2^- (*m*/*z* 32), or CO_3^- (*m*/*z* 60). One reason for the low abundance of these species is the low lifetime of these ions in ambient air. For example, O_2^- exhibits a lifetime below 10^{-5} s while NO_3^- and NO_2^- have lifetimes in the range of 10 s and >1 s, respectively (Sekimoto and Takayama, 2011). A second reason is the lower concentration of CO_2 in ambient air compared to N_2 and O_2, which is necessary for the production of C-containing ions such as CO_3^-. In addition to these primary reagent ions, signals for silicon containing oxides, such as SiO^- (*m*/*z* 44), can be observed due to the utilization of a ceramic discharge cell. A list of common primary reagent ions that are present in plasma-based ion sources operating under ambient conditions, such as FAPA or APCI, and assigned background signals in the negative mode is given in Table 2.3.2.

Table 2.3.2: Background ions that were observed for ambient desoprtion FAPA–MS in negative ion mode.

m/z	Corresponding Ion	Comment / Reference
16	O^-	Schilling *et al.* (2010)
17	HO^-	Sekimoto *et al.* (2011)
		Schilling *et al.* (2010)
32	O_2^-	Sekimoto *et al.* (2011)
		Schilling *et al.* (2010)
33	HO_2^-	Sekimoto *et al.* (2011)
		Schilling *et al.* (2010)
44	SiO^-	Schilling *et al.* (2010)
45	HCO_2^-	Sekimoto *et al.* (2012)
46	NO_2^-	Sekimoto *et al.* (2011)
		Schilling *et al.* (2010)
48	O_3^-	Schilling *et al.* (2010)
60	CO_3^-	Sekimoto *et al.* (2011)
	SiO_2^-	Schilling *et al.* (2010)
61	HCO_3^-	Nagato *et al.* (2006)
62	NO_3^-	Sekimoto *et al.* (2011)
63	$(H_2O)HCO_2^-$	Water cluster of *m/z* 45
64	$(H_2O)NO_2^-$	Sekimoto *et al.* (2012)
76	CO_4^-	Nagato *et al.* (2006)
	SiO_3^-	Schilling *et al.* (2010)
77	HCO_4^-	Sekimoto *et al.* (2011)
79	$(H_2O)HCO_3^-$	Sekimoto *et al.* (2012)
83	–	–
89	$[(\text{Oxalic Acid})–H]^-$	Ubiquitous acid
100	–	–
108	$(NO_2)NO_3^-$	Nagato *et al.* (2006)
109	$(HNO_3)NO_2^-$	Nagato *et al.* (2006)
117	–	–
123	$(HNO_3)CO_3^-$	Nagato *et al.* (2006)
124	$(HNO_3)HCO_3^-$	Nagato *et al.* (2006)
125	$H(NO_3)_2^-$	Sekimoto *et al.* (2011)
162	–	–
188	$H_2(NO_3)_3^-$	Sekimoto *et al.* (2011)

2.3.2 Assessing Ionization Characteristics of FAPA–MS for Different Compound Classes

In order to assess and critically evaluate the FAPA's ionization characteristics a range of different organic compound classes was analyzed, comprising alkanes, alcohols, aldehydes, ketones, carboxylic acids, organic peroxides, and alkaloids. A complete list of all compounds can be found in the Supplemental Material (Table 5.5.3). From these measurements a comprehensive list of observed adducts and losses in correlation to the corresponding compound classes was constructed, as can be seen in Table 2.3.3. In addition, a possible origin for the observed mass difference is given.

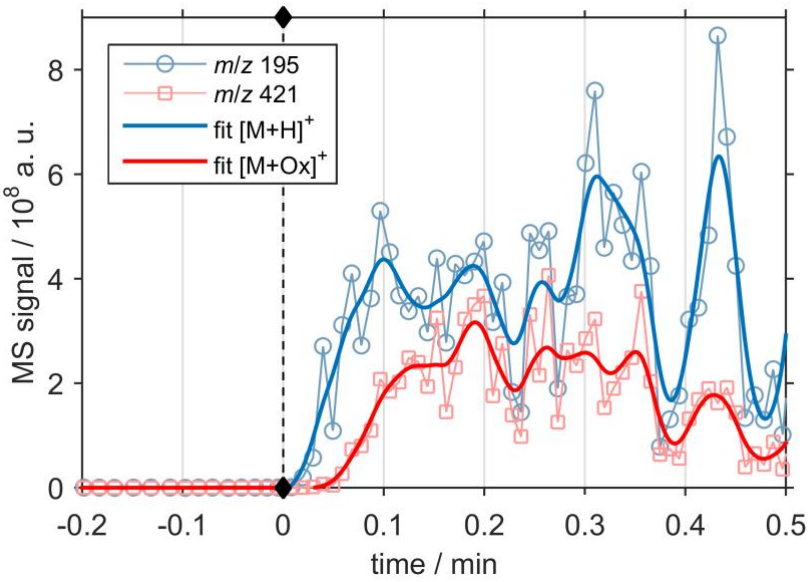

Figure 2.3.3: Analysis of a methanolic caffeine solution from a glass slide (sample deposition at 0 min). The signal of the oxidation product (*m*/*z* 421) appears much slower than for the quasimolecular ion at *m*/*z* 195 ($[M+H]^+$), demonstrating the competition between adduct formation and oxidation of the analyte in the afterglow region.

In the positive ion mode, for almost all oxygen- and/or nitrogen-containing compounds one of the most abundant signals is correlating to protonation during ionization, yielding $[M+H]^+$. Additionally, adduct formation with primary reagent ions, such as O^+, NO^+, O_2^+ and NO_2^+, or even ammonium (NH_4^+) was observed with high abundances for the majority of these compounds. Fragmentations, such as the loss of H_2O, CO, or CO_2, were only observed to a low extent, suggesting that FAPA–MS is a soft-ionization method. However, besides adduct formation signals correlating to oxidation processes occurring in the afterglow region were observed to a large extent for compounds containing long carbon chains, such as fatty acids or alkanes. For the compounds tested in this work the extent of oxidation was increasing with the number of CH_2 groups and the time of the sample in the afterglow region. In particular, for low vapor pressure compounds, such as stearic acid, signals correlating to oxidation were dominating the mass spectrum during desorption and ionization of the sample. However, even for more volatile compounds which showed intense signals for their corresponding quasimolecular ion, i.e. $[M+H]^+$ or $[M–H]^–$, oxidation products could be observed with increasing analysis time, clearly demonstrating the competition between adduct formation and oxidation of compounds in the afterglow region. As can be seen in Figure 2.3.3, during the analysis of caffeine the quasimolecular ion at *m*/*z* 195 ($[M+H]^+$) is almost immediately formed after sample deposition. Yet, after a few seconds the signals of an oxidation product at *m*/*z* 421 are also showing significant

abundances and are increasing with time. Therefore it is assumed that adduct formation in the gas phase is a rapid process, happening in <<1 s, whereas the formation of oxidation products, desorption and subsequent ionization requires a certain time interval. Thus, the gas-phase transfer might represent a time critical step, meaning that low volatile compounds are more prone to oxidation processes than semi- or high volatile compounds which are rapidly desorbed into the gas phase. In addition, the number of possible attack sites for reactive oxygen species is increasing with the number of CH_2 groups, explaining the large extent of oxidation for fatty acids.

In the negative ion mode, a similar trend could be observed. Not surprisingly, for carboxylic acids, signals corresponding to deprotonation were among the most abundant since these compounds exhibit high gas-phase acidities. However, for less acidic compounds adduct formation with primary reagent ions was observed, in most cases for $[M+NO_3]^-$, which is possibly due to the long lifetime of this reagent ion in ambient air. Additionally, adduct formation with chloride was observed when DCM was used as solvent. Similar to the positive ion mode, fragmentation processes were only observed to a low extent and only for rather labile compounds. Furthermore, oxidation of carbon chains was also observed, although, less corresponding signals were detected in total. Nonetheless, signals for oxidation were also increasing with the number of CH_2 groups and decreasing vapor pressures.

Based on these measurements it is generally assumed that ambient desorption FAPA–MS is best suited for polar analytes containing nitrogen- and/or oxygen functionalities with low molecular weights and high vapor pressures. For measurements in the positive ion mode nitrogen-containing compounds, such as amines and alkaloids, represent ideal analytes since these species are readily protonated However, for negative mode measurements the analytes should show high gas-phase acidities, such as carboxylic acids, giving $[M–H]^-$ ions. Since low volatile compounds are easily prone to oxidation processes occurring in the afterglow, the compounds of interest should exhibit a certain volatility to get easily desorbed and transferred into the gas phase where subsequent ionization occurs.

Table 2.3.3: Adducts and losses for offline FAPA–MS in positive and negative mode.

	Mass difference	Origin	Mainly observed for
Positive Mode	+1	Protonation $[M+H]^+$	Alcohols, Ketones, Carboxylic Acids, Sugars, Alkaloids/Amines
	+13	Oxidation	Fatty Acids, Long Carbon Chains
	+15	Oxidation	Fatty Acids, Long Carbon Chains
	+17	Oxidation $[M+H+O]^+$	Fatty Acids, Long Carbon Chains
	+18	Ammonium adduct $[M+NH_4]^+$	Carboxylic Acids, Peroxides, Sugars
	+25	Oxidation	Fatty Acids, Long Carbon Chains
	+29	Oxidation	Fatty Acids, Long Carbon Chains
	+31	Oxidation	Fatty Acids, Long Carbon Chains
	+32	Oxygen adduct $[M+O_2]^+$	Ketones, Carboxylic Acids, Peroxides
	+46	NO_2 adduct $[M+NO_2]^+$	Ketones, Carboxylic Acids
	-1	Oxidation & loss of water $[M+O+H–H_2O]^+$	Fatty Acids, Long Carbon Chains
	-18	Loss of H_2O	Carboxylic Acids, Alcohols
	-28	Loss of CO	Ketones, Aldehydes
	-44	Loss of CO_2	Carboxylic Acids
Negative Mode	-44	Loss of CO_2	Carboxylic Acids
	-28	Loss of CO	Ketones, Aldehydes
	-18	Loss of H_2O	Carboxylic Acids, Alcohols
	-1	Deprotonation $[M–H]^-$	Carboxylic acids
	+16	Oxygen adduct $[M+O]^-$	Aromatics, Carboxylic Acids,
	+31/+32	Oxygen adduct $[M–H+O_2]^-/[M+O_2]^-$	Aromatics, Fatty Acids, Sugars
	+46	Nitrite adduct $[M+NO_2]^-$	Fatty Acids, Amines
	+62	Nitrate adduct $[M+NO_3]^-$	Carboxylic Acids, Amines, Sugars
	+92	Oxidation	Fatty Acids
	+108	Oxidation	Fatty Acids
	+123	Adduct $[M+(HNO_3)CO_3]^-$	Carboxylic Acids, Fatty Acids
	+124	Adduct $[M+(HNO_3)HCO_3]^-$	Fatty Acids
	+139	Oxidation	Fatty Acids
	+155	Oxidation	Fatty Acids
	+171	Oxidation	Fatty Acids

2.3.3 Applications of Ambient Desorption/Ionization FAPA–MS

Detection and Identification of Cocaine on Banknotes

It is well known that traces of cocaine and other illicit drugs are worldwide nearly ubiquitous found on banknotes due to the distribution of these substances by consumers, dealers, and particularly contaminated counting-machines in banks (Oyler *et al.*, 1996; Sleeman *et al.*, 2000). Despite these high background levels of controlled substances,

several studies have shown that it is still possible to distinguish normal background contaminated banknotes from drug money, i.e. banknotes that were used for buying, selling or consuming these substances (Sleeman *et al.*, 2000). In order to identify these highly contaminated banknotes, MS has proven a suitable tool due to its high sensitivity. However, prior to mass spectrometric detection common methods typically require extraction steps like solvent extraction and/or solid-phase microextraction (SPME) which are then followed by chromatographic separation. Thus, the analysis of a large amount of banknotes can become a tedious and time-consuming task. Moreover, additional evidence on the surface of banknotes, e.g. fingerprints, may get lost during the extraction and processing steps. Addressing these drawbacks several studies have shown that ambient ionization/desorption MS techniques, may be an alternative method in sensing paper currency for controlled substances and drug money (Talaty *et al.*, 2008; Eberlin *et al.*, 2010).

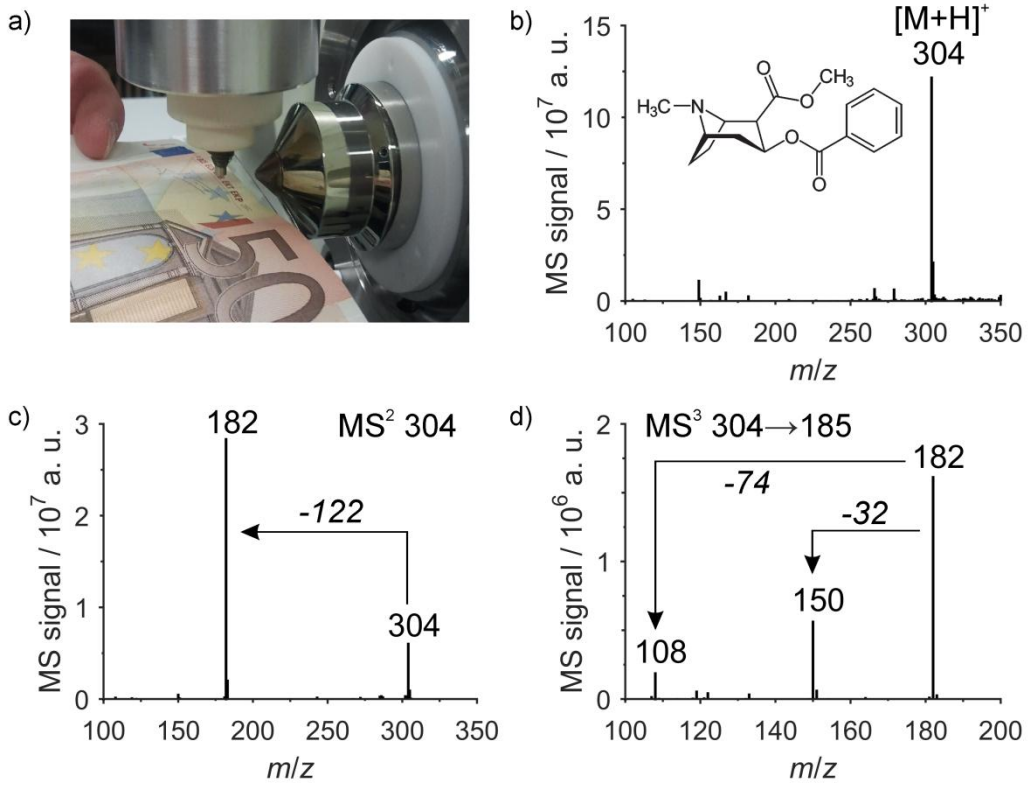

Figure 2.3.4: Detection of traces of cocaine on a 50 Euro banknote. (a) Photograph of the experimental setup during the analysis. (b) Full scan mass spectrum in the positive mode. An intense signal for the quasimolecular ion of cocaine $[M+H]^+$ can be observed at *m/z* 304. (c) MS^2 spectrum of the ion at *m/z* 304, showing the loss of benzoic acid (–122 u). (d) MS^3 spectrum of *m/z* 304 →182 showing the loss of methanol (–32 u) and $C_3H_6O_2$ (–74 u).

It has been shown that FAPA–MS is capable of ionizing and detecting trace amounts of organic compounds on a variety of substrates (Andrade *et al.*, 2008; Shelley *et al.*, 2011). Therefore, as a proof-of-principle study FAPA–MS was applied for the detection and unambigous identification of cocaine on Euro banknotes. As can be seen from Figure 2.3.4, in the full scan spectrum (panel b) an intense signal for the quasimolecular ion of cocaine (*m*/*z* 304, $[M+H]^+$) was observed when a 50 Euro banknote was placed in the afterglow region in front of the MS inlet. Similar observations were made for other banknotes with values ranging from 5 to 50 Euros. Remarkably, the abundance of the signals at *m*/*z* 304 was not correlating with the value of the banknote but rather with its estimated age, as can be seen in Figure 2.3.5. To estimate the age of the banknotes the serialnumbers and printing codes were used and correlated with annual productions and a banknote tracing information service (www.eurotracer.net). Although not representative, this observation is in agreement with the hypothesis that the main source for cocaine contamination on paper currency are counting-machines in banks since the older banknotes were probably more often counted by such machines than the newer ones (Oyler *et al.*, 1996; Sleeman *et al.*, 2000).

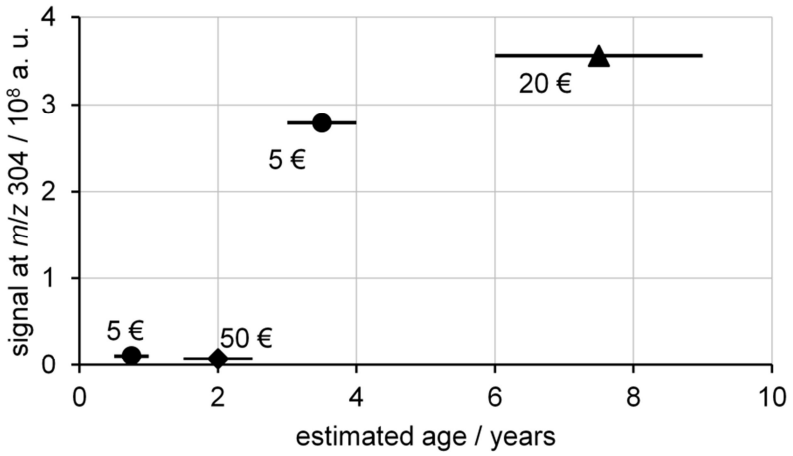

Figure 2.3.5: Signal for the quasimolecular ion (*m*/*z* 304, $[M+H]^+$) of cocaine as a function of estimated banknote age.

In order to unambiguously identify the quasimolecular ion of cocaine at *m*/*z* 304 several MS^n experiments were performed. Figure 2.3.4 (panel c) shows an MS^2 spectrum of the signal at *m*/*z* 304 (CID at 33.0%) that was acquired during the analysis of a 50 Euro banknote. The spectrum shows a loss of a neutral fragment with a mass of 122 u, which corresponds to the loss of benzoic acid (C_6H_5COOH), leading to an intense signal at *m*/*z* 182. This fragmentation pathway is in agreement with the structure of cocaine and the

signal at *m*/*z* 182 is often used for quantification studies (Esteve-Turrillas *et al.*, 2005). To gain more structural information this fragment ion was again isolated and an MS^3 spectrum was recorded (panel d). Again in good agreement with the structure of cocaine, intense signals were observed at *m*/*z* 150 and 108 which correspond to the loss of methanol (–32 u) and the loss of $C_3H_6O_2$ (–74 u), respectively (Smith and Casale, 2010).

From these measurements it was concluded that ambient desorption FAPA–MS is capable of detecting and identifying cocaine in trace amounts on banknotes. Moreover, the high abundance of the quasimolecular ion $[M+H]^+$ and the small degree of fragmentation led to mass spectra that were easy to interpret, making extensive data analysis procedures unnecessary.

Analysis of Organic Aerosol Samples

The chemical analysis of atmospheric aerosol samples from filters or impactor plates is commonly conducted by extraction, preconcentration, and subsequent detection of the analytes by methods such as LC–MS. However, as mentioned before, the necessary extraction and processing steps can be tedious and time-consuming. In contrast, ambient desorption FAPA–MS does not require any extraction or processing steps prior to analysis of substrates and, thus, might facilitate the analysis of such aerosol samples.

In order to assess the suitability of FAPA–MS for the analysis of OA particles, pure organic aerosol marker compounds (see Supplemental Material 2.5.1) and a filter sample of laboratory-generated secondary OA were used for the analysis by FAPA–MS (Figure 2.3.6). The secondary OA particles were generated by oxidizing gaseous limonene by ozone under dark and dry conditions in the presence of TME as an OH source. Subsequently, the resulting secondary OA particles were sampled on a TFE-coated fiber filter. The products of this reaction are well-known from previous studies (Glasius *et al.*, 2000; Yasmeen *et al.*, 2011) and, thus, are a good model system for a proof-of-principle study by FAPA–MS.

Figure 2.3.6 shows the mass spectrum and the TIC of the analysis of the filter sample. As can be seen from the inset the TIC exhibits an immediate increase when the sample is brought into the afterglow region as it was already observed for the analysis of pure compounds from filter samples. Afterwards, the signal decays exponentially which is probably due to the removal of the analytes from the surface by desorption. During desorption, the mass spectrum exhibits signals for well-known oxidation products, such as norlimonic acid (*m*/*z* 234, $[M+NO_3]^-$), limonic acid (*m*/*z* 248, $[M+NO_3]^-$), or 7-hydroxyketolimononic acid (*m*/*z* 264, $[M+NO_3]^-$). Interestingly, no signals for

deprotonation ($[M–H]^-$) but solely for nitrate adduct formation ($[M+NO_3]^-$) could be observed. All these compounds contain carboxylic acid groups and, thus, should favor deprotonation over adduct formation, as it was observed in all previous experiments. A possible explanation for this observation might be the influence of matrix effects. Due to the presence of several compounds on the filter sample, the ionization mechanisms might follow different pathways and charges are probably transferred several times between different analytes. Moreover, nitrate ions exhibit the longest lifetime of all primary ions in the afterglow and, therefore, might represent a terminal stage for ionization pathways. Alternatively, the use of TFE-coated filters might introduce yet undiscovered sample substrate effects on the ionization mechanisms occurring in the afterglow region.

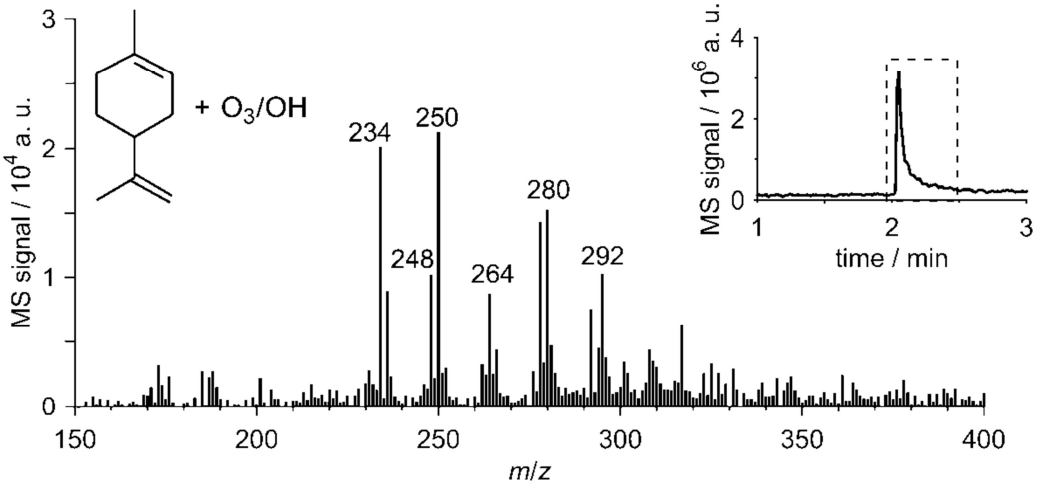

Figure 2.3.6: Analysis of limonene oxidation products from a TFE-coated filter using FAPA–MS in negative ion mode. The inset shows the TIC and the time range of the averaged mass spectrum.

Despite adduct formation, a clear signal assignment was possible since signals for fragmentation or additional signals correlating to the analytes were only present to a minor extent. Thus, ambient desorption FAPA–MS allowed the analysis of filter samples in order to detect and identify oxidation products in OA particles. However, a quantification of the analytes was not possible since the method exhibits a rather low reproducibility. When analyzing the filter sample at different spots the signal for one species could vary by over ±50%, making any effort for quantification impossible. The reason for this large variation is most probably due to the relative positioning of the ion source to the sample substrate, which was difficult to reproduce even during the same analysis. Furthermore, aerosol particles are deposited irregularly on the filter surface, leading inevitably to variations in the recorded signals.

Detection of Surface Contamination during Storage of Stalagmite Samples

Speleothems such as stalagmites are calcareous secondary mineral deposits in caves and can be used as environmental records. They have been investigated for reconstruction of both climatic changes (Lauritzen and Lundberg, 1999; McGarry and Baker, 2000; Scholz *et al.*, 2012) and fluctuations in vegetation regimes (Blyth *et al.*, 2007; Bosle *et al.*, 2014). However, due to the low amount of organic material that is stored in stalagmites, the danger of contamination by sample transport, storage and processing is inevitably high, requiring careful sampling and laboratory control. For example, recent studies identified cholesterol, phthalates, and n-alkanes as common surface contaminants of speleothems (Wynn and Brocks, 2014).

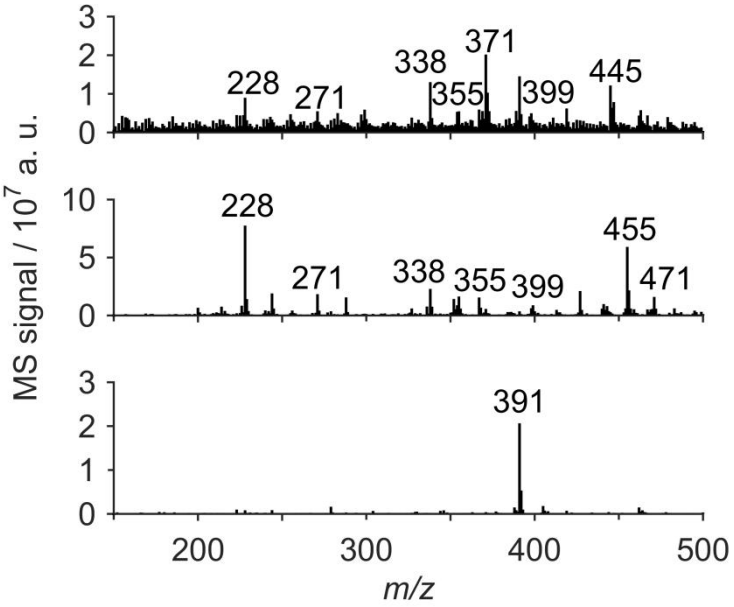

Figure 2.3.7: Detection of contamination on the surface of a stalagmite sample. Top panel: Mass spectrum of the analysis of the stalagmite surface after washing in dichloromethane/methanol (9:1) and storage in a polyethylene (PE) bag. Middle panel: Mass spectrum of the analysis of a PE bag. Bottom panel: Mass spectrum of the analysis of a cracked stalagmite.

The detection of such contamination sources can be a time-consuming and expensive task since it requires tedious extraction procedures and specially purified solvents. Therefore, ambient desorption/ionization FAPA–MS was investigated as a possible alternative for the analysis of stalagmite samples. Prior to the analysis, the stalagmite surface was cleaned by sonication in a dichloromethane/methanol (9:1) bath and afterwards stored in a PE bag. As can be seen in Figure 2.3.7 (top panel), several signals with significant abundances were observed in the mass spectrum when the stalagmite sample was placed in the afterglow region. In order to detect possible contaminations on

the stalagmite's surface, the PE bag was analyzed by FAPA–MS as well (Figure 2.3.7, middle panel). Remarkably, the mass spectrum of the PE bag analysis exhibited several intense signals at identical *m*/*z* ratios as observed before for the stalagmite sample. In particular, signals at *m*/*z* 228, 271, 338, 355, and 399 showed a good agreement when comparing the two mass spectra. Although a comprehensive structural elucidation of these signals was not conducted, these signals are assumed to be mainly oxidation products of PE formed in the afterglow region. Since these signals were absent when a freshly cracked stalagmite surface was analyzed (Figure 2.3.7, bottom panel) they probably correspond to contamination of the sample by abrasion of PE which is subsequently deposited on the stalagmite during storage and transport. The analysis of the cracked stalagmite further reveals that signal intensities in general are quite low when no contamination is present. The signal observed at *m*/*z* 391 is considered to be present in ambient laboratory air and is not corresponding to compounds on the sample surface (see section 2.3.1). FAPA–MS is, therefore, possibly not capable of reliably detecting organic compounds stored inside stalagmite samples but can be used for contamination control of such samples.

2.4 Conclusion

The results of this study demonstrate the capabilities and limitations of ambient desorption FAPA–MS. After a comprehensive elucidation and discussion of background mass spectra and reagent ions, a variety of compound classes were analyzed in order to identify desorption/ionization characteristics of ambient desoprtion FAPA–MS. In general, the method is best suited for polar analytes containing nitrogen- and/or oxygen functionalities, e.g. carboxylic acids, with low molecular weights and high vapor pressures. These compounds can easily be desorbed and transferred into the gas phase where subsequent ionization occurs. However, low volatile compounds with long carbon chains and/or high molecular weights may represent difficult analytical tasks since oxidation processes occurring in the afterglow region are impeding a clear signal assignment and, thus, the detection of the analytes.

In order to demonstrate the capabilities of the method, ambient/desorption FAPA–MS was applied for three different analysis tasks which are commonly considered as tedious and time-consuming. The analysis of regular Euro banknotes without any sample pretreatment demonstrated the ease of the method. Traces of cocaine were easily detected and identified by MS^n experiments. Although not representative, a correlation between

signal intensity and estimated age of the banknote was found. Furthermore, the analysis of a filter sample containg secondary organic aerosol particles proved that even complex mixtures can be analyzed by FAPA–MS. Several common limonene oxidation products were found and identified. Although all previous results showed that carboxylic acids favor the formation of quasimolecular ions ($[M–H]^-$) when measured by FAPA–MS, in this case the acidic marker compounds were invariably detected as nitrate adducts ($[M+NO_3]^-$). This deviation from the previous observations can possibly be explained by matrix effects and/or sample substrate effects, however, further experiments are needed to verify this assumption. Finally, the analysis of a stalgmite sample showed that FAPA–MS may be utilized for contamination control. By analysing both the stalagmite's surface and its storage bag it was possible to show that abrasion of the PE bag led to contamination of the sample. However, the analysis of a freshly cracked stalagmite also revealed that FAPA–MS is not capable of reliably detecting organic compounds within stalgmite samples.

Besides detection and identification of organic compounds on a variety of substrates, the quantification of analytes was not possible within this study. The positioning of the ion source and the sample, the sample surface structure, and the analyte distribution within the sample led to large variations in the recorded signals. In general, the application of a more reproducible sample positioning system or application of internal standards might allow quantitative analyses of samples in future studies.

Acknowledgements

This work was supported by the Max Planck Graduate Center with the Johannes Gutenberg-Universität Mainz (MPGC).

2.5 Additional Information and Results

The following results and information are not part of the actual manuscript, however, are supporting the results discussed above. Further supplementary material can be found in the Appendix (section A).

2.5.1 Detection of Organic Aerosol Marker Compounds on Different Substrates

In general, metal surfaces are common sample substrates for the collection of aerosol particles by inertial impaction in impactors. Typically, the chemical analysis of such

aerosol samples is conducted by extraction, preconcentration, and subsequent detection of the analytes by methods such as LC–MS. However, the necessary extraction and processing steps can be tedious and time-consuming. In contrast, ambient desorption FAPA–MS does not require any extraction or processing steps prior to analysis of substrates and, thus, might facilitate the analysis of such aerosol samples. In order to assess the suitability of FAPA–MS for the analysis of OA particles from metal surfaces, possible effects on desorption and ionization characteristics were investigated.

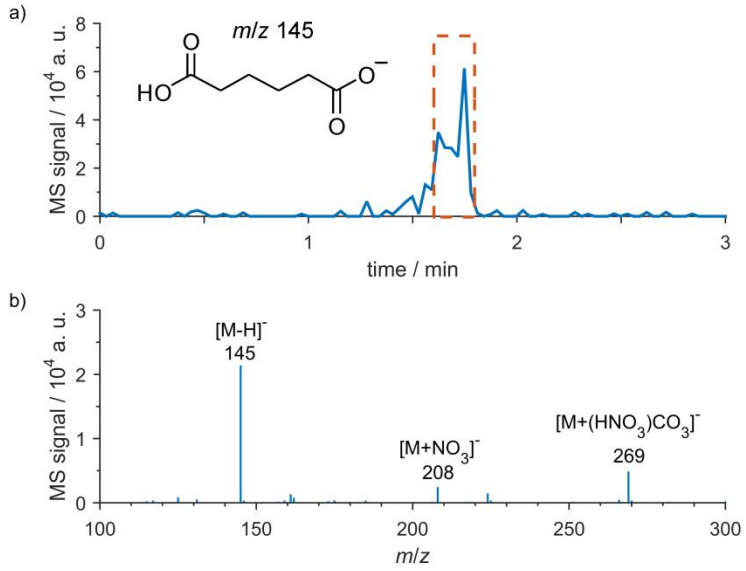

Figure 2.5.1: Detection of adipic acid on a stainless steel surface. (a) Signal for the quasimolecular ion $[M–H]^-$ of adipic acid (*m*/*z* 145) while the sample is in the FAPA's afterglow region; the box represents the time range of the averaged mass spectrum depicted in panel (b). Besides the deprotonated quasimolecular ion, adducts with primary reagent ions where observed at *m*/*z* 208 ($[M+NO_3]^-$) and 269 ($[M+(HNO_3)CO_3]^-$).

Figure 2.5.1 shows the detection of traces of adipic acid on a stainless steel surface. With a vapor pressure of $9.8 \cdot 10^{-6}$ Pa (Bilde *et al.*, 2003) and a molecular weight of only 146 $g \cdot mol^{-1}$, adipic acid allows a rapid gas-phase transfer by thermal desorption in the afterglow region. Additionally, the molecule contains two carboxylic acid groups, clearly favoring the formation of a deprotonated quasimolecular ion ($[M–H]^-$) in the negative mode. Thus, adipic acid can be considered an ideal analyte for ambient desorption FAPA–MS and any effects resulting from the steel surface should be easy to recognize.

As can be seen from the figure (top panel), the signal for the quasimolecular ion $[M–H]^-$ (*m*/*z* 145) exhibits an immediate response and strong increase when placing the spatula in the afterglow region at min 1.2. The observed exponential behavior of the signal can possibly be explained by the heat dissipation of the steel surface. This dissipation results in

an exponential increase of the surface temperature which eventually leads to an exponential volatilization of the analyte. The signal shows a significant abundance for about 0.5 min and decreases to background levels again in the range of seconds when the spatula is removed from the afterglow region, demonstrating the rapid response of the method and the absence of memory effects. The bottom panel shows the average mass spectrum for the time when the spatula was present in the afterglow region. The quasimolecular ion $[M–H]^-$ (*m/z* 145) shows the highest abundance in the spectrum while adducts with primary reagent ions ($[M+NO_3]^-$, $[M+(HNO_3)CO_3]^-$) are only observed to a minor extent. No signals for fragmentation or oxidation processes could be observed. Besides the effects of heat dissipation, from these measurements no significant differences could be observed compared to the detection of pure compounds from glass slides.

Another widespread sample substrate for the collection of aerosol particles are TFE-coated borosilicate fiber filters since they are easy to handle and require only a minimum of instrumentation for sampling. However, similar to the analysis of impactor samples the analysis typically requires several processing steps, such as extraction and preconcentration prior to analysis. To assess the suitability of FAPA–MS for the detection of typical components of OA particles, possible effects from TFE-coated fiber filters on desorption and ionization characteristics were investigated.

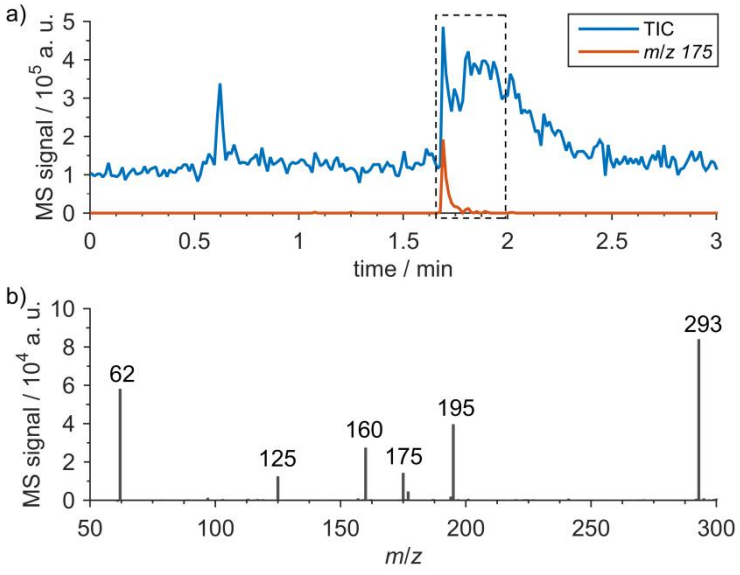

Figure 2.5.2: Detection of TCA on a TFE-coated borosilicate filter (background subtracted). (a) Signal for the quasimolecular ion $[M–H]^-$ of tricarballylic acid (*m/z* 175) and the TIC while depositing 10 ng of TCA in 10 µL methanol on the filter substrate; the box represents the time range of the averaged mass spectrum depicted in panel (b).

Figure 2.5.2 shows the detection of tricarballylic acid on a TFE-coated borosilicate fiber filter. Tricarballylic acid is a proxy for the aging marker MBTCA which is typically found in photochemically aged secondary OAs. Although the vapor pressure of this compound of ~$8 \cdot 10^{-8}$ Pa (calculated with SIMPOL.1) (Pankow and Asher, 2008) is quite low, it could easily be detected by FAPA–MS, which is possibly due to its high gas-phase acidity. As can be seen from the figure (top panel), the signal for the quasimolecular ion at *m*/*z* 175 ($[M–H]^-$) as well as the TIC exhibit a distinct and immediate increase when the sample solution (10 ng TCA in 10 µL methanol) is deposited on the filter substrate. In contrast to desorption from a steel surface, for the TFE-coated filters no heat dissipation takes place and the analyte is rapidly transferred into the gas phase. Shortly after the maximum, the signal decays exponentially again due to desorption and volatilization of the analyte, reaching background levels after roughly 20 seconds. The averaged mass spectrum during desorption exhibits several signals for background ions, such as nitrate (*m*/*z* 62, 125), and signals correlating either to solvent clusters or components of the filter material (*m*/*z* 160, 195, 293). However, only one signal correlating to TCA is observed, i.e. the quasimolecular ion $[M–H]^-$ at *m*/*z* 175. Furthermore, no signals for adducts, fragmentations or oxidation products could be identified.

3 Real-Time Analysis of Ambient Organic Aerosols Using AeroFAPA–MS

This chapter is a reprint of the article:

Martin Brüggemann, Einar Karu, Torsten Stelzer, Thorsten Hoffmann

Real-Time Analysis of Ambient Organic Aerosols Using Aerosol Flowing Atmospheric-Pressure Afterglow Mass Spectrometry (AeroFAPA–MS)

Environmental Science & Technology, **2015**, *49* (9), pp 5571–5578,
doi: 10.1021/es506186c

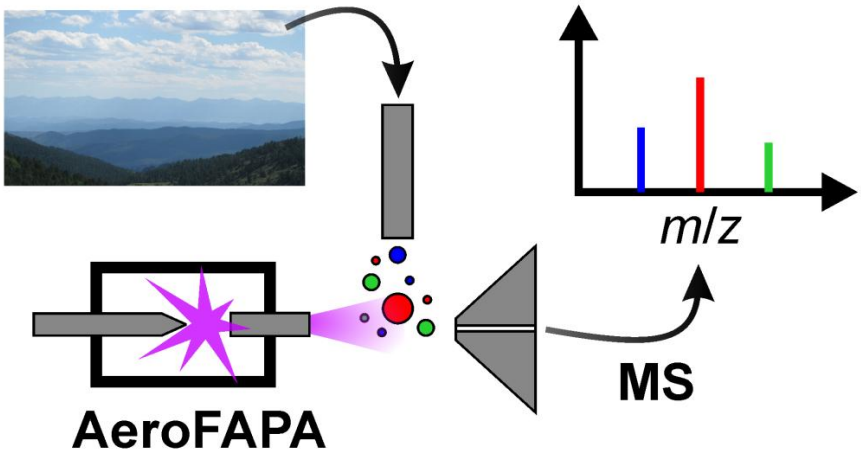

Abstract

Organic compounds contribute to a major fraction of atmospheric aerosols and have significant impacts on climate and human health. However, because of their chemical complexity, their measurement remains a major challenge for analytical instrumentation. Here we present the development and characterization of a new soft ionization technique that allows mass spectrometric real-time detection of organic compounds in aerosols. The aerosol flowing atmospheric-pressure afterglow (AeroFAPA) ion source is based on a helium glow discharge plasma which generates excited helium species and primary reagent ions. Ionization of the analytes occurs in the afterglow region after thermal desorption and produces mainly intact quasimolecular ions, facilitating the interpretation of the acquired mass spectra. We illustrate that changes in aerosol composition and concentration are detected on the time scale of seconds and in the ng·m^{-3} range. Additionally, the successful application of AeroFAPA–MS during a field study in a mixed forest region is presented. In general, the observed compounds are in agreement with previous offline studies; however, the acquisition of chemical information and compound identification is much faster. The results demonstrate that AeroFAPA–MS is a suitable tool for organic aerosol analysis and reveal the potential of this technique to enable new insights into aerosol formation, growth and transformation in the atmosphere.

3.1 Introduction

Organic aerosol (OA) particles are ubiquitous in the Earth's atmosphere and often account for the majority of atmospheric aerosol particles. They affect the climate by scattering solar radiation and acting as cloud condensation nuclei (Hallquist *et al.*, 2009; IPCC, 2014; Ehn *et al.*, 2014). Moreover, OA particles can have severe impacts on human health by entering and damaging the respiratory and cardiovascular systems (Davidson *et al.*, 2005).

Despite their relevance for climate and human health, there remain significant uncertainties about the sources, composition, transformations and properties of OA due to a lack of suitable instrumentation (Hallquist *et al.*, 2009; IPCC, 2014). Recent studies show that OAs are a highly complex mixture and may comprise 10^4 – 10^5 different chemical species (Goldstein and Galbally, 2007). Furthermore, the chemical composition is changing continuously due to condensation, partitioning and aging processes occurring in the gas phase as well as in the particle phase (Chen *et al.*, 2011). In addition, the amounts

of sample are usually very limited, typically in the nanogram range. This time-dependent chemical complexity represents a major challenge for current aerosol measurement techniques and is probably one of the main barriers to a deeper insight into OA formation and growth. Therefore, suitable aerosol measurement techniques should be able to analyze the chemical composition of OAs with a high level of time, chemical and particle size resolution at low concentrations, allowing the detection of single compounds in real time (Hallquist *et al.*, 2009). To accomplish these requirements, mass spectrometry (MS) has shown to be a powerful tool by providing high sensitivity and the ability to detect a wide range of chemical species (Pratt and Prather, 2012b, 2012a).

In general, OA measurement techniques can be divided into two classes: “online” and “offline” techniques (Hoffmann *et al.*, 2011). Online techniques usually perform the analysis of OA in or near real time, providing a high time resolution, whereas offline techniques separate the sampling from the subsequent analysis step, often leading to a higher chemical resolution.

Offline techniques typically comprise sampling of OA particles on filters or by inertial impaction with sampling times ranging from hours to weeks. Afterward, the sampled aerosol particles have to be processed in a laboratory, for example by extraction, sonification or derivatization, and are analyzed by separation techniques followed by MS detection, such as liquid chromatography- or gas chromatography–MS. Due to the possibility to separate single or multiple organic species, the chemical complexity of the aerosol particles can be reduced and quantification of specific marker compounds is possible. However, the large sampling times often impede studies on reactive or (semi-)volatile compounds since they may react or evaporate on the time scale of minutes or even seconds. In addition, the processing of the sampled particles is often time-consuming and may introduce further artifacts into the resulting data (Hoffmann *et al.*, 2011; Pratt and Prather, 2012a).

One of the main online techniques that is used in the field of aerosol research nowadays is the aerosol mass spectrometer (AMS), which is commercially available from Aerodyne. Typically, aerosol particles are introduced into a vacuum chamber by means of an aerodynamic lens that focuses the sampled aerosol particles to a beam. The particle beam is directed onto an evaporation unit, which is heated to 600 °C, volatilizing the entire particle mass. The evaporated compounds are subsequently ionized by electron ionization (EI) at 70 eV and analyzed by MS (Canagaratna *et al.*, 2007; Pratt and Prather, 2012b). The application of EI allows the analysis of a wide range of chemical species. However, EI

induces a high degree of fragmentation of organic compounds due to excess internal energy imparted during the ionization processes. Usually, these fragmentation steps impede the identification and quantification of individual particle phase organics, thus, leading to a relatively low level of chemical information (Hoffmann *et al.*, 2011). Therefore, recent instrumental developments focus on softer ionization techniques such as atmospheric pressure chemical ionization (APCI–MS) (Vogel *et al.*, 2013a; Brüggemann *et al.*, 2014), extractive electrospray ionization (EESI–MS) (Gallimore and Kalberer, 2013) or near-infrared (IR) laser desorption ionization (Geddes *et al.*, 2010).

Yet unexplored in aerosol research are the latest developments in soft ionization techniques that have been made during the advent of ambient desorption/ionization mass spectrometry (ADI–MS). The newly developed ionization techniques comprise ion sources such as the low temperature plasma probe (LTP) (Albert and Engelhard, 2012), the DART source (Cody *et al.*, 2005), the flowing atmospheric-pressure afterglow (FAPA) source (Andrade *et al.*, 2008) or the desorption electrospray ionization (DESI) source (Takats, 2004). All these techniques have in common to operate under ambient conditions without the need of preprocessing the sampled material prior to analysis. Typical applications for ADI–MS are the detection of pesticides (Jecklin *et al.*, 2008), illicit drugs (Chen *et al.*, 2009; Schaper *et al.*, 2012), explosives (Shelley *et al.*, 2011) or even counterfeit electronics (Pfeuffer *et al.*, 2014) on a variety of samples. A more detailed overview of recent advances in the field of ADI–MS can be found elsewhere (Albert *et al.*, 2014).

The aerosol flowing atmospheric-pressure afterglow (AeroFAPA) source, presented here, is based on the pin-to-capillary FAPA source design, first described by Shelley *et al.* (Shelley *et al.*, 2011). The AeroFAPA–MS setup allows a real-time detection of single or multiple organic compounds in aerosols without the need of any preprocessing of the sampled aerosol. Moreover, compared to similar ion source developments, such as EESI–MS (Gallimore and Kalberer, 2013), no solvents are necessary for the analysis, preventing the introduction of measurement artifacts or alteration of the aerosols' chemical composition. After optimization of different source parameters, such as positioning, discharge currents and gas flows, the AeroFAPA source was used to measure laboratory-generated aerosol particles composed of pure compounds as well as organic compounds in ambient aerosols during the Fichtelgebirge-Biogenic Emissions and Aerosol Chemistry (F-BEACh) 2014 field campaign. The temperatures reached in the afterglow region of the source were measured at different discharge currents and found to be below 150 °C, which even allows the detection of certain thermolabile substances in OA without thermal

decomposition. Furthermore, AeroFAPA–MS enabled the detection of organic compounds in OA on the time scale of seconds and at concentrations in the ng·m^{-3} range.

3.2 Experimental

3.2.1 Design and Setup of the AeroFAPA Source

The AeroFAPA source and the aerosol inlet are held in place by a stainless steel manifold in front of the MS. The exit of the ion source and the aerosol inlet are arranged orthogonal to each other and to the MS inlet. The AeroFAPA source consists of a ceramic discharge chamber (Macor, MCI UG, Neumünster, Germany) which holds two electrodes made of stainless steel (Figure 3.2.1, panel a). The cathode (outer diameter 3.00 mm) is sharpened to tip, whereas the anode is a small capillary (outer diameter 3.18 mm, inner diameter 1.40 mm). Helium is introduced through a small port in the back of the discharge chamber. The gap between the tip of the inner electrode and the capillary electrode was set to 7 mm and the gap between the MS inlet and the ion source was adjusted to roughly 2–3 mm. During operation, a glow discharge plasma is maintained in the discharge chamber by applying a negative potential to the pin electrode. The voltage is fed through a 5 kΩ ballast resistor which is installed in series with a high-voltage dc power supply (PTV-3N200, Spellman High Voltage Electronics Corporation, Hauppauge, NY, USA) in order to create a stable discharge, compensate for the negative dynamic resistance of the discharge, and prevent arcing. The capillary electrode is held at the potential of the MS inlet, typically ±15 V, to create a field-free region between the ion source and the MS inlet. The discharge is operated in current-controlled mode at currents between 5–55 mA, resulting in a discharge voltage of 300–500 V. Helium gas exiting the discharge through the capillary electrode forms the afterglow region in front of the AeroFAPA source.

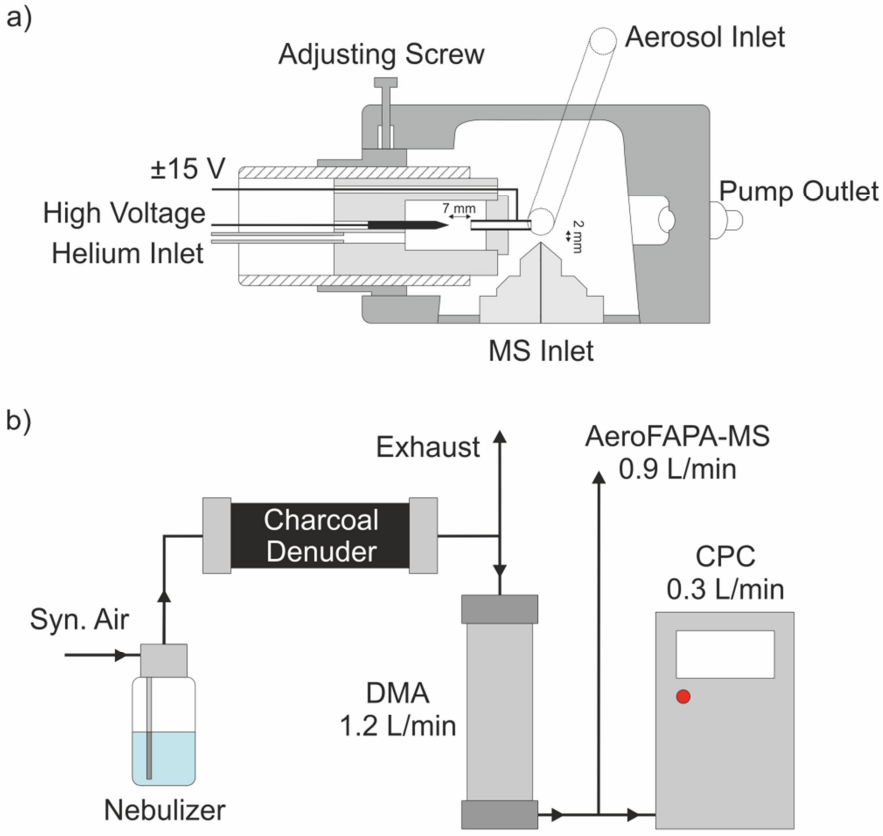

Figure 3.2.1: (a) Cross sectional view of the AeroFAPA. The aerosol inlet is arranged orthogonal to the MS inlet and the capillary electrode, respectively. In standard operation mode the helium flow is 0.6 $L \cdot min^{-1}$ and 55 mA are applied to the pin electrode. Excited helium species can exit the discharge region through the capillary electrode. The capillary electrode is held at a potential of ±15 V to maintain a field free region in front of the MS inlet. (b) Experimental setup used for size selection and AeroFAPA–MS analysis of aerosol particles. After nebulization of the solution, methanol was removed by a charcoal denuder. A total flow of 1.2 $L \cdot min^{-1}$ was drawn through a differential mobility analyzer (DMA) and afterward divided for condensation particle counter (CPC) (0.3 $L \cdot min^{-1}$) and AeroFAPA–MS (0.9 $L \cdot min^{-1}$) analysis.

3.2.2 Ionization and Desorption Mechanisms of the AeroFAPA Source

The desorption and ionization processes taking place in the AeroFAPA source allow the analysis of organic compounds in aerosols at atmospheric pressure. The plasma produces excited and ionized helium species (He^m, He_2*, and He_2^+) which interact with compounds in the afterglow region (Andrade *et al.*, 2006; Orejas *et al.*, 2012; Shelley *et al.*, 2012). Helium is used as discharge gas due to its high-energy metastables (19.8 and 20.4 eV) with nonradiative lifetimes in the range of seconds which can ionize nearly every molecule by chemi-ionization (Andrade *et al.*, 2008; Raizer *et al.*, 2011). Moreover, the sputtering activity of helium is rather low which extends the lifetime of the ion source electrodes.

Since a detailed description of the main ionization processes occurring in the afterglow region can be found elsewhere (Andrade *et al.*, 2008; Schilling *et al.*, 2010; Shelley *et al.*, 2011; Orejas *et al.*, 2014) only a brief description will be given here. In general, chemical ionization is the main pathway for ionization of analytes in positive and negative mode, although a direct interaction of helium metastables with the compounds of interest is possible. In the positive ion mode, protonated water clusters are formed via Penning ionization of ambient N_2 and H_2O followed by charge-transfer reactions. The protonated water clusters can then transfer a proton to a thermally desorbed molecule to form a protonated quasimolecular ion. Besides protonated water clusters, the presence of NO^+, O_2^+, and CO_2^+ ions in the afterglow was reported (Andrade *et al.*, 2008). In negative ion mode, O_2^- ions are produced by the interaction of thermal electrons in the afterglow region with ambient oxygen. Gaseous compounds with a higher gas-phase acidity than O_2^- will be deprotonated producing $[M–H]^-$ ions. Besides the abundance of O_2^- ions, the presence of O^-, OH^-, HO_2^-, O_3^-, NO_2^-, and NO_3^- ions in the afterglow region was reported (Schilling *et al.*, 2010; Shelley *et al.*, 2011). The desorption process taking place in the afterglow region, which allows the analysis of compounds in the particle phase, is believed to be mainly temperature-driven, and thus, requires a certain volatility of the analytes. However, other desorption processes, such as photoinduced desorption or chemical sputtering, have been proposed recently and would allow the analysis of very low or even nonvolatile species (Shelley and Hieftje, 2011).

3.2.3 Generation and Classification of Known Organic Aerosol Particles

Aerosol particles were produced by nebulization of methanolic solutions with concentrations ranging from 0.5 to 1.0 $mmol \cdot L^{-1}$ of the selected compounds. Methanol was removed after nebulization using an activated charcoal denuder. Synthetic air was used for nebulization. Prior to AeroFAPA–MS analysis, the polydisperse aerosol particles were size-selected by a differential mobility analyzer (DMA) (model L-DMA 55-900, Grimm Aerosol Technik, Ainring, Germany) and counted by a condensational particle counter (CPC) (model CPC 5416, Grimm Aerosol Technik, Ainring, Germany). Typically, an aerosol flow of 1.2 $L \cdot min^{-1}$ and a DMA sheath air flow of 12 $L \cdot min^{-1}$ were used throughout the experiments. After removal of the solvent and particle size selection, the flow was split and 0.3 $L \cdot min^{-1}$ were directed to the CPC, whereas the residual 0.9 $L \cdot min^{-1}$ were transferred to the AeroFAPA–MS (Figure 3.2.1, panel b).

3.2.4 Site Description and Setup During the F-BEACh 2014 Field Campaign

The AeroFAPA–MS was used during the F-BEACh 2014 field study from July 15th–27th. The measurement site was located in the Bavarian Fichtel Mountains in Germany (BayCEER Waldstein observatory, 50°08'35"N, 11°51'49"E, operated by the University of Bayreuth) at an altitude of 766 m above sea level. The area is covered by mixed forest with spruce being the dominant species (ca. 90%) and a mixture of larch, beech, maple and pine, which account for the rest of the tree population.

The AeroFAPA–MS setup, used during the measurement period, was slightly different from the laboratory setup. To ensure a complete volatilization of the sampled aerosol particles prior to ionization and to be independent from any yet unknown desorption dependent mechanisms, the aerosol inlet of the AeroFAPA source was heated to 200 °C using a resistive heating wire wrapped around the inlet tubings. Acquired mass spectra were background subtracted by measuring a blank sample for half an hour every day. Gaseous species present in the sampled aerosol were removed prior to analysis by passing the aerosol stream through an activated charcoal denuder. Possible negative artifacts due to the use of the charcoal denuder, that is, loss of particle phase compounds, are assumed to be small since the residence time of the aerosol particles in the denuder region is in the range of seconds and, thus, lower than estimated equilibration times of gas/particle partitioning for organic aerosols (Shiraiwa and Seinfeld, 2012).

3.2.5 Mass Spectrometric Analyses

Mass spectrometric measurements were conducted on an LCQ Deca XP Plus ion trap MS (Thermo, San José, CA, USA). In positive ion mode, potentials of +15 V and 0 V were applied to the MS inlet capillary and the tube lens, respectively. In negative ion mode, the potentials were set to −15 V and 0 V. The MS inlet capillary was heated to 200 °C. Spectra were collected in automatic gain-control mode with five microscans per spectrum and a maximum ion trap injection time of 200 ms. MS^n experiments were performed by collision-induced dissociation (CID) to improve signal-to-noise-ratios and to confirm the presence of the tested compounds. Data were recorded using XCalibur 2.0.7 and the recorded mass spectra were averaged over one minute afterward.

3.2.6 Temperature Measurements of the Afterglow

The temperature of the gas stream exiting the ion source was measured using a thermocouple (K-type) which was placed directly in front of the exit capillary of the ion

source. The resulting voltage was recorded by a voltmeter and converted into a corresponding temperature. Each temperature measurement at a certain discharge current was conducted in triplicate.

3.3 Results and Discussion

3.3.1 Optimization and Characterization of the AeroFAPA Source

At first, flow rates for helium and the analyzed aerosols were optimized. Different flow rates of helium ranging from 0.3–1.2 $L \cdot min^{-1}$ were tested with the AeroFAPA source. Flow rates below 0.6 $L \cdot min^{-1}$ led to a compromised sensitivity, whereas higher flow rates caused vacuum problems with the ion trap MS. A helium flow rate of 0.6 $L \cdot min^{-1}$ was found to give the best balance between MS signal intensity and vacuum stability of the MS. Besides the helium flow rates, different aerosol flow rates between 0.5 and 1.5 $L \cdot min^{-1}$ were tested. Best sensitivity was found for aerosol flow rates of 0.9 $L \cdot min^{-1}$, leading to a residence time of ~150–300 µs for aerosol particles in the afterglow region (see Supplemental Material). At lower flow rates, helium which exits the plasma was not pumped away efficiently enough causing vacuum problems with the MS. At higher flow rates the residence time of the aerosol particles is decreased, compromising the detection limits of the AeroFAPA source. Finally, the AeroFAPA source was moved in small steps inside its manifold using an adjustment screw to give best sensitivity and signal intensity. The optimum distance between the AeroFAPA exit capillary and MS inlet capillary was found to be at roughly 2–3 mm. This distance was used throughout the following experiments. In order to extend the range of possible flow rates for analyses by AeroFAPA–MS, the application of a jet separator, e.g. Vapur interface, seems promising for future studies (Gross, 2014).

Additionally, afterglow temperatures were measured as a function of the current applied to the pin electrode of the AeroFAPA source. Five different currents between 15 and 55 mA were tested and the resulting afterglow temperature was measured with a thermocouple which was placed directly in front of the AeroFAPA exit (distance < 1 mm). Figure 3.3.1(a) shows the time series for the temperature measurements depending on the applied current and Figure 3.3.1(b) the terminal temperatures reached in the afterglow region. Terminal temperatures of the afterglow region and equilibration time scales increase linearly with the applied current within the observed range. Here, the afterglow temperature increases with roughly 1.7 $°C \cdot mA^{-1}$. For the lowest current (15 mA) the

terminal temperature of ~80 °C is already reached after 10 minutes, whereas for the highest current of 55 mA the terminal temperature of ~150 °C is reached after roughly 30 minutes. Similar temperature ranges were reported before for comparable ion sources (Shelley *et al.*, 2011) and provide the possibility to measure even thermolabile substances, e.g. organic peroxides, with minimal to no thermal decomposition. The relatively long equilibration times compared to other ADI sources are due to the fact that the AeroFAPA manifold heats up during operation and affects the terminal temperatures reached in the afterglow region. The self-heating of the discharge is, however, also one of the main advantages over other plasma-based ADI sources since no additional heat source is necessary to volatilize the analytes.

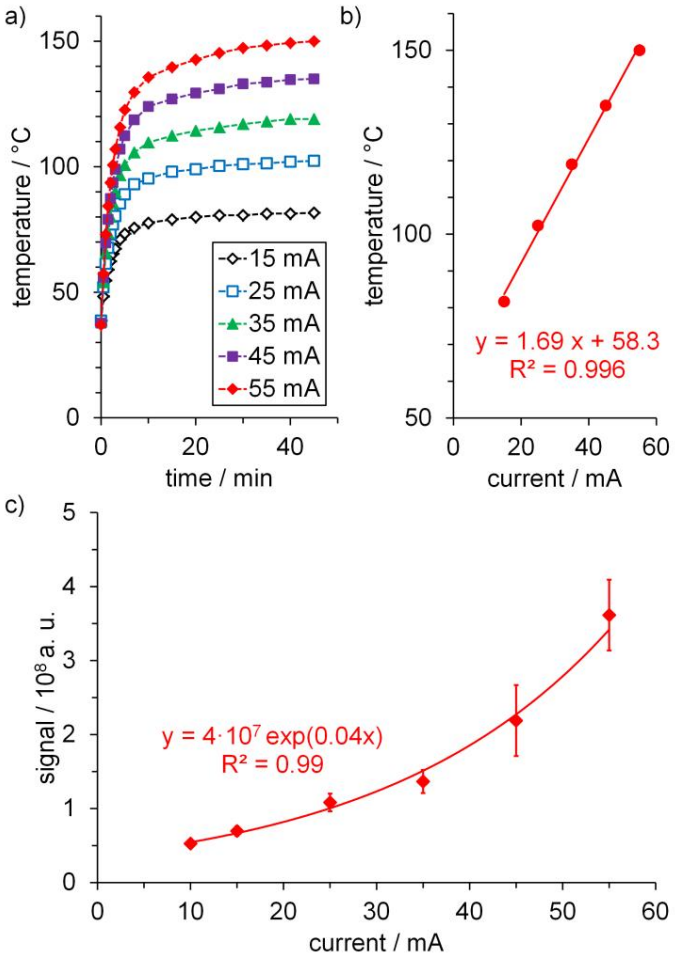

Figure 3.3.1: Characterization of the AeroFAPA source: Measurements of the influence of the applied current on the afterglow temperature and the MS signal intensity. (a) Time series of the afterglow temperature for five different currents between 15–55 mA. (b) Terminal temperatures reached in the afterglow region as a function of the applied discharge current. (c) MS signal intensity plotted versus the applied current (10–55 mA) for the measurement of tricarballylic acid (TCA) particles; each data point is the average intensity of one minute, error bars indicate one standard deviation.

Besides the afterglow temperatures, the MS signal intensity was measured at different discharge currents in order to find optimum values for the aerosol particle analysis. Figure 3.3.1(c) shows the signal intensity of tricarballylic acid (TCA) aerosol particles with AeroFAPA–MS at a constant concentration of 5 µg·m^{-3}. The MS signal of the deprotonated ion at *m*/*z* 175 ([M–H]$^-$) was monitored for this purpose and the applied current was adjusted to different values ranging from 10 to 55 mA. Each data point represents the average signal intensity of 1 minute; error bars indicate the standard deviation. The signal for TCA increases with the applied current and exhibits an exponential behavior for the range observed. This may be explained, firstly, by the increasing temperatures in the afterglow region which support a more efficient volatilization of the aerosol particles in the afterglow region. Secondly, the elevated flux of primary reagent ions and excited helium species at higher discharge currents may enhance the ionization efficiency of the AeroFAPA source. The highest signal intensity was found for a discharge current of 55 mA. Due to limitations of the high voltage power supply, experiments with higher discharge currents were not performed. Thus, currents of 55 mA were used throughout the following experiments.

3.3.2 AeroFAPA–MS Analysis of Known Organic Aerosol Particles

In order to assess ionization processes and fragmentation patterns of the AeroFAPA, aerosols of pure organic compounds were analyzed. The tested compounds comprised mono-, di-, and tricarboxylic acids with molecular weights ranging from 146 to 284 g·mol^{-1}. These compound classes are among the most abundant organic compounds observed in ambient aerosols (van Pinxteren *et al.*, 2014). Additionally, organic acids can readily be measured in negative ion mode which exhibits much lower background signals compared to the positive ion mode. For all studied compounds the deprotonated quasimolecular ion signal showed the highest intensity and no significant fragmentation could be observed (Table 3.3.1). Solely, the loss of water and the corresponding nitrate adducts were measured with intensities below 5% of the maximum intensity. Since the ionization in the afterglow region occurs at ambient pressure, remaining excess energy of the ionization can be transferred by collision to a third molecule. This collisional cooling can prevent fragmentation processes and explains the low fragmentation rate found here. Since nitrate is one of the major primary ions, the mass spectra always exhibit background signals at *m*/*z* 62 (NO_3^-), *m*/*z* 125 ($H(NO_3)_2^-$) and minor signals for corresponding adducts with the compound of interest, e.g. [M+NO_3]$^-$. However, since NO_2^- and NO_3^- adducts

always have an even *m*/*z* ratio in combination with nitrogen-free compounds these adducts could easily be identified for the tested compounds. Similar observations were made by Shelley *et al.* using the original FAPA setup (Shelley *et al.*, 2011). Figure 3.3.2 shows an example mass spectrum of a TCA aerosol at a concentration of 5 µg·m^{-3}. TCA serves as a chemical proxy for 3-methyl-1,2,3-butane-tricarboxylic acid (MBTCA) which is a typical and often used aging marker for ambient OAs (Szmigielski *et al.*, 2007; Donahue *et al.*, 2012a; Müller *et al.*, 2012). Interestingly, also signals for esterification products of TCA with methanol were observed with intensities around 10% of the maximum intensity. This finding supports hypotheses which assume an increased reactivity of carboxylic acids toward accretion reactions, such as esterification, in aerosol particles (Isaacs, 1991; Bateman *et al.*, 2008) and should be part of future studies.

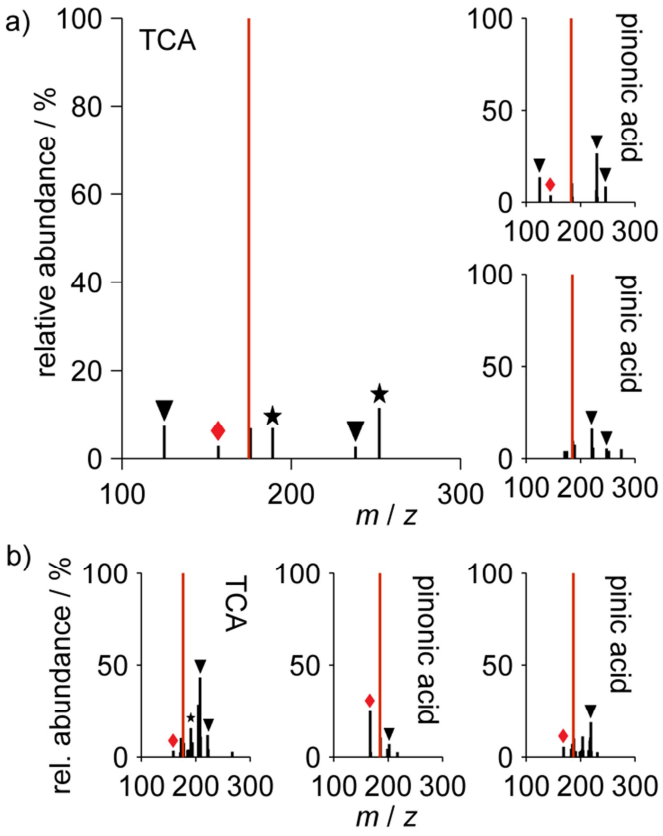

Figure 3.3.2:(a) Mass spectra of the analysis of TCA, pinonic acid and pinic acid aerosols in the negative ion mode (c = 5–10 µg·m^{-3}). The signal for the deprotonated molecule (red) showed the highest intensity and almost no fragmentation was observed. Red diamonds indicate the loss of water ([M-H-H_2O]$^-$). Signals originating from esterification products are marked with stars; signals correlating to the formation of NO_3^-, NO_2^- and corresponding adducts are marked with triangles. (b) Mass spectra in the positive ion mode. The signal for the protonated molecule (red) showed the highest intensity. Red diamonds indicate the loss of water ([M-H-H_2O]$^-$). Signals correlating to the formation of O_2^+, NO_2^+ and corresponding adducts are marked with triangles. All spectra are background subtracted (see Supplemental Material).

Table 3.3.1: List of analyzed compounds and the most abundant species identified with AeroFAPA–MS. Almost no fragmentation or signals other than protonated or deprotonated quasimolecular ions were observed in the recorded mass spectra, except for the fatty acids, for which signals of oxygen containing ions were obtained in the positive ion mode.

	Compound name	Structure	Molecular weight / g mol^{-1}	Most abundant species in	
				positive mode	negative mode
	Methanol	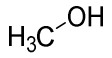	32	$[2M+H]^+$	No signal
mono-carboxylic acids	Pinonic acid	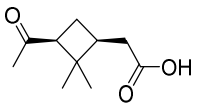	184	$[M+H]^+$	$[M–H]^–$
	Palmitic acid	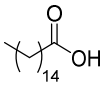	256	$[M+H+O_2]^+$	$[M–H]^–$
	Oleic acid	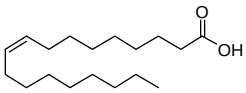	282	$[M+H]^+$	$[M–H]^–$
	Stearic acid	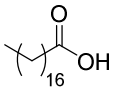	284	$[M+H+O_2]^+$	$[M–H]^–$
di-	Adipic acid	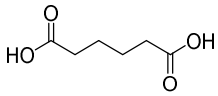	146	$[M+H]^+$	$[M–H]^–$
	Pinic acid	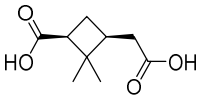	186	$[M+H]^+$	$[M–H]^–$
tri-	Tricarballylic acid	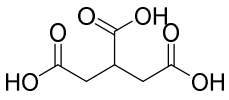	176	$[M+H]^+$	$[M–H]^–$

In the positive ion mode, for most of the analyzed compounds the signal for the protonated quasimolecular ion ($[M+H]^+$) showed the highest intensity. Solely for the two fatty acids, i.e. palmitic and stearic acid, significant signals for oxygenated products were observed (Table 3.3.1). This behavior might be explained by the long carbon chain of these molecules which might incorporate oxygen from atmospheric O_2 during the ionization process. Similar signals for oxygenation products have been reported for other ADI–MS sources and are still under investigation (Gross, 2014). In addition to the tested carboxylic acids, pure methanol was measured since it was used as a solvent for the nebulizer solutions. In the negative ion mode, no correlation between the observed background signals and the introduction of methanol could be observed. The absence of any methanol signals is, however, not surprising since methanolate, i.e. its conjugated base, is a strong

base and has a lower gas-phase acidity than O_2^- or any other primary reagent ion in the afterglow region. In the positive ion mode, methanol gives solely signals for its protonated forms, i.e. mainly $[2M+H]^+$ but also $[M+H]^+$ and $[3M+H]^+$.

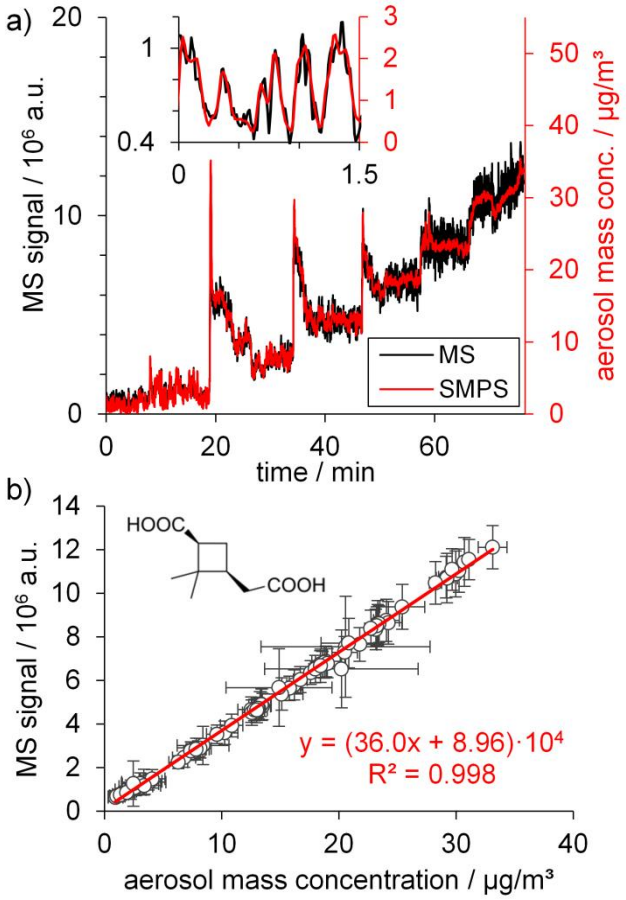

Figure 3.3.3:(a) MS signal as a function of time and aerosol mass concentration for the analysis of a pinic acid aerosol. In order to visualize the close correlation in time and intensity, the inset shows the time range from minute 0–1.5. The response time of AeroFAPA–MS shows to be smaller than the CPC's measurement frequency of 1 Hz. (b) Correlation between aerosol mass and MS signal for pinic acid ($[M-H]^-$). Each data point represents the average signal of 1 minute; error bars indicate one standard deviation.

The AeroFAPA–MS setup enabled the analysis of submicron OAs in real time with high sensitivity and reproducibility. Figure 3.3.3 shows the analysis of 100 nm pure pinic acid particles. The aerosol mass delivered to the ion source was varied by adjusting the flow rate through the nebulizer. Particle number concentrations were measured with a CPC and the resulting aerosol mass concentrations were calculated to range from 0.13 – 35 $\mu g \cdot m^{-3}$. The mass spectrometer was used in single ion monitoring mode for detecting the signal of the deprotonated quasimolecular ion of pinic acid at *m*/*z* 185. As can be seen in the figure, the MS signal intensity and the aerosol mass introduced into the ion source are highly correlated and follow each other very closely in time as well as in intensity. A

very fast response of the MS signal was observed when the aerosol mass concentration was changed, allowing the detection of even very rapid concentration variations with the AeroFAPA–MS. The response time was measured to be below 1 s, which was the lowest possible time interval between the data obtained by the CPC. The detection limit for pinic acid in particulate matter was calculated to be at ~7 $ng \cdot m^{-3}$ using the average blank signals at the *m*/*z* ration of the quasimolecular ion and adding three times its standard deviation. On the basis of measurements with other acids, the detection limit is generally assumed to be in the lower $ng \cdot m^{-3}$ range for small carboxylic acids.

3.3.3 Analysis of Atmospheric Aerosols Using AeroFAPA–MS

In order to test the applicability of AeroFAPA–MS to studies of aerosol formation and aging, the instrument was operated during a field campaign in summer 2014 (F-BEACh 2014). During the field study in the mixed forest, the AeroFAPA–MS was used to detect oxidation products of biogenic volatile organic compounds (VOCs) in the particle phase of ambient aerosols. In the following, we will focus only on the general possibility to use AeroFAPA–MS for the analysis of OA at ambient conditions, since an extensive data analysis for the entire measurement period, in respect to data evaluation concerning meteorological conditions or trajectory analyses, would be beyond the scope of this article.

Figure 3.3.4(a) shows a typical mass spectrum that was obtained in the negative ion mode on the 27th of July 2014. The average OA mass concentration, determined by an AMS, was at ~7 $\mu g \cdot m^{-3}$ during this time period. The spectrum exhibits the highest intensity for signals at *m*/*z* 203. By using the possibility to perform online tandem MS experiments, this signal was clearly identified as MBTCA, an aging marker of biogenic secondary OA that is formed via gas-phase oxidation of pinonic acid (Müller *et al.*, 2012). Additionally, the presence of the isobaric compound 3-carboxyheptanediocic acid was detected, which is a major photooxidation product of *d*-limonene (Figure 3.3.4b) (Jaoui *et al.*, 2006). Similar assignments were made for other signals and showed that AeroFAPA–MS was able to detect and identify single organic species in ambient aerosols (see Supplemental Material for MS^n spectra and structural assignments). Not surprisingly, the majority of these signals correspond to the formation of oxidation products of biogenic VOCs, such as pinic acid (*m*/*z* 185) (Yasmeen *et al.*, 2011), 2-hydroxyterpenylic acid (*m*/*z* 187), diaterpenylic acid actetate (*m*/*z* 231) (Claeys *et al.*, 2009) and possible isobaric isomers. However, the relatively high signal intensity of the tricarboxlyic acid MBTCA (*m*/*z* 203) was not anticipated since MBTCA is a later-generation oxidation product of

VOCs. In contrast, other earlier-generation oxidation products, such as pinic acid (*m/z* 185), exhibit lower signal intensities throughout the entire measurement period. Moreover, a significant increase in signal intensity was observed on several days for MBTCA (*m/z* 203) during the daytime and a corresponding decay during the nighttime (Figure 3.3.4c). These findings indicate the occurrence of fast aging processes of the aerosol masses, such as OH-initiated oxidation, during the measurement period (Zhang *et al.*, 2010; Donahue *et al.*, 2012a; Müller *et al.*, 2012).

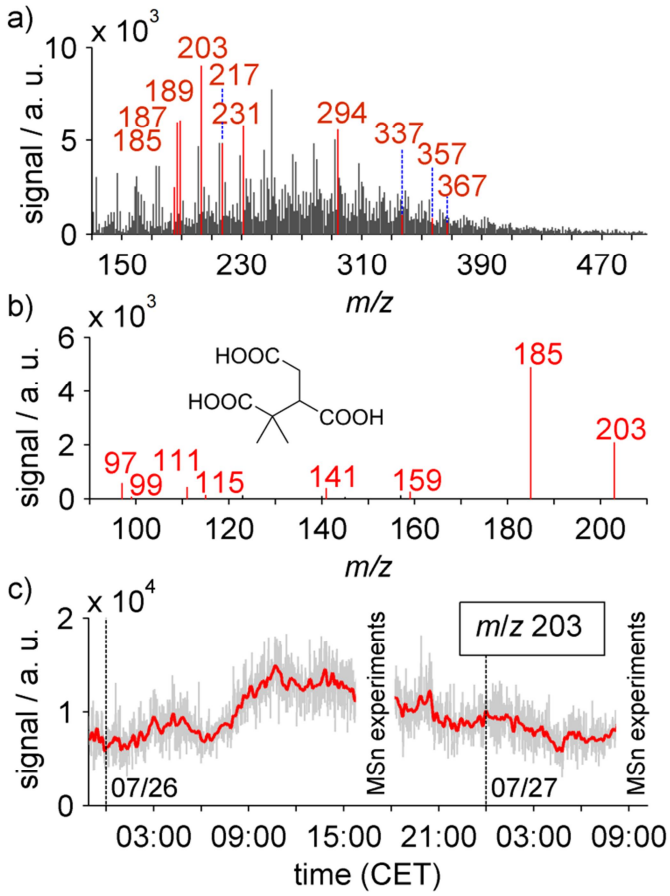

Figure 3.3.4: (a) Average mass spectrum of the AeroFAPA–MS obtained on the 27th of July 2014 (8:35-9:35AM, Central European Time) during the F-BEACh 2014 campaign at the Waldstein observatory (background subtracted). Signals with red annotations were identified by MS^n experiments; signals with black annotations could not be identified by MS^n experiments, however, have been observed and identified before by other groups (Müller *et al.*, 2009; Kristensen *et al.*, 2013). (b) MS^2 spectrum of *m/z* 203. The fragmentation pattern clearly reveals the presence of MBTCA. The signals in red have been reported before: *m/z* 203 = $[M–H]^-$, *m/z* 185 = $[203–H_2O]^-$, *m/z* 159 = $[203–CO_2]^-$, *m/z* 141 = $[203–H_2O–CO_2]^-$, *m/z* 115 = $[141–CO+H_2]^-$, *m/z* 97 = $[141–CO_2]^-$. The minor signals at *m/z* 111 and 99 might also indicate the presence of the isobaric compound 3-carboxyheptanediocic acid (Yasmeen *et al.*, 2011). (c) Time trace of MBTCA (*m/z* 203, $[M-H]^-$) from 26th to 27th of July 2014. The signal in red depicts a 10-min average of the originally obtained data (gray). Periods of MS^n experiments and blank measurements are left blank.

Besides carboxylic acid-containing molecules, nitrooxy organosulfates could clearly be identified as major contributors to OA at the site. The signal at *m*/*z* 294 can be assigned to the quasimolecular ion of a nitrooxy organosulfate ($C_{10}H_{17}NO_7S$). This species was observed and identified before from filter measurements of atmospheric aerosols in several studies (Surratt *et al.*, 2007) and is probably formed from biogenic VOCs in anthropogenically influenced air masses, in which NO_2 and SO_2 emissions affect the formation of oxidation products. To our knowledge, this is the first online observation of nitrooxy organosulfates from field measurements. Moreover, it was possible to detect signals for certain high molecular weight esters, e.g. at *m*/*z* 337, 357 and 367, which are assumed to play an important role in the early steps of aerosol formation and growth (Müller *et al.*, 2009; Kristensen *et al.*, 2013). However, an unambiguous identification and detection of these compounds was not possible due to the limited mass resolution and detection limit of the applied MS.

3.3.4 Implications and Perspectives

The new AeroFAPA ion source developed and characterized here offers a number of advantages for the analysis of OAs in real time. AeroFAPA–MS shows to be a soft ionization technique which produces mainly intact quasimolecular ions with little to no fragmentation during the ionization process. Therefore, characterization of the molecular composition of complex matrices, such as ambient OAs, and identification of single organic marker compounds in these systems is much easier than for other online techniques. This novel online technique will help to elucidate aerosol reaction mechanisms, formation pathways and molecular properties in high detail and time resolution. Due to the low detection limits, it is not only possible to analyze aerosols in laboratory experiments but also at ambient conditions without the need for any preconcentration. Changes in aerosol mass concentrations were detected on the time scale of seconds, and thus, allow a real-time detection of organic species present in the sampled aerosol. Additional insights into the desorption and ionization processes occurring in the afterglow region are still needed to obtain quantitative information on chemical transformations and mechanisms in OAs and will be focus of future studies.

Acknowledgements

This work was supported by the Max Planck Graduate Center with the Johannes Gutenberg-Universität Mainz (MPGC).

M.B. gratefully acknowledges the support from Johannes Schneider, Frank Drewnick, and Stephan Borrmann from the Max Planck Institute for Chemistry (MPIC) and the Institute for Physics of the Atmosphere (IPA) in Mainz.

M.B. and T.S. gratefully acknowledge the support during the F-BEACh campaign from Andreas Held from the University of Bayreuth and the entire F-BEACh team.

3.4 Additional Information and Results

The following results and information are not part of the actual manuscript, however, are supporting the results discussed above. Further supplementary material can be found in the Appendix (section B).

In order to test the applicability of AeroFAPA–MS to studies of aerosol formation and aging, a proof-of-principle experiment involving the ozonolysis of a terpene was conducted. Here, the ozonolysis of α-pinene was used as a model system for the formation of secondary OAs in the atmosphere. α-Pinene is the most abundant terpene found in boreal forests and one of the main precursor compounds for biogenic secondary OA. Additionally, it is well characterized and its reaction products have been studied extensively in the past (Jaoui and Kamens, 2003; Hallquist *et al.*, 2009; Yasmeen *et al.*, 2011).

The ozonolysis of α-pinene was carried out under dark and dry conditions in a continuous-flow reaction chamber. Drawing $0.9\ \mathrm{L \cdot min^{-1}}$ from the chamber into the AeroFAPA source, the resulting aerosol was directly analyzed by MS. It has to be noted that in this case the entire aerosol, i.e. including gas-phase compounds, was analyzed. Thus, information about partitioning behavior of single compounds is not available but may be part of future studies. Figure 3.4.1(a) shows an average mass spectrum obtained in the negative mode during such an experiment after the reactants and aerosol concentrations had reached a steady state inside the reaction chamber. The mass spectrum exhibits two distinct ranges. The lower mass range (*m*/*z* 150–250) shows strong signals for a variety of oxidation products. In contrast, the signal intensities of the higher mass range (*m*/*z* >250) are weaker by an order of magnitude. The strongest signal was obtained at *m*/*z* 185 which correlates to the formation of pinic acid ($[M–H]^-$). This compound is a typical oxidation product for the ozonolysis of α-pinene (Table 3.3.1) (Yasmeen *et al.*, 2011). Other typical oxidation products that could be observed in the lower mass range are: norpinolic acid at

m/*z* 157 ([M–H]$^-$), norpinonic acid at *m*/*z* 169 ([M–H]$^-$), norpinic acid and terpenylic acid at *m*/*z* 171 ([M–H]$^-$), pinonic acid at *m*/*z* 183 ([M–H]$^-$), 10-hydroxypinonic acid at *m*/*z* 199 ([M–H]$^-$), and diaterpenylic acid acetate at *m*/*z* 231 ([M–H]$^-$) (Figure 3.4.1b) (Glasius *et al.*, 2000; Gao *et al.*, 2006; Claeys *et al.*, 2009). In the higher *m*/*z* range (Figure 3.4.1c), some second-generation products with high molecular weights can be found: *m*/*z* 337, *m*/*z* 357, *m*/*z* 367. These products have also been found on filter samples in laboratory and field experiments before and are of special interest regarding new particle formation and particle growth processes (Müller *et al.*, 2009; Kristensen *et al.*, 2013).

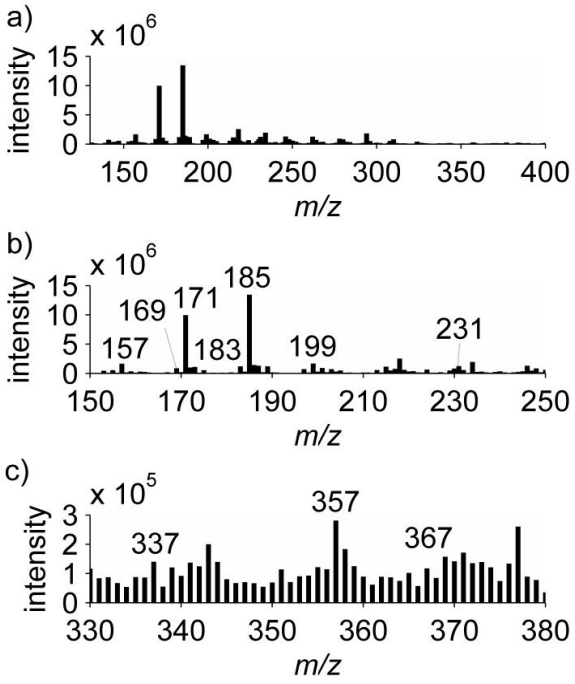

Figure 3.4.1: Negative mode AeroFAPA mass spectrum of the analysis of secondary OA produced by α-pinene ozonolysis. (a) Full range mass spectrum from *m*/*z* 130–400. (b) Lower mass range enlarged (*m*/*z* 150–250). (c) Higher mass range enlarged (*m*/*z* 330–380). Labeled signals have already been found and identified in ambient and laboratory-generated OAs.

The lower molecular weight products are presumably gas-phase compounds, whereas the higher molecular weight compounds reside in the particle phase. Thus, AeroFAPA–MS allows a combined analysis of gas-phase and particle-phase compounds of OAs without the need for a separation step. Although, pre-separation of gas-phase and particle-phase compounds by denuders or filters may be desirable if information on partitioning behavior or vapor pressures is needed. Additionally, the ionization of gas-phase compounds is presumably favored over the ones residing in the particle phase since no desorption or volatilization step is necessary prior to ion formation. Thus, a pre-separation of gas-phase compounds would possibly enhance signals for particle-phase compounds.

4 Application of AeroFAPA–MS during the F-BEACh 2014 field study

This chapter is a reprint of the article:

Martin Brüggemann, Laurent Poulain, Andreas Held, Torsten Stelzer, Stefanie Richters, Anke Mutzel, René Rabe, Dominik van Pinxteren, Hartmut Herrmann, Thorsten Hoffmann

Detection of Highly Oxidized Organosulfates and BSOA Marker Compounds in Real Time During the F-BEACh 2014 Field Study

In preparation for Atmospheric Chemistry and Physics

Abstract

The chemical composition of the organic aerosol fraction was analyzed using complementary mass spectrometric techniques during a field study in Central Europe during July 2014 (Fichtelgebirge – Biogenic Emission and Aerosol Chemistry, F-BEACh 2014). Aerosols were analyzed in real time by techniques such as aerosol flowing atmospheric-pressure afterglow mass spectrometry (AeroFAPA–MS), aerosol mass spectrometry (AMS), and chemical ionization atmospheric-pressure interface time-of-flight mass spectrometry (CI–APiToF–MS). In addition, offline detection of acidic organic compounds was conducted by non-target screening of filter samples using ultra high resolution mass spectrometry (UHRMS).

In total, 93 acidic organic compounds were identified as major contributors to the organic aerosol mass at the site. Among the CHO-containing compounds several common biogenic secondary organic aerosol (BSOA) marker compounds were detected. High concentrations were found for the monoterpene photooxidation products 3-methyl-1,2,3-butanetricarboxlyic acid (MBTCA) and 3-carboxyheptanedioic acid, suggesting that *α*-/*β*-pinene and *d*-limonene oxidation products were dominating the organic aerosol fraction. In agreement, volatile organic compound (VOC) measurements showed high mixing ratios for these monoterpenes in and above canopy level. Moreover, the high abundance of MBTCA and 3-carboxyheptanedioic acid and their ratios to earlier-generation oxidation products, such as pinic acid, indicate that relatively aged aerosol masses were present during the campaign period. Additionally, HYSPLIT trajectory calculations revealed that most of the arriving air masses traveled long distances (>1500 km) over land under cloud-free conditions, further supporting this hypothesis.

Around 47% of the detected compounds from the filter sample analysis were sulfur-containing, suggesting a high anthropogenic impact on biogenic emissions and their oxidation processes. Among the sulfur-containing compounds, several organosulfates, nitrooxy organosulfates, and highly oxidized organosulfates (HOOS) were unambiguously identified. In addition, correlations among HOOS classes, sulfate and gas-phase highly oxidized multifunctional organic compounds (HOMs) were investigated and identified from the online measurements. In agreement with previous studies, the results support the hypothesis that larger HOOS are formed by reactions of gas-phase HOMs with particulate sulfate. However, from the obtained results it is assumed that smaller HOOS might mainly represent decomposition products which are formed during filter sampling, storage and/or processing of the samples. Furthermore, a good agreement was found between larger

HOOS formation and gas-phase peroxyradicals ($RO_2^{\bullet}$) concentration, suggesting $RO_2^{\bullet}$ to be either direct or indirect precursors for HOOS. In addition, periods with high relative humidity revealed that aqueous-phase chemistry is presumably playing a major role in HOOS production.

4.1 Introduction

Secondary organic aerosols (SOAs) are a major component of tropospheric particulate matter and known to affect the Earth's climate as well as human health (Pöschl, 2005; Hallquist *et al.*, 2009; IPCC, 2014; Nozière *et al.*, 2015). In general, SOA is formed by phase transition of oxidation products of volatile organic compounds (VOCs). Depending on the source of these VOCs the resulting SOA can be classified as anthropogenic SOA (ASOA), e.g. from biomass burning or fossil fuel combustion, or biogenic SOA (BSOA), e.g. from terrestrial or marine ecosystems (Hallquist *et al.*, 2009; Nozière *et al.*, 2015). Globally, BSOA is expected to dominate the annual mass budget of SOA to a large extent (Henze *et al.*, 2008; Hallquist *et al.*, 2009), although it was shown that regionally ASOA can represent the main fraction of aerosol mass (Aiken *et al.*, 2009; Fushimi *et al.*, 2011).

In the past, several marker compounds were discovered which often allow a source apportionment and, hence, a differentiation between ASOA and BSOA. Common BSOA marker compounds for monoterpenes mostly comprise carboxylic acids and corresponding derivates, such as pinic acid (Hoffmann *et al.*, 1998; Yu *et al.*, 1998), 2-hydroxyterpenylic acid (Claeys *et al.*, 2009) or diaterpenylic acid acetate (Yasmeen *et al.*, 2011). These oxidation products are formed by reactions of VOCs with atmospheric oxidants such as ozone, OH radicals or NO_3 radicals and are ideally characteristic for their precursor VOC. Moreover, oxidation products such as 3-methyl-1,2,3-butanetricarboxylic acid (MBTCA) are formed by photochemical oxidation of earlier-generation marker compounds, thus, allowing to trace chemical ageing of SOA in the atmosphere (Szmigielski *et al.*, 2007; Müller *et al.*, 2012). In addition to these solely CHO-containing compounds, the class of organosulfates (OS) and nitrooxy organosulfates (NOS) is almost ubiquitously found in SOA particles, exhibiting supplementary marker compounds for VOC precursors. However, OS and NOS compounds might represent oxidation products of biogenic VOCs in anthropogenically influenced air masses (Goldstein *et al.*, 2009; Zhang *et al.*, 2009). Studies have shown that OS and NOS are formed in the condensed phase from VOC gas-phase oxidation products with sulfuric acid in acidic sulfate aerosols (Iinuma *et al.*, 2005;

Liggio and Li, 2006; Iinuma *et al.*, 2007; Surratt *et al.*, 2007; Surratt *et al.*, 2008). Moreover, radical mechanisms involving photochemically generated sulfate radicals might represent an additional formation pathway in aerosol particles at neutral pH (Nozière *et al.*, 2010).

Lately, a new class of monoterpene oxidation products in the gas phase was described, named highly oxidized multifunctional organic compounds (HOMs) (sometimes also referred to as extremely low volatile organic compounds, ELVOCs) (Ehn *et al.*, 2012; Ehn *et al.*, 2014). These compounds exhibit O/C ratios of 0.5–1.1 and, thus, should contain several functional groups, decreasing their vapor pressures to ranges which are significantly lower than for typical BSOA marker compounds (Ehn *et al.*, 2014). Since their formation is explained by auto-oxidation processes it is expected that multiple hydroperoxide groups are typically present per molecule (Crounse *et al.*, 2013; Ehn *et al.*, 2014). In agreement with this auto-oxidation hypothesis, Mutzel *et al.* recently showed that several HOMs contain at least one carbonyl group in their structure (Mutzel *et al.*, 2015). Yet, until now a comprehensive structural elucidation of HOMs was neither in the gas phase nor the particle phase possible. Nonetheless, it is assumed that these compounds largely contribute to both particle formation and growth (Riipinen *et al.*, 2011; Donahue *et al.*, 2012b; Zhao *et al.*, 2013).

Although the existence of HOMs was clearly demonstrated several times from gas-phase measurements, their fate after phase transition still remains quite unclear (Ehn *et al.*, 2012; Rissanen *et al.*, 2014; Ehn *et al.*, 2014; Mutzel *et al.*, 2015; Mentel *et al.*, 2015; Jokinen *et al.*, 2015). It has been hypothesized that due to the presence of hydroperoxide groups HOMs might participate in accretion reactions (Hallquist *et al.*, 2009; Shiraiwa *et al.*, 2013) or decompose via the Korcek mechanism (Mutzel *et al.*, 2015), resulting in the formation of carboxylic acids, including common BSOA marker compounds. Furthermore, from recent measurements it was speculated that the simultaneous presence of gas-phase HOMs and particulate sulfate might lead to the formation of highly oxidized organosulfates (HOOS), i.e. organosulfates with O/C ratios >1.0 (Mutzel *et al.*, 2015). However, evidence for this hypothesis is rather unsatisfactory since it is mainly based on model calculations and offline measurements.

In this study, several state-of-the-art mass spectrometric techniques were used in a complementary approach to characterize the organic aerosol fraction at a rural field site in Central Europe during summer 2014. The applied techniques comprise the recently described aerosol flowing atmospheric-pressure afterglow mass spectrometry (AeroFAPA–

MS) (Brüggemann *et al.*, 2015), high resolution time-of-flight aerosol mass spectrometry (AMS) (Canagaratna *et al.*, 2007), and chemical ionization atmospheric-pressure interface time-of-flight mass spectrometry (CI–APiToF–MS) (Jokinen *et al.*, 2012). Furthermore, the detection of acidic organic compounds, such as carboxylic acids and OS, was extended by non-target analyses of filter samples using ultra high resolution mass spectrometry (UHRMS) in combination with ultra-high pressure liquid chromatography (UHPLC). Besides the detection and identification of common BSOA marker compounds, the formation of HOOS and their correlation to HOMs was investigated using online and offline instrumentation.

4.2 Experimental

4.2.1 Field Site Description

All measurements were conducted in July 2014 (15^{th}-27^{th}) during the F-BEACh 2014 (Fichtelgebirge - Biogenic Emissions and Aerosol Chemistry) field campaign. The measurement site was located in a rural area at an altitude of 766 m a.s.l. in the Fichtelgebirge mountain range in Southeast Germany (BayCEER Waldstein Observatory, 50°08’35” N, 11°51’49” E, operated by the University of Bayreuth). The site is surrounded by a coniferous forest which is dominated by Norway spruce (~90%). A mixture of larch, beech, maple, and pine accounts for the rest of the tree population.

4.2.2 AeroFAPA–MS Measurements

The Aerosol Flowing Atmospheric-Pressure Afterglow (AeroFAPA) ion source was used in combination with an ion trap mass spectrometer (LCQ Deca XP Plus, Thermo, San José, CA, USA) for real-time analysis of ambient organic aerosol particles. Since a detailed description of the technique can be found elsewhere (Brüggemann *et al.*, 2015), only a brief description will be given here.

In general, AeroFAPA–MS is a soft-ionization technique which allows the online detection of organic compounds in aerosol particles. The negative mode, which was applied throughout the field study, is selective towards acidic compounds, such as carboxylic acids and (nitrooxy) organosulfates. For the analysis, aerosol particles were drawn from a height of ~4 m above ground into the manifold of the AeroFAPA at a flow rate of 0.9 L min^{-1}. Before reaching the AeroFAPA–MS, the aerosol stream passed an activated charcoal denuder in order to remove gaseous species from the aerosol sample.

Evaporation of organic aerosol components prior to ionization was ensured by heating the inlet to 200 °C. Then, a helium glow discharge plasma was used to generate excited helium atoms and primary reagent ions which ionized the compounds of interest in the so-called afterglow region. During the campaign, a current of 55 mA was used, resulting in a discharge voltage of ~400 V. In addition, a potential of –15 V was applied to the exit capillary of the AeroFAPA to enhance ion transmission. The resulting analyte ions, typically $[M–H]^-$, were then sampled and detected by the mass spectrometer. A voltage of –15 V was applied to the mass spectrometer inlet capillary, equaling the potential of the AeroFAPA's exit capillary. The tube lens was held at 0 V. All mass spectra were recorded in automatic gain-control mode with 300 microscans spectrum^{-1}, giving roughly one full scan mass spectrum (*m/z* 130–500) per minute. The maximum ion trap injection time was set to 200 ms. MS^n experiments were performed to elucidate the structure of the detected compounds. Data were recorded using XCalibur 2.0.7. Background subtraction of the acquired mass spectra was conducted by measuring a blank sample for half an hour every day. For the subsequent data analysis all files were converted to text files and analyzed using Matlab (R2014b, Mathworks Inc., USA). In order to compare and correlate data from different instruments a unified time vector was created with time intervals of 10 minutes. Thus, all signals, except the filter sample data, are average values for 10 minutes.

4.2.3 Filter Sample Analysis Using UHPLC-(-)ESI-UHRMS

Filter samples were taken twice a day by passing an air flow of 27.5 L min^{-1} from ~6 m above ground ($PM_{2.5}$) through tetrafluorethylene-coated borosilicate filters (70 mm, Pallflex T60A20, Pall Life Science, USA). The sampling time was ~8 hours for daytime filters (9 a.m.–5 p.m.) and ~16 hours for nighttime filters (5 p.m.–9 a.m.). After sampling the filters were stored at <-18 °C until analysis. Blank filters were taken every 2 to 3 days by placing a filter into the filter holder for ~20 min without sample flow.

For the extraction procedure one half of a filter sample was cut into pieces and 1.5 mL of a methanol/water solution (9:1) were added as extracting agent. Then, the sample was sonicated for 30 min. The extract was transferred into a separate glass vial and the filter sample extracted three more times in the same way. The combined extracts were then evaporated to dryness under a gentle stream of nitrogen at 50 °C. Afterwards, the residue was dissolved in 200 µL using a solution of acetonitrile/water (2:8).

For the LC separation of the filter extracts a UHPLC system (Dionex UltiMate 3000, Thermo Scientific, Germany) equipped with a Hypersil Gold column (C18, 50x2.0 mm, 1.9 µm, Thermo Scientific, Germany) was used. The injection volume was 20 µL per run and each sample was measured in triplicate. As eluents served solutions of ultrapure water with 2% acentonitrile and 0.04% formic acid (eluent A) and a solution of acetonitrile with 2% of ultrapure water (eluent B). At a flow rate of 500 µL min^{-1} the following gradient was used to optimize the separation: 5% B at 0.00 min, 5% B at 0.50 min, 20% b at 1.00 min, 20% B at 1.50 min, 90% B at 2.00 min, 90% B at 4.00 min, 5% B at 4.05 min, and 5% B at 4.10 min.

The UHPLC system was coupled to a Q-Exactive mass spectrometer (Thermo Scientific, Germany) which was used to obtain high resolution mass spectra (resolution of $R=7\cdot10^4$ at *m*/*z* 200). Ionization of the LC eluent was carried out using electrospray ionization (ESI) in the negative mode with 40 psi sheath gas (N_2) and 20 psi aux gas (N_2). The capillary temperature was set to 350 °C and a potential of –3.0 kV was applied to the ESI needle. During each LC run the mass spectrometer operated in full scan mode with a scan range of *m*/*z* 80–550.

The obtained LC–MS data were recorded by XCalibur 2.2 (Thermo Scientific, USA) and further analyzed by Sieve 2.2 (Thermo Scientific, USA) which allowed a non-target screening of the obtained data set. The threshold for signal abundance was set to $2.5\cdot10^6$ a.u. for the detection of significant signals in the obtained chromatograms after background subtraction by the software. For the elemental formula assignments the following isotopes and conditions were used: ^{12}C (0–50), ^{1}H (0–100), ^{16}O (0–40), ^{14}N (0–4) and ^{32}S (0–4). The mass tolerance was set to ±5 ppm. Afterwards, the obtained compound list was checked for chemically unreasonable formula assignments, such as the absence of hydrogen in carbon-containing compounds or impossible O/C ratios.

4.2.4 AMS Measurements

An High Resolution Time-of-Flight Aerosol Mass Spectrometer (HR-ToF-AMS, Aerodyne, USA, Canagaratna *et al.*, 2007) was used to measure the submicron mass concentrations and size distributions of non-refractory particulate organic matter, sulfate, nitrate, ammonium and chloride. The AMS was sitting in an adjacent laboratory container together with a large suite of instrumentation including a Twin Scanning Mobility Particle Sizer (T-SMPS), Aethalometer (Model AE33, Magee Scientific), a Multi-Angle Absorption Photometer (MAAP, Model 5012, Thermo Scientific,), and a Nephelometer

(TSI Model 3563). All instruments were connected to the same sampling line made of a PM_{10} inlet located at ~6 m above ground level. Relative humidity on the sampling line was maintained below 35% using a Nafion dryer. A chemical dependent collection efficiency (CDCE) was applied on the AMS data according to Middlebrook *et al.* (2012). The data quality insurance of the AMS results was made by successfully comparing the mass closure of the PM_1 aerosol chemical mass concentration as measured by the AMS to the estimated mass concentration measured by the TDMPS as previously described in Poulain *et al.* (2014).

4.2.5 CI–APiTOF–MS Measurements

Gas-phase concentrations of HOMs and sulfuric acid were measured using a CI–APiTOF–MS (chemical ionization atmospheric-pressure interface time-of-flight mass spectrometer). A detailed description of the instrument can be found elsewhere (Jokinen *et al.*, 2012). Briefly, an ^{241}Am source was used to produce nitrate ions which were electrostatically guided into the sample flow to give nitrate clusters with gas-phase compounds present in the sampled air. Then, the resulting clusters were transferred into the high vacuum region and detected by TOF–MS. Calibration of the instrument was performed using sulfuric acid (*m*/*z* 96.9601, HSO_4^-).

4.2.6 SMPS Measurements

Particle number size distributions were measured with a scanning mobility particle sizer (SMPS) custom-built by TROPOS (Leipzig, Germany) according to the design recommended by Wiedensohler *et al.* (2012). The instrument includes membrane dryers to keep the relative humidity below 40% both in the sample and the sheath flows. The aerosol sample is brought to bipolar charge equilibrium using a commercial ^{85}Kr neutralizer and sent to a Hauke-type differential mobility analyzer (DMA). The mobility diameter range from 10 nm to 710 nm was scanned in 71 size bins with a time resolution of 5 min. The closed-loop sheath flow rate was set to 5 L min^{-1} while the sample flow was directed to a Model 3772 condensation particle counter (TSI Inc., Shoreview, Minnesota, USA) for particle detection with a flow rate of 1 L min^{-1}.

4.2.7 VOC measurements

VOCs were sampled on adsorbent cartridges in and above the spruce canopy at 12 m and 31 m above ground level for subsequent offline gas chromatographic analysis. Samples were taken during daytime from 09:00 to 20:00 (CET) on four selected days

during F-BEACh 2014. VOCs were actively sampled on commercial two-stage cartridges filled with Tenax TA/Carbograph 5TD (Markes International, Cincinnati, Ohio, USA) for 30 min with a flow rate of 0.1 L min^{-1}. Ozone scrubbers coated with potassium iodide were used to minimize oxidation of collected compounds. After sampling, the cartridges were sealed immediately with metal caps, put in a screw-cap PTFE container and kept refrigerated until analysis.

In the laboratory, VOCs are analyzed using standard thermal desorption gas chromatography with flame ionization detection (TD-GC-FID). The sample cartridges are thermally desorbed (200 °C), pre-focussed on a Peltier-cooled trap (–15 °C), injected onto an Rxi-5ms column (30 m, 0.32 mm, 1.00 µm, Restek, Bad Homburg, Germany) in a Sichromat 1 (Siemens AG, Germany) gas chromatograph, and quantified by flame ionization detection.

4.3 Results and Discussion

4.3.1 Detection of acidic oxidation products in SOA particles using online and offline mass spectrometry

In total, the non-target analysis of the filter samples by LC–MS gave 695 compounds which showed significant signal intensities after background subtraction. From this large number of compounds only those compounds were selected for the subsequent analysis which had a formula assignment within a mass accuracy range of ±5 ppm and showed an integrated peak area of $>10^7$ a. u. for at least two separate filter samples. Eventually, these thresholds led to 93 compounds which were identified from the data analysis (Figure 4.3.1 and Supplemental Material). In general, the entire group of CHO compounds can be assigned to the class of organic acids since all measurements were carried out in the negative ion mode which is selective towards acidic compounds. Among these organic acids several common biogenic SOA marker compounds were detected, such as pinic acid (*m*/*z* 185.0819, $[M–H]^-$) (Yasmeen *et al.*, 2011) or terpenylic acid (*m*/*z* 171.0663, $[M–H]^-$) (Claeys *et al.*, 2009). The concentrations of these marker compounds in $PM_{2.5}$ were estimated using pinic acid as calibration standard. Table 4.3.1 gives an overview of some identified marker compounds and their average concentrations during the campaign period. A comprehensive list of all detected compounds is given in the Supplemental Material.

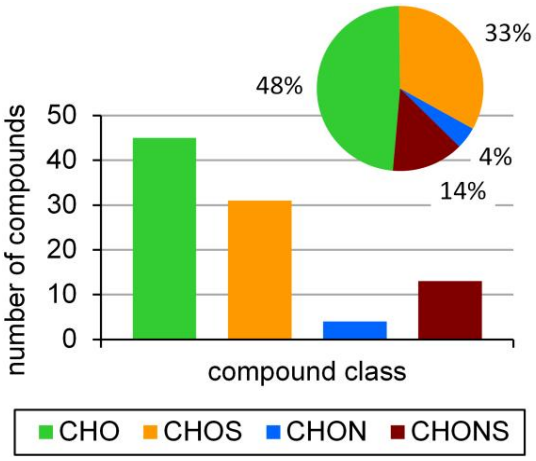

Figure 4.3.1: Number and ratio of identified compounds by LC–MS analysis of filter sample extracts for each compound class.

Table 4.3.1: Common BSOA marker compounds which were identified among the CHO compounds. The average concentrations were determined using pinic acid as reference. Standard deviations are given in brackets. A complete list of all identified CHO compounds can be found in the Supplemental Material.

formula for $[M–H]^-$	measured *m/z*	assigned compound	average conc. / ng m³
$C_8H_{11}O_4$	171.0663	terpenylic acid	6.4 (± 3.8)
$C_8H_{11}O_5$	187.0612	2-hydroxyterpenylic acid	7.7 (± 5.0)
$C_8H_{11}O_6$ [a]	203.0561	MBTCA 3-carboxyheptanedioic acid	13.8 (± 9.0) 10.2 (± 6.6)
$C_9H_{13}O_4$	185.0819	pinic acid	4.7 (± 2.5)
$C_{10}H_{15}O_6$	231.0874	diaterpenylic acid acetate	5.2 (± 2.7)
$C_{13}H_{19}O_5$	255.1238	β-nocaryophillinic acid	– [b]
$C_{17}H_{25}O_8$	357.1555	pinyl-diaterpenylic ester	– [b]

[a] isobaric compounds; [b] below detection limit

The most dominant marker compounds during the campaign period were MBTCA and 3-carboxyheptanedioic acid with average concentrations of 13.8 (± 9.0) ng·m^{-3} and 10.2 (± 6.6) ng·m^{-3}, respectively. While MBTCA depicts a later-generation oxidation product of *α*-/*β*-pinene (Szmigielski *et al.*, 2007; Müller *et al.*, 2012), 3-carboxyheptanedioic acid is a major oxidation product of *d*-limonene (Jaoui *et al.*, 2006). Firstly, these findings suggest that the site is strongly influenced by biogenic emissions consisting mainly of *α*-/*β*-pinene and *d*-limonene and their corresponding oxidation products. This hypothesis is further supported by monoterpene measurements in and above canopy level (12 m and 31 m above ground, respectively) which show mixing ratios of 38% *α*-pinene, 23% *β*-pinene, 19% limonene, 12% Δ-3-carene and 8% camphene. For all of the measured monoterpenes, higher mixing ratios were found within canopy level than above, clearly demonstrating monoterpene emission from vegetation at the site (Table

4.3.2). In addition, from a comparison with the MEGAN emission model (Guenther *et al.*, 2012), the five monoterpenes *α*-/*β*-pinene, limonene, Δ-3-carene, and camphene are estimated to contribute about 80 % to the total monoterpene emissions at the F-BEACh site.

Table 4.3.2: Median mixing ratios of the five measured monoterpenes in and above canopy level.

compound	**median mixing ratio / ppb**	
	at canopy level (12 m)	**above canopy level (31 m)**
α-pinene	0.67	0.28
β-pinene	0.35	0.18
limonene	0.25	0.16
Δ-3-carene	0.16	0.08
camphene	0.13	0.05

Secondly, MBTCA as well as 3-carboxyheptanedioic acid are known to be formed via photooxidation of their monoterpene precursors (Jaoui *et al.*, 2006; Szmigielski *et al.*, 2007), demonstrating the occurrence of fast photochemical aging processes, as it was already assumed previously for the site (Brüggemann *et al.*, 2015). The high concentrations of these compounds, moreover, may explain the rather low abundances of other earlier-generation monoterpene oxidation products in the particle phase, such as pinic acid (c = 4.7 (± 6.6) ng·m^{-3}) or pinonic acid (c < *detection limit*), further supporting the hypothesis of rapid oxidation of the aerosol masses during the campaign period. Besides several monoterpene oxidation products, also a marker compound for sesquiterpene oxidation, i.e. *β*-nocaryophillinic acid, could be identified. However, since this compound was only found in rather low abundances the impact of sesquiterpene oxidation products on particle composition is expected to be small.

As can be seen from Figure 4.3.1, several sulfur and nitrogen-containing compounds were found on the filter samples, i.e. CHOS, CHON, and CHONS. Similar to the CHO group, all these compounds have to exhibit a certain acidity which allows the detection as $[M–H]^-$ ions in the negative ion mode. Therefore, the CHOS and CHONS compounds were assigned to organosulfates and nitrooxy organosulfates, respectively, which contain a deprotonable sulfonic acid ($R–OSO_3H$) functionality. The CHON group might possibly comprise acidic organonitrates, although, no further evidence can be given here. While only 4% of the compounds were classified as CHON compounds, about 47% of the compounds are either belonging to the CHOS or the CHONS group. This large number of organosulfates and nitrooxy organosulfates is, however, not surprising since these compound classes are ubiquitously found in organic aerosol particles and readily

accessible for deprotonation via electrospray ionization (Hallquist *et al.*, 2009; Nozière *et al.*, 2015). A comprehensive list of all sulfur- and nitrogen-containing compounds is given in the Supplemental Material.

Several of the identified sulfur-containing compounds were already studied in the past and found in field and laboratory studies (Surratt *et al.*, 2008; Altieri *et al.*, 2009; Lin *et al.*, 2012; Nguyen *et al.*, 2012). In general, it is assumed that organosulfates and nitrooxy organosulfates have a mixed biogenic/anthropogenic origin, possibly involving particulate sulfuric acid, SO_2, NO_X and radical-initiated chemistry (Surratt *et al.*, 2008; Zhang *et al.*, 2009; Nozière *et al.*, 2015). As can be seen from Table 4.3.3, among the CHOS compounds several highly oxidized organosulfates (HOOS) were found on the filter samples. This recently described compound class exhibits O/C ratios greater than 1.0 and is possibly connected to the presence of gas-phase HOMs and, thus, might have implications for new particle formation processes (Ehn *et al.*, 2014; Mutzel *et al.*, 2015).

Table 4.3.3: Identified highly oxidized organosulfates (HOOS) by LC–MS from filter sample extracts. A comprehensive list of all detected sulfur- and nitrogen-containing compounds is given in the Supplemental Material.

formula for $[M–H]^-$	measured *m/z*	Δ*m* / ppm	O:C
$C_7H_{11}O_7S$	239.0231	0.0	1.0
$C_7H_{13}O_7S$	241.0376	1.0	1.0
$C_7H_7O_8S$	250.9868	-0.4	1.1
$C_7H_9O_8S$	253.0028	-1.7	1.1
$C_8H_{11}O_9S$	283.0127	-3.1	1.1
$C_8H_{13}O_9S$	285.0280	0.6	1.1
$C_8H_{13}O_{10}S$	301.0231	-2.3	1.3
$C_9H_{13}O_8S$	281.0334	0.9	0.9
$C_9H_{13}O_9S$	297.0282	1.3	1.0
$C_{10}H_{15}O_{10}S$	327.0387	1.3	1.0
$C_{10}H_{13}O_{11}S$	341.0209	0.3	1.1

Real-time analysis of aerosol particles reaching the site was carried out using a HR-ToF-AMS and the recently described AeroFAPA–MS (Brüggemann *et al.*, 2015). While the AMS was used for a general classification of the aerosol particles' components in ammonium, sulfate, nitrate, chloride and organics, the AeroFAPA–MS was resolving the organic fraction on a molecular level. In summary, the majority of the aerosol particles was classified as organic compounds (63.4%), followed by sulfate (21.1%), ammonium (8.7%) and nitrate (6.7%).

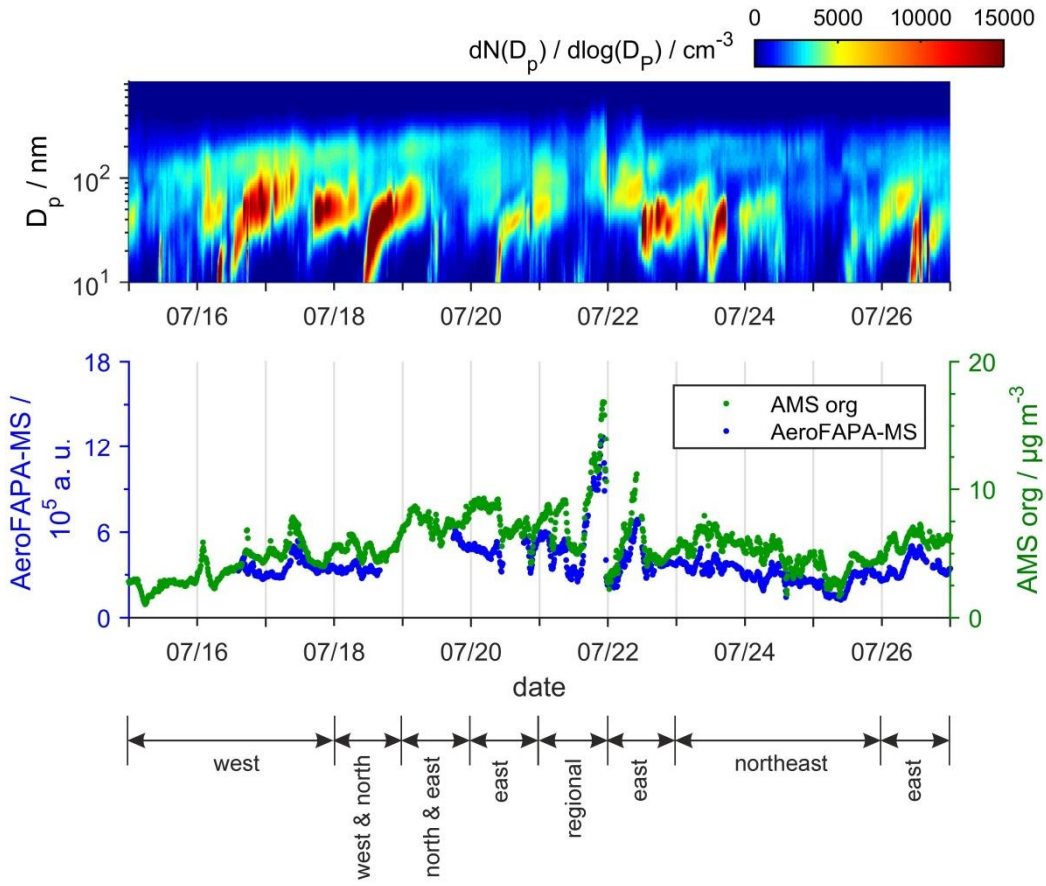

Figure 4.3.2: Top panel: Number size distribution of aerosol particles which was measured by an SMPS. Middle panel: Time traces of the total ion current of the AeroFAPA–MS (blue) and the organic aerosol mass measured by the AMS (green). Bottom panel: Major source directions of 96 hours backward trajectories arriving at the site (25 m above ground level).

Figure 4.3.2 shows the recorded concentrations of organics, measured by the AMS, in comparison to the total ion current (TIC) measured by the AeroFAPA–MS. It is assumed that the TIC only shows signals for organic compounds since inorganic species are typically not ionized by the AeroFAPA ion source. Additionally, the particle number size distributions and the main directions of 96 hours backward trajectories, calculated by HYSPLIT (Draxler and Rolph, 2013), are given for the campaign period. As can be seen from the figure, the signals of AMS and AeroFAPA–MS follow generally the same trends. Both instruments give a maximum of signals during the night of the 21st of July which can be explained by particles with relatively large diameters (median diameter ~150 nm) from regional sources reaching the site. For the organic aerosol fraction a maximum concentration of 16.9 µg·m^{-3} was determined by the AMS for this period. The days before the 21st of July are mainly characterized by trajectories coming from West Europe and North Germany while afterwards the trajectories are arriving almost exclusively from East

and Northeast Europe, i.e. Estonia and Russia. Deviations between the two instruments are mostly observed during nighttime which is possibly due to the formation of non-acidic compounds, such as alcohols, aldehydes, or ketones, possibly formed by nighttime nitrate chemistry, eluding detection by AeroFAPA–MS. In contrast, compounds containing organic bonded sulfate, such as organosulfates or nitrooxy organosulfates, are readily measured by the AeroFAPA–MS (Brüggemann *et al.*, 2015). However, the AMS cannot differentiate between inorganic sulfate and organic bonded sulfate. Thus, all sulfate signals were assigned to the inorganic fraction, possibly leading to an underestimation of the organic aerosol mass (Liggio and Li, 2006; Farmer *et al.*, 2010).

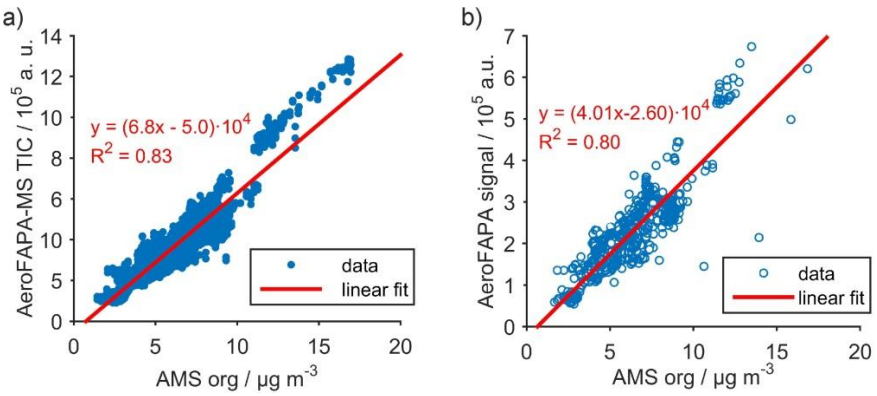

Figure 4.3.3: Correlation between organic aerosol mass (AMS org) and AeroFAPA–MS signals. Panel a: Total ion current of AeroFAPA as function of organic aerosol mass (blue dots) and linear fit (red line). Panel b: AeroFAPA–MS signals for compounds that were identified by LC–MS analysis of filter samples as a function of organic aerosol mass (blue circles) and linear fit (red line).

In order to quantify the portion of organic compounds in aerosol particles that was detectable by AeroFAPA–MS, the signals of AMS organics and the TIC of AeroFAPA–MS were plotted against each other. As depicted in Figure 4.3.3 (panel a), the data of the two instruments exhibit a linear correlation for the entire campaign period. By calculation of a linear regression fit a correlation coefficient of $R^2 = 0.83$ was determined, suggesting that about 83% of the variability of the organic aerosol mass can be explained by the AeroFAPA–MS signals. Furthermore, the AeroFAPA–MS data show good agreement with the LC–MS data that were acquired from filter samples. As can be seen in panel (b) of Figure 4.3.3, the AeroFAPA–MS signals ($[M–H]^-$) of the 93 compounds that were unambiguously identified as major contributors to the organic aerosol fraction were plotted as a function of organic aerosol mass. Similar to the correlation of the TIC of the AeroFAPA–MS to organic aerosol mass, a linear correlation was found. Interestingly, still about 80% of the organic aerosol's variability can be explained by these signals. Although

from the AeroFAPA–MS data an unambiguous formula assignment is not possible due to the low mass resolution, this finding further supports the hypothesis that these 93 compounds were the main components of organic aerosol mass during the measurement period.

As can be seen from the summed mass spectra in Figure 4.3.4, a further comparison of AeroFAPA–MS and LC–MS data supports the aforementioned hypothesis that aerosol masses reaching the site were dominated by BSOA marker compounds such as 2-hydroxyterpenylic acid (*m*/*z* 187), MBTCA and 3-carboxyheptanedioic acid (both *m*/*z* 203). Moreover, the signals for pinonic acid (*m*/z 183) and pinic acid (*m*/*z* 185) remain quite low over the entire campaign period, as it was already observed for the filter samples. The ratio of MBTCA and pinic acid, which is often used as aging proxy for organic aerosols, shows an average value of 5.76, however, even ratios of >32 were observed for single days. These extremely high values suggest that mainly aged aerosol masses reached the site. In agreement, HYSPLIT trajectory calculations reveal that arriving air masses typically traveled several days over land with distances of >1500 km at low altitudes (see Supplemental Material Figure 5.5.16 and Figure 5.5.20). Moreover, the majority of the trajectories is accompanied by cloud-free skies without any precipitation along their way, leading to a high degree of solar radiation and, therefore, photochemical processing of the transported aerosol masses.

In general, most acidic monoterpene oxidation products show odd *m*/*z* ratios in the mass spectra of the AeroFAPA–MS, since they are detected as $[M–H]^-$ ions and only contain carbon, hydrogen and oxygen atoms. However, the sum of AeroFAPA–MS spectra also exhibits elevated signals at even *m*/*z* ratios, such as *m*/*z* 308, showing as well a high linear correlation ($R^2 = 0.76$) to the organic aerosol mass measured by the AMS (Figure 4.3.4). According to the nitrogen rule, these signals correspond to nitrogen-containing compounds with an odd number of nitrogen atoms. In agreement, from the LC–MS data only one compound was found at the nominal *m*/*z* ratio 308 with the chemical formula $C_{11}H_{18}O_9N$ (*m*/*z* 308.0987, $[M–H]^-$). Since the AeroFAPA–MS is selective towards acidic compounds this signal possibly indicates the presence of a highly oxidized nitrogen-containing carboxylic acid, such as a nitrooxy carboxylic acid. Similarly, a signal at *m*/*z* 250 is found in the AeroFAPA–MS spectra, showing a linear correlation to the AMS data. In this case, however, the signals of the LC–MS analysis exhibited abundances below the data processing threshold at *m*/*z* 250. Only by manual data analysis a significant signal could be identified at *m*/*z* 250.0208, resembling $C_7H_8O_9N$. Due to the high oxygen content of these

two compounds and their low corresponding signals from the LC–MS analysis, it is assumed that they possibly decompose during sampling, transport, storage or processing of the filter samples. Moreover, it is nitrooxy compounds are also known to be prone to nucleophilic substitution by SO_4^{2-}, forming their more stable organosulfate derivates (Darer *et al.*, 2011). Thus, only online detection methods such as AeroFAPA–MS would allow a reliable detection of such highly oxidized nitrooxy carboxylic acids in organic aerosols.

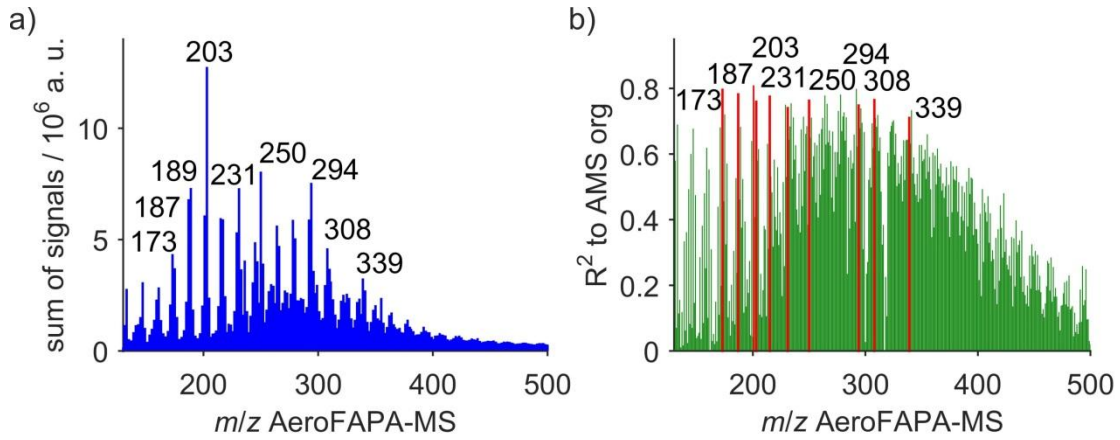

Figure 4.3.4: (a) sum of signals during the campaign period of the AeroFAPA–MS; (b) linear correlations between *m*/*z* ratios of AeroFAPA–MS and total organic aerosol mass measured by the AMS.

In addition to these even *m*/*z* ratios, another signal with high abundances in the AeroFAPA–MS spectra and a high correlation to organic aerosol mass was observed at *m*/*z* 339. From the LC–MS data this compound could not be unambiguously identified and possible formula assignments are $C_{12}H_{19}O_9S$ (*m*/*z* 339. 0755, $[M–H]^-$), $C_{11}H_{19}O_{10}N_2$ (*m*/*z* 339.1060, $[M–H]^-$) or $C_{14}H_{27}O_7S$ (*m*/*z* 339.1482, $[M–H]^-$). However, for all three signals only low abundances were found, possibly also suggesting a decomposition of this compound on the filter surface.

4.3.2 Real-time detection of HOOS in the field

In order to detect HOOS in real time with the AeroFAPA–MS, four representative compounds were chosen from Table 4.3.3. The selection procedure for these representative compounds was based on the following criteria: Firstly, the HOOS were grouped according to their number of carbon atoms per molecule into C7 to C10 compounds. Secondly, since the AeroFAPA–MS exhibits only unit mass resolution the signals of the representative HOOS had to show a higher intensity on their nominal *m*/*z* ratio than any other signal. Moreover, special care was taken that no HOOS with identical nominal *m*/*z*

ratios but different carbon numbers were chosen as representative, as it is the case for e.g. $C_9H_{13}O_9S$ and $C_{10}H_{17}O_8S$ (both at nominal *m/z* 297). Finally, the high mass resolution data of the LC–MS analysis were checked for HOOS that meet these criteria.

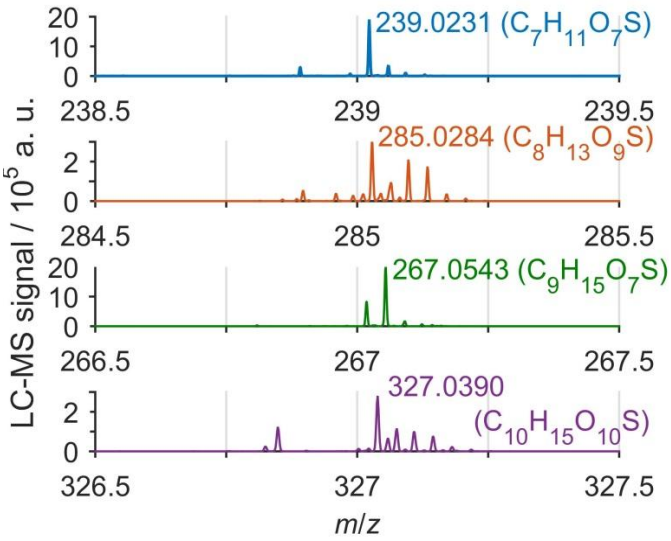

Figure 4.3.5: Mass spectra of the LC–MS analysis of a filter sample with a mass resolution of R=7·10^4 at *m/z* 200. Four HOOS compounds were chosen as representative according to their number of carbon atoms (C_7–C_{10}) and signal abundance.

As can be seen in Figure 4.3.5, for each of the HOOS classes one appropriate compound was found. For the C7 HOOS the signal at *m/z* 239.0231 was chosen, resembling $C_7H_{11}O_7S$ ($[M–H]^-$). This signal shows the highest abundance of all HOOS compounds from the filter measurements, as it was already reported by Mutzel *et al.* (Mutzel *et al.*, 2015), and almost no other signal was detected in significant abundances at this nominal *m/z* ratio. For the C9 HOOS an intense signal at *m/z* 267.0543 ($C_9H_{15}O_7S$, $[M–H]^-$) met the criteria and was selected. The *m/z* ratio at 285.0284, embodying $C_8H_{13}O_9S$ ($[M–H]^-$), was chosen as representative for the C8 HOOS although the signal was only observed in lower abundances and additional signals were found on the nominal *m/z* ratio. Yet, this signal showed the best agreement with the selection criteria for the C8 class. A similar case was observed for the C10 HOOS for which the signal at *m/z* 327.0390 ($C_{10}H_{15}O_{10}S$, $[M–H]^-$) was chosen as representative. Although all of the selected compounds exhibit other signals on their nominal *m/z* ratios, it was assumed that these extraneous signals only have a minor effect on the overall signal for HOOS over time. Furthermore, it was assumed that AeroFAPA–MS detects the selected HOOS also as $[M–H]^-$ ions, and thus, at the same nominal *m/z* ratio as for the LC–MS data.

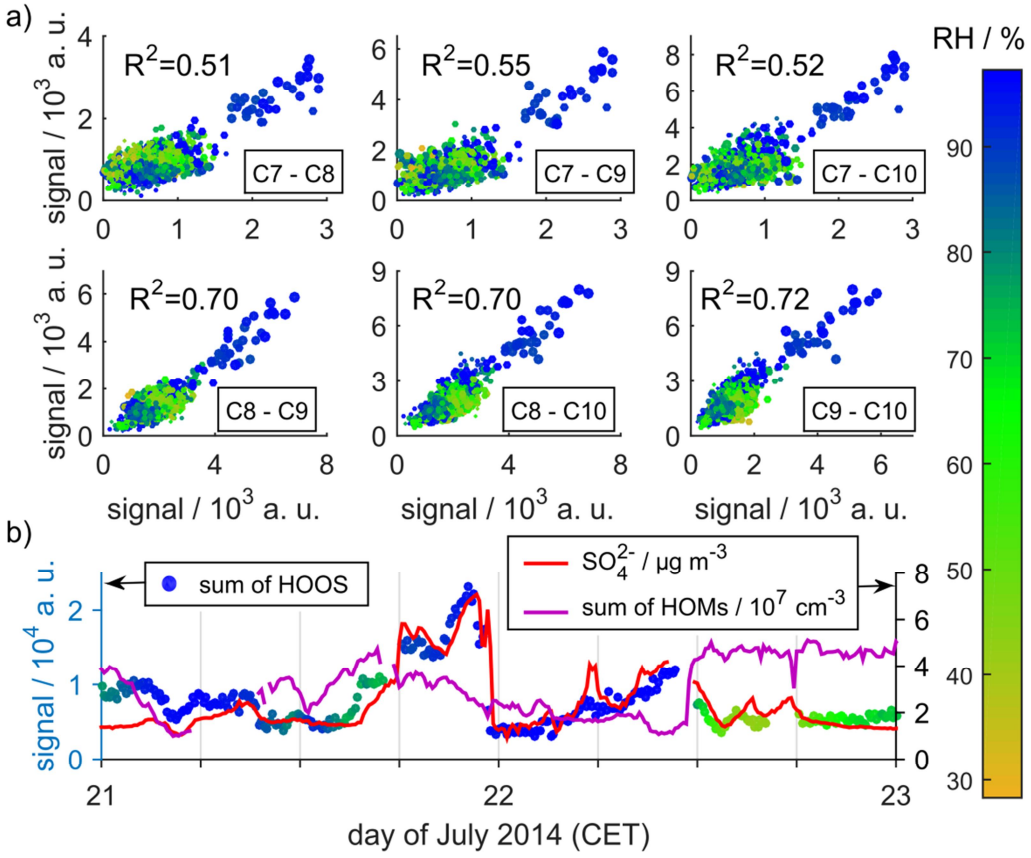

Figure 4.3.6: (a) Correlations among the HOOS classes and effect of RH (color code) and particulate sulfate on their formation (marker size). (b) Comparison of the sum of HOOS signals, particulate sulfate, and sum concentration of gas-phase HOMs during July 21st–23rd , demonstrating good agreement between HOOS and sulfate for high RH periods.

Figure 4.3.6 (panel a) depicts the signals of the AeroFAPA–MS which were plotted as a function of each other and checked for linear correlations among them. In addition, the particulate sulfate concentrations and relative humidity (RH) are given by the marker size and the color code, respectively. In general, all four HOOS classes show a linear correlation to each other, suggesting similar sources for these compounds. However, the group of C7 HOOS exhibits significant lower correlation coefficients of 0.51, 0.55 and 0.52 to the C8, C9, and C10 HOOS, respectively. This decreased correlation might indicate that the source for the C7 class is somewhat different to the larger HOOS. In fact, while the signal for $C_7H_{11}O_7S^-$ (*m/z* 239.0231,$[M–H]^-$) shows the highest abundances of all HOOS from the filter sample analysis, as it was also reported by Mutzel et *al.* (Mutzel *et al.*, 2015), the AeroFAPA–MS measurements exhibit only low signals for this compound, further suggesting a different source than for the other HOOS. Possibly, this compound is a decomposition product of the larger HOOS compounds which is also formed over time on the filter surface during sampling, storage and/or processing of the sample. This hypothesis

is further supported by comparing time traces for HOOS on single days (see Supplemental Material) and the previously proposed nucleophilic attack of HSO_4^- after decomposition of HOMs (Mutzel *et al.*, 2015).

As can be seen from the figure, all HOOS classes yield the strongest signals for high particulate sulfate concentrations, however, no linear correlation could be observed over the entire campaign period but only for single days. Moreover, the most intense signals for HOOS were found during high RH periods which coincided to a large extent with the high sulfate concentrations, suggesting that aqueous-phase chemistry plays a major role for HOOS production, as it is known for other OS compounds (Herrmann *et al.*, 2015).

In particular, the sulfate concentrations and signals for HOOS show a linear correlation (R^2=0.70) during the high RH period from 21st–23rd of July. Figure 4.3.6 (panel b) depicts the time trace of the signals for the HOOS and the particulate sulfate concentrations. Additionally, the RH is given by the color code. For the beginning of July 21st the signals for HOOS and the sulfate concentrations still show some minor deviation, however, starting roughly from 9 a.m. both time traces follow almost exactly the same trend for the rest of this period. For the majority of this period RH values exceed 80%. Therefore, it is assumed that during high RH periods dissolved HSO_4^- might react with HOMs after phase transition via a nucleophilic attack to give HOOS, as it was already proposed by Mutzel *et al*. (2015). A rapid phase transition of gas-phase HOMs into the particle phase is further supported by the signal for the sum of HOMs, measured by the CI–APiTOF–MS. As depicted in the figure, until ~11 a.m. of July 22nd the signal for gas-phase HOMs is hardly correlated to the HOOS signal or the sulfate concentration and shows rather low abundances, however, as soon as the RH value decreases to values <60% the gas-phase concentrations of HOMs exhibit an immediate and strong increase, roughly tripling the concentration within ~1.5 hours.

In theory, dissolved SO_2 and HOMs might even explain the elevated particulate sulfate concentrations to a certain degree. Since HOMs are presumably organic peroxides they can possibly oxidize dissolved SO_2, i.e. HSO_3^-, and form HSO_4^-, as it is known for smaller organic peroxides such as methylhydroperoxide or peroxyacetic acid (Lind *et al.*, 1987; Seinfeld and Pandis, 2006). Thus, dissolved SO_2 and HOMs would generate the sulfur-containing nucleophile for HOOS production in a previous reaction step, eventually enhancing HOOS formation and HOM loss rates. However, due to the limited data set and ambient conditions, the exact reaction mechanisms for HOMs and HOOS in aqueous media cannot be discriminated here. It should also be noted that besides the suggested

nucleophilic attack by HSO_4^- alternative mechanisms, such as radical-radical reactions involving photochemically generated $HSO_4^{\bullet}$ radicals, might also explain the formation of HOOS during daytime and were already reported for smaller OS originating from isoprene, methylvinyl ketone, methacrolein, α-pinene and glycoaldehyde (Perri *et al.*, 2010; Nozière *et al.*, 2010).

For dryer periods the correlation between particulate sulfate and HOOS formation is less distinct. Thus in contrast to the high RH periods, gas-phase H_2SO_4, which is produced by oxidation of gaseous SO_2, might present an additional sulfur source for HOOS generation during these periods, as can be seen in Figure 4.3.7 (panel b). However, no clear correlation was observed over the entire campaign but only for single days when high HOOS signals coincided with high gas-phase H_2SO_4 concentrations. Furthermore, it is assumed that the presence of precursor HOMs is the rate-limiting step in HOOS production since concentrations for particulate sulfate as well as gas-phase H_2SO_4 are typically orders of magnitude higher. The hypothesized reaction mechanisms for the humid periods, therefore, are probably still valid for the low RH periods.

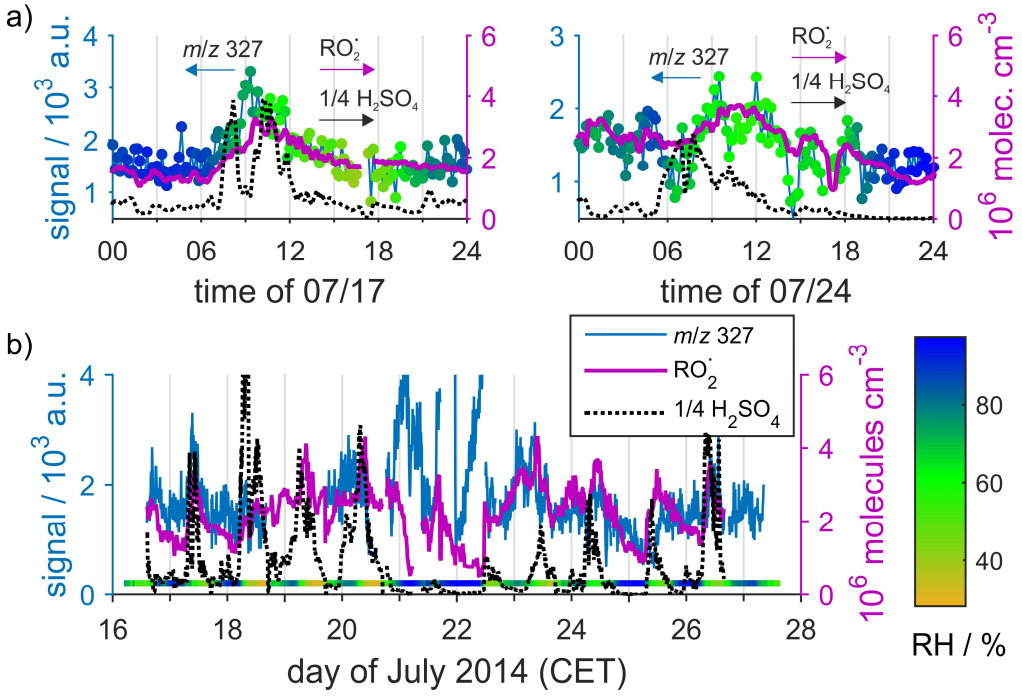

Figure 4.3.7: Signals for C10 HOOS (*m/z* 327), gas-phase H_2SO_4, $RO_2^{\bullet}$ ($C_{10}H_{15}O_8^{\bullet}$), and RH. Panel a: Time traces for the signals for July 17th and 24th, showing good agreement between C10 HOOS and $RO_2^{\bullet}$. Panel b: Time traces for the entire campaign period, demonstrating the influence of RH on HOOS formation and $RO_2^{\bullet}$ abundance. For better visibility the HOOS signal is allowed to go off scale for July 21st and 22nd.

In order to further investigate the formation of HOOS and the role of possible precursor HOMs, single *m*/*z* ratios of the CI–APiTOF–MS were closer analyzed. For the low RH periods, signals of the CI–APiTOF–MS with an odd *m*/*z* ratio dominate the HOM concentrations (see Supplemental Material Figure 5.5.21). As it was reported previously (Jokinen *et al.*, 2014; Ehn *et al.*, 2014), several of these compounds represent peroxyradicals ($RO_2^{\bullet}$) which may act as precursors for closed-shell HOMs. Remarkably, the signals for $RO_2^{\bullet}$ and HOOS follow the same trends during the dry periods, possibly revealing a connection between these species. As an example Figure 4.3.7 depicts the time traces of the representative C10 HOOS (*m*/*z* 327, $C_{10}H_{15}O_{10}S$, $[M–H]^-$) and the most abundant $RO_2^{\bullet}$, i.e. $C_{10}H_{15}O_8^{\bullet}$ (*m*/*z* 325, $[M+NO_3]^-$), which might represent a possible precursor species. In addition, the gas-phase concentration of H_2SO_4 (divided by 4) and RH are given. As can be seen for July 17th and 24th (panel a) the signal for $RO_2^{\bullet}$ is increasing with time, showing its maximum at ~$4 \cdot 10^6$ molecules cm^{-3} for both days around 11 a.m., and is afterwards slowly decreasing again. For both days also a significant amount of gas-phase H_2SO_4 was present, giving maximum values of ~$1.6 \cdot 10^7$ molecules cm^{-3} and ~$1.3 \cdot 10^7$ molecules cm^{-3} for July 17th and 24th, respectively. In contrast, the particulate sulfate concentration was rather high during July 17th (maximum at ~5.7 µg m^{-3}) but quite low for July 24th (maximum at ~2.8 µg m^{-3}). In each case, the signal for the C10 HOOS follows almost exactly the concentration of the $RO_2^{\bullet}$. Therefore, $RO_2^{\bullet}$ is assumed to be either a direct, or at least indirect, precursor for HOOS. Since it can be assumed that not only closed-shell HOMs contain carbonyl-functionalities, as it was recently shown (Mutzel *et al.*, 2015), but also their corresponding precursor $RO_2^{\bullet}$, a nucleophilic attack by HSO_4^- is in any case possible and might explain HOOS formation in the particle phase.

4.4 Conclusion

The chemical composition of the organic aerosol fraction was analyzed during the F-BEACh 2014 campaign with complementary mass spectrometric techniques. The non-target analysis of filter samples by LC–MS revealed 93 acidic organic compounds that accounted for a major fraction of the organic aerosol mass. In addition, it was shown that around 47% of the identified compounds were sulfur-containing, suggesting a rather high anthropogenic impact on biogenic emissions and their oxidation processes. Among the sulfur-containing compounds, several OS, NOS, and HOOS were unambiguously identified. The CHO-containing compounds exhibited several common BSOA marker

compounds, showing rather high concentrations for the monoterpene photooxidation products MBTCA and 3-carboxyheptanedioic acid. This finding suggests that aerosol masses reaching the site were mostly dominated by *α*-/*β*-pinene and *d*-limonene oxidation products. In agreement, VOC measurements showed high mixing ratios for these monoterpenes in and above canopy level. Furthermore, the abundance of MBTCA and 3-carboxyheptanedioic acid and their ratios to earlier-generation oxidation products, such as pinic acid, suggest that relatively aged aerosol masses were present during the campaign period. In agreement, HYSPLIT trajectories revealed that most of the air masses traveled long distances (>1500 km) over land under cloud-free conditions.

In general, real-time measurements of the aerosol masses using AeroFAPA–MS, AMS and CI–APiTOF–MS further supported these findings. In addition, correlations among HOOS classes, sulfate and gas-phase HOMs were checked and identified. In agreement with previous studies the results support the hypothesis that HOOS are formed by reactions of gas-phase HOMs with particulate sulfate, i.e. HSO_4^- (Mutzel *et al.*, 2015). Since the signals for the C7 HOOS show rather low abundances and only low correlations to the other HOOS it is assumed that these HOOS are rather decomposition products of larger HOOS. This finding is, however, not contradicting previous publications which found the highest concentrations for C7 HOOS from filter sample analyses (Mutzel *et al.*, 2015). It is rather suggesting that larger HOOS decompose not only in the atmosphere but also during filter sampling, storage or processing, forming the observed C7 decomposition products. Furthermore, gas-phase $RO_2^{\bullet}$ are assumed to be precursors for HOOS since a good agreement was found between HOOS formation and $RO_2^{\bullet}$ concentration during rather dry periods. High RH periods, however, revealed that aqueous-phase chemistry is presumably playing a major role in HOOS production since the highest HOOS signals coincided with high RH values and high particulate sulfate concentrations.

Acknowledgements

This work was supported by the Max Planck Graduate Center with the Johannes Gutenberg-Universität Mainz (MPGC).

The authors gratefully acknowledge the NOAA Air Resources Laboratory (ARL) for the provision of the HYSPLIT transport and dispersion model and READY website (*http://www.ready.noaa.gov*) used in this publication.

Note: Supplementary material can be found in the Appendix (section C).

5 Probing the Interfacial Layer of Organic Aerosol Particles Using AeroFAPA–MS

This chapter is a reprint of the article:

Martin Brüggemann, Einar Karu, Thorsten Hoffmann

Particle Desorption Characteristics of AeroFAPA–MS – Is Depth Profiling of Organic Aerosol Particles Possible?

In preparation for Analytical Chemistry

Abstract

Particle desorption characteristics of the recently described AeroFAPA–MS technique were investigated, using tricarballylic acid (TCA) aerosol particles as a model system. The ion signal was found to scale with the surface size distribution of the analyzed particles, suggesting that the interfacial region of particles is desorbed in the ionization region. In agreement, desorption radii of 2.5–36.6 nm were observed for particles with an initial diameter of 112 nm at discharge currents of 15–55 mA. Comparisons of the data with results of a simplified aerosol evaporation model suggest that particle residence times in the desorption/ionization region are in the microsecond range. Moreover, the calculated residence times are decreasing with increasing discharge currents, indicating that mixing of aerosol particles and helium is hampered at higher discharge currents due to rising helium viscosities and the resulting more laminar helium flow. In agreement with this assumption, residence times of particles with higher inertia are less affected by increasing discharge currents.

Additionally, aerosol particles with known core-shell morphology were analyzed in a proof-of-principal study. TCA seed particles were coated with α-pinene oxidation products, giving an average coating thickness of ~65 nm. The mass spectrometric analysis of these particles showed that signals for pinic acid, i.e. a major oxidation product of α-pinene, exhibited a distinct increase with increasing discharge currents and, thus, probing depths. In contrast, the increase of ion signals for TCA was rather moderate. To our knowledge, AeroFAPA–MS thus represents the first field-deployable technique which is capable of probing the interfacial layer of organic aerosol particles.

5.1 Introduction

Secondary organic aerosols (SOAs) are a major contributor to tropospheric organic aerosol and have implications for climate and human health. They are formed by phase transition of low-volatile oxidation products which are generated by oxidation of volatile organic compounds in the atmosphere. Their properties are greatly affected by aerosol particle size, chemical composition, morphology, mixing, and phase state (IPCC, 2014; Pöschl and Shiraiwa, 2015).

While commonly SOA particles are assumed to be well-mixed liquid droplets in equilibrium gas/particle partioning theory (Pankow and Bidleman, 1991; Pankow, 1994b), a number of more recent studies showed that SOA particles can reside in a highly viscous,

amorphous semi-solid or even solid state under atmospherically relevant conditions (Virtanen *et al.*, 2010; Shiraiwa *et al.*, 2011; Saukko *et al.*, 2012; Shiraiwa *et al.*, 2012). Moreover, it was demonstrated that, besides evaporation kinetics and volatility (Cappa and Wilson, 2011; Vaden *et al.*, 2011), diffusion within the particles is strongly decreased with increasing viscosities (Shiraiwa *et al.*, 2011). Since low diffusion rates impede the formation of well-mixed particles, reaction products which are formed on the surface of a particle, e.g. by OH, NO_3 or ozone chemistry, cannot diffuse into the particles' core and remain at the surface. The same applies for condensation of low-volatile compounds from the gas phase. Eventually, this leads to particles with core-shell morphology. In the particles' cores initial compounds are preserved, whereas the shells contain mainly oxidation and condensation products. In fact, it was shown that under dry conditions oxidation of compounds in the core of aerosol particles can be slowed down or entirely suppressed by organic coatings due to slow diffusion through the organic layer (Zhou *et al.*, 2012; Zhou *et al.*, 2013). Thus, by analyzing the particles' cores and shells separately, it might be possible to obtain valuable information on the formation and evolution of the aerosols' particle and gas phase.

However, up to now there are only few techniques available which allow separate analyses of compounds residing in aerosol particles' shells and cores, i.e. depth profiling. In general, mass spectrometry (MS) has proven a suitable and versatile tool, capable of detecting and identifying trace amounts of substances in complex systems, such as ambient aerosol particles. For example, instruments such as the aerosol mass spectrometer (AMS) are nowadays standard instrumentation in aerosol research, allowing the real-time characterization of submicron aerosol particles (Pratt and Prather, 2012b). Nonetheless, only few MS methods are available for depth profiling of such particles. Furthermore, these methods are often time-consuming, tedious and/or not able to identify single organic compounds (Pratt and Prather, 2012b; Laskin *et al.*, 2013). For depth profiling of ambient aerosol particles collected by impaction or filter sampling, most studies utilized secondary ion mass spectrometry (SIMS), although known to result in significant surface damage, substantial fragmentation of organic molecules, and in relatively low ionization yields. Moreover, the time resolution of such measurements is rather low due to offline sampling of the particles (Laskin *et al.*, 2013). Depth profiling of organic aerosol particles suspended in air was first accomplished using laser ablation single-particle MS, yet, organic compounds of the sampled particles can only be monitored by characteristic signals in the mass spectra and no clear compound identification is possible from these measurements

(Zelenyuk *et al.*, 2008; Bente *et al.*, 2008; Vaden *et al.*, 2010). A more promising approach was presented by Nah *et al*. using direct analysis in real-time MS (DART–MS) to detect and identify ozonolysis products of oleic acid in the interfacial layer of organic aerosol particles (Nah *et al.*, 2013). However, due to its open setup configuration, this method requires rather high aerosol mass concentrations and, thus, is not applicable to ambient measurements.

Regarding this lack of suitable instrumentation, the particle desorption characteristics of the recently described aerosol flowing atmospheric-pressure afterglow (AeroFAPA) technique (Brüggemann *et al.*, 2015) were investigated in this study to assess its application for depth profiling studies of organic aerosol particles in real time.

AeroFAPA–MS is a novel soft ionization technique which was shown to allow the mass spectrometric analysis of bulk submicron organic aerosols. The ion source is based on a helium glow discharge plasma at atmospheric pressure which generates excited helium species and primary reagent ions. These primary species exit the discharge region and are transferred into the so-called afterglow region where desorption and ionization of the analytes occurs. Due to relatively low temperatures of only 80 °C to 150 °C and ambient pressure in the afterglow region, the ionization process is rather soft and almost no fragmentation of organic molecules is observed, resulting in mass spectra that are easy to interpret and allowing the identification of single aerosol components.

In the first part of this study, the extent of particle desorption and its dependence on AeroFAPA discharge currents were investigated. In addition, a simplified aerosol evaporation model is utilized to estimate desorption radii and residence times of the sampled particles in the afterglow region. The purpose of the second part is to demonstrate the general capability of AeroFAPA–MS to perform depth profiling of organic aerosol particles by adjusting the probing depth via AeroFAPA discharge currents.

5.2 Experimental

5.2.1 Reagents and Materials

Methanol (HPLC grade, >99.9%) was purchased from Fisher Scientific. Tricarballylic acid (≥99%) and (+)-α-pinene (≥99%) were purchased from Sigma-Aldrich. High purity helium (≥99.999%) and synthetic air (N_2 79.5 vol%, O_2 20.5 vol%, hydrocarbon free) were obtained from Westfalen AG, Germany.

5.2.2 Particle Generation and AeroFAPA–MS Measurements

The AeroFAPA ion source was used in combination with an ion trap mass spectrometer (LCQ Deca XP Plus, Thermo, San José, CA, USA). A detailed description of the instrument can be found elsewhere (Brüggemann *et al.*, 2015), thus, only a brief description will be given here. In general, AeroFAPA–MS is a soft-ionization technique which allows the mass spectrometric analysis of organic aerosol particles in real time. To ionize organic compounds, the so-called afterglow region of a helium glow discharge plasma is utilized, comprising several primary reagent ions and excited helium species. Thus, common ionization pathways are Penning Ionization and charge transfer reactions. In the negative mode, which was applied throughout this study, ionization is selective towards acidic compounds, such as carboxylic acids and (nitrooxy) organosulfates, due to the presence of O_2^- ions. The source was used in current controlled mode at discharge currents of 15–55 mA, resulting in afterglow temperatures of ~80–150 °C.

The experimental setup used for characterization of particle desorption in the afterglow region is depicted in Figure 5.2.1 (panel a). A methanolic solution of TCA was nebulized to produce aerosol particles. Prior to particle size-selection by a differential mobility analyzer (DMA, Model 3081, TSI Inc., USA), the aerosol stream passed an activated charcoal denuder to remove residual methanol. Then, the monodisperse particles were transferred to a condensation particle counter (CPC, Model 3025, TSI Inc., USA) and AeroFAPA–MS. Afterward, a scanning mobility particle sizer (SMPS, SMPS+C 5.416, Grimm Aerosol Technik, Germany) was used to measure the particle number size distribution of particles leaving the afterglow region. The aerosol inlet flow of the AeroFAPA was set to 0.9 $L \cdot min^{-3}$, and the helium flow rate to 0.6 $L \cdot min^{-3}$ throughout all experiments. In contrast to previous studies, the aerosol inlet of the AeroFAPA manifold was kept at room temperature to avoid pre-evaporation of the analyzed particles. A brief discussion of the effects of inlet heating is given in the Supplemental Material (Figure 5.5.3).

The experimental setup used for generation and analysis of particles with core-shell morphology is illustrated in panel (b) of the figure. First, TCA aerosol particles were generated by nebulization of a methanolic solution, as explained above. Then, particles were size-selected by a DMA and introduced into a 100 L cylindrical reaction chamber. After reaching a steady state inside the chamber, gaseous α-pinene (~500 ppb) and ozone (~1 ppm) were added to produce corresponding low-volatile oxidation products which condensed on the pre-existing seed particles. A detailed description of the procedure can be

found elsewhere (Müller *et al.*, 2008; Brüggemann *et al.*, 2014). The coated particles were guided through an activated charcoal denuder to remove gas-phase oxidation products and were then size-selected by a second DMA. Subsequently, particle concentrations were monitored by a CPC and the particles analyzed by AeroFAPA–MS.

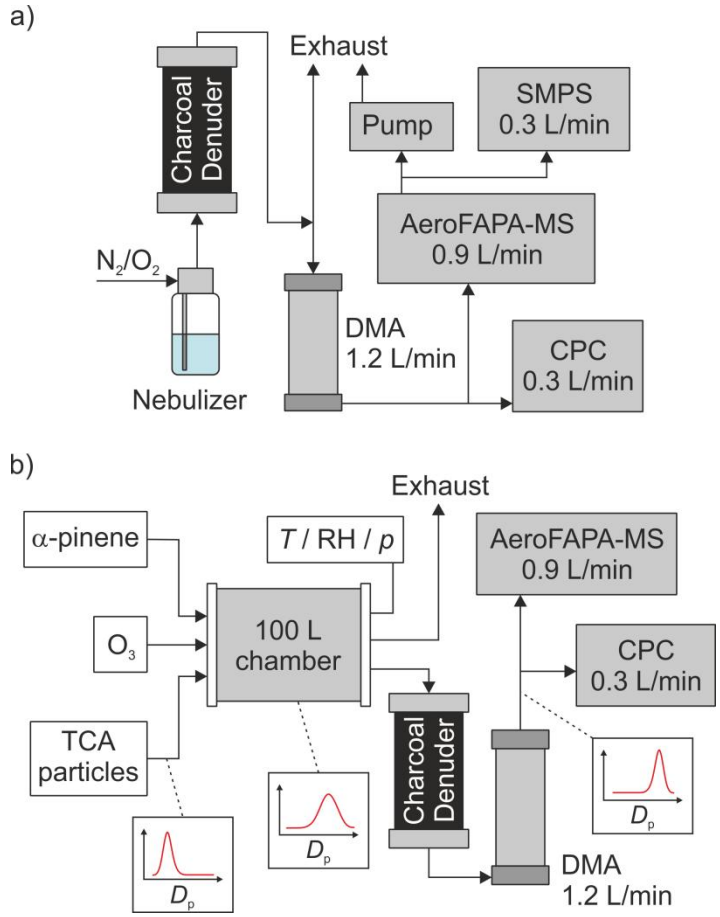

Figure 5.2.1: (a) Experimental setup used for characterization of particle desorption in the afterglow region. After nebulization, particles were size-selected by a differential mobility analyzer (DMA) and guided to a condensation particle counter (CPC) and the AeroFAPA–MS. A scanning mobility particle sizer (SMPS) measured the particle number size distribution of particles leaving the ion source. (b) Experimental setup used for generation and analysis of core-shell particles. Monodisperse TCA aerosol particles were introduced into the reaction chamber. Afterward, α-pinene and ozone were added to coat the seed particles with corresponding oxidation products. Gas-phase oxidation products were removed by a charcoal denuder prior to size-selection by a DMA. Subsequently, particles were counted by a CPC and analyzed by AeroFAPA–MS.

5.3 Results and Discussion

5.3.1 Characterization of Particle Desorption in the Afterglow Region

To investigate particle desorption characteristics of AeroFAPA–MS, TCA aerosol particles were chosen as a model system. As reported previously, TCA is readily ionized and detected by AeroFAPA–MS in the negative mode with a low degree of fragmentation and, thus, allows even the detection of variations in the ng·m^{-3} range (Brüggemann *et al.*, 2015). As can be seen in Figure 5.3.1, mainly the quasimolecular ion of TCA, i.e. $[M–H]^-$, was observed at *m*/*z* 175 at high abundances in the mass spectrum when pure TCA aerosol particles at a mass concentration of 10 µg·m^{-3} were analyzed. Signals corresponding to the loss of water were only detected to a rather low extent at *m*/*z* 157 ($[M–H–H_2O]^-$). Furthermore, signals for esterification products were observed due to the use of methanol as solvent at *m*/*z* 189 ($[M–H]^-$) and 252 ($[M+NO_3]^-$). However, in general these signals contributed less than 10% to the recorded mass spectra. Therefore, only the signal for the quasimolecular at *m*/*z* 175 was monitored during the following desorption experiments in order to enhance detection limits and time resolution.

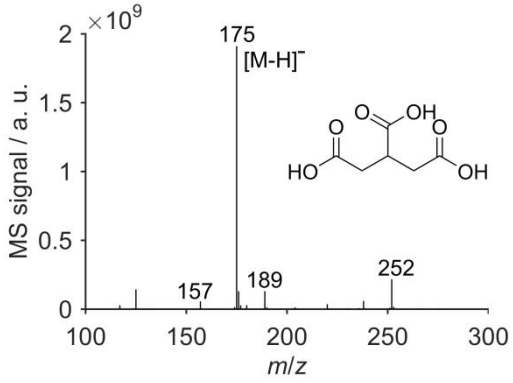

Figure 5.3.1: Mass spectrum of tricarballylic acid aerosol particles in the negative mode at a discharge current of I = 55 mA. The main signal at *m*/*z* 175 is corresponding to the quasimolecular ion ($[M–H]^-$). Furthermore, signals corresponding to loss of water (*m*/*z* 157, $[M–H–H_2O]^-$) and methanol esterification were observed (*m*/*z* 189, 252).

Figure 5.3.2 shows the number size distribution (dotted), corresponding surface size distribution (blue), and mass size distribution (black) of TCA aerosol particles, determined by the SMPS. While the SMPS was scanning through the selected range of particle sizes (26–260 nm), a portion of the monodisperse aerosol was guided to the AeroFAPA–MS for mass spectrometric analysis. During all measurements the total particle number was held at 2.34±0.17·10^5 cm^{-3} and the number size distribution exhibited a median diameter of

85.9±0.89 nm. Since particle desorption was expected to be dependent on the afterglow temperature, two different discharge currents of I = 35 mA (panels a and b) and 55 mA (panels c and d) were investigated, leading to afterglow temperatures of T = 119 °C and 150 °C, respectively (Table 5.3.1).

As can be seen from the figure, for the lower discharge current of 35 mA the AeroFAPA–MS signal at m/z 175 is generally increasing with the selected particle size. In particular, for particle diameters <100 nm the signal stays between the surface and the mass size distribution, however, for particles >100 nm in diameter the signal clearly follows the surface size distribution. Therefore, it is assumed that only an outer shell of the aerosol particles is evaporated in the afterglow region and, thus, available for ionization and mass spectrometric detection by AeroFAPA–MS. Furthermore, the probing depth is presumably decreasing with increasing diameters of the analyzed particles due to the inherent increase in particle mass, eventually leading to the observed agreement between ion signal and surface size distribution. In general, a similar trend was observed for the measurements at the higher discharge current of I = 55 mA, however, the agreement of the TCA ion signal and the surface size distribution is less distinct. For particle sizes of ~80–150 nm the ion signal is still above the mass size distribution but clearly below the surface size distribution, thus, suggesting an enhanced particle evaporation due to the increased afterglow temperature. Only for particle diameters >150 nm the signal starts to follow the surface size distribution. Although these measurements solely give a qualitative estimation of particle desorption in the afterglow region they clearly demonstrate that AeroFAPA–MS is capable of chemically characterizing the particles' interface instead of the bulk aerosol phase. Moreover, the probing depth can possibly be varied by the applied discharge current.

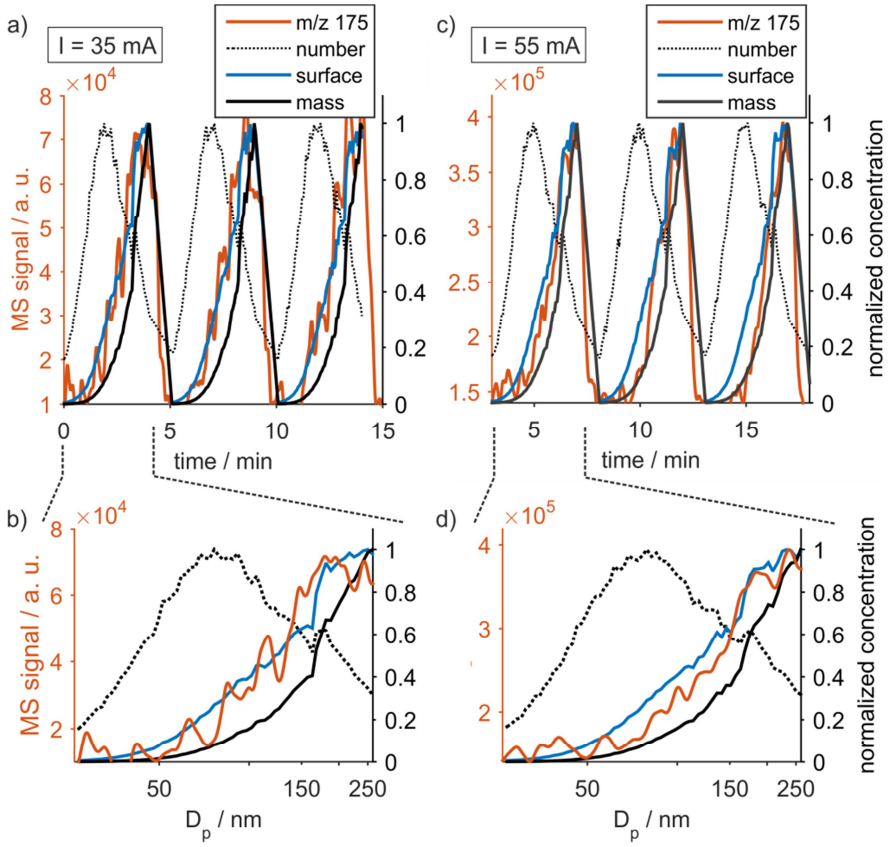

Figure 5.3.2: SMPS analysis of TCA aerosol particles and response of AeroFAPA–MS for the quasimolecular ion at *m/z* 175 ($[M–H]^-$). Panels (a) and (c) depict the normalized particle number size distributions (dotted), surface size distributions (blue), and mass size distributions (black) of three subsequent scans of the SMPS and the simultaneously recorded AeroFAPA–MS signal at *m/z* 175 (orange) at I = 35 mA and 55 mA, respectively. Panels (b) and (d) show the data for the first scan in correlation to the particle diameter set by the SMPS.

To further investigate the dependence between particle desorption and discharge current, monodisperse TCA aerosol particles with a median diameter ($D_{p,mean}$) of 112±1.0 nm were introduced into the afterglow region of the AeroFAPA. Simultaneously, the particle number size distribution of particles leaving the ion source was measured by the SMPS. As depicted in Figure 5.3.3, the median diameter of the particle number distribution is decreasing with increasing discharge currents, which can probably be explained by the rising temperatures of the afterglow region. While for the lowest of the investigated discharge currents (I = 15 mA) the median particle diameter only decreases by ~2.5 nm, a median diameter change of ~36.6 nm is observed for the highest current (I = 55 mA). Table 5.3.1 gives an overview of the applied discharge currents, corresponding afterglow temperatures and changes in median particle diameter ($\Delta D_{p,mean}$). In agreement with the scanning experiments discussed above, the probing depth, i.e. the difference in particle radius ($\Delta D_{p,mean}/2$), for I = 35 mA is significantly lower than for

I = 55 mA, explaining the observed trends for TCA ion signal and surface/mass size distribution.

Additionally, for I = 45 mA and 55 mA it can be seen that a portion of the original number size distribution was still present after passing the ion source, suggesting that not all particles were affected by the helium stream exiting the discharge cell. This is, however, not surprising since the inner diameter of the aerosol inlet is roughly three times the inner diameter of the AeroFAPA's exit capillary. Moreover, it was shown that for similar setups turbulence of the helium stream only starts after a distance of ~50–60 mm (Pfeuffer *et al.*, 2013b). Thus, it can be assumed that the introduced aerosol particles encounter a rather laminar helium flow in the AeroFAPA source manifold, although, this stream might be perturbed to a certain extent by the incoming aerosol stream.

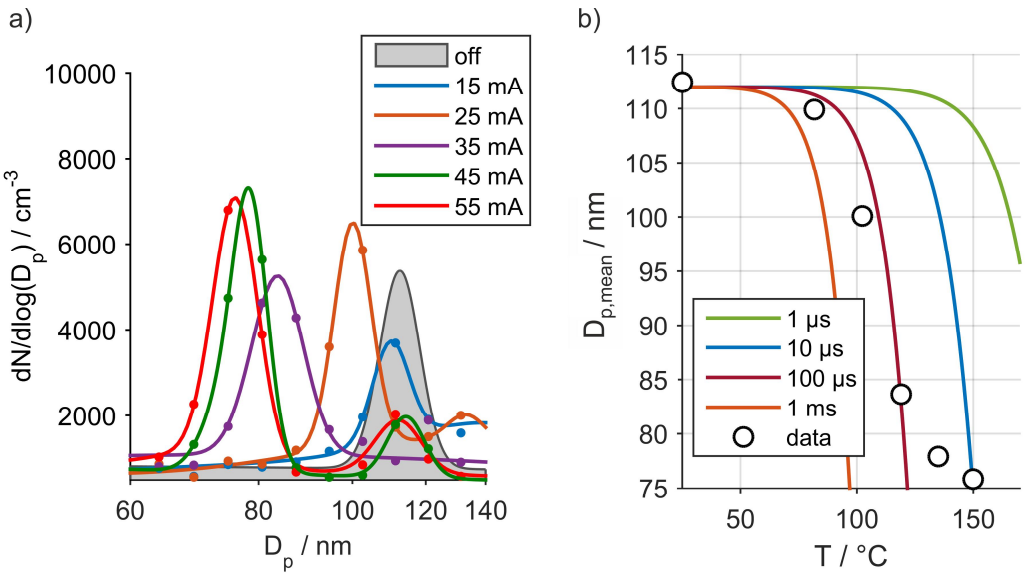

Figure 5.3.3: (a) Particle number size distributions of TCA aerosol particles before (gray) and after passing the afterglow region at different discharge currents. (b) Median particle diameter (circles) as a function of afterglow temperature. The colored lines depict aerosol evaporation model calculations for different particle residence times in the afterglow region.

Table 5.3.1: Afterglow temperature (T), median particle diameter ($D_{p,mean}$), and change in median diameter ($\Delta D_{p,mean}$) at different AeroFAPA discharge currents (I).

I / mA	T / °C [a]	$D_{p,mean}$ / nm	$\Delta D_{p,mean}$ / nm
–	25	112.4	–
15	82	109.9	-2.5
25	102	100.1	-12.3
35	119	83.6	-28.8
45	135	77.9	-34.5
55	150	75.8	-36.6

[a] from Brüggemann *et al.*, 2015

Since ionization of analytes in the afterglow region is believed to occur mainly in the gas phase for AeroFAPA–MS, particle desorption is crucial for detection of the analytes. Thus, the observed evaporation of TCA particles and corresponding changes in $D_{p,mean}$ were compared to results obtained by an established aerosol evaporation model (Riipinen *et al.*, 2010). The time-dependent evaporation of TCA aerosol particles in the afterglow was modeled by solving the mass transfer equations of a monodisperse particle population and assuming the absence of other dynamic processes, such as nucleation and/or coagulation. The time-dependent gas-phase concentration of TCA ($c_{g,TCA}$) was calculated using the equation (5.1).

$$\frac{dc_{g,TCA}}{dt} = \frac{2\pi D_p p M D_{TCA} \beta_m}{RT} \ln\left[\frac{1 - p_{TCA}/p}{1 - p^0_{TCA}/p}\right] \cdot N \qquad (5.1)$$

The particle diameter D_p was set to 112 nm, as determined for the non-affected particle size distribution by SMPS measurements. p is the ambient pressure (101.13 hPa) and M the molecular weight of TCA (176.12 g·mol^{-1}). N is the total number concentration of particles, R the gas constant, and T the temperature in the afterglow region. p^0_{TCA} and p_{TCA} are the partial vapor pressures of TCA at the particle surface and far away from the particles, respectively. However, p_{TCA} is set to zero since the steady aerosol stream is ideally removing any gas-phase compounds rapidly from the afterglow region and only a small mass fraction of the aerosol particles is expected to be vaporized. Using the Clausius-Clapeyron equation, the saturation vapor pressure of TCA at afterglow temperature T was estimated from $p_{sat,TCA}$ at room temperature. Moreover, the temperature dependence of the diffusion coefficient D_{TCA} was estimated by $D_{TCA}(T) = D_{TCA}(298\ K)\left(\frac{T}{298\ K}\right)^{\mu}$ with $\mu = 2$, as suggested for carboxylic acids (Faulhaber *et al.*, 2009; Riipinen *et al.*, 2010). Furthermore, the calculations were corrected for kinetic and transition regime effects by the correction factor β_m (Riipinen *et al.*, 2010). To obtain the total evaporated mass in the afterglow region, $c_{g,TCA}$ was multiplied by the estimated volume of the afterglow region (i.e. $(4\ mm)^3 = 6.4 \cdot 10^{-8}\ m^{-3}$). A comprehensive list of all parameters used for the model calculations is given in the Supplemental Material.

As can be seen in Figure 5.3.3 (panel b), the model was used to calculate the resulting particle diameters after desorption by AeroFAPA at different discharge currents and, hence, afterglow temperatures. Moreover, particle residence times in the afterglow region were varied from t = 1 µs to 1 ms in the model calculations in order to capture the observed

decrease in particle diameter. Previous calculations estimated the residence time of particles in the afterglow region to the range of 150–300 µs (Brüggemann *et al.*, 2015), however, the performed model calculations suggest that the actual residence times decrease with higher discharge currents down to ~10 µs. An estimated residence time of ~100 µs gives a good agreement between modeled and measured particle diameters for the lower discharge currents of I = 15–35 mA. Yet, with increasing afterglow temperatures the measured particle diameters are deviating from these calculations, showing better agreement with shorter residence times. Nonetheless, it has to be noted that these calculations are neglecting any mixing and/or turbulence which might occur when aerosol stream and helium flow encounter each other. It also should be noted that the model is quite sensitive to uncertainties in p^0_{TCA}, ρ, D_{TCA}, and ΔH_{vap}, which may have significant effects on the estimated residence times. Moreover, the temperature within the afterglow region exhibits a steep temperature gradient which is not reflected in the calculations, inevitably leading to shorter residence times for the model.

Although exact values for residence times cannot be retrieved from the calculations the general trend of decreasing residence times with increasing afterglow temperatures seems plausible. Higher helium temperatures, which are caused by the increased discharge currents, lead to a higher dynamic viscosity of the helium. Therefore, the entrainment of aerosol particles into the helium stream is hampered at higher discharge currents. Additionally, the increased plasma temperatures result in an enhanced heat expansion of the helium in the discharge cell and are, thus, increasing the helium velocity. Moreover, previously it was shown that higher discharge currents also lead to a more laminar flow of the helium stream due to increased viscosities, further impeding a mixing of aerosol particles and the helium current by turbulence (Pfeuffer *et al.*, 2013b).

To investigate the behavior of particles at different aerosol loadings and particle sizes, calibration curves for TCA were measured with AeroFAPA–MS at discharge currents of I = 35 and 55 mA and at particle diameters of D_{p} = 100, 200, and 300 nm. Afterwards, model calculations were conducted with the residence times determined above. Figure 5.3.4 (panel a) shows the response of AeroFAPA–MS at I = 35 mA as a function of aerosol mass concentration. For all particle diameters and mass concentrations a linear response was found, however, the slope of the calibration curves was decreasing with increasing particle size, supporting the hypothesis that only an outer shell of the particles is desorbed and analyzed by AeroFAPA–MS. Additionally, particle evaporation was modeled for the different aerosol mass loadings and particle diameters assuming an afterglow temperature

of $T = 119$ °C and a particle residence time of $t = 100$ µs, as determined by the measurements and calculations discussed above. Since these data were obtained for particle sizes of 112 nm, the calibration factor between calculated mass and MS signal was adjusted to fit the obtained data for particle diameters of 100 nm. However, for particle sizes of 200 and 300 nm the model then significantly underpredicted the evaporated mass in the afterglow region, as can be seen from the figure. Similar observations were made for the measurements at $I = 55$ mA, as depicted in panel (b) of the figure. Again, a linear response of AeroFAPA–MS to increasing aerosol mass concentrations was observed, yet, the total signal was enhanced by a factor of ~2–3 due to the increased discharge current. In this case, the model calculations were performed using an afterglow temperature of $T = 150$ °C and a particle residence time of $t = 10$ µs. As already observed for the lower discharge current, the model showed significant underpredictions for particles diameters of 200 and 300 nm when the evaporated mass was adjusted to the MS signals for 100 nm particles.

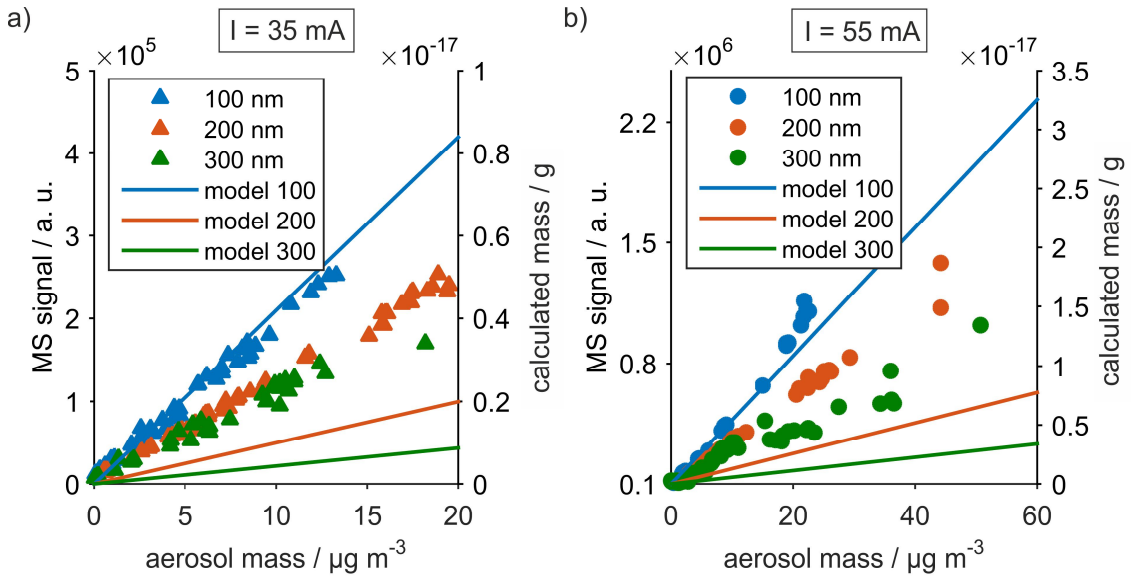

Figure 5.3.4: AeroFAPA–MS signal at *m*/*z* 175 and calculated mass evaporation as a function of TCA aerosol mass concentration at discharge currents of 35 mA (panel a) and 55 mA (panel b). While the evaporation model is in good agreement with the AeroFAPA–MS data for 100 nm particles, significant underpredictions were observed for bigger particle diameters.

This finding further supports the assumption that aerosol particles are encountering a rather viscous laminar helium flow in the afterglow region. While smaller particles with low inertia are not able to fully penetrate the helium current, bigger particles with higher inertia are able to enter the gas stream and, thus, are evaporated faster and to a larger extent. For example, a 100 nm TCA particle has a mass of merely $6.4 \cdot 10^{-16}$ g, whereas

200 nm and 300 nm particles have masses of $5.1 \cdot 10^{-15}$ g and $1.7 \cdot 10^{-14}$ g, resembling roughly an increase of factor ~8 and ~27, respectively. Therefore, the model is not necessarily underpredicting the evaporated mass for particle sizes of 200 and 300 nm, but rather overpredicting particle desorption for 100 nm particles. Similar observations were also made for the analysis of pinic acid particles, as shown in the Supplemental Material (Figure 5.5.2). Nonetheless, since particle mass and surface scale with D_p the ratio of desorbed mass to actual mass in the afterglow region is still higher for smaller particles as it was shown during the SMPS scanning experiments (Figure 5.3.2).

5.3.2 Generation and Analysis of Core-Shell Particles

To show that AeroFAPA–MS is chemically characterizing the outer shell of aerosol particles instead of the entire particle phase, core-shell particles were generated and analyzed in a proof-of-principle study. For this purpose, monodisperse TCA particles with a median diameter of ~180 nm were introduced into a 100 L glass cylinder, which served as continuous-flow reaction vessel. Coating of the TCA seed particles was accomplished by adding gaseous α-pinene and ozone which produced corresponding low-volatile oxidation products, condensing on the primary particles. In order to produce particles with a distinct core-shell morphology, the coating was conducted under dark and dry (RH<30%) conditions at ~21 °C. For 3-methylbutane-1,2,3-tricarboxylic acid (MBTCA), which is chemically similar to TCA, it was shown that glass transition occurs under dry conditions at ~305 K (~32 °C) (Dette *et al.*, 2014), therefore, TCA seed particles were assumed to reside in a semisolid or even solid state, impeding mixing of shell and core compounds by diffusion (Shiraiwa *et al.*, 2011). Additionally, SOA, produced by a-pinene ozonolysis at low RH values (<30%), was also found to be semisolid or even glassy at ambient temperatures, further decreasing self-diffusion of the condensed oxidation products (Renbaum-Wolff *et al.*, 2013). As can be seen in Figure 5.3.5 (panel a) at the beginning solely TCA particles were present in the reaction chamber, giving a total number concentration of $2.7 \cdot 10^4$ cm^{-3} (~150 μg·m^{-3}). Besides the main mode at ~180 nm, a second minor mode was observed around ~260–270 nm, which was probably caused by coagulating particles. After ~10 min α-pinene and ozone were introduced into the chamber which led to an increase in median particle diameter over ~90 min, eventually giving a particle mode of ~310 nm. This increase in particle diameter from 180 to 310 nm thus equals an average coating thickness of ~65 nm. The observed decrease in particle number

and mass is due to the additional gas flows carrying α-pinene and ozone, diluting the chamber aerosol to a particle number concentration of ~$6.3 \cdot 10^3$ cm^{-3} (~66 $\mu g \cdot m^{-3}$).

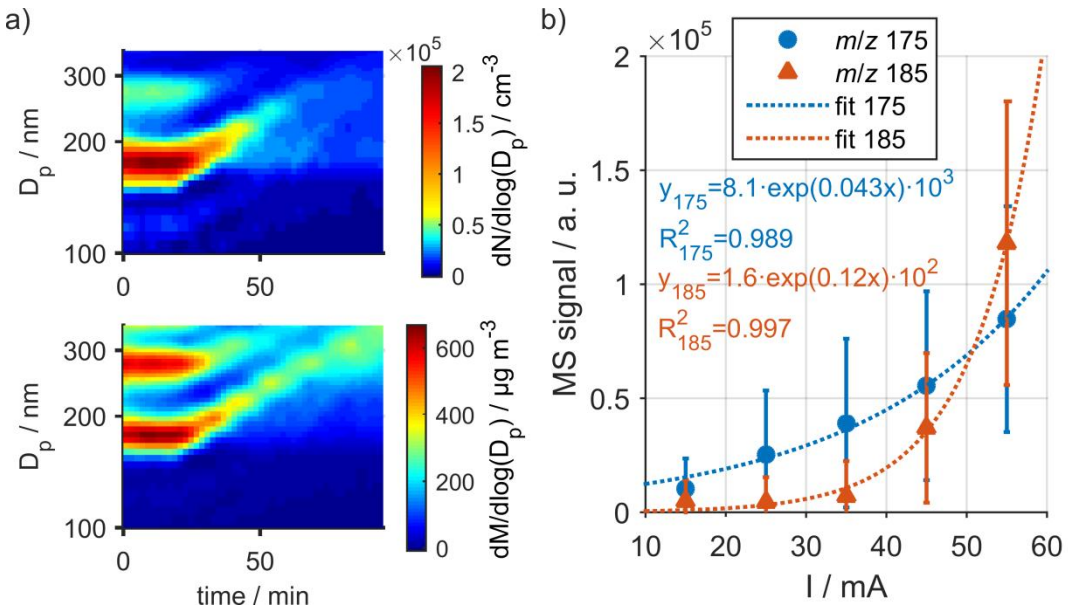

Figure 5.3.5: (a) Number size distribution (top) and mass size distribution (bottom) during the generation of coated TCA particles. (b) AeroFAPA–MS signals and corresponding exponential fits for the quasimolecular ion signals of TCA (*m/z* 175, $[M–H]^-$) and pinic acid (*m/z* 185, $[M–H]^-$) for the analysis of coated TCA particles at different discharge currents. The errorbars indicate one standard deviation.

After the median diameter of the generated core-shell particles was constant for several minutes, the aerosol was analyzed by AeroFAPA–MS at different discharge currents to probe the outer shell of the particles. Since pinic acid is a major oxidation product of the α-pinene-ozonolysis (Yasmeen *et al.*, 2011) and known to be efficiently ionized by AeroFAPA–MS (Brüggemann *et al.*, 2015) the corresponding quasimolecular ion signal at *m/z* 185 ($[M–H]^-$) was used as a proxy for all generated α-pinene oxidation products. The abundance of TCA was estimated from the ion signal at *m/z* 175 ($[M–H]^-$), as discussed before. As depicted in panel (b) of Figure 5.3.5, both signals showed an exponential increase with increasing discharge currents. In general, this behavior is not surprising and was already reported for AeroFAPA–MS measurements of pure compounds. The reason for this trend is probably twofold: Firstly, the increased discharge currents lead to an enhanced volatilization of particles in the afterglow due to higher temperatures. And secondly, higher discharge currents are followed by an elevated flux of primary reagent ions and excited helium species, yielding a more efficient ionization (Brüggemann *et al.*, 2015). However, commonly TCA gives a more intense signal in AeroFAPA–MS measurements compared to pinic acid, which can also be seen from the measurements at

I = 15–35 mA. Although TCA is coated with other oxidation products the corresponding ion signal still shows high abundances, which are even more intense than the ion signals corresponding to pinic acid. Yet, at a discharge current of I = 45 mA the signals are almost at the same level. Furthermore, at I = 55 mA the ion signal of pinic acid is even more abundant than the ion signal of TCA. In fact, this finding is in agreement with the assumed core-shell particle morphology and an increasing probing depth at higher discharge currents. At a coating-thickness of ~65 nm the mass of oxidation products in the outer shell is roughly four times higher than the mass of the TCA core. In addition, the outer shell is probably evaporated to a larger extent than the core of the particles, as suggested by the measurements and calculations discussed above. Therefore, in an ideal case the signal for TCA would remain at background levels until the probing depths are larger than the coating-thickness, whereas the ion signal for pinic acid showed the commonly known exponential increase with rising discharge currents. However, since coating of the particles is probably not homogeneous and a mixing of core and shell compounds cannot be excluded the ion signal of TCA is also increasing with higher discharge currents. In particular, the heating of the particles in the afterglow region might even enhance mixing processes between shell and core compounds. Furthermore, it cannot be ruled out that residual TCA seed particles were exiting the chamber without being coated by oxidation products since a significant number of particles was still present at particle diameters of ~180 nm. Nonetheless, the results demonstrate that mainly the surface and outer shell of aerosol particles is desorbed and analyzed by AeroFAPA–MS, suggesting that this method might not only be used for bulk analysis of ambient organic aerosols, but also for chemically characterizing the corresponding interfacial layer of particles.

5.4 Conclusion

The particle desorption characteristics of AeroFAPA–MS were investigated, using TCA aerosol particles as a model system. It was shown that the ion signal of TCA scaled with the surface size distribution of the analyzed particles, suggesting that only the interfacial region of the particles is desorbed in the afterglow region and available for subsequent gas-phase ionization. Further experiments revealed that the amount of desorbed material is depending on the afterglow temperature and, thus, chosen discharge current of the AeroFAPA source. For particles with an initial diameter of 112 nm, desorption radii of 2.5–36.6 nm were observed at discharge currents of 15–55 mA, supporting the hypothesis

that only an outer shell of the aerosol particles is analyzed. The obtained data were compared to results of an aerosol evaporation model. Although the discussed calculations rather give a qualitative description of the processes occurring in the afterglow region, the model showed that the residence times of particles in the afterglow region are decreasing with increasing discharge currents. Possibly, because of the rising viscosity of the helium flow at higher temperatures and a more laminar helium flow, the mixing of aerosol current and helium stream is hampered at higher discharge currents, leading to the observed decrease in particle residence times. In agreement with this assumption, it was shown that bigger particles with a higher inertia are less affected by the increasing helium viscosity at higher discharge currents.

Further evidence was found when aerosol particles with known core-shell morphology were analyzed by AeroFAPA–MS. In a proof-of-principal study, TCA seed particles (D_p = 180 nm) were coated with α-pinene oxidation products, giving an average coating thickness of ~65 nm. The mass spectrometric analysis of these particles showed that ion signals for pinic acid, which is a major oxidation product of α-pinene, exhibited a distinct increase with increasing discharge currents and, thus, probing depths. In contrast, the increase in ion signals for TCA was rather moderate. Therefore, it was concluded that AeroFAPA–MS predominantly desorbed and ionized compounds residing in an outer shell and, thus, interfacial layer of the aerosol particles. Although exact probing depths are presumably prone to changes in particle composition, AeroFAPA–MS is assumed to be generally capable of depth profiling of organic aerosol particles.

Acknowledgements

The authors gratefully acknowledge Dr. John Crowley from the Max Planck Institute for Chemistry (Mainz, Germany) for the loan of the SMPS.

This work was supported by the Max Planck Graduate Center (MPGC) with the Johannes Gutenberg University Mainz.

5.5 Additional Information and Results

5.5.1 Desorption of Pinic Acid Particles in the Afterglow Region

Scanning SMPS experiments with pinic acid aerosol particles showed similar results to the TCA experiments. As can be seen in Figure 5.5.1, the quasimolecular ion signal of pinic acid (*m*/*z* 185, $[M–H]^-$) is following the trend of the particle mass size distribution at low particle diameters, however, as particle diameters increase the signal starts to show better agreement with the surface size distribution, indicating the hypothesized desorption and ionization of compounds in the particles' interfacial layer.

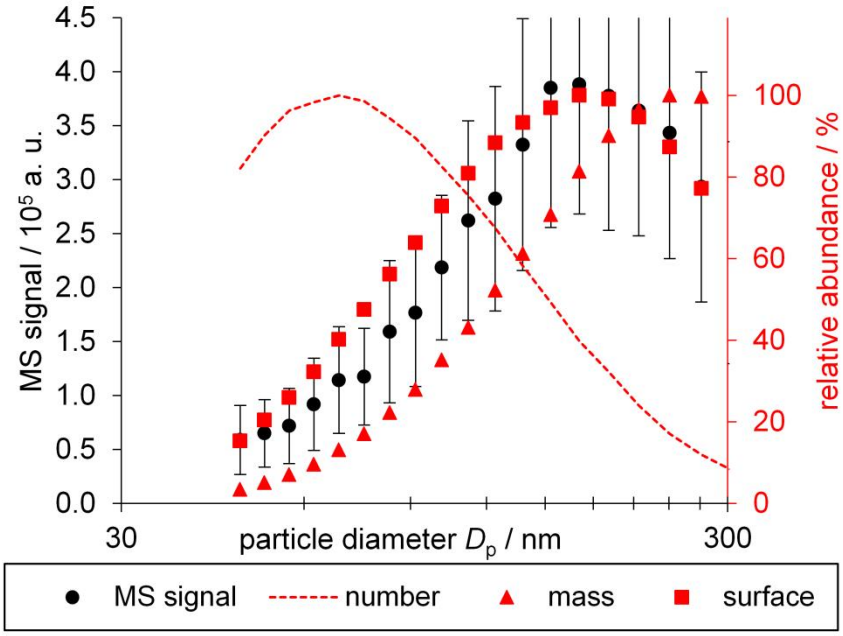

Figure 5.5.1: SMPS analysis of pinic acid aerosol particles and response of AeroFAPA–MS for the quasimolecular ion at *m*/*z* 185 ($[M–H]^-$); error bars indicate one standard deviation.

Similar to the analysis of TCA particles, the response of AeroFAPA–MS shows a linear correlation to increasing aerosol mass concentrations for pinic acid aerosol particles, as can be seen in Figure 5.5.2. Again, a decrease in the slope of the resulting calibration curves is observed for increasing particle sizes, suggesting desorption and ionization of an outer shell of particles in the afterglow region. As already observed and discussed for TCA, model predictions are either overpredicting the evaporation for 100 nm particles or underpredicting it for bigger particle sizes.

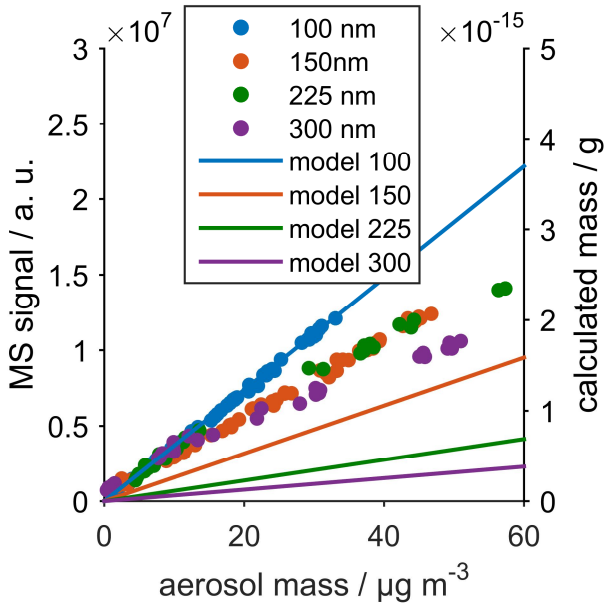

Figure 5.5.2: AeroFAPA–MS ion signal for pinic acid at *m/z* 185 ($[M–H]^-$) and calculated mass evaporation as a function of pinic acid aerosol mass concentration at discharge currents of 55 mA. While the evaporation model is in good agreement with the AeroFAPA–MS data for 100 nm particles, significant discrepancies are observed for bigger particle diameters.

5.5.2 Aerosol Evaporation Model Parameters

The parameters used for the calculations of the aerosol evaporation model are summarized in Table 5.5.1. Ambient pressure p was always set to 101.13 hPa. Diffusion coefficients D_{TCA} for TCA and D_{PA} for pinic acid were estimated to $5 \cdot 10^{-6}$ $m^2 \cdot s^{-1}$. Surface tension σ was assumed to be 0.06 $N \cdot m^{-1}$.

Table 5.5.1: Summary of parameters used for aerosol evaporation calculations.

Compound	Molecular Weight M / g·mol^{-1}	Density ρ / g·cm^{-3}	Vaporization Enthalpy ΔH_{vap} / kJ·mol^{-1}	vapor pressure p^0_{sat} (298 K) / 10^{-6} Pa
tricarballylic acid	176.12	1.2	104[a]	0.58[a]
pinic acid	186.21	1.2	109[b]	32[b]

[a] calculated by SIMPOL.1 (Pankow *et al.*, 2008); [b] Bilde *et al.*, 2015

5.5.3 Effects of Aerosol Inlet Heating on Particle Desorption

In addition to the experiments discussed above, particle desorption was also investigated when pinic acid particles were pre-evaporated by heating of the AeroFAPA's aerosol inlet, as it was initially reported for this method (Brüggemann *et al.*, 2015). Particle number size distributions were measured before and after the AeroFAPA manifold when

the ion source was not operating. As can be seen from Figure 5.5.3, beside particle losses due to turbulence and sampling of the MS inlet, no significant change in the particle number size distribution was observed, giving an average particle diameter of ~70 nm. However, after ignition of the discharge at I = 55 mA an immediate decrease in particle diameters was observed, yielding a mean diameter of ~35 nm. It should be noted that this probing depth is exactly in the same range as previously found for TCA particles (Figure 5.3.3 and Table 5.3.1). While without additional heating of the aerosol inlet particle desorption for diameters >150 nm was incomplete, the amount of residual particles in this region decreased with every heating step, eventually giving almost no particles for D_p > 150 nm at an inlet temperature of 200 °C. Additionally, the mean diameters of the particles decreased down to ~25 nm. However, this value might be biased to a certain extent due to the possibility of recondensation of volatilized particle compounds in the SMPS transfer line. Nonetheless, these results, firstly, corroborate the observed values for probing depths at I = 55 mA. And secondly, they support the assumption of a rather quantitative analysis of organic aerosol particles with AeroFAPA–MS when the aerosol inlet is heated to 200 °C.

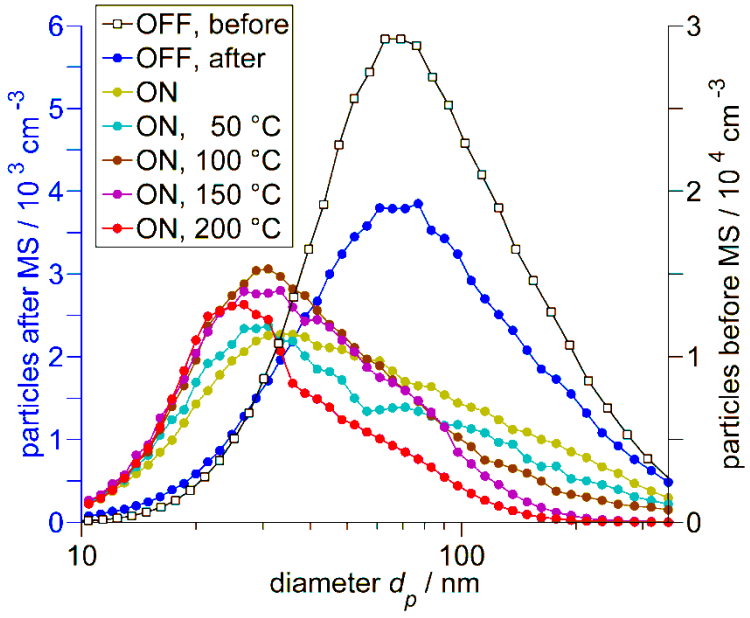

Figure 5.5.3: Effects of aerosol inlet heating on particle desorption when pinic acid aerosol particles were analyzed by AeroFAPA–MS.

6 Conclusions and Outlook

The applicability of FAPA–MS for the analysis of OA particles in both offline and online mode was extensively explored and assessed in laboratory as well as field measurements. Furthermore, ionization patterns and pathways as well as desorption characteristics of the method were thoroughly investigated, revealing the capabilities and limitations of this novel soft ionization technique.

The characterization and application of ambient desorption FAPA–MS in surface analysis experiments of pure compounds as well as in proof-of-principle studies demonstrated that the method is best suited for polar analytes with high volatilities and low molecular weights, ideally containing nitrogen- and/or oxygen functionalities (e.g. carboxylic acids, amines,…). Compounds meeting these criteria are readily desorbed and ionized in the afterglow region and can, thus, be easily detected even in trace amounts. Commonly, such compounds show signals for their quasimolecular ions, i.e. $[M+H]^+$ and $[M–H]^-$ in the positive and the negative ion mode, respectively, and fragmentation or oxidation of the analytes is rarely observed. In contrast, compounds with low vapor pressures, containing long carbon chains and/or high molecular weights, often represent a serious analytical challenge. Due to the presence of reactive nitrogen and oxygen intermediates in the afterglow region, desorption and ionization is in direct competition with oxidation of the analytes, leading to the formation of adducts and oxidation products which impede a clear signal assignment in the acquired mass spectra. Nonetheless, FAPA–MS showed to be capable of detecting and identifying common limonene oxidation products in SOA particles on a filter sample and, thus, is considered a suitable method for offline analysis of OA particles. In order to facilitate future measurements, it should be noted that setups which allow exact positioning of both samples and the FAPA source, e.g. xyz-stages, are highly desirable since reproducibility and, therefore, also quantification was a major difficulty during the offline measurements conducted within this study.

Online analysis of OA particles was accomplished using AeroFAPA–MS. After optimization and characterization, the method was used to measure a range of model compounds and to evaluate typical ionization patterns in the positive and the negative ion mode. Again, predominantly signals for quasimolecular ions were found in the mass spectra while signals for fragmentation were solely detected to a minimum extent.

However, in contrast to the offline studies, less adduct formation and oxidation of the analytes was observed which can possibly be assigned to the short residence times of aerosol particles in the afterglow region. AeroFAPA–MS showed to be a powerful tool for the real time analysis of OA particles in laboratory as well as in field studies. During the F–BEACh 2014 campaign in Central Europe the method was used in combination with complementary MS techniques, such as AMS and CI–APiToF–MS, to resolve and characterize aerosol chemistry of biogenic SOA particles at the site. Using AeroFAPA–MS, several common SOA marker compounds were identified in real time by MS^n experiments, indicating that photochemically aged SOA particles were present during the campaign period. Furthermore, it was shown that the method was able to detect compounds of a recently described class of highly oxidized sulfur-containing compounds, i.e. HOOS, in the particle phase. Comparisons with AMS and CI–APiToF–MS measurements suggest that both particulate sulfate as well as highly oxidized peroxyradicals in the gas phase might play a role during formation of these species.

In order to get a deeper understanding of underlying mechanisms of particle desorption in AeroFAPA–MS, particle sizes before and after passing the afterglow region were determined at different discharge currents. It was found that ion signals were scaling with the surface size distribution of the analyzed OA particles, suggesting that only an interfacial layer is desorbed from the particles' surface and available for subsequent ionization. For particles with initial diameters of 112 nm, desorption radii of 2.5–36.6 nm were found at discharge currents of 15–55 mA from these measurements. Additionally, calculations using an aerosol evaporation model revealed that particle residence times are presumably decreasing with increasing discharge currents due to increased helium viscosities which result in a more laminar flow in the afterglow region. In agreement with this hypothesis, it was found that particles with larger diameters and, thus, higher inertia are less affected by elevated discharge currents. Since probing the interfacial layer of OA particles might reveal valuable information on formation and evolution of particles, a proof-of-principle study was conducted by analyzing particles with known core-shell morphology. As expected, predominantly compounds residing in the shell of the particles were desorbed and ionized with increasing probing depths. Simultaneously, compounds in the core showed merely a rather moderate signal increase, suggesting that AeroFAPA–MS might represent a promising technique for depth profiling of OA particles in future studies.

In order to facilitate prospective measurements using AeroFAPA–MS and to extend the range of possible flow rates, the application of a jet separator, e.g. Vapur interface, seems a

promising approach. Such interfaces would possibly allow the operation at higher helium flow rates by adding an additional pumping stage to the mass spectrometer inlet. Moreover, since mixing of aerosol sample flow and afterglow stream is crucial for desorption of aerosol particles and ionization of the analytes sample introduction setups such as mixing tees or concentric geometries, e.g. found in the halo-FAPA setup (Pfeuffer *et al.*, 2013a), should be explored in future studies.

Besides technical improvements, especially the possibility of performing depth profiling studies should be focused in upcoming projects due to its uniqueness. Furthermore, the application of AeroFAPA–MS in combination with complementary MS techniques might further aid in comprehensively characterizing OA particles during field studies. Additionally, preliminary results of recent laboratory studies suggest that AeroFAPA–MS might also be used for the analysis of gaseous halogen species, such as Br_2, HBr or BrCl, which can play a key role in atmospheric processes in marine environments or in the proximity of volcanoes.

7 References

Aiken AC, Salcedo D, Cubison MJ, Huffman JA, DeCarlo PF, Ulbrich IM, Docherty KS, Sueper D, Kimmel JR, Worsnop DR, Trimborn A, Northway M, Stone EA, Schauer JJ, Volkamer RM, Fortner E, Foy B de, Wang J, Laskin A, Shutthanandan V, Zheng J, Zhang R, Gaffney J, Marley NA, Paredes-Miranda G, Arnott WP, Molina LT, Sosa G, Jimenez JL (2009) Mexico City aerosol analysis during MILAGRO using high resolution aerosol mass spectrometry at the urban supersite (T0) – Part 1: Fine particle composition and organic source apportionment. Atmos. Chem. Phys. 9(17):6633–6653. doi: 10.5194/acp-9-6633-2009

Albert A, Engelhard C (2012) Characteristics of Low-Temperature Plasma Ionization for Ambient Mass Spectrometry Compared to Electrospray Ionization and Atmospheric Pressure Chemical Ionization. Anal. Chem. 84(24):10657–10664. doi: 10.1021/ac302287x

Albert A, Shelley J, Engelhard C (2014) Plasma-based ambient desorption/ionization mass spectrometry: state-of-the-art in qualitative and quantitative analysis. Anal Bioanal Chem 406(25):6111-6127. doi: 10.1007/s00216-014-7989-z

Altieri KE, Turpin BJ, Seitzinger SP (2009) Oligomers, organosulfates, and nitrooxy organosulfates in rainwater identified by ultra-high resolution electrospray ionization FT-ICR mass spectrometry. Atmos. Chem. Phys. 9(7):2533–2542. doi: 10.5194/acp-9-2533-2009

Andrade FJ, Shelley JT, Wetzel WC, Webb MR, Gamez G, Ray SJ, Hieftje GM (2008) Atmospheric pressure chemical ionization source. 1. Ionization of compounds in the gas phase. Anal. Chem. 80(8):2646–2653. doi: 10.1021/Ac800156y

Andrade FJ, Wetzel WC, Chan GCY, Webb MR, Gamez G, Ray SJ, Hieftje GM (2006) A new, versatile, direct-current helium atmospheric-pressure glow discharge. J. Anal. Atom. Spectrom. 21(11):1175–1184. doi: 10.1039/B607544d

Bahreini R, Ervens B, Middlebrook AM, Warneke C, Gouw JA de, DeCarlo PF, Jimenez JL, Brock CA, Neuman JA, Ryerson TB, Stark H, Atlas E, Brioude J, Fried A, Holloway JS, Peischl J, Richter D, Walega J, Weibring P, Wollny AG, Fehsenfeld FC (2009) Organic aerosol formation in urban and industrial plumes near Houston and Dallas, Texas. J. Geophys. Res. 114. doi: 10.1029/2008JD011493

Barbara J. Finlayson-Pitts JNP (2000) Chemistry of the upper and lower atmosphere. Teory, experiments and applications. Academic Press, London

Bateman AP, Nizkorodov SA, Laskin J, Laskin A (2011) Photolytic processing of secondary organic aerosols dissolved in cloud droplets. Phys. Chem. Chem. Phys. 13(26):12199. doi: 10.1039/c1cp20526a

Bateman AP, Walser ML, Desyaterik Y, Laskin J, Laskin A, Nizkorodov SA (2008) The Effect of Solvent on the Analysis of Secondary Organic Aerosol Using Electrospray Ionization Mass Spectrometry. Environ. Sci. Technol. 42(19):7341–7346. doi: 10.1021/es801226w

Bente M, Sklorz M, Streibel T, Zimmermann R (2008) Online Laser Desorption-Multiphoton Postionization Mass Spectrometry of Individual Aerosol Particles:

Molecular Source Indicators for Particles Emitted from Different Traffic-Related and Wood Combustion Sources. Anal. Chem. 80(23):8991–9004. doi: 10.1021/ac801295f

Bilde M, Svenningsson B, Mønster J, Rosenørn T (2003) Even−Odd Alternation of Evaporation Rates and Vapor Pressures of C3−C9 Dicarboxylic Acid Aerosols. Environ. Sci. Technol. 37(7):1371–1378. doi: 10.1021/es0201810

Blyth AJ, Asrat A, Baker A, Gulliver P, Leng MJ, Genty D (2007) A new approach to detecting vegetation and land-use change using high-resolution lipid biomarker records in stalagmites. Quaternary Research 68(3):314–324. doi: 10.1016/j.yqres.2007.08.002

Boone EJ, Laskin A, Laskin J, Wirth C, Shepson PB, Stirm BH, Pratt KA (2015) Aqueous Processing of Atmospheric Organic Particles in Cloud Water Collected via Aircraft Sampling. Environ. Sci. Technol. 49(14):8523–8530. doi: 10.1021/acs.est.5b01639

Bosle J, Mischel S, Schulze A, Scholz D, Hoffmann T (2014) Quantification of low molecular weight fatty acids in cave drip water and speleothems using HPLC-ESI-IT/MS — development and validation of a selective method. Anal Bioanal Chem 406(13):3167-3177. doi: 10.1007/s00216-014-7743-6

Brüggemann M, Karu E, Stelzer T, Hoffmann T (2015) Real Time Analysis of Ambient Organic Aerosols Using Aerosol Flowing Atmospheric-Pressure Afterglow Mass Spectrometry (AeroFAPA–MS). Environ. Sci. Technol. 49(9):5571–5578. doi: 10.1021/es506186c

Brüggemann M, Lucas Vogel A, Hoffmann T (2014) Analysis of organic aerosols using a micro-orifice volatilization impactor (MOVI) coupled to an atmospheric-pressure chemical ionization mass spectrometer (APCI–MS). European Journal of Mass Spectrometry 20(1):31-41. doi: 10.1255/ejms.1260

Canagaratna M, Jayne J, Jimenez J, Allan J, Alfarra M, Zhang Q, Onasch T, Drewnick F, Coe H, Middlebrook A, Delia A, Williams L, Trimborn A, Northway M, DeCarlo P, Kolb C, Davidovits P, Worsnop D (2007) Chemical and microphysical characterization of ambient aerosols with the aerodyne aerosol mass spectrometer. Mass Spectrom. Rev. 26(2):185–222. doi: 10.1002/mas.20115

Cappa CD, Wilson KR (2011) Evolution of organic aerosol mass spectra upon heating: implications for OA phase and partitioning behavior. Atmos. Chem. Phys. 11(5):1895–1911. doi: 10.5194/acp-11-1895-2011

Carlson JF (2013) Carlson's Guide to Landscape Painting. Dover Art Instruction. Dover Publications, Newburyport

Chan MN, Nah T, Wilson KR (2013) Real time in situ chemical characterization of sub-micron organic aerosols using Direct Analysis in Real Time mass spectrometry (DART–MS): the effect of aerosol size and volatility. Analyst 138(13):3749–3757. doi: 10.1039/C3AN00168G

Chen LC, Hashimoto Y, Furuya H, Takekawa K, Kubota T, Hiraoka K (2009) Rapid detection of drugs in biofluids using atmospheric pressure chemi/chemical ionization mass spectrometry. Rapid Commun. Mass Spectrom. 23(3):333–339. doi: 10.1002/Rcm.3877

Chen Q, Liu Y, Donahue NM, Shilling JE, Martin ST (2011) Particle-Phase Chemistry of Secondary Organic Material: Modeled Compared to Measured O:C and H:C Elemental Ratios Provide Constraints. Environ. Sci. Technol. 45(11):4763–4770. doi: 10.1021/es104398s

Claeys M, Iinuma Y, Szmigielski R, Surratt JD, Blockhuys F, van Alsenoy C, Böge O, Sierau B, Gómez-González Y, Vermeylen R, van der Veken P, Shahgholi M, Chan AWH, Herrmann H, Seinfeld JH, Maenhaut W (2009) Terpenylic Acid and Related Compounds from the Oxidation of α-Pinene: Implications for New Particle Formation and Growth above Forests. Environ. Sci. Technol. 43(18):6976–6982. doi: 10.1021/es9007596

Cody RB, Laramee JA, Durst HD (2005) Versatile new ion source for the analysis of materials in open air under ambient conditions. Anal. Chem. 77(8):2297–2302. doi: 10.1021/Ac050152j

Crounse JD, Nielsen LB, Jørgensen S, Kjaergaard HG, Wennberg PO (2013) Autoxidation of Organic Compounds in the Atmosphere. J. Phys. Chem. Lett. 4(20):3513–3520. doi: 10.1021/jz4019207

Crutzen PJ (2002) Geology of mankind. Nature 415(6867):23. doi: 10.1038/415023a

Crutzen PJ, Stoermer EF (2000) The "Anthropocene" 41:17–18

da Vinci L, Rigaud JF (1721) Trattato della pittura (A Treatise on Painting). Senex and Taylor, London.

Darer AI, Cole-Filipiak NC, O'Connor AE, Elrod MJ (2011) Formation and Stability of Atmospherically Relevant Isoprene-Derived Organosulfates and Organonitrates. Environ. Sci. Technol. 45(5):1895–1902. doi: 10.1021/es103797z

Davidson CI, Phalen RF, Solomon PA (2005) Airborne Particulate Matter and Human Health: A Review. Aerosol Science and Technology 39(8):737–749. doi: 10.1080/02786820500191348

DeCarlo PF, Ulbrich IM, Crounse J, Foy B de, Dunlea EJ, Aiken AC, Knapp D, Weinheimer AJ, Campos T, Wennberg PO, Jimenez JL (2010) Investigation of the sources and processing of organic aerosol over the Central Mexican Plateau from aircraft measurements during MILAGRO. Atmos. Chem. Phys. 10(12):5257–5280. doi: 10.5194/acp-10-5257-2010

Dette HP, Qi M, Schröder DC, Godt A, Koop T (2014) Glass-Forming Properties of 3-Methylbutane-1,2,3-tricarboxylic Acid and Its Mixtures with Water and Pinonic Acid. J. Phys. Chem. A 118(34):7024–7033. doi: 10.1021/jp505910w

Dominici F, Greenstone M, Sunstein CR (2014) Particulate Matter Matters. Science 344(6181):257–259. doi: 10.1126/science.1247348

Donahue NM, Henry KM, Mentel TF, Kiendler-Scharr A, Spindler C, Bohn B, Brauers T, Dorn HP, Fuchs H, Tillmann R, Wahner A, Saathoff H, Naumann K, Mohler O, Leisner T, Muller L, Reinnig M, Hoffmann T, Salo K, Hallquist M, Frosch M, Bilde M, Tritscher T, Barmet P, Praplan AP, DeCarlo PF, Dommen J, Prevot ASH, Baltensperger U (2012a) Aging of biogenic secondary organic aerosol via gas-phase OH radical reactions. Proceedings of the National Academy of Sciences 109(34):13503–13508. doi: 10.1073/pnas.1115186109

Donahue NM, Kroll JH, Pandis SN, Robinson AL (2012b) A two-dimensional volatility basis set – Part 2: Diagnostics of organic-aerosol evolution. Atmos. Chem. Phys. 12(2):615–634. doi: 10.5194/acp-12-615-2012

Donahue NM, Robinson AL, Stanier CO, Pandis SN (2006) Coupled partitioning, dilution, and chemical aging of semivolatile organics. Environ. Sci. Technol. 40(8):2635–2643. doi: 10.1021/Es052297c

Donahue NM, Trump ER, Pierce JR, Riipinen I (2011) Theoretical constraints on pure vapor-pressure driven condensation of organics to ultrafine particles. Geophys. Res. Lett. 38(16):n/a. doi: 10.1029/2011GL048115

Draxler R, Rolph G HYSPLIT (HYbrid Single-Particle Lagrangian Integrated Trajectory) Model. http://www.arl.noaa.gov/HYSPLIT.php

Eberlin LS, Ferreira CR, Dill AL, Ifa DR, Cheng L, Cooks RG (2011) Nondestructive, Histologically Compatible Tissue Imaging by Desorption Electrospray Ionization Mass Spectrometry. ChemBioChem 12(14):2129–2132. doi: 10.1002/cbic.201100411

Eberlin LS, Haddad R, Sarabia Neto RC, Cosso RG, Maia DRJ, Maldaner AO, Zacca JJ, Sanvido GB, Romao W, Vaz BG, Ifa DR, Dill A, Cooks RG, Eberlin MN (2010) Instantaneous chemical profiles of banknotes by ambient mass spectrometry. Analyst 135(10):2533–2539. doi: 10.1039/C0AN00243G

Edmond Hoffmann VS de (2007) Mass spectrometry, Third edition. Principles and applications. John Wiley & Sons Ltd, Chichester

Ehn M, Kleist E, Junninen H, Petäjä T, Lönn G, Schobesberger S, Dal Maso M, Trimborn A, Kulmala M, Worsnop DR, Wahner A, Wildt J, Mentel TF (2012) Gas phase formation of extremely oxidized pinene reaction products in chamber and ambient air. Atmos. Chem. Phys. 12(11):5113–5127. doi: 10.5194/acp-12-5113-2012

Ehn M, Thornton JA, Kleist E, Sipila M, Junninen H, Pullinen I, Springer M, Rubach F, Tillmann R, Lee B, Lopez-Hilfiker F, Andres S, Acir I, Rissanen M, Jokinen T, Schobesberger S, Kangasluoma J, Kontkanen J, Nieminen T, Kurten T, Nielsen LB, Jorgensen S, Kjaergaard HG, Canagaratna M, Maso MD, Berndt T, Petaja T, Wahner A, Kerminen V, Kulmala M, Worsnop DR, Wildt J, Mentel TF (2014) A large source of low-volatility secondary organic aerosol. Nature 506(7489):476–479

Esteve-Turrillas FA, Armenta S, Moros J, Garrigues S, Pastor A, La Guardia M de (2005) Validated, non-destructive and environmentally friendly determination of cocaine in euro bank notes. Journal of Chromatography A 1065(2):321–325. doi: 10.1016/j.chroma.2004.12.076

Ewing KJ, Gibson D, Sanghera J, Miklos F (2013) Sampler for Collection and Analysis of Low Vapor Pressure Chemical (LVPC) Particulates/Aerosols. Anal. Chem. 85(20):9508–9513. doi: 10.1021/ac401100r

Farmer DK, Jimenez JL (2010) Real-time Atmospheric Chemistry Field Instrumentation. Anal. Chem. 82(19):7879–7884. doi: 10.1021/Ac1010603

Farmer DK, Matsunaga A, Docherty KS, Surratt JD, Seinfeld JH, Ziemann PJ, Jimenez JL (2010) Response of an aerosol mass spectrometer to organonitrates and organosulfates and implications for atmospheric chemistry. Proceedings of the National Academy of Sciences 107(15):6670–6675. doi: 10.1073/pnas.0912340107

Faulhaber AE, Thomas BM, Jimenez JL, Jayne JT, Worsnop DR, Ziemann PJ (2009) Characterization of a thermodenuder-particle beam mass spectrometer system for the study of organic aerosol volatility and composition. Atmos. Meas. Tech. 2(1):15–31

Fushimi A, Wagai R, Uchida M, Hasegawa S, Takahashi K, Kondo M, Hirabayashi M, Morino Y, Shibata Y, Ohara T, Kobayashi S, Tanabe K (2011) Radiocarbon (14C) Diurnal Variations in Fine Particles at Sites Downwind from Tokyo, Japan in Summer. Environ. Sci. Technol. 45(16):6784–6792. doi: 10.1021/es201400p

Fuzzi S, Andreae MO, Huebert BJ, Kulmala M, Bond TC, Boy M, Doherty SJ, Guenther A, Kanakidou M, Kawamura K, Kerminen VM, Lohmann U, Russell LM, Poschl U (2006) Critical assessment of the current state of scientific knowledge, terminology, and research needs concerning the role of organic aerosols in the atmosphere, climate, and global change. Atmos. Chem. Phys. 6:2017–2038

Gallimore PJ, Kalberer M (2013) Characterizing an Extractive Electrospray Ionization (EESI) Source for the Online Mass Spectrometry Analysis of Organic Aerosols. Environ. Sci. Technol. 47(13):7324–7331. doi: 10.1021/es305199h

Gao S, Surratt JD, Knipping EM, Edgerton ES, Shahgholi M, Seinfeld JH (2006) Characterization of polar organic components in fine aerosols in the southeastern United States: Identity, origin, and evolution. Journal of Geophysical Research-Atmospheres 111(D14)

Geddes S, Nichols B, Todd K, Zahardis J, Petrucci GA (2010) Near-infrared laser desorption/ionization aerosol mass spectrometry for measuring organic aerosol at atmospherically relevant aerosol mass loadings. Atmos. Meas. Tech. 3(4):1175–1183. doi: 10.5194/amt-3-1175-2010

Glasius M, Lahaniati M, Calogirou A, Di Bella D, Jensen NR, Hjorth J, Kotzias D, Larsen BR (2000) Carboxylic acids in secondary aerosols from oxidation of cyclic monoterpenes by ozone. Environ. Sci. Technol. 34(6):1001–1010

Goldstein AH, Galbally IE (2007) Known and unexplored organic constituents in the earth's atmosphere. Environ. Sci. Technol. 41(5):1514–1521. doi: 10.1021/es072476p

Goldstein AH, Koven CD, Heald CL, Fung IY (2009) Biogenic carbon and anthropogenic pollutants combine to form a cooling haze over the southeastern United States. Proceedings of the National Academy of Sciences 106(22):8835–8840. doi: 10.1073/pnas.0904128106

Gómez-González Y, Surratt JD, Cuyckens F, Szmigielski R, Vermeylen R, Jaoui M, Lewandowski M, Offenberg JH, Kleindienst TE, Edney EO, Blockhuys F, van Alsenoy C, Maenhaut W, Claeys M (2008) Characterization of organosulfates from the photooxidation of isoprene and unsaturated fatty acids in ambient aerosol using liquid chromatography/(−) electrospray ionization mass spectrometry. J. Mass Spectrom. 43(3):371–382. doi: 10.1002/jms.1329

Gouw JA de (2005) Budget of organic carbon in a polluted atmosphere: Results from the New England Air Quality Study in 2002. J. Geophys. Res. 110(D16). doi: 10.1029/2004JD005623

Gross J (2014) Direct analysis in real time—a critical review on DART–MS. Anal Bioanal Chem 406(1):63-80. doi: 10.1007/s00216-013-7316-0

Gross JH (Heidelberg : Imprint: Springer Spektrum, 2013) Massenspektrometrie. Ein Lehrbuch. Imprint: Springer Spektrum, Berlin, Heidelberg

Guenther AB, Jiang X, Heald CL, Sakulyanontvittaya T, Duhl T, Emmons LK, Wang X (2012) The Model of Emissions of Gases and Aerosols from Nature version 2.1 (MEGAN2.1): an extended and updated framework for modeling biogenic emissions. Geosci. Model Dev. 5(6):1471–1492. doi: 10.5194/gmd-5-1471-2012

Guenther A, Hewitt CN, Erickson D, Fall R, Geron C, Graedel T, Harley P, Klinger L, Lerdau M, Mckay WA, Pierce T, Scholes B, Steinbrecher R, Tallamraju R, Taylor J, Zimmerman P (1995) A Global-Model of Natural Volatile Organic-Compound Emissions. J. Geophys. Res. Atmos. 100(D5):8873–8892

Hallquist M, Wenger JC, Baltensperger U, Rudich Y, Simpson D, Claeys M, Dommen J, Donahue NM, George C, Goldstein AH, Hamilton JF, Herrmann H, Hoffmann T, Iinuma Y, Jang M, Jenkin ME, Jimenez JL, Kiendler-Scharr A, Maenhaut W, McFiggans G, Mentel TF, Monod A, Prevot ASH, Seinfeld JH, Surratt JD, Szmigielski R, Wildt J (2009) The formation, properties and impact of secondary organic aerosol. current and emerging issues. Atmos. Chem. Phys. 9(14):5155–5236

Henze DK, Seinfeld JH, Ng NL, Kroll JH, Fu T, Jacob DJ, Heald CL (2008) Global modeling of secondary organic aerosol formation from aromatic hydrocarbons: high- vs. low-yield pathways. Atmos. Chem. Phys. 8(9):2405–2420. doi: 10.5194/acp-8-2405-2008

Herrmann H, Schaefer T, Tilgner A, Styler SA, Weller C, Teich M, Otto T (2015) Tropospheric Aqueous-Phase Chemistry: Kinetics, Mechanisms, and Its Coupling to a Changing Gas Phase. Chem. Rev. 115(10):4259–4334. doi: 10.1021/cr500447k

Hoffmann T, Bandur R, Marggraf U., Linscheid M. (1998) Molecular composition of organic aerosols formed in the alpha-pinene/O3 reaction: Implications for new particle formation processes. Geophys. Res. Lett. 103(D19):25569–25578

Hoffmann T, Huang RJ, Kalberer M (2011) Atmospheric Analytical Chemistry. Anal. Chem. 83(12):4649–4664. doi: 10.1021/Ac2010718

Iinuma Y, Boge O, Miao Y, Sierau B, Gnauk T, Herrmann H (2005) Laboratory studies on secondary organic aerosol formation from terpenes. Faraday Discuss 130(0):279–294. doi: 10.1039/B502160J

Iinuma Y, Keywood M, Gnauk T, Herrmann H (2009) Diaterebic Acid Acetate and Diaterpenylic Acid Acetate: Atmospheric Tracers for Secondary Organic Aerosol Formation from 1,8-Cineole Oxidation. Environ. Sci. Technol. 43(2):280–285. doi: 10.1021/es802141v

Iinuma Y, Müller C, Berndt T, Böge O, Claeys M, Herrmann H (2007) Evidence for the Existence of Organosulfates from β-Pinene Ozonolysis in Ambient Secondary Organic Aerosol. Environ. Sci. Technol. 41(19):6678–6683. doi: 10.1021/es070938t

Intergovernmental Panel on Climate Change (ed) (2014) Climate Change 2013 - The Physical Science Basis. Cambridge University Press, Cambridge

Isaacs NS (1991) The role of high pressure methods in organic chemistry. Tetrahedron 47(40):8463–8497. doi: 10.1016/S0040-4020(01)82392-9

Jaoui M, Corse E, Kleindienst TE, Offenberg JH, Lewandowski M, Edney EO (2006) Analysis of Secondary Organic Aerosol Compounds from the Photooxidation of d - Limonene in the Presence of NO X and their Detection in Ambient PM 2.5. Environ. Sci. Technol. 40(12):3819–3828. doi: 10.1021/es052566z

Jaoui M, Kamens RM (2003) Gaseous and Particulate Oxidation Products Analysis of a Mixture of α-pinene + β-pinene/O3/Air in the Absence of Light and α-pinene + β-pinene/NOx/Air in the Presence of Natural Sunlight. J. Atmos. Chem. 44:259–297

Jecklin MC, Gamez G, Touboul D, Zenobi R (2008) Atmospheric pressure glow discharge desorption mass spectrometry for rapid screening of pesticides in food. Rapid Commun. Mass Spectrom. 22(18):2791–2798. doi: 10.1002/rcm.3677

Jimenez JL, Canagaratna MR, Donahue NM, Prevot ASH, Zhang Q, Kroll JH, DeCarlo PF, Allan JD, Coe H, Ng NL, Aiken AC, Docherty KS, Ulbrich IM, Grieshop AP, Robinson AL, Duplissy J, Smith JD, Wilson KR, Lanz VA, Hueglin C, Sun YL, Tian

J, Laaksonen A, Raatikainen T, Rautiainen J, Vaattovaara P, Ehn M, Kulmala M, Tomlinson JM, Collins DR, Cubison MJ, Dunlea J, Huffman JA, Onasch TB, Alfarra MR, Williams PI, Bower K, Kondo Y, Schneider J, Drewnick F, Borrmann S, Weimer S, Demerjian K, Salcedo D, Cottrell L, Griffin R, Takami A, Miyoshi T, Hatakeyama S, Shimono A, Sun JY, Zhang YM, Dzepina K, Kimmel JR, Sueper D, Jayne JT, Herndon SC, Trimborn AM, Williams LR, Wood EC, Middlebrook AM, Kolb CE, Baltensperger U, Worsnop DR (2009) Evolution of Organic Aerosols in the Atmosphere. Science 326(5959):1525–1529. doi: 10.1126/science.1180353

Jokinen T, Berndt T, Makkonen R, Kerminen V, Junninen H, Paasonen P, Stratmann F, Herrmann H, Guenther AB, Worsnop DR, Kulmala M, Ehn M, Sipilä M (2015) Production of extremely low volatile organic compounds from biogenic emissions: Measured yields and atmospheric implications. Proceedings of the National Academy of Sciences 112(23):7123–7128. doi: 10.1073/pnas.1423977112

Jokinen T, Sipilä M, Junninen H, Ehn M, Lönn G, Hakala J, Petäjä T, Mauldin III RL, Kulmala M, Worsnop DR (2012) Atmospheric sulphuric acid and neutral cluster measurements using CI–APi-TOF. Atmos. Chem. Phys. 12(9):4117–4125. doi: 10.5194/acp-12-4117-2012

Jokinen T, Sipilä M, Richters S, Kerminen V, Paasonen P, Stratmann F, Worsnop D, Kulmala M, Ehn M, Herrmann H, Berndt T (2014) Rapid Autoxidation Forms Highly Oxidized RO2 Radicals in the Atmosphere. Angew. Chem. Int. Ed. 53(52):14596–14600. doi: 10.1002/anie.201408566

Kanakidou M, Seinfeld JH, Pandis SN, Barnes I, Dentener FJ, Facchini MC, van Dingenen R, Ervens B, Nenes A, Nielsen CJ, Swietlicki E, Putaud JP, Balkanski Y, Fuzzi S, Horth J, Moortgat GK, Winterhalter R, Myhre CEL, Tsigaridis K, Vignati E, Stephanou EG, Wilson J (2005) Organic aerosol and global climate modelling: a review. Atmos. Chem. Phys. 5(4):1053–1123. doi: 10.5194/acp-5-1053-2005

Keller BO, Sui J, Young AB, Whittal RM (2008) Interferences and contaminants encountered in modern mass spectrometry. Analytica Chimica Acta 627(1):71–81. doi: 10.1016/j.aca.2008.04.043

Kesselmeier J, Staudt M (1999) Biogenic Volatile Organic Compounds (VOC): An Overview on Emission, Physiology and Ecology. Journal of Atmospheric Chemistry 33(1):23–88. doi: 10.1023/A:1006127516791

Kingdon KH (1923) A Method for the Neutralization of Electron Space Charge by Positive Ionization at Very Low Gas Pressures. Phys. Rev. 21(4):408–418. doi: 10.1103/PhysRev.21.408

Kristensen K, Enggrob KL, King SM, Worton DR, Platt SM, Mortensen R, Rosenoern T, Surratt JD, Bilde M, Goldstein AH, Glasius M (2013) Formation and occurrence of dimer esters of pinene oxidation products in atmospheric aerosols. Atmos. Chem. Phys. 13(7):3763–3776. doi: 10.5194/acp-13-3763-2013

Kroll JH, Seinfeld JH (2008) Chemistry of secondary organic aerosol. Formation and evolution of low-volatility organics in the atmosphere. Atmos. Environ. 42(16):3593–3624. doi: 10.1016/j.atmosenv.2008.01.003

Kulkarni P, Baron PA, Willeke K (2011) Aerosol Measurement: Principles, Techniques, and Applications, 3rd edn. Wiley, Hoboken

Kulmala M, Kontkanen J, Junninen H, Lehtipalo K, Manninen HE, Nieminen T, Petaja T, Sipila M, Schobesberger S, Rantala P, Franchin A, Jokinen T, Jarvinen E, Aijala M,

Kangasluoma J, Hakala J, Aalto PP, Paasonen P, Mikkila J, Vanhanen J, Aalto J, Hakola H, Makkonen U, Ruuskanen T, Mauldin RL, Duplissy J, Vehkamaki H, Back J, Kortelainen A, Riipinen I, Kurten T, Johnston MV, Smith JN, Ehn M, Mentel TF, Lehtinen KEJ, Laaksonen A, Kerminen V, Worsnop DR (2013) Direct Observations of Atmospheric Aerosol Nucleation. Science 339(6122):943–946. doi: 10.1126/science.1227385

Laskin J, Laskin A, Nizkorodov SA (2013) New mass spectrometry techniques for studying physical chemistry of atmospheric heterogeneous processes. Int. Rev. Phys. Chem. 32(1):128–170. doi: 10.1080/0144235X.2012.752904

Laskin J, Laskin A, Roach PJ, Slysz GW, Anderson GA, Nizkorodov SA, Bones DL, Nguyen LQ (2010) High-Resolution Desorption Electrospray Ionization Mass Spectrometry for Chemical Characterization of Organic Aerosols. Anal. Chem. 82(5):2048–2058. doi: 10.1021/ac902801f

Lauritzen S, Lundberg J (1999) Calibration of the speleothem delta function: an absolute temperature record for the Holocene in northern Norway. holocene 9(6):659–669. doi: 10.1191/095968399667823929

Liggio J, Li S (2006) Organosulfate formation during the uptake of pinonaldehyde on acidic sulfate aerosols. Geophys. Res. Lett. 33(13):n/a. doi: 10.1029/2006GL026079

Lind JA, Lazrus AL, Kok GL (1987) Aqueous phase oxidation of sulfur(IV) by hydrogen peroxide, methylhydroperoxide, and peroxyacetic acid. J. Geophys. Res. 92(D4):4171–4177. doi: 10.1029/JD092iD04p04171

Lin P, Yu JZ, Engling G, Kalberer M (2012) Organosulfates in Humic-like Substance Fraction Isolated from Aerosols at Seven Locations in East Asia: A Study by Ultra-High-Resolution Mass Spectrometry. Environ. Sci. Technol. 46(24):13118–13127. doi: 10.1021/es303570v

Makarov A (2000) Electrostatic Axially Harmonic Orbital Trapping: A High-Performance Technique of Mass Analysis. Anal. Chem. 72(6):1156–1162. doi: 10.1021/ac991131p

McGarry SF, Baker A (2000) Organic acid fluorescence: applications to speleothem palaeoenvironmental reconstruction. Quaternary Science Reviews 19(11):1087–1101. doi: 10.1016/S0277-3791(99)00087-6

Mentel TF, Springer M, Ehn M, Kleist E, Pullinen I, Kurtén T, Rissanen M, Wahner A, Wildt J (2015) Formation of highly oxidized multifunctional compounds: autoxidation of peroxy radicals formed in the ozonolysis of alkenes – deduced from structure–product relationships. Atmos. Chem. Phys. 15(12):6745–6765. doi: 10.5194/acp-15-6745-2015

Middlebrook AM, Bahreini R, Jimenez JL, Canagaratna MR (2012) Evaluation of Composition-Dependent Collection Efficiencies for the Aerodyne Aerosol Mass Spectrometer using Field Data. Aerosol Science and Technology 46(3):258–271. doi: 10.1080/02786826.2011.620041

Monge ME, Harris GA, Dwivedi P, Fernández FM (2013) Mass Spectrometry: Recent Advances in Direct Open Air Surface Sampling/Ionization. Chem. Rev. 113(4):2269–2308. doi: 10.1021/cr300309q

Morelato M, Beavis A, Ogle A, Doble P, Kirkbride P, Roux C (2012) Screening of gunshot residues using desorption electrospray ionisation–mass spectrometry (DESI–MS). Forensic Science International 217(1-3):101–106. doi: 10.1016/j.forsciint.2011.10.030

Müller L, Reinnig MC, Hayen H, Hoffmann T (2009) Characterization of oligomeric compounds in secondary organic aerosol using liquid chromatography coupled to electrospray ionization Fourier transform ion cyclotron resonance mass spectrometry. Rapid Commun. Mass Spectrom. 23(7):971–979. doi: 10.1002/Rcm.3957

Müller L, Reinnig M, Naumann KH, Saathoff H, Mentel TF, Donahue NM, Hoffmann T (2012) Formation of 3-methyl-1,2,3-butanetricarboxylic acid via gas phase oxidation of pinonic acid – a mass spectrometric study of SOA aging. Atmos. Chem. Phys. 12(3):1483–1496. doi: 10.5194/acp-12-1483-2012

Müller L, Reinnig M, Warnke J, Hoffmann T (2008) Unambiguous identification of esters as oligomers in secondary organic aerosol formed from cyclohexene and cyclohexene/α-pinene ozonolysis. Atmos. Chem. Phys. 8(5):1423–1433. doi: 10.5194/acp-8-1423-2008

Murphy DM, Cziczo DJ, Froyd KD, Hudson PK, Matthew BM, Middlebrook AM, Peltier RE, Sullivan A, Thomson DS, Weber RJ (2006) Single-particle mass spectrometry of tropospheric aerosol particles. J. Geophys. Res. 111(D23). doi: 10.1029/2006JD007340

Mutzel A, Poulain L, Berndt T, Iinuma Y, Rodigast M, Böge O, Richters S, Spindler G, Sipilä M, Jokinen T, Kulmala M, Herrmann H (2015) Highly Oxidized Multifunctional Organic Compounds Observed in Tropospheric Particles: A Field and Laboratory Study. Environ. Sci. Technol. 49(13):7754–7761. doi: 10.1021/acs.est.5b00885

Nagato K, Matsui Y, Miyata T, Yamauchi T (2006) An analysis of the evolution of negative ions produced by a corona ionizer in air. International Journal of Mass Spectrometry 248(3):142–147. doi: 10.1016/j.ijms.2005.12.001

Nah T, Chan M, Leone SR, Wilson KR (2013) Real Time in Situ Chemical Characterization of Submicrometer Organic Particles Using Direct Analysis in Real Time-Mass Spectrometry. Anal. Chem. 85(4):2087–2095. doi: 10.1021/ac302560c

Nguyen TB, Lee PB, Updyke KM, Bones DL, Laskin J, Laskin A, Nizkorodov SA (2012) Formation of nitrogen- and sulfur-containing light-absorbing compounds accelerated by evaporation of water from secondary organic aerosols. J. Geophys. Res. 117(D1). doi: 10.1029/2011JD016944

Nizkorodov SA, Laskin J, Laskin A (2011) Molecular chemistry of organic aerosols through the application of high resolution mass spectrometry. Phys. Chem. Chem. Phys. 13(9):3612. doi: 10.1039/c0cp02032j

Nozière B, Ekström S, Alsberg T, Holmström S (2010) Radical-initiated formation of organosulfates and surfactants in atmospheric aerosols. Geophys. Res. Lett. 37(5):n/a. doi: 10.1029/2009GL041683

Nozière B, Kalberer M, Claeys M, Allan J, D'Anna B, Decesari S, Finessi E, Glasius M, Grgić I, Hamilton JF, Hoffmann T, Iinuma Y, Jaoui M, Kahnt A, Kampf CJ, Kourtchev I, Maenhaut W, Marsden N, Saarikoski S, Schnelle-Kreis J, Surratt JD, Szidat S, Szmigielski R, Wisthaler A (2015) The Molecular Identification of Organic Compounds in the Atmosphere: State of the Art and Challenges. Chem. Rev. doi: 10.1021/cr5003485

Odum JR, Hoffmann T, Bowman F, Collins D, Flagan RC, Seinfeld JH (1996) Gas/particle partitioning and secondary organic aerosol yields. Environ. Sci. Technol. 30(8):2580–2585

Orejas J, Pfeuffer K, Ray S, Pisonero J, Sanz-Medel A, Hieftje G (2014) Effect of internal and external conditions on ionization processes in the FAPA ambient desorption/ionization source. Anal Bioanal Chem:1-11. doi: 10.1007/s00216-014-8088-x

Orejas J, Pisonero J, Bordel N, Nelis T, Guillot P, Sanz-Medel A (2012) Bidimensional characterization of the emission spectra in a direct current atmospheric pressure glow discharge. Honoring Issue: A Collection of Papers on Plasma and Laser Spectrochemistry. Dedicated to Gary M. Hieftje on the occasion of his 70th birthday. 76(0):166–174. doi: 10.1016/j.sab.2012.06.044

Oyler J, Darwin WD, Cone EJ (1996) Cocaine Contamination of United States Paper Currency. Journal of Analytical Toxicology 20(4):213–216. doi: 10.1093/jat/20.4.213

Pankow JF (1994a) An Absorption-Model of Gas-Particle Partitioning of Organic-Compounds in the Atmosphere. Atmos. Environ. 28(2):185–188

Pankow JF (1994b) An Absorption-Model of the Gas Aerosol Partitioning Involved in the Formation of Secondary Organic Aerosol. Atmos. Environ. 28(2):189–193

Pankow JF, Asher WE (2008) SIMPOL.1: a simple group contribution method for predicting vapor pressures and enthalpies of vaporization of multifunctional organic compounds. Atmos. Chem. Phys. 8(10):2773–2796. doi: 10.5194/acp-8-2773-2008

Pankow JF, Bidleman TF (1991) Effects of temperature, TSP and per cent non-exchangeable material in determining the gas-particle partitioning of organic compounds. Atmospheric Environment. Part A. General Topics 25(10):2241–2249. doi: 10.1016/0960-1686(91)90099-S

Parshintsev J, Hyötyläinen T (2014) Methods for characterization of organic compounds in atmospheric aerosol particles. Analytical and Bioanalytical Chemistry:1-21. doi: 10.1007/s00216-014-8394-3

Perri MJ, Lim YB, Seitzinger SP, Turpin BJ (2010) Organosulfates from glycolaldehyde in aqueous aerosols and clouds: Laboratory studies. Atmospheric Environment 44(21–22):2658–2664. doi: 10.1016/j.atmosenv.2010.03.031

Pfeuffer KP, Caldwell J, Shelley JT, Ray SJ, Hieftje GM (2014) Detection of counterfeit electronic components through ambient mass spectrometry and chemometrics. Analyst 139(18):4505. doi: 10.1039/C4AN01071J

Pfeuffer KP, Schaper JN, Shelley JT, Ray SJ, Chan GC, Bings NH, Hieftje GM (2013a) Halo-Shaped Flowing Atmospheric Pressure Afterglow: A Heavenly Design for Simplified Sample Introduction and Improved Ionization in Ambient Mass Spectrometry. Anal. Chem. 85(15):7512–7518. doi: 10.1021/ac401524x

Pfeuffer KP, Shelley JT, Ray SJ, Hieftje GM (2013b) Visualization of mass transport and heat transfer in the FAPA ambient ionization source. J. Anal. Atom. Spectrom. 28(3):379. doi: 10.1039/c3ja30353e

Pope CA, Dockery DW (2013) Air pollution and life expectancy in China and beyond. Proceedings of the National Academy of Sciences 110(32):12861–12862. doi: 10.1073/pnas.1310925110

Poulain L, Birmili W, Canonaco F, Crippa M, Wu ZJ, Nordmann S, Spindler G, Prévôt ASH, Wiedensohler A, Herrmann H (2014) Chemical mass balance of 300 °C non-volatile particles at the tropospheric research site Melpitz, Germany. Atmos. Chem. Phys. 14(18):10145–10162. doi: 10.5194/acp-14-10145-2014

Pöschl U (2005) Atmospheric aerosols. Composition, transformation, climate and health effects. Angew. Chem. Int. Edit. 44(46):7520–7540. doi: 10.1002/anie.200501122

Pöschl U, Shiraiwa M (2015) Multiphase Chemistry at the Atmosphere–Biosphere Interface Influencing Climate and Public Health in the Anthropocene. Chem. Rev. 115(10):4440–4475. doi: 10.1021/cr500487s

Pratt KA, Prather KA (2012a) Mass spectrometry of atmospheric aerosols - Recent developments and applications. Part I: Off-line mass spectrometry techniques. Mass Spectrom. Rev. 31(1):1–16. doi: 10.1002/mas.20322

Pratt KA, Prather KA (2012b) Mass spectrometry of atmospheric aerosols - Recent developments and applications. Part II: On-line mass spectrometry techniques. Mass Spectrom. Rev. 31(1):17–48. doi: 10.1002/mas.20330

Raizer Y, Kisin V, Allen J (2011) Gas Discharge Physics. Springer Berlin Heidelberg

Ramanathan V (2001) Aerosols, Climate, and the Hydrological Cycle. Science 294(5549):2119–2124. doi: 10.1126/science.1064034

Renbaum-Wolff L, Grayson JW, Bateman AP, Kuwata M, Sellier M, Murray BJ, Shilling JE, Martin ST, Bertram AK (2013) Viscosity of -pinene secondary organic material and implications for particle growth and reactivity. P. Natl. Acad. Sci. USA 110(20):8014–8019. doi: 10.1073/pnas.1219548110

Riccobono F, Rondo L, Sipilä M, Barmet P, Curtius J, Dommen J, Ehn M, Ehrhart S, Kulmala M, Kürten A, Mikkilä J, Paasonen P, Petäjä T, Weingartner E, Baltensperger U (2012) Contribution of sulfuric acid and oxidized organic compounds to particle formation and growth. Atmos. Chem. Phys. 12(20):9427–9439. doi: 10.5194/acp-12-9427-2012

Riccobono F, Schobesberger S, Scott CE, Dommen J, Ortega IK, Rondo L, Almeida J, Amorim A, Bianchi F, Breitenlechner M, David A, Downard A, Dunne EM, Duplissy J, Ehrhart S, Flagan RC, Franchin A, Hansel A, Junninen H, Kajos M, Keskinen H, Kupc A, Kürten A, Kvashin AN, Laaksonen A, Lehtipalo K, Makhmutov V, Mathot S, Nieminen T, Onnela A, Petäjä T, Praplan AP, Santos FD, Schallhart S, Seinfeld JH, Sipilä M, Spracklen DV, Stozhkov Y, Stratmann F, Tomé A, Tsagkogeorgas G, Vaattovaara P, Viisanen Y, Vrtala A, Wagner PE, Weingartner E, Wex H, Wimmer D, Carslaw KS, Curtius J, Donahue NM, Kirkby J, Kulmala M, Worsnop DR, Baltensperger U (2014) Oxidation Products of Biogenic Emissions Contribute to Nucleation of Atmospheric Particles. Science 344(6185):717–721. doi: 10.1126/science.1243527

Riipinen I, Pierce JR, Donahue NM, Pandis SN (2010) Equilibration time scales of organic aerosol inside thermodenuders: Evaporation kinetics versus thermodynamics. Atmospheric Environment 44(5):597–607. doi: 10.1016/j.atmosenv.2009.11.022

Riipinen I, Pierce JR, Yli-Juuti T, Nieminen T, Häkkinen S, Ehn M, Junninen H, Lehtipalo K, Petäjä T, Slowik J, Chang R, Shantz NC, Abbatt J, Leaitch WR, Kerminen V, Worsnop DR, Pandis SN, Donahue NM, Kulmala M (2011) Organic condensation: a vital link connecting aerosol formation to cloud condensation nuclei (CCN) concentrations. Atmos. Chem. Phys. 11(8):3865–3878. doi: 10.5194/acp-11-3865-2011

Rissanen MP, Kurtén T, Sipilä M, Thornton JA, Kangasluoma J, Sarnela N, Junninen H, Jørgensen S, Schallhart S, Kajos MK, Taipale R, Springer M, Mentel TF, Ruuskanen T, Petäjä T, Worsnop DR, Kjaergaard HG, Ehn M (2014) The Formation of Highly

Oxidized Multifunctional Products in the Ozonolysis of Cyclohexene. J. Am. Chem. Soc. 136(44):15596–15606. doi: 10.1021/ja507146s

Roach PJ, Laskin J, Laskin A (2010) Molecular Characterization of Organic Aerosols Using Nanospray-Desorption/Electrospray Ionization-Mass Spectrometry. Anal. Chem. 82(19):7979–7986. doi: 10.1021/Ac101449p

Rosenfeld D, Lohmann U, Raga GB, O'Dowd CD, Kulmala M, Fuzzi S, Reissell A, Andreae MO (2008) Flood or Drought: How Do Aerosols Affect Precipitation? Science 321(5894):1309–1313. doi: 10.1126/science.1160606

Saukko E, Kuuluvainen H, Virtanen A (2012) A method to resolve the phase state of aerosol particles. Atmos. Meas. Tech. 5(1):259–265. doi: 10.5194/amt-5-259-2012

Schaper JN, Pfeuffer KP, Shelley JT, Bings NH, Hieftje GM (2012) Drop-on-Demand Sample Introduction System Coupled with the Flowing Atmospheric-Pressure Afterglow for Direct Molecular Analysis of Complex Liquid Microvolume Samples. Anal. Chem.:121025085257006. doi: 10.1021/ac3020164

Schilling GD, Shelley JT, Barnes IV JH, Sperline RP, Denton MB, Barinaga CJ, Koppenaal DW, Hieftje GM (2010) Detection of Positive and Negative Ions from a Flowing Atmospheric Pressure Afterglow Using a Mattauch-Herzog Mass Spectrograph Equipped with a Faraday-Strip Array Detector. J. Am. Soc. Mass. Spectrom. 21(1):97–103. doi: 10.1016/j.jasms.2009.09.009

Schneidemesser E von, Monks PS, Allan JD, Bruhwiler L, Forster P, Fowler D, Lauer A, Morgan WT, Paasonen P, Righi M, Sindelarova K, Sutton MA (2015) Chemistry and the Linkages between Air Quality and Climate Change. Chem. Rev. 115(10):3856–3897. doi: 10.1021/acs.chemrev.5b00089

Schobesberger S, Junninen H, Bianchi F, Lonn G, Ehn M, Lehtipalo K, Dommen J, Ehrhart S, Ortega IK, Franchin A, Nieminen T, Riccobono F, Hutterli M, Duplissy J, Almeida J, Amorim A, Breitenlechner M, Downard AJ, Dunne EM, Flagan RC, Kajos M, Keskinen H, Kirkby J, Kupc A, Kurten A, Kurten T, Laaksonen A, Mathot S, Onnela A, Praplan AP, Rondo L, Santos FD, Schallhart S, Schnitzhofer R, Sipila M, Tome A, Tsagkogeorgas G, Vehkamaki H, Wimmer D, Baltensperger U, Carslaw KS, Curtius J, Hansel A, Petaja T, Kulmala M, Donahue NM, Worsnop DR (2013) Molecular understanding of atmospheric particle formation from sulfuric acid and large oxidized organic molecules. Proceedings of the National Academy of Sciences 110(43):17223–17228. doi: 10.1073/pnas.1306973110

Scholz D, Frisia S, Borsato A, Spötl C, Fohlmeister J, Mudelsee M, Miorandi R, Mangini A (2012) Holocene climate variability in north-eastern Italy: potential influence of the NAO and solar activity recorded by speleothem data. Clim. Past 8(4):1367–1383. doi: 10.5194/cp-8-1367-2012

Schwartz SE (1996) The whitehouse effect—Shortwave radiative forcing of climate by anthropogenic aerosols: an overview. Journal of Aerosol Science 27(3):359–382. doi: 10.1016/0021-8502(95)00533-1

Seinfeld J, Pandis S (2006) Atmospheric chemistry and physics: from air pollution to climate change. Wiley

Sekimoto K, Sakai M, Takayama M (2012) Specific Interaction Between Negative Atmospheric Ions and Organic Compounds in Atmospheric Pressure Corona Discharge Ionization Mass Spectrometry. J. Am. Soc. Mass. Spectrom. 23(6):1109–1119. doi: 10.1007/s13361-012-0363-5

Sekimoto K, Takayama M (2011) Observations of different core water cluster ions Y−(H2O)n (Y = O2, HOx, NOx, COx) and magic number in atmospheric pressure negative corona discharge mass spectrometry. J. Mass. Spectrom. 46(1):50–60. doi: 10.1002/jms.1870

Shelley JT, Chan GC, Hieftje GM (2012) Understanding the Flowing Atmospheric-Pressure Afterglow (FAPA) Ambient Ionization Source through Optical Means. J. Am. Soc. Mass. Spectrom. 23(2):407–417. doi: 10.1007/s13361-011-0292-8

Shelley JT, Hieftje GM (2011) Ambient mass spectrometry. Approaching the chemical analysis of things as they are. J. Anal. Atom. Spectrom. 26(11):2153–2159. doi: 10.1039/C1ja10158g

Shelley JT, Wiley JS, Chan GCY, Schilling GD, Ray SJ, Hieftje GM (2009) Characterization of direct-current atmospheric-pressure discharges useful for ambient desorption/ionization mass spectrometry. J. Am. Soc. Mass. Spectrom. 20(5):837–844. doi: 10.1016/j.jasms.2008.12.020

Shelley JT, Wiley JS, Hieftje GM (2011) Ultrasensitive Ambient Mass Spectrometric Analysis with a Pin-to-Capillary Flowing Atmospheric-Pressure Afterglow Source. Anal. Chem. 83(14):5741–5748. doi: 10.1021/Ac201053q

Shiraiwa M, Ammann M, Koop T, Poschl U (2011) Gas uptake and chemical aging of semisolid organic aerosol particles. P. Natl. Acad. Sci. USA 108(27):11003–11008. doi: 10.1073/pnas.1103045108

Shiraiwa M, Pfrang C, Koop T, Pöschl U (2012) Kinetic multi-layer model of gas-particle interactions in aerosols and clouds (KM-GAP): linking condensation, evaporation and chemical reactions of organics, oxidants and water. Atmos. Chem. Phys. 12(5):2777–2794. doi: 10.5194/acp-12-2777-2012

Shiraiwa M, Seinfeld JH (2012) Equilibration timescale of atmospheric secondary organic aerosol partitioning. Geophys. Res. Lett. 39(24):L24801. doi: 10.1029/2012GL054008

Shiraiwa M, Zuend A, Bertram AK, Seinfeld JH (2013) Gas–particle partitioning of atmospheric aerosols: interplay of physical state, non-ideal mixing and morphology. Phys. Chem. Chem. Phys. 15(27):11441. doi: 10.1039/c3cp51595h

Sleeman R, Burton F, Carter J, Roberts D, Hulmston P (2000) Peer Reviewed: Drugs on Money. Anal. Chem. 72(11):397 A. doi: 10.1021/ac002826p

Smith RM, Casale JF (2010) The Mass Spectrum of Cocaine: Deuterium Labeling and MS/MS Studies. Microgram Journal 7(1):16–41

Surratt JD, Gómez-González Y, Chan AWH, Vermeylen R, Shahgholi M, Kleindienst TE, Edney EO, Offenberg JH, Lewandowski M, Jaoui M, Maenhaut W, Claeys M, Flagan RC, Seinfeld JH (2008) Organosulfate Formation in Biogenic Secondary Organic Aerosol. J. Phys. Chem. A 112(36):8345–8378. doi: 10.1021/jp802310p

Surratt JD, Kroll JH, Kleindienst TE, Edney EO, Claeys M, Sorooshian A, Ng NL, Offenberg JH, Lewandowski M, Jaoui M, Flagan RC, Seinfeld JH (2007) Evidence for Organosulfates in Secondary Organic Aerosol. Environ. Sci. Technol. 41(2):517–527. doi: 10.1021/es062081q

Szmigielski R, Surratt JD, Vermeylen R, Szmigielska K, Kroll JH, Ng NL, Murphy SM, Sorooshian A, Seinfeld JH, Claeys M (2007) Characterization of 2-methylglyceric acid oligomers in secondary organic aerosol formed from the photooxidation of isoprene

using trimethylsilylation and gas chromatography/ion trap mass spectrometry. Journal of Mass Spectrometry 42(1):101–116. doi: 10.1002/jms.1146

Takats Z (2004) Mass Spectrometry Sampling Under Ambient Conditions with Desorption Electrospray Ionization. Science 306(5695):471–473. doi: 10.1126/science.1104404

Talaty N, Mulligan CC, Justes DR, Jackson AU, Noll RJ, Cooks RG (2008) Fabric analysis by ambient mass spectrometry for explosives and drugs. Analyst 133(11):1532–1540. doi: 10.1039/B807934J

Thomson JJ (1913) Rays of positive electricity and their application to chemical analyses. Longmans, Green and Co., London

Thorenz UR, Kundel M, Muller L, Hoffmann T (2012) Generation of standard gas mixtures of halogenated, aliphatic, and aromatic compounds and prediction of the individual output rates based on molecular formula and boiling point. Anal. Bioanal. Chem. 404(8):2177–2183. doi: 10.1007/s00216-012-6202-5

Vaden TD, Imre D, Beránek J, Shrivastava M, Zelenyuk A (2011) Evaporation kinetics and phase of laboratory and ambient secondary organic aerosol. Proceedings of the National Academy of Sciences 108(6):2190–2195. doi: 10.1073/pnas.1013391108

Vaden TD, Song C, Zaveri RA, Imre D, Zelenyuk A (2010) Atmospheric Chemistry Special Feature: Morphology of mixed primary and secondary organic particles and the adsorption of spectator organic gases during aerosol formation. P. Natl. Acad. Sci. USA 107(15):6658–6663. doi: 10.1073/pnas.0911206107

van Pinxteren D, Brüggemann E, Gnauk T, Müller K, Thiel C, Herrmann H (2010) A GIS based approach to back trajectory analysis for the source apportionment of aerosol constituents and its first application. J Atmos Chem 67(1):1-28. doi: 10.1007/s10874-011-9199-9

van Pinxteren D, Neusüß C, Herrmann H (2014) On the abundance and source contributions of dicarboxylic acids in size-resolved aerosol particles at continental sites in central Europe. Atmos. Chem. Phys. 14(8):3913–3928. doi: 10.5194/acp-14-3913-2014

Virtanen A, Joutsensaari J, Koop T, Kannosto J, Yli-Pirila P, Leskinen J, Makela JM, Holopainen JK, Poschl U, Kulmala M, Worsnop DR, Laaksonen A (2010) An amorphous solid state of biogenic secondary organic aerosol particles. Nature 467(7317):824–827. doi: 10.1038/Nature09455

Vogel AL, Äijälä M, Brüggemann M, Ehn M, Junninen H, Petäjä T, Worsnop DR, Kulmala M, Williams J, Hoffmann T (2013a) Online atmospheric pressure chemical ionization ion trap mass spectrometry (APCI–IT–MS^n) for measuring organic acids in concentrated bulk aerosol – a laboratory and field study. Atmos. Meas. Tech. 6(2):431–443. doi: 10.5194/amt-6-431-2013

Vogel AL, Äijälä M, Corrigan AL, Junninen H, Ehn M, Petäjä T, Worsnop DR, Kulmala M, Russell LM, Williams J, Hoffmann T (2013b) In situ submicron organic aerosol characterization at a boreal forest research station during HUMPPA-COPEC 2010 using soft and hard ionization mass spectrometry. Atmos. Chem. Phys. 13(21):10933–10950. doi: 10.5194/acp-13-10933-2013

Weber RJ, Sullivan AP, Peltier RE, Russell A, Yan B, Zheng M, Gouw J de, Warneke C, Brock C, Holloway JS, Atlas EL, Edgerton E (2007) A study of secondary organic aerosol formation in the anthropogenic-influenced southeastern United States. J. Geophys. Res. 112(D13):n/a. doi: 10.1029/2007JD008408

Wiedensohler A, Birmili W, Nowak A, Sonntag A, Weinhold K, Merkel M, Wehner B, Tuch T, Pfeifer S, Fiebig M, Fjäraa AM, Asmi E, Sellegri K, Depuy R, Venzac H, Villani P, Laj P, Aalto P, Ogren JA, Swietlicki E, Williams P, Roldin P, Quincey P, Hüglin C, Fierz-Schmidhauser R, Gysel M, Weingartner E, Riccobono F, Santos S, Grüning C, Faloon K, Beddows D, Harrison R, Monahan C, Jennings SG, O'Dowd CD, Marinoni A, Horn H, Keck L, Jiang J, Scheckman J, McMurry PH, Deng Z, Zhao CS, Moerman M, Henzing B, Leeuw G de, Löschau G, Bastian S (2012) Mobility particle size spectrometers: harmonization of technical standards and data structure to facilitate high quality long-term observations of atmospheric particle number size distributions. Atmos. Meas. Tech. 5(3):657–685. doi: 10.5194/amt-5-657-2012

Wynn PM, Brocks JJ (2014) A framework for the extraction and interpretation of organic molecules in speleothem carbonate. Rapid Commun. Mass Spectrom. 28(8):845–854. doi: 10.1002/rcm.6843

Yasmeen F, Szmigielski R, Vermeylen R, Gómez-González Y, Surratt JD, Chan AWH, Seinfeld JH, Maenhaut W, Claeys M (2011) Mass spectrometric characterization of isomeric terpenoic acids from the oxidation of α-pinene, β-pinene, d-limonene, and Δ3-carene in fine forest aerosol. J. Mass. Spectrom. 46(4):425–442. doi: 10.1002/jms.1911

Yasmeen F, Vermeylen R, Maurin N, Perraudin E, Doussin J, Claeys M (2012) Characterisation of tracers for aging of α-pinene secondary organic aerosol using liquid chromatography/negative ion electrospray ionisation mass spectrometry. Environ. Chem. 9(3):236–246

Yasmeen F, Vermeylen R, Szmigielski R, Iinuma Y, Böge O, Herrmann H, Maenhaut W, Claeys M (2010) Terpenylic acid and related compounds: precursors for dimers in secondary organic aerosol from the ozonolysis of α- and β-pinene. Atmos. Chem. Phys. 10(19):9383–9392. doi: 10.5194/acp-10-9383-2010

Yoshinari K (2000) Theoretical and numerical analysis of the behavior of ions injected into a quadrupole ion trap mass spectrometer. Rapid Commun. Mass Spectrom. 14(4):215–223. doi: 10.1002/(SICI)1097-0231(20000229)14:4<215:AID-RCM867>3.0.CO;2-T

Yu J, Flagan RC, Seinfeld JH (1998) Identification of Products Containing −COOH, −OH, and −CO in Atmospheric Oxidation of Hydrocarbons. Environ. Sci. Technol. 32(16):2357–2370. doi: 10.1021/es980129x

Zelenyuk A, Yang J, Song C, Zaveri RA, Imre D (2008) “Depth-Profiling” and Quantitative Characterization of the Size, Composition, Shape, Density, and Morphology of Fine Particles with SPLAT, a Single-Particle Mass Spectrometer. J. Phys. Chem. A 112(4):669–677. doi: 10.1021/jp077308y

Zhang Q, Jimenez JL, Canagaratna MR, Allan JD, Coe H, Ulbrich I, Alfarra MR, Takami A, Middlebrook AM, Sun YL, Dzepina K, Dunlea E, Docherty K, DeCarlo PF, Salcedo D, Onasch T, Jayne JT, Miyoshi T, Shimono A, Hatakeyama S, Takegawa N, Kondo Y, Schneider J, Drewnick F, Borrmann S, Weimer S, Demerjian K, Williams P, Bower K, Bahreini R, Cottrell L, Griffin RJ, Rautiainen J, Sun JY, Zhang YM, Worsnop DR (2007) Ubiquity and dominance of oxygenated species in organic aerosols in anthropogenically-influenced Northern Hemisphere midlatitudes. Geophys. Res. Lett. 34(13):n/a. doi: 10.1029/2007GL029979

Zhang R, Wang L, Khalizov AF, Zhao J, Zheng J, McGraw RL, Molina LT (2009) Formation of nanoparticles of blue haze enhanced by anthropogenic pollution.

Proceedings of the National Academy of Sciences 106(42):17650–17654. doi: 10.1073/pnas.0910125106

Zhang YY, Müller L, Winterhalter R, Moortgat GK, Hoffmann T, Pöschl U (2010) Seasonal cycle and temperature dependence of pinene oxidation products, dicarboxylic acids and nitrophenols in fine and coarse air particulate matter. Atmos. Chem. Phys. 10(16):7859–7873. doi: 10.5194/ACP-10-7859-2010

Zhao J, Ortega J, Chen M, McMurry PH, Smith JN (2013) Dependence of particle nucleation and growth on high-molecular-weight gas-phase products during ozonolysis of α-pinene. Atmos. Chem. Phys. 13(15):7631–7644. doi: 10.5194/acp-13-7631-2013

Zhou S, Lee AKY, McWhinney RD, Abbatt JPD (2012) Burial Effects of Organic Coatings on the Heterogeneous Reactivity of Particle-Borne Benzo[a]pyrene (BaP) toward Ozone. J. Phys. Chem. A 116(26):7050–7056. doi: 10.1021/jp3030705

Zhou S, Shiraiwa M, McWhinney RD, Pöschl U, Abbatt JPD (2013) Kinetic limitations in gas-particle reactions arising from slow diffusion in secondary organic aerosol. Faraday Discuss 165:391–406. doi: 10.1039/C3FD00030C

Zubarev RA, Makarov A (2013) Orbitrap Mass Spectrometry. Anal. Chem. 85(11):5288–5296. doi: 10.1021/ac4001223

8 Appendix

A. Supplemental Material to Chapter 2

A.1 Reagents and Materials

Table 5.5.2: List of all reagents and materials used in this study.

Name	Chemical formula	Purity	Supplier
Methanol	CH_3OH	≥99.9%	Sigma-Aldrich
cis-Pinonic acid	$CH_3COC_4H_4(CH_3)_2CH_2CO_2H$	98%	Sigma-Aldrich
Caffeine	$C_8H_{10}N_4O_2$	98.5%	Acros Organics
Tricarballylic acid	$(HO_2CCH_2)_2CHCO_2H$	≥99%	SAFC
Oxalic acid	HO_2CCO_2H	99.999% (purified grade)	Sigma-Aldrich
Adipic acid	$HOOC(CH_2)_4COOH$	≥99.5%	Fluka Analytical, Sigma-Aldrich
Sebacic acid	$HO_2C(CH_2)_8CO_2H$	98%	Acros Organics
Citric acid (monohydrate)	$HOC(COOH)(CH_2COOH)_2$ x H_2O	≥98%	Sigma-Aldrich
o-Acetylsalicylic acid	$2\text{-}(CH_3CO_2)C_6H_4CO_2H$	>99% (HPLC)	Fluka Chemika
4-Ketopimelic acid	$HO_2CCH_2CH_2COCH_2CH_2CO_2H$	98%	Sigma-Aldrich
α-Ketoglutaric acid	$HOOCCH_2CH_2COCOOH$	≥99.0%	Fluka Analytical
Palmitic acid	$CH_3(CH_2)_{14}COOH$	Analytical standard	Fluka Analytical, Sigma-Aldrich
Stearic acid	$CH_3(CH_2)_{16}COOH$	Analytical standard	Fluka Analytical, Sigma-Aldrich
Benzoyl peroxide	$(C_6H_5CO)_2O_2$	For synthesis, with 25% H_2O as stabiliser	Merck
Decanal	$CH_3(CH_2)_8CHO$	≥98% (GC)	Sigma-Aldrich
Levoglucosan	$C_6H_{10}O_5$	>99%	Acros Organics
tert-Butyl peroxy-3,5,5-trimethylhexanoate	$C_{13}H_{26}O_3$	97%	Acros Organics
Pinic acid	$C_9H_{14}O_4$	self-synthesized in the lab	–
Dichloromethane	CH_2Cl_2	≥99.9% (Rotisolv®, HPLC)	Roth GmbH
Lauroyl peroxide	$[CH_3(CH_2)_{10}CO]_2O_2$	97%	Sigma-Aldrich
Oleic acid	$CH_3(CH_2)_7CH{=}CH(CH_2)_7COOH$	90%	Fluka
Lauric acid	$CH_3(CH_2)_{10}COOH$	≥98%	Sigma-Aldrich
Myristic acid	$CH_3(CH_2)_{12}COOH$	≥99%	Sigma-Aldrich
Palmitic acid	$CH_3(CH_2)_{14}COOH$	≥99%	Sigma-Aldrich
Stearic acid	$CH_3(CH_2)_{16}COOH$	≥98.5%	Sigma-Aldrich
Arachidic acid	$CH_3(CH_2)_{18}COOH$	≥99%	Sigma-Aldrich
Dodecane	$CH_3(CH_2)_{10}CH_3$	>99%	Aldrich
(+)-α-Pinene	$C_{10}H_{16}$	≥99%	Aldrich
(−)-β-Pinene	$C_{10}H_{16}$	99%	Aldrich
(R)-(+)-Limonene	$C_{10}H_{16}$	97% (98% ee/GLC)	Aldrich
(+)-Δ^3-Carene	$C_{10}H_{16}$	Analytical standard, for terpene analysis	Fluka
Helium	He (Helium 5.0)	≥99.999%	Westfalen AG
Synthetic air	20.5 vol% O_2, 79.5 vol% N_2	Hydrocarbon free	Westfalen AG

A.2 Compound Library

Table 5.5.3: Complete compound library for ambient desorption FAPA–MS in negative and positive mode.

	Compound	Formula	M / g/mol	Most abundant signals in	
				Positive mode	Negative mode
Solvents	Methanol (MeOH)	CH_4O	32	**65 [2M+H]$^+$** **97 [3M+H]$^+$**	–
	Dichloromethane (DCM)	CH_2Cl_2	85	-	135 [2M–Cl]$^-$
	Acetone	C_3H_6O	58	**59 [M+H]$^+$** **117 [2M+H]$^+$**	–
Carboxylic Acids in MeOH	Pinonic Acid	$C_{10}H_{16}O_3$	184	**185 [M+H]$^+$** 167 [M+H–H2O]$^+$ 202 [M+NH$_4$]$^+$ **369 [2M+H]$^+$**	**246 [M+NO$_3$]$^-$** 323 [M–H–CO$_2$]$^-$ **367 [2M–H]$^-$**
	o-Acetylsalicylic Acid	$C_9H_8O_4$	180	240 [M+60]$^+$ 163 [M-H$_2$O+H]$^+$ 121 [M–OAc+H]$^+$ **181 [M+H]$^+$** 198 [M+NH$_4$]$^+$ 360 [2M]$^{+\bullet}$ **361 [2M+H]$^+$** 378 [2M+NH$_4$]$^+$	182 [M+2]$^-$ 137 [M–C$_2$H$_3$O]$^-$ 153 [137+O]$^-$ 195 [M–H+O]$^-$ 200 [M+20]$^-$ 211 [M–H+O$_2$]$^-$ 224 [M+44]$^-$ 240 [M+60]$^-$ 258 [M+78]$^-$ 259 [M+79]$^-$ 274 [M+94]$^-$ 287 [M+107]$^-$ 303 [M+123]$^-$ **359 [2M–H]$^-$**
	Pinic Acid	$C_9H_{14}O_4$	186	**187 [M+H]$^+$** 169 [M–H$_2$O+H]$^+$ 185 [169+O]$^+$ 202 [M–H$_2$O+O+NH$_4$]$^+$ 204 [M+NH$_4$]$^+$ 220 [204+O]$^+$ **373 [2M+H]$^+$**	201 [M–H+O]$^-$ **185 [M–H]$^-$** 264 [M+78]$^-$ 281 [M+95]$^-$ 283 [M+98]$^-$ 326 [M+140]$^-$
	Oxalic Acid	$C_2H_2O_4$	90	173 [M+83]$^+$ 191 [M+101]$^+$ 208 [M+118]$^+$	**89 [M–H]$^-$** **179 [2M–H]$^-$** **152 [M+NO$_3$]$^-$**
	α-Ketoglutaric Acid	$C_5H_6O_5$	146	192 [M+NO$_2$]$^+$ 175 [M+29]$^+$ 157 [175–H$_2$O]$^+$ **147 [M+H]$^+$** 129 [M+H–H$_2$O]$^+$ 164 [M+NH$_4$]$^+$ **293 [2M+H]$^+$**	**145 [M–H]$^-$** **208 [M+NO$_3$]$^-$** **291 [2M–H]$^-$**
	4-Ketopimelic Acid	$C_7H_{10}O_5$	174	157 [M–H$_2$O+H]$^+$ **175 [M+H]$^+$** 192 [M+NH$_4$]$^+$ **349 [2M+H]$^+$**	**236 [M+NO$_3$]$^-$** **173 [M–H]$^-$**
	Adipic Acid	$C_6H_{10}O_4$	146	**147 [M+H]$^+$** 164 [M+NH$_4$]$^+$ 129 [M–H$_2$O+H]$^+$ 111 [M–2H$_2$O+H]$^+$ **293 [2M+H]$^+$** 310 [2M+NH$_4$]$^+$	**208 [M+NO$_3$]$^-$** 269 [M+123]$^-$ **145 [M–H]$^-$**
	Sebacic Acid	$C_{10}H_{18}O_4$	202	220 [M+NH$_4$]$^+$ **203 [M+H]$^+$**	325 [M+123]$^-$ **264 [M+NO$_3$]$^-$**

				405 [2M+H]$^+$ 185 [M–H_2O+H]$^+$	231 [M+29]$^-$ 294 [231–H+NO_3]$^-$ 262 [M+60]$^-$ 187 [231–CO_2]$^-$ **201 [M–H]$^-$** 247 [M–H+NO_2]$^-$ 278 [262+O]$^-$
	Tricarballylic Acid	$C_6H_8O_6$	176	194 [M+NH_4]$^+$ **177 [M+H]$^+$** 159 [M–H_2O+H]$^+$ 141 [M–2H_2O+H]$^+$ 370 [2M+NH_4]$^+$ **353 [2M+H]$^+$**	**175 [M–H]$^-$** 157 [M–H–H_2O]$^-$
	Citric Acid	$C_6H_8O_7$	192	210 [M+NH_4]$^+$ **193 [M+H]$^+$** 175 [M–H_2O+H]$^+$ 157 [M–2H_2O+H]$^+$ 147 [M–COOH]$^+$	**191 [M–H]$^-$** 347 [2M–H–2H_2O]$^-$ 365 [2M–H–H_2O]$^-$ **383 [2M–H]$^-$**
Fatty Acids in DCM	Lauric Acid	$C_{12}H_{24}O_2$	200	**201 [M+H]$^+$** 213 [M+13]$^+$ 229 [M+29]$^+$ **401 [2M+H]$^+$**	355 [2M–H–CO_2]$^-$ 371 [2M–H–CO_2+O]$^-$ 339 [M+139]$^-$ 324 [M+124]$^-$ 308 [M+108]$^-$ 292 [M+92]$^-$
	Myristic Acid	$C_{14}H_{28}O_2$	228	**229 [M+H]$^+$** 243 [M+15]$^+$ 241 [M+13]$^+$ 257 [241+O]$^+$ **457 [2M+H]$^+$** 481 [2M+25]$^+$	191 [M–37]$^-$ 400 [M+172]$^-$ 367 [M+139]$^-$ 369 [M+141]$^-$ 416 [M+188]$^-$ 383 [M+155]$^-$ 336 [M+108]$^-$ 353 [M+H(NO_3)$_2$]$^-$ 351 [M+123]$^-$ 320 [M+92]$^-$ 432 [M+204]$^-$ 309[M+81]$^-$
	Palmitic Acid	$C_{16}H_{32}O_2$	256	**257 [M+H]$^+$** 271 [M+15]$^+$ 285 [M+29]$^+$ **513 [2M+H]$^+$**	395 [M+139]$^-$ 301 [M+45]$^-$ 348 [M+92]$^-$ 364 [M+108]$^-$ 380 [M+124]$^-$ 411 [M+155]$^-$ 427 [M+171]$^-$ **511 [2M–H]$^-$**
	Stearic Acid	$C_{18}H_{36}O_2$	284	297 [M+13]$^+$ 299[M+15]$^+$ 313 [M+29]$^+$ 283 [M-H_2O+O+H]$^+$ 599 [2M+31]$^+$ 601 [2M+33]$^+$	423 [M+139]$^-$ 330 [M+NO_2]$^-$ 365 [M+109]$^-$ 376 [M+92]$^-$ 392 [M+111]$^-$ 408 [M+124]$^-$ 439 [M+155]$^-$ 453 [M+169]$^-$ 469 [M+185]$^-$ 484 [M+200]$^-$ 500 [M+216]$^-$
	Oleic Acid	$C_{18}H_{34}O_2$	282	**283 [M+H]$^+$** 299 [M+O+H]$^+$ 316 [M+O+NH_4]$^+$ 345 [M+63]$^+$	423 [M+141]$^-$ **344 [M+NO_3]$^-$** 374 [M+92]$^-$ 390 [M+108]$^-$ 406 [M+124]$^-$ 421 [M+139]$^-$

					437 $[M+155]^-$ 453 $[M+171]^-$ 457 $[M+175]^-$ 469 $[M+187]^-$ 473 $[M+191]^-$ 485 $[M+203]^-$
	Arachidic Acid	$C_{20}H_{40}O_2$	312	325 $[M+13]^+$ 327 $[M+15]^+$ 311 $[M–H_2O+O+H]^+$ 341 $[M+29]^+$ 344$[M+32]^+$ 655 $[2M+31]^+$	451 $[M+139]^-$ **374 $[M+NO_3]^-$** 404 $[M+92]^-$ 420 $[M+108]^-$ 435 $[M+123]^-$ 467 $[M+155]^-$ 483 $[M+171]^-$ **623 $[2M–H]^-$**
Peroxides	tert-Butylperoxy-trimethylhexanoate (in MeOH)	$C_{13}H_{26}O_3$	230	478 $[2M+NH_4]^+$ 248 $[M+NH_4]^+$ **461 $[2M+H]^+$** 478 $[2M+NH4]^+$	–
	Benzoyl Peroxide (in DCM)	$C_{14}H_{10}O_4$	242	199 $[M–43]^+$ 181 $[M–61]^+$ 216 $[M–26]^+$ 260 $[M+NH_4]^+$ 275 $[M+O_2+H]^+$ 292 $[M+O_2+NH_4]^+$	–
	Dilauroyl Peroxide (in DCM)	$C_{24}H_{46}O_4$	398	429 $[M+31]^+$ 367 $[M–31]^+$ 341 $[M–57]^+$ 411 $[M+13]^+$	462 $[M+64]^-$ 323 $[M–75]^-$ 353 $[M–H–CO_2]^-$ 418 $[M+20]^-$
Other	Caffeine (in MeOH)	$C_8H_{10}N_4O_2$	194	**195 $[M+H]^+$** **389 $[2M+H]^+$** 421 $[2M+O_2+H]^+$	209 $[M–H+O]^-$ 272 $[M+O+NO_3]^-$ 288 $[M+O_2+NO_3]^-$ 419 $[M+225]^-$ 435 $[2M+47]^-$ 451 $[2M+63]^-$ 482 $[2M+94]^-$ 498 $[2M+110]^-$
	Levoglucosan (in MeOH)	$C_6H_{10}O_5$	162	342 $[2M+NH_4]^+$ **325 $[2M+H]^+$** **163 $[M+H]^+$** 180 $[M+NH_4]^+$ 145 $[M–H2O+H]^+$ 127 $[M–2H_2O+H]^+$	**224 $[M+NO_3]^-$** 146 $[M–O]^-$ 162 $[M]^-$ 238 $[M+76]^-$ **386 $[2M+NO_3]^-$**
	Decanal (in MeOH)	$C_{10}H_{20}O$	156	171 $[M+15]^+$ 169 $[M+13]^+$ 187 $[M+31]^+$ 185 $[M+29]^+$ 295 $[M+139]^+$ 311 $[M+155]^+$ 313 $[M+157]^+$ 330 $[M+174]^+$	–
	Dodecane (in DCM)	$C_{12}H_{26}$	170	201 $[M+31]^+$ 183 $[M+13]^+$ 180 $[M+10]^+$ 163 $[M-7]^+$	–

B. Supplemental Material to Chapter 3

B.1 Reagents and Materials

High-purity helium (purity 5.0, Westfalen AG, Münster, Germany) was used as discharge gas in all cases. Cis-pinic acid was synthesized according to Moglioni *et al.*(2000). Synthetic air (hydrocarbon free, Westfalen AG, Münster Germany) was used for nebulization of methanolic solutions. Methanol (HPLC grade) was purchased from Fisher Scientific. Adipic acid, stearic acid, oleic acid, pinonic acid, palmitic acid, tricarballylic acid, and α-pinene were purchased from Sigma-Aldrich. All reagents were analytical-grade.

B.2 Estimation of the Particles' Residence Time in the Afterglow Region

The estimation of the residence time was conducted by assuming a linear velocity profile for all gas flows. Furthermore, we assumed that ionization and efficient ion transmission into the MS only occurs in a distance of max. 2 mm from the MS inlet and the exit of the AeroFAPA (Figure 5.5.4). Eventually, this approach led to calculated residence times of 150–300 µs for the aerosol particles in the afterglow region at typical operating conditions.

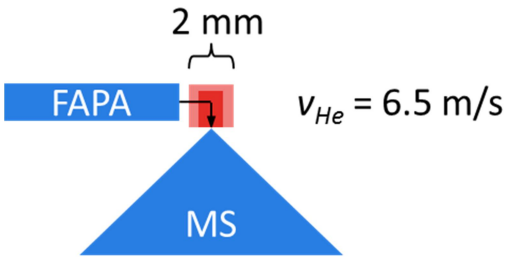

Figure 5.5.4: Estimation of the aerosol particles' residence times in the afterglow region. The red area symbolizes the afterglow region; the AeroFAPA source exit and the MS inlet capillary are depicted in blue.

B.3 Background Mass Spectra in the Negative and the Positive Ion Mode

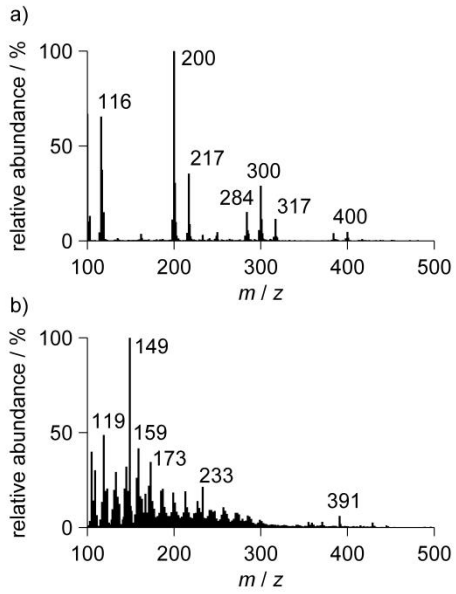

Figure 5.5.5: (a) Background mass spectrum of the AeroFAPA source in the negative mode at typical operating conditions (I = 55 mA, helium flow = 0.6 L·min^{-1}, sample flow = 0.9 L·min^{-1}). (b) Background mass spectrum in the positive ion mode at typical operating conditions.

B.4 Correlation between Aerosol Mass and MS Signal

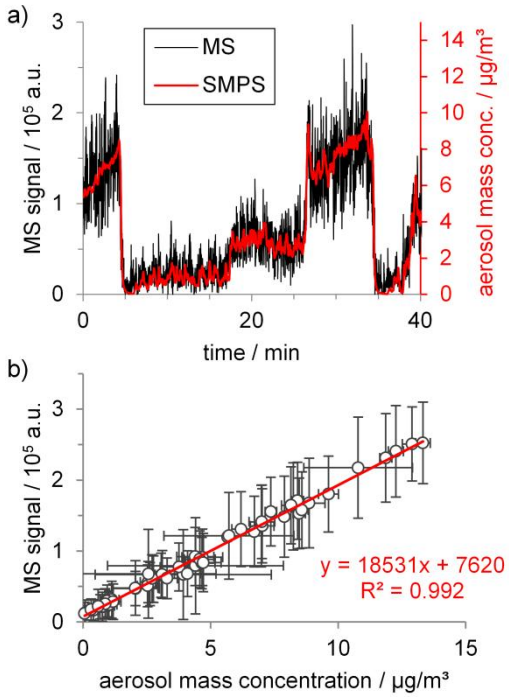

Figure 5.5.6: (a) MS signal as a function of time and aerosol mass concentration for the analysis of a tricarballylic acid aerosol (d_p = 100 nm). (b) Correlation between aerosol mass and MS signal for tricarballylic acid ([M-H]$^-$). Each data point represents the average signal of 1 minute; error bars indicate one standard deviation.

B.5 MS^n Experiments for Identification of Organic Species in Ambient Aerosols during the F-BEACh 2014 Field Study

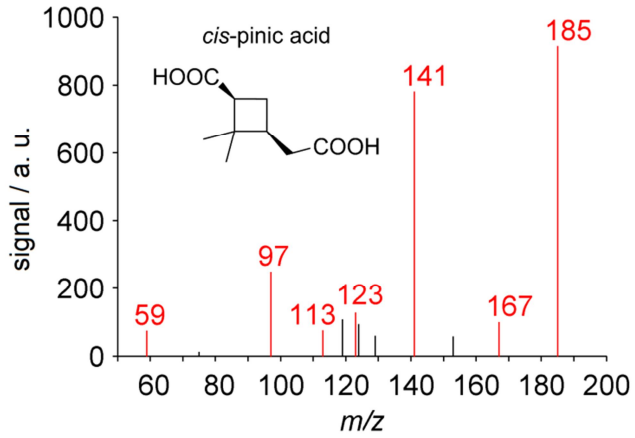

Figure 5.5.7: MS^2 spectrum of *m/z* 185. The signals indicate the presence of pinic acid. The highlighted signals in red have been reported before by. The signal at *m/z* 113 might be correlated to the abundance of caric acid or limonic acid. The signal at *m/z* 59 might indicate the presence of homoterpenylic acid (Yasmeen *et al.*, 2011).

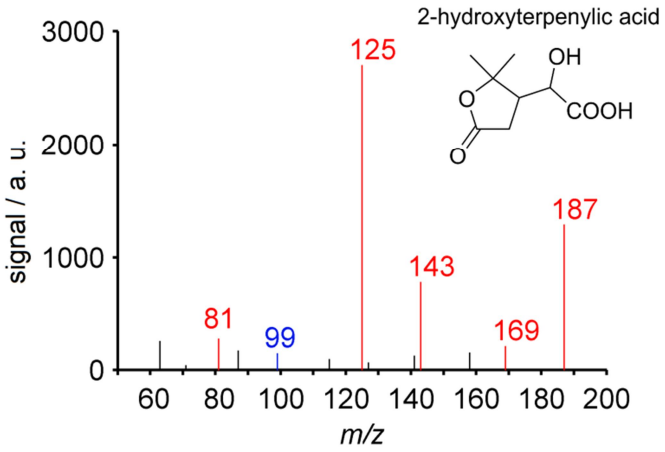

Figure 5.5.8: MS^2 of *m/z* 187. The signals suggest the abundance of 2-hydroxy terpenylic acid. The highlighted signals in red have been reported before by others. In addition, the signals at *m/z* 169, 143 and 125 might also indicate the presence of a precursor compound to 3-methyl-1,2,3-butanetricarboxylic acid (MBTCA) (Claeys *et al.*, 2009). The signal at *m/z* 99 might correlate to the formation of $[M\text{-}H_2O\text{-}2xCO_2]^-$ and is in agreement with the proposed structure.

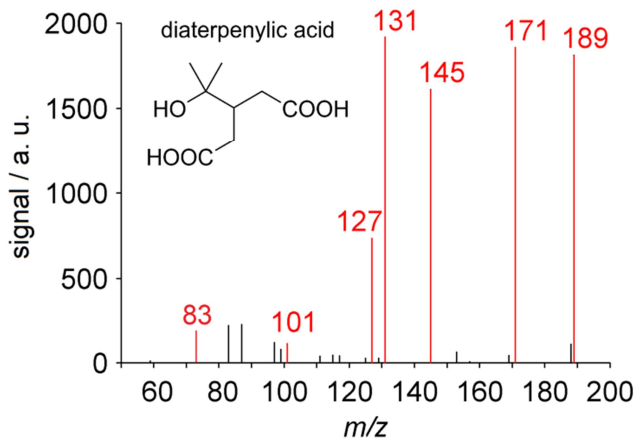

Figure 5.5.9: MS^2 of *m/z* 189. The signals suggest the abundance of diaterpenylic acid. The highlighted Signals in red have been reported before by others and are in agreement with the proposed structure (Yasmeen *et al.*, 2012).

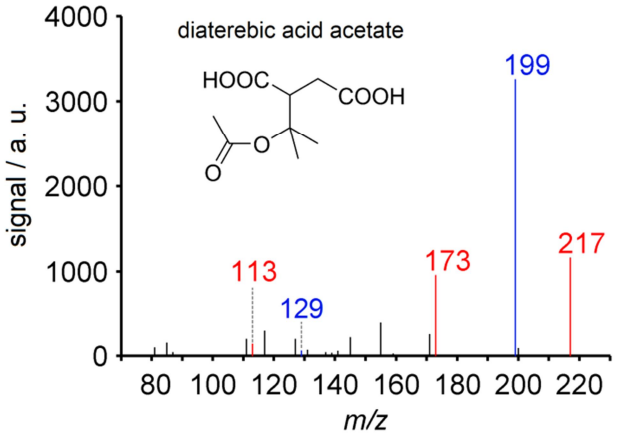

Figure 5.5.10: MS^2 of *m/z* 217. The signals suggest the abundance of diaterebic acid acetate. The highlighted signals in red have been reported before by others (Iinuma *et al.*, 2009). Besides, the signals in blue are in agreement with the proposed structure: *m/z* 199 = $[M\text{-}H\text{-}H_2O]^-$, *m/z* 129 = $[M\text{-}H\text{-}2xCO_2]^-$.

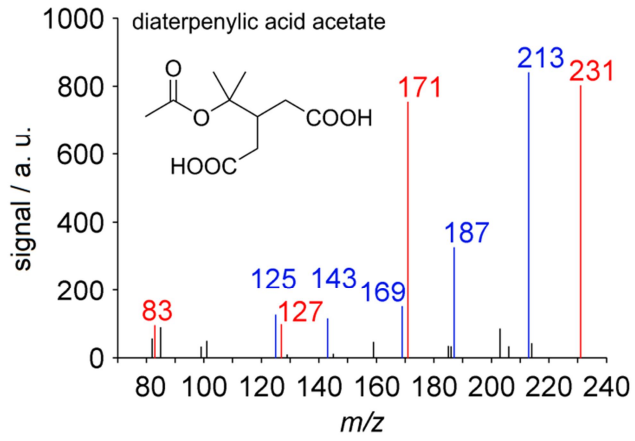

Figure 5.5.11: MS^2 of *m/z* 231. The signals suggest the abundance of diaterpenylic acid acetate. The highlighted signals in red have been reported before by others (Claeys *et al.*, 2009). Besides, the signals in blue are in agreement with the proposed structure: *m/z* 213 = $[M\text{-}H\text{-}H_2O]^-$, *m/z* 187 = $[M\text{-}H\text{-}CO_2]^-$, *m/z* 169 = $[187\text{-}H_2O]^-$, *m/z* 143 = $[187\text{-}CO_2]^-$, *m/z* 125 = $[143\text{-}H_2O]^-$.

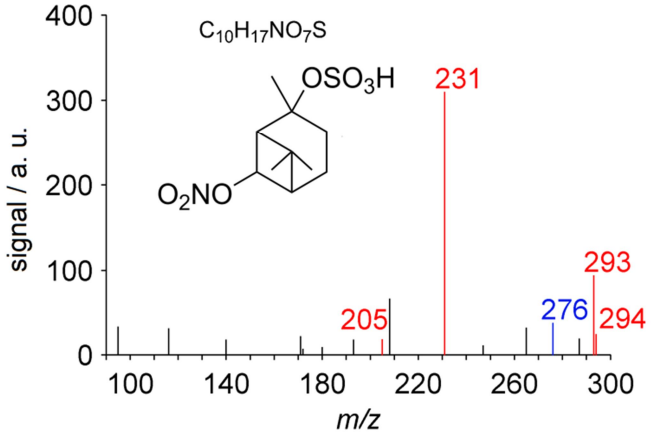

Figure 5.5.12: MS^2 of *m/z* 294. The signals suggest the abundance of the nitrooxy organosulfate ($C_{10}H_{17}NO_7S$). The highlighted Signals in red have been reported before (Surratt *et al.*, 2008). The signal at *m/z* 276 might correlate to an additional loss of water ($[M\text{-}H\text{-}H_2O]^-$).

C. Supplemental Material to Chapter 4

C.1 Identified compounds from UHPLC-(-)ESI-UHRMS analysis of filter samples

Table 5.5.4: List of CHO-containing compounds that were identified by UHPLC-(-)ESI-UHRMS analysis of the filter samples.

formula for $[M–H]^-$	*m/z* for $[M–H]^-$	measured *m/z*	Δ*m* / ppm	Number of Oxygen	Number of Carbon	O:C
C4H5O5	133.0142	133.0141	1.1	5	4	1.3
C6H7O4	143.0350	143.0349	0.6	4	6	0.7
C6H9O4	145.0506	145.0506	0.2	4	6	0.7
C6H9O5	161.0455	161.0454	0.9	5	6	0.8
C6H13O6	181.0718	181.0718	-0.2	6	6	1.0
C6H7O7	191.0197	191.0197	0.1	7	6	1.2
C7H9O3	141.0557	141.0557	0.1	3	7	0.4
C7H9O4	157.0506	157.0505	0.9	4	7	0.6
C7H11O4	159.0663	159.0661	1.2	4	7	0.6
C7H9O5	173.0455	173.0453	1.4	5	7	0.7
C7H11O5	175.0612	175.0611	0.6	5	7	0.7
C7H7O6	187.0248	187.0247	0.6	6	7	0.9
C7H9O6	189.0405	189.0403	0.9	6	7	0.9
C8H13O3	157.0870	157.0871	-0.5	3	8	0.4
C8H11O4	171.0663	171.0662	0.5	4	8	0.5
C8H11O5	187.0612	187.061	1.1	5	8	0.6
C8H13O5*	189.0768	189.0767	0.8	5	8	0.6
C8H9O6	201.0405	201.0403	0.8	6	8	0.8
C8H11O6*	203.0561	203.0561	0.1	6	8	0.8
C9H7O4	179.0350	179.0351	-0.7	4	9	0.4
C9H13O4	185.0819	185.0818	0.7	4	9	0.4
C9H11O5	199.0612	199.0612	0.0	5	9	0.6
C9H13O5	201.0768	201.0768	0.2	5	9	0.6
C9H15O5	203.0925	203.0925	0.0	5	9	0.6
C9H9O6	213.0405	213.0405	-0.2	6	9	0.7
C9H11O6	215.0561	215.0555	2.9	6	9	0.7
C9H13O6	217.0718	217.0716	0.8	6	9	0.7
C9H9O7	229.0354	229.0348	2.5	7	9	0.8
C9H11O7	231.0510	231.0505	2.3	7	9	0.8
C10H15O3	183.1027	183.1026	0.4	3	10	0.3
C10H13O5	213.0768	213.0768	0.2	5	10	0.5
C10H15O5	215.0925	215.0924	0.5	5	10	0.5
C10H13O6	229.0718	229.0715	1.2	6	10	0.6
C10H15O6	231.0874	231.0872	0.9	6	10	0.6
C10H11O7	243.0510	243.0506	1.8	7	10	0.7
C10H15O7	247.0823	247.0822	0.5	7	10	0.7

C11H15O6	243.0874	243.0873	0.5	6	11	0.5
C11H17O6*	245.1031	245.103	0.3	6	11	0.5
C12H19O5	243.1238	243.1237	0.4	5	12	0.4
C12H21O5	245.1394	245.1392	1.0	5	12	0.4
C13H19O5	255.1238	255.1239	-0.4	5	13	0.4
C13H19O6	271.1187	271.1188	-0.3	6	13	0.5
C14H21O5*	269.1394	269.1394	0.2	5	14	0.4
C17H25O8	357.1555	357.1559	-1.1	8	17	0.5

*isobaric compounds detected

Table 5.5.5: List of CHONS-containing compounds that were identified by UHPLC-(-)ESI-UHRMS analysis of the filter samples.

formula for $[M–H]^-$	***m/z* for $[M–H]^-$**	**measured *m/z***	**Δ*m* / ppm**	**Number of Oxygen**	**Number of Carbon**	**O:C**
C5H10O9NS	260.0071	260.0079	-3.1	9	5	1.8
C5H9O11N2S	304.9922	304.9932	-3.4	11	5	2.2
C6H10O9NS	272.0071	272.0081	-3.7	9	6	1.5
C7H10O9NS	284.0071	284.0080	-3.2	9	7	1.3
C7H10O10NS	300.0020	300.0029	-3.0	10	7	1.4
C10H16O7NS	294.0642	294.0657	-5.1	7	10	0.7
C10H14O8NS	308.0435	308.0448	-4.3	8	10	0.8
C10H16O8NS	310.0591	310.0605	-4.5	8	10	0.8
C10H16O9NS	326.0540	326.0551	-3.3	9	10	0.9
C10H16O10NS	342.0489	342.0497	-2.2	10	10	1.0
C10H18O10NS	344.0646	344.0655	-2.6	10	10	1.0
C10H17O11N2S	373.0548	373.0558	-2.8	11	10	1.1
C10H15O12N2S	387.0340	387.0350	-2.5	12	10	1.2

Table 5.5.6: List of CHON-containing compounds that were identified by UHPLC-(-)ESI-UHRMS analysis of the filter samples.

formula for $[M–H]^-$	***m/z* for $[M–H]^-$**	**measured *m/z***	**Δ*m* / ppm**	**Number of Oxygen**	**Number of Carbon**	**O:C**
C7H4O5N	182.0095	182.0096	-0.6	5	7	0.7
C7H3O7N2	226.9946	226.9947	-0.5	7	7	1.0
C10H16O8N	278.0881	278.0882	-0.2	8	10	0.8
C11H18O9N	308.0987	308.0988	-0.3	9	11	0.8

Table 5.5.7: List of CHOS-containing compounds that were identified by UHPLC-(-)ESI-UHRMS analysis of the filter samples.

formula for $[M–H]^-$	*m/z* for $[M–H]^-$	measured *m/z*	Δ*m* / ppm	Number of Oxygen	Number of Carbon	O:C
C2H3O6S	154.9656	154.9656	-0.1	6	2	3.0
C3H5O6S	168.9812	168.9812	0.2	6	3	2.0
C4H7O6S	182.9969	182.9967	1.0	6	4	1.5
C5H9O6S	197.0125	197.0124	0.7	6	5	1.2
C5H11O6S	199.0282	199.0280	0.9	6	5	1.2
C5H7O7S	210.9918	210.9916	0.9	7	5	1.4
C5H9O7S	213.0074	213.0075	-0.2	7	5	1.4
C5H11O7S	215.0231	215.0229	0.9	7	5	1.4
C5H7O8S	226.9867	226.9865	0.9	8	5	1.6
C6H11O6S	211.0282	211.0280	0.9	6	6	1.0
C7H11O6S	223.0271	223.0280	-4.1	6	7	0.9
C7H11O7S	239.0231	239.0231	0.0	7	7	1.0
C7H13O7S	241.0387	241.0385	1.0	7	7	1.0
C7H7O8S	250.9867	250.9868	-0.4	8	7	1.1
C7H9O8S	253.0024	253.0028	-1.7	8	7	1.1
C8H13O7S	253.0377	253.0384	-3.0	7	8	0.9
C8H11O9S	283.0118	283.0127	-3.1	9	8	1.1
C8H13O9S	285.0286	285.0284	0.6	9	8	1.1
C8H13O10S	301.0224	301.0231	-2.3	10	8	1.3
C9H15O6S	251.0584	251.0593	-3.6	6	9	0.7
C9H15O7S	267.0533	267.0540	-2.6	7	9	0.8
C9H13O8S	281.0337	281.0334	0.9	8	9	0.9
C9H13O9S	297.0286	297.0282	1.3	9	9	1.0
C10H17O5S	249.0791	249.0801	-3.9	5	10	0.5
C10H15O7S	279.0533	279.0544	-3.9	7	10	0.7
C10H17O7S	281.0690	281.0698	-3.0	7	10	0.7
C10H17O8S	297.0639	297.0646	-2.5	8	10	0.8
C10H15O9S	311.0431	311.0440	-2.8	9	10	0.9
C10H17O9S	313.0588	313.0596	-2.6	9	10	0.9
C10H15O10S	327.0391	327.0387	1.3	10	10	1.0
C10H13O11S	341.0184	341.0183	0.3	11	10	1.1
C11H19O7S	295.0846	295.0858	-4.1	7	11	0.6

C.2 Trajectory calculations for the campaign period

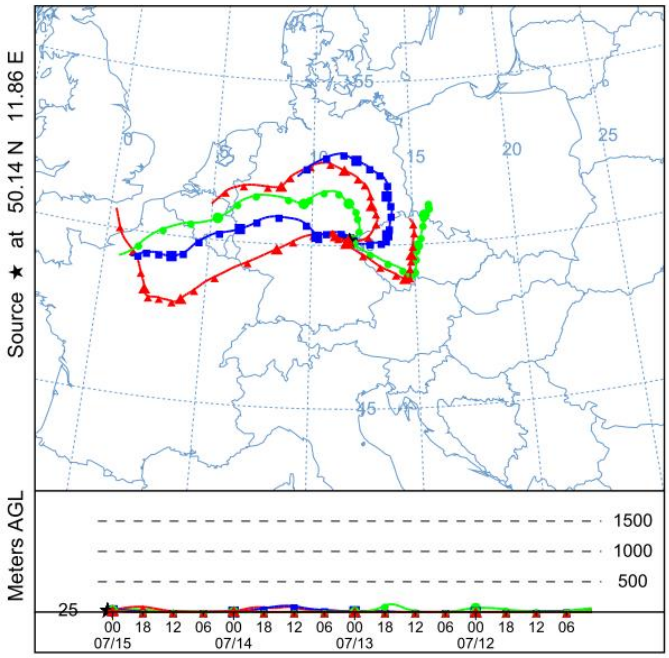

Figure 5.5.13:96 hours backward HYSPLIT trajectory calculations for the 15th-21st of July (each at 12 midnight CET), showing that air masses were mainly arriving from West Europe and North Germany and traveling at low altitudes (Draxler and Rolph).

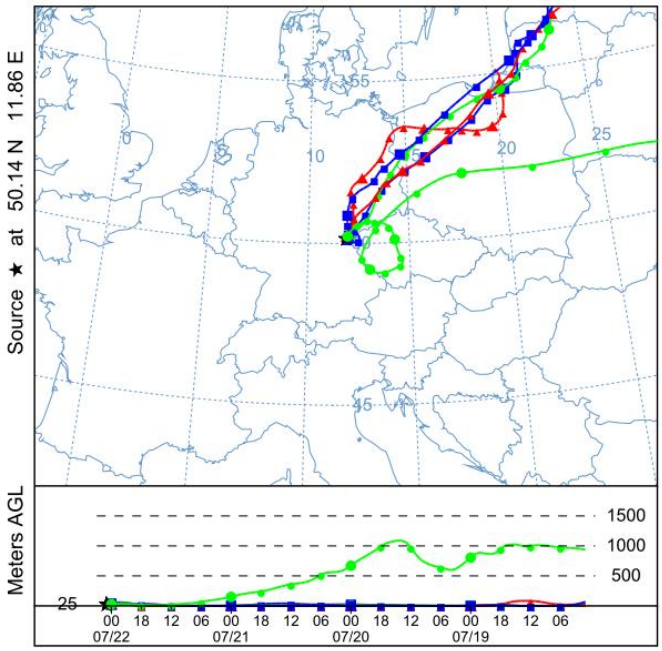

Figure 5.5.14: 96 hours backward HYSPLIT trajectory calculations for the 22nd–27th of July (each at 12 midnight CET), showing that air masses were mainly arriving from East Europe and traveling at low altitudes (Draxler and Rolph).

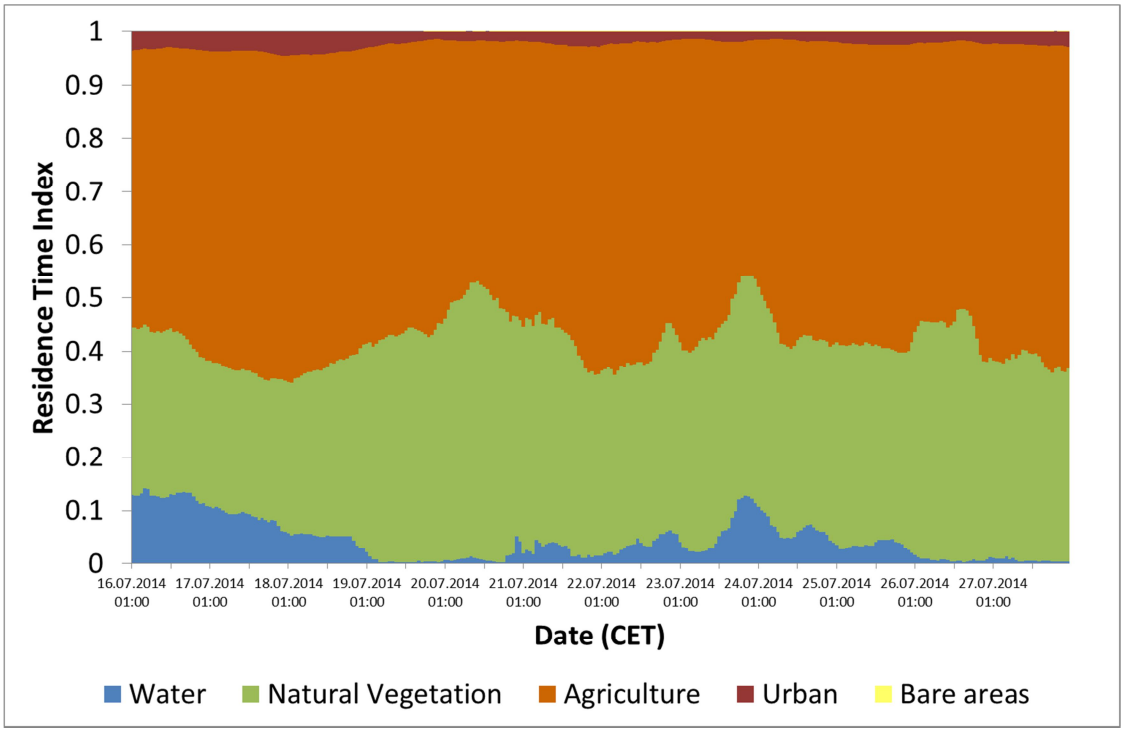

Figure 5.5.15: Residence times for 96 hours backward trajectories arriving at the site intersected with satellite-derived global landcover data to give indications of influences of main land cover classes. A detailed description of the calculation method can be found elsewhere (van Pinxteren *et al.*, 2010).

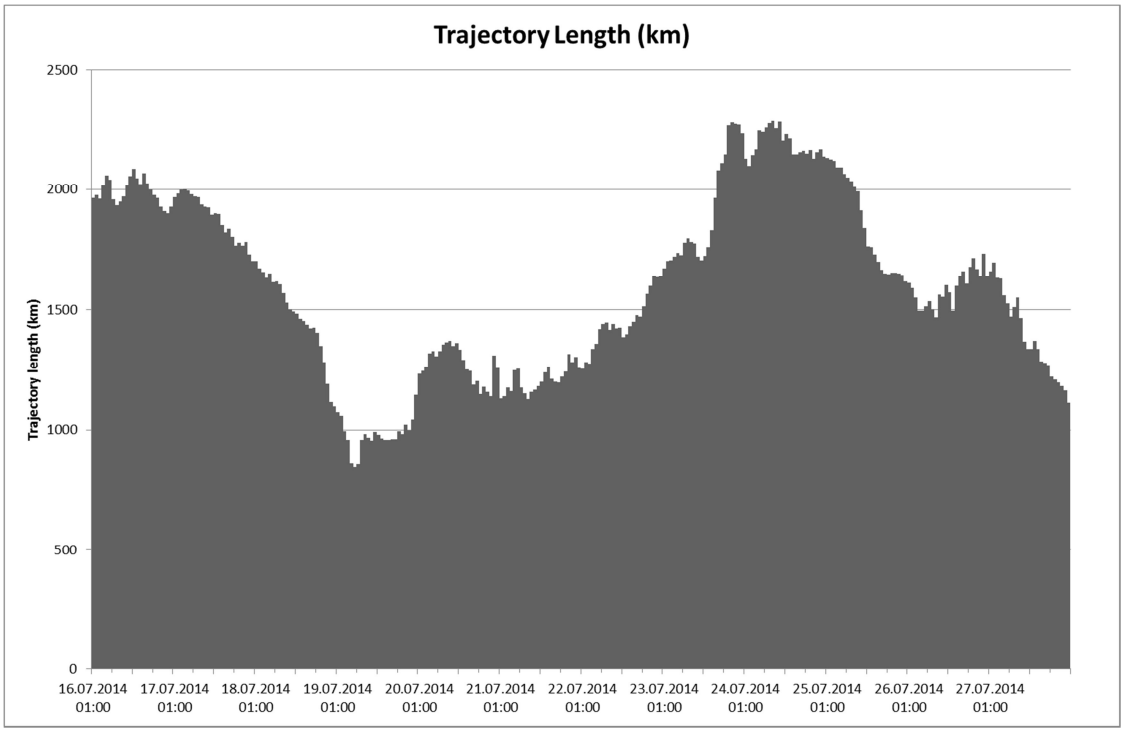

Figure 5.5.16: Trajectory lengths for 96 hours backward trajectories arriving at the site. For details see van Pinxteren *et al.* (2010).

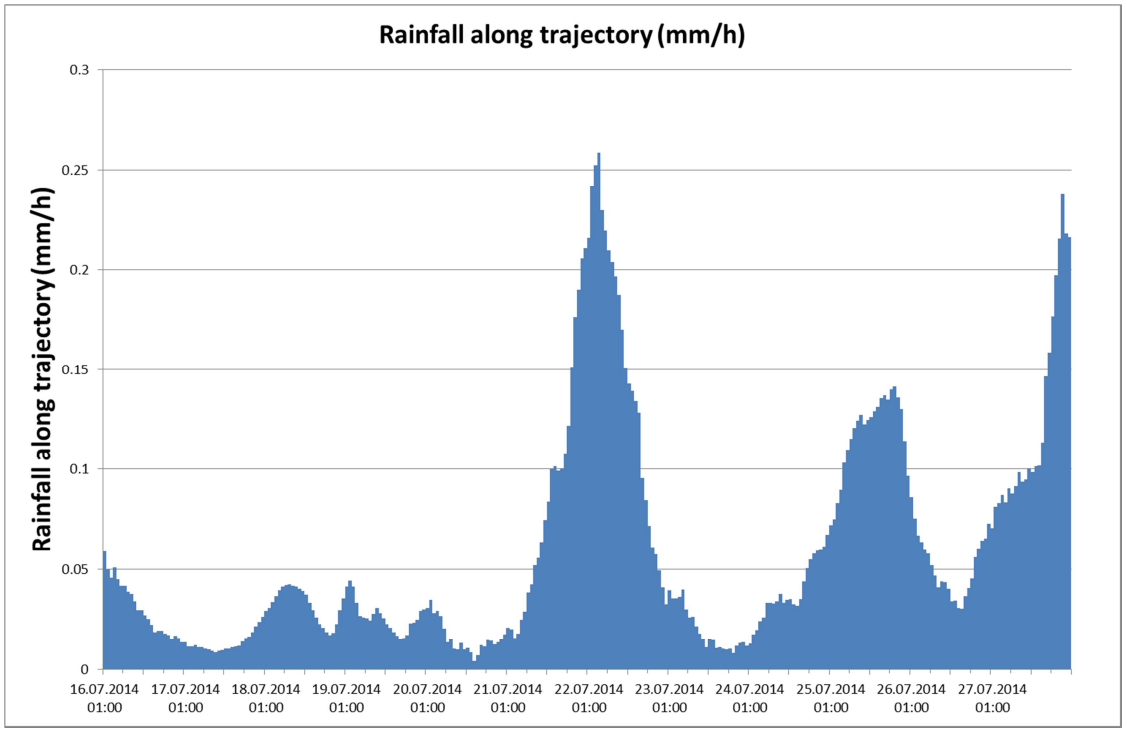

Figure 5.5.17: Rainfall along the calculated 96 hours backward trajectories arriving at the site. For details see van Pinxteren *et al.* (2010).

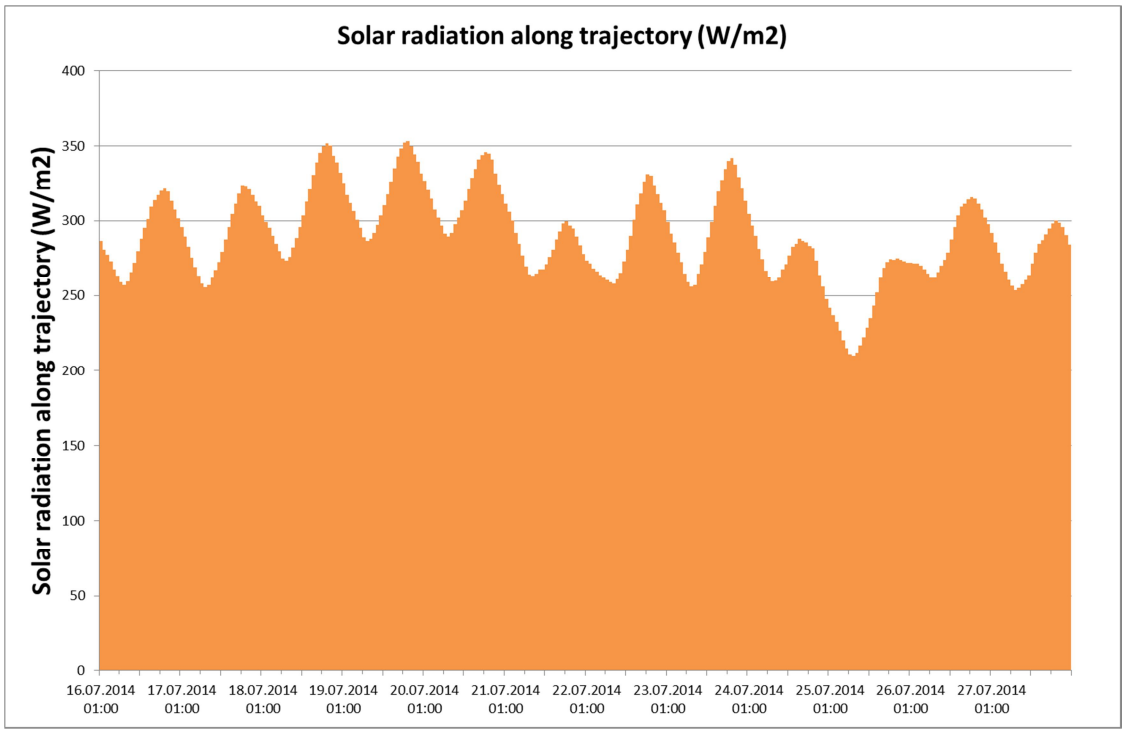

Figure 5.5.18: Solar radiation along the calculated 96 hours backward trajectories arriving at the site. For details see van Pinxteren *et al.* (2010).

C.3 Supplementary mass spectrometric data

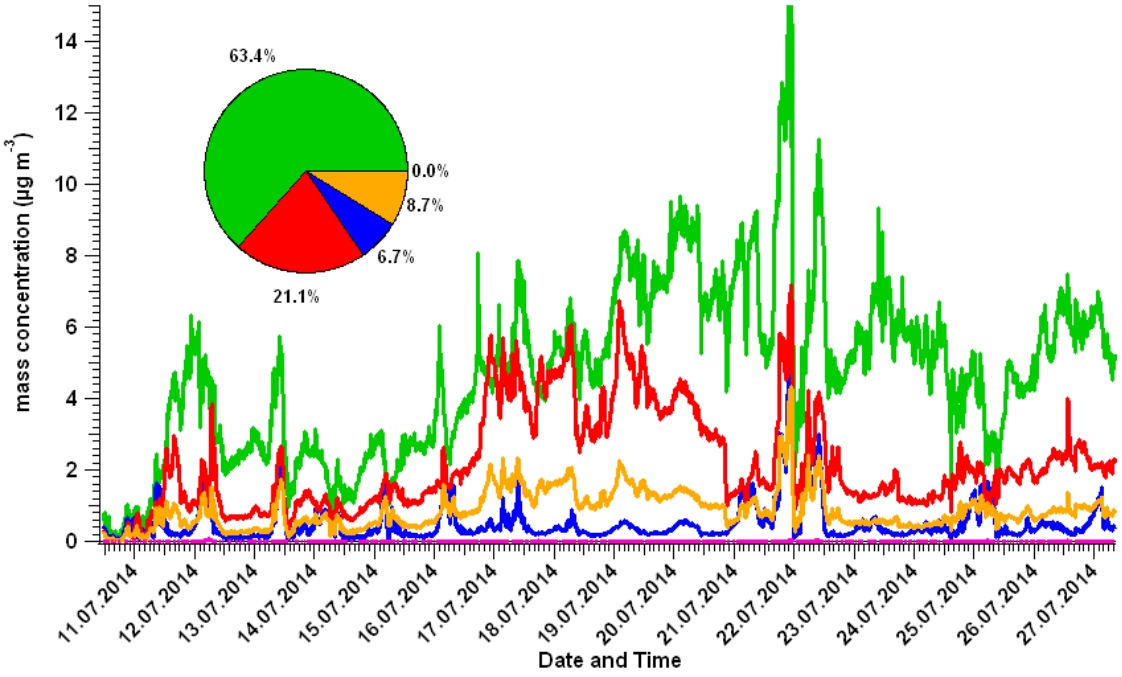

Figure 5.5.19: HR-ToF-AMS data for the campaign period, showing that aerosols were mostly made of organics and ammonium sulfate.

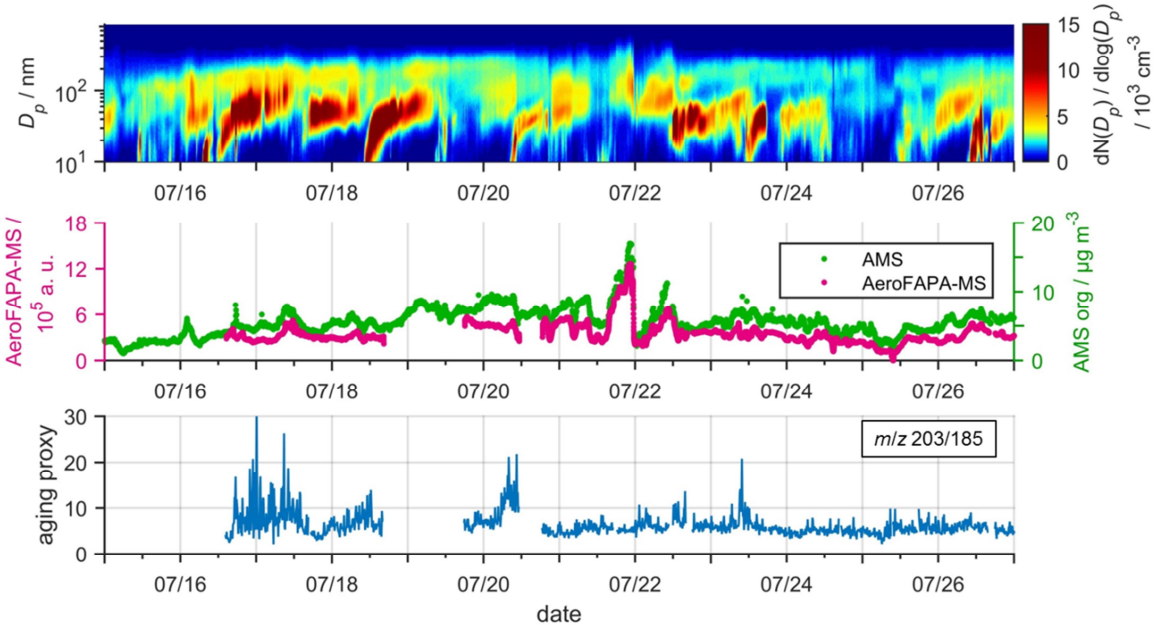

Figure 5.5.20: Top panel: Number size distribution of aerosol particles which was measured by an SMPS. Middle panel: Time traces of the total ion current of the AeroFAPA–MS (magenta) and the organic aerosol mass measured by an AMS (green). Bottom panel: Ratio of *m/z* 203/185 as aging proxy for SOA particles at the site.

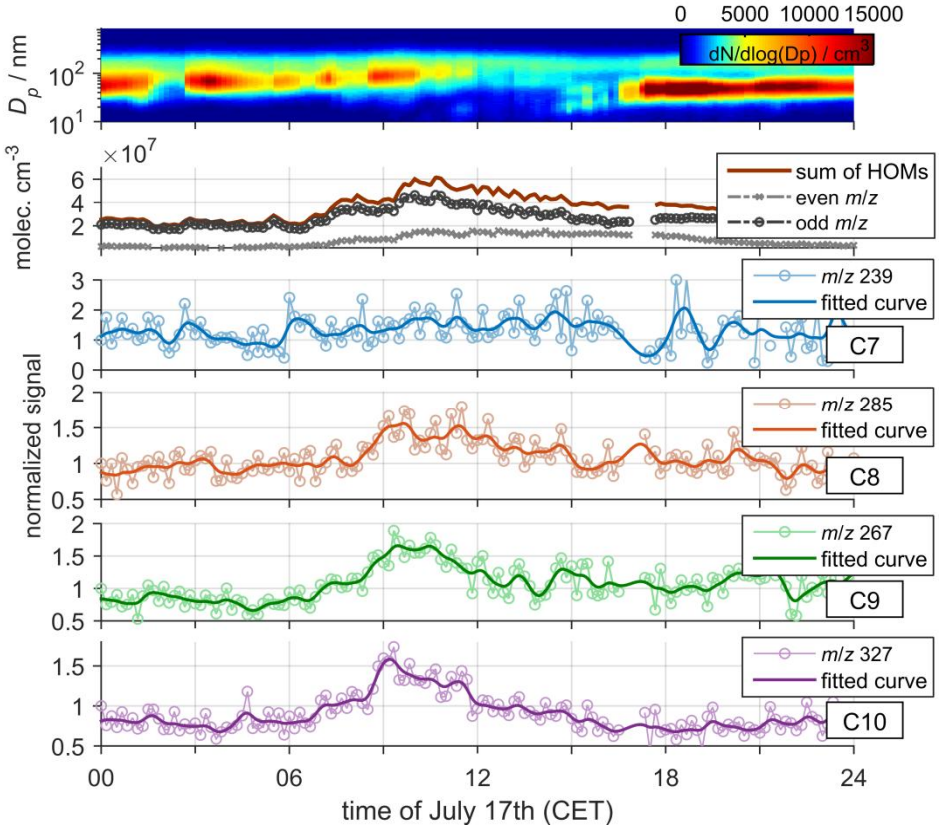

Figure 5.5.21: Time traces for C7-C10 HOOS, gas-phase HOMs and particle number size distribution during July 17th. HOM concentration is dominated by ions with even *m/z* ratios ($[M+NO_3]^-$), indicating the presence of peroxyradicals ($RO_2^{\bullet}$), organonitrates ($RONO_2$) and peroxynitrates (RO_2NO_2). While the larger HOOS are following the trend of the HOM signals with even *m/z* ratios, the C7 HOOS differ from this behavior, supporting the assumption that these species are not directly formed but by decomposition of the lager HOOS.

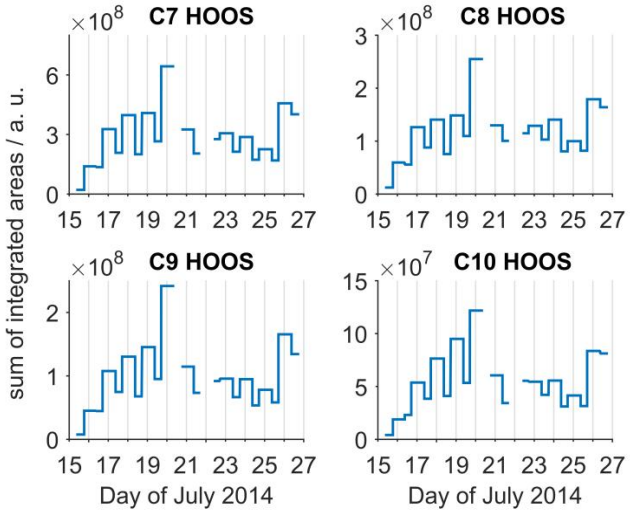

Figure 5.5.22: Sum of integrated areas for the different HOOS groups from the LC–MS analysis of the filter extracts. In contrast to the online measurement, the C7 HOOS show the most intense signals, suggesting a decomposition of larger HOOS during filter sampling, storage or processing.

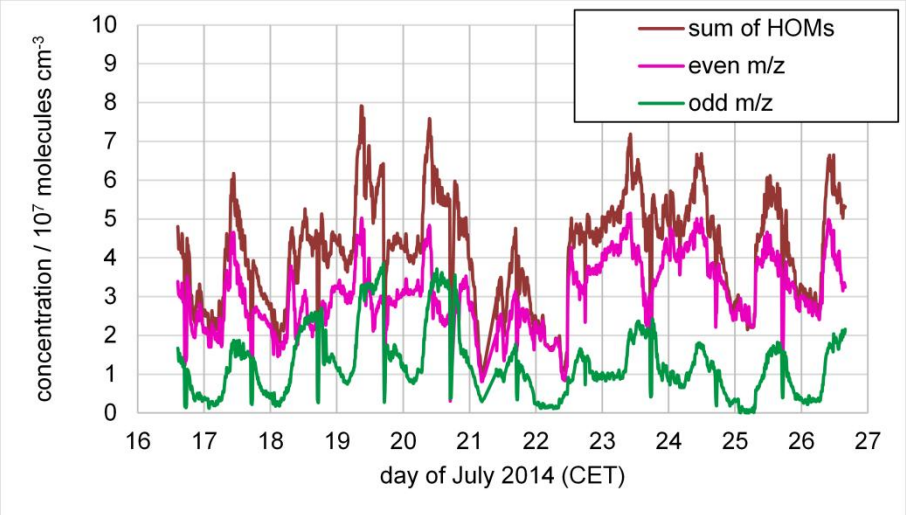

Figure 5.5.23: Concentrations of gas-phase HOMs measured by the CI–APiToF–MS over the entire campaign period.

Table 5.5.8: Signals and assignments for gas-phase HOMs detected by CI–APiTOF–MS.

formula assignment	**classification**	**molecular weight**	**m/z for $[M+NO_3]^-$**	**reference**
C7H10O4	HOM	158	220	Ehn *et al.*, 2014
		225	287	
C10H15O6	RO_2 radical	231	293	Jokinen *et al.*, 2014
		232	294	
		233	295	
		235	297	
C8H12O8	HOM	236	298	Ehn *et al.*, 2014
		245	307	
C10H14O7	HOM	246	308	Ehn *et al.*, 2014
		247	309	
C9H12O8 / C10H16O7	HOM	248	310	Ehn *et al.*, 2014
C10H17O7	RO_2 radical	249	311	Jokinen *et al.*, 2014
C10H15O8	RO_2 radical	263	325	Jokinen *et al.*, 2014
C10H16O8 / C9H12O9	HOM	264	326	Ehn *et al.*, 2014
		265	327	
		267	329	
	RO_2NO_2 (*m/z* 293+NO2)	277	339	Jokinen *et al.*, 2014
C10H14O9	HOM	278	340	Ehn *et al.*, 2014
C10H16O9	HOM	280	342	Ehn *et al.*, 2014
	$RONO_2$ (*m/z* 325+NO)	293	355	Jokinen *et al.*, 2014
C10H15O10	RO_2 radical	295	357	Jokinen *et al.*, 2014
C10H16O10	HOM	296	358	Ehn *et al.*, 2014
		308	370	
C10H14O11	HOM	310	372	Ehn *et al.*, 2014
C10H16O11	HOM	312	374	Ehn *et al.*, 2014

C.4 Meteorological data and concentration of trace gases

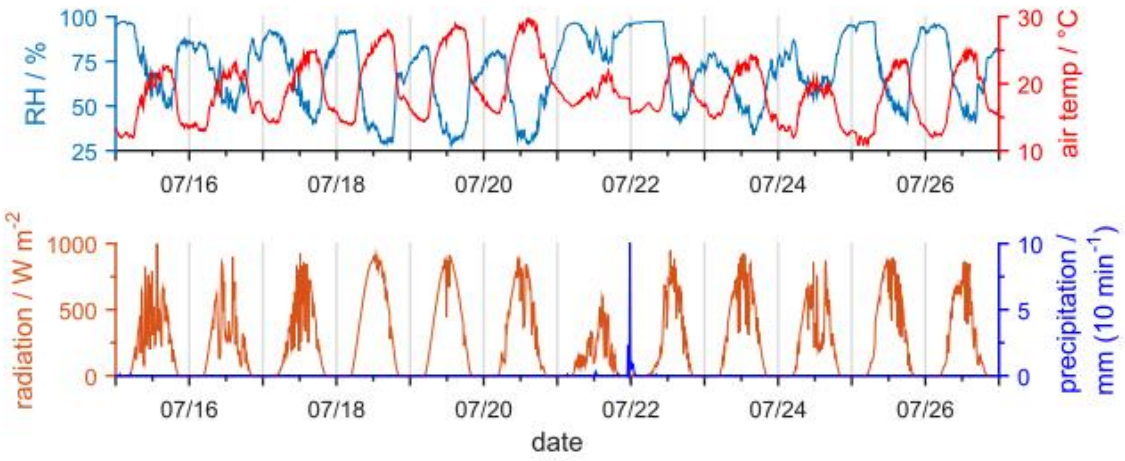

Figure 5.5.24: Meteorological data for the measurement site comprising relative humidity (RH, light blue), air temperature in °C (red), solar radiation (orange) and precipitation (blue).

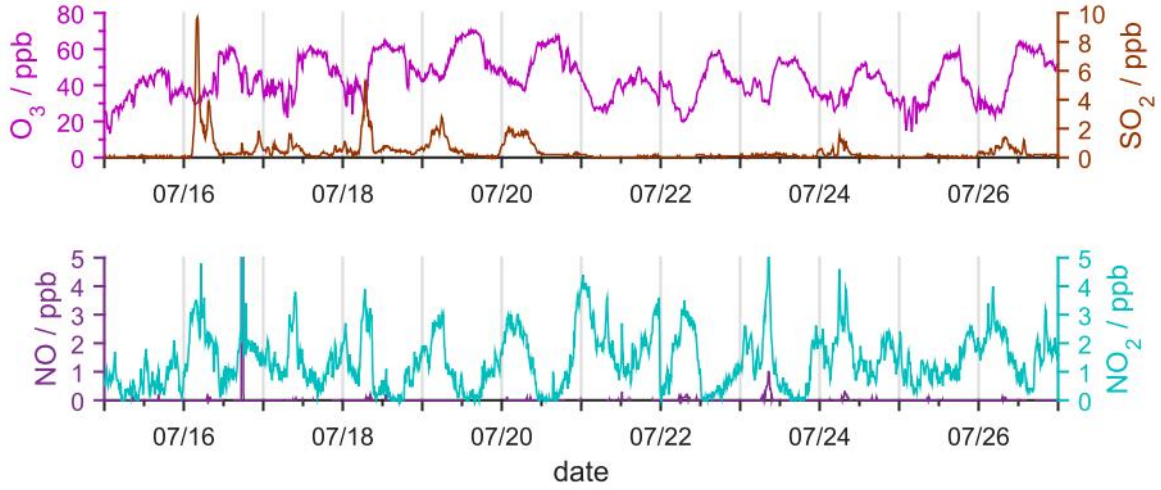

Figure 5.5.25: Trace gas concentrations in ppb for the measurement site comprising ozone (purple), SO_2 (brown), NO (dark purple) and NO_2 (light blue).

D. Technical Drawings and Documents of the FAPA source

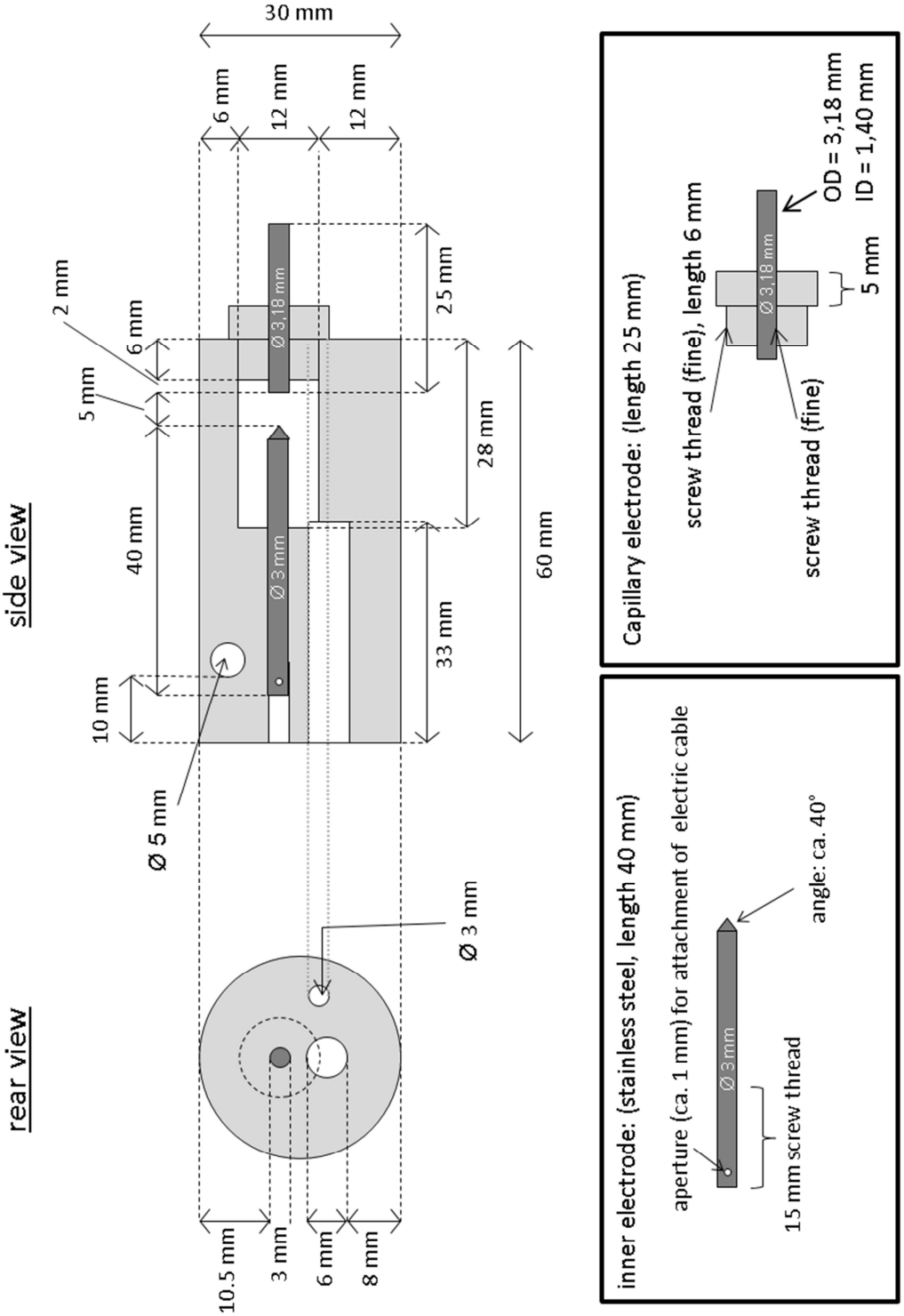

Drawing A: Cross sectional drawing of the FAPA source with exact distance indications. The source body is made of Marcor and the electrodes are made of stainless steel.

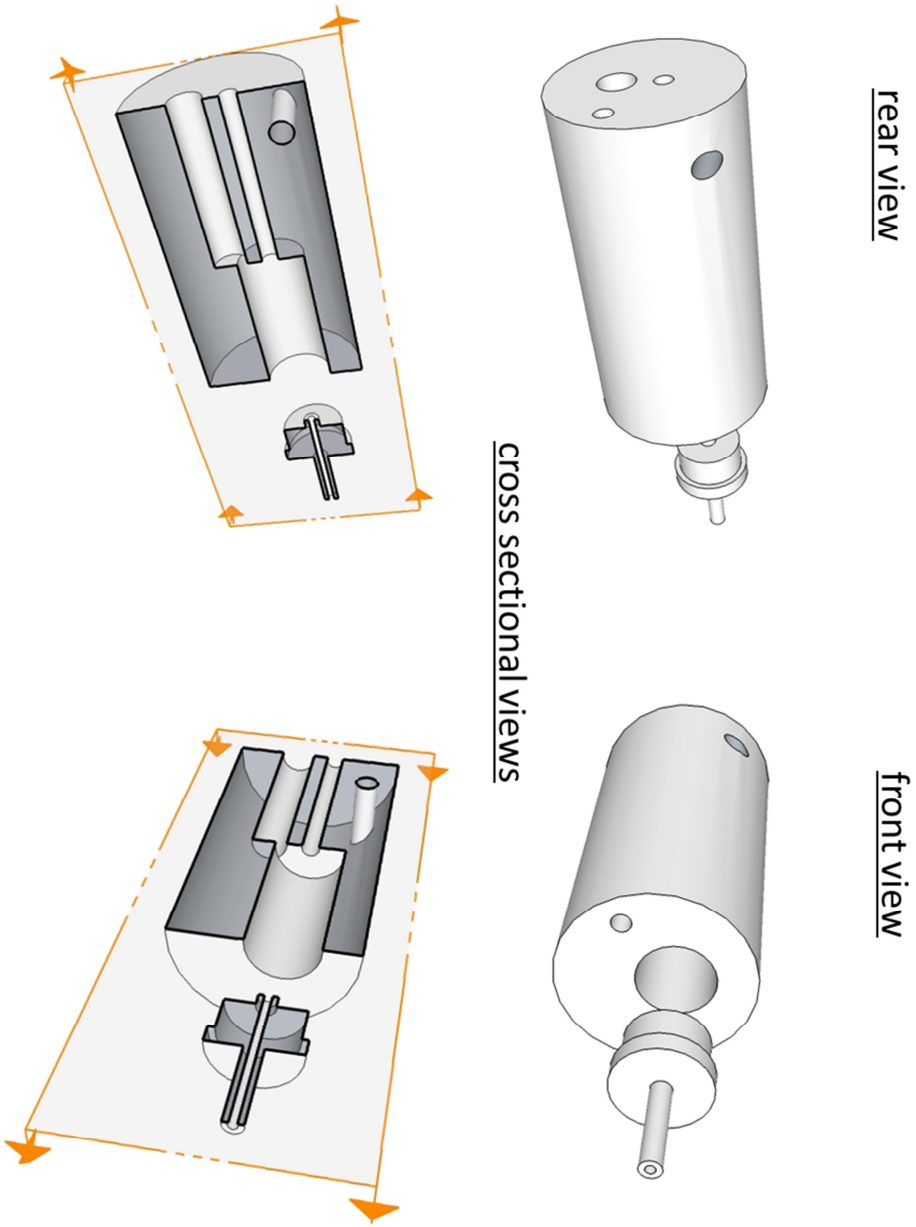

Drawing B: Three-dimensional view and corresponding cross sectional views of the FAPA source.

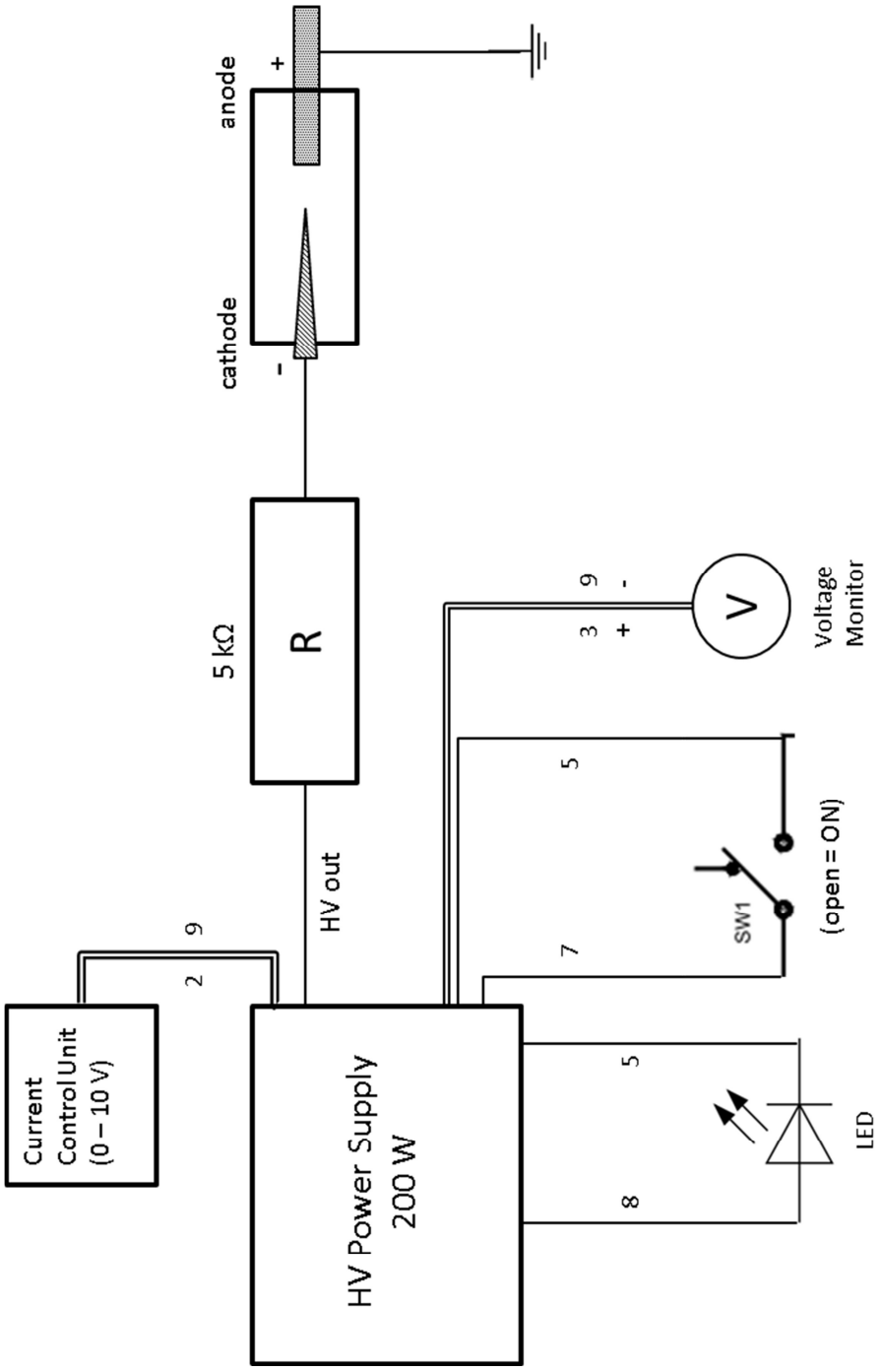

Drawing C: Simplified circuit layout of the FAPA source. The numbers refer to the connectors of the HV power supply (PTV3N200, Spellman).

E. List of Figures and Drawings

F. List of Tables

G. List of Related Publications and Presentations

Peer-reviewed publications:

Brüggemann M., Karu E., Stelzer T., Hoffmann T. (2015) Real-Time Analysis of Ambient Organic Aerosols Using Aerosol Flowing Atmospheric-Pressure Afterglow Mass Spectrometry (AeroFAPA–MS). *Environ. Sci. Technol.* 49(9):5571–5578. doi: 10.1021/es506186c

Brüggemann M., Vogel A.L., Hoffmann T. (2014) Analysis of organic aerosols using a micro-orifice volatilization impactor (MOVI) coupled to an atmospheric-pressure chemical ionization mass spectrometer (APCI–MS). *European Journal of Mass Spectrometry* 20(1):31-41. doi: 10.1255/ejms.1260

Vogel A.L., Äijälä M., Brüggemann M., Ehn M., Junninen H., Petäjä T., Worsnop D.R., Kulmala M., Williams J., Hoffmann T. (2013) Online atmospheric pressure chemical ionization ion trap mass spectrometry (APCI-IT–MS^n) for measuring organic acids in concentrated bulk aerosol – a laboratory and field study. *Atmos. Meas. Tech.* 6(2):431–443. doi: 10.5194/amt-6-431-2013

Oral Presentations:

12/2014

Brüggemann M., Karu E., Stelzer T., Hoffmann T.: „Mass spectrometric analysis of organic aerosols in real time using the AeroFAPA technique“. *Lecture Cycle of the Max Planck Graduate Center*, Mainz, Germany

09/2014

Brüggemann M., Karu E., Hoffmann T.: “Depth profiling and surface analysis of submicron organic aerosols in real time using AeroFAPA–MS”. *International Aerosol Conference 2014*, Busan, Korea

11/2013

Brüggemann M., Hoffmann T.: “Towards depth profiling of organic aerosols”, *TESLA seminar*, Braemar, Scotland

07/2012

Brüggemann M., Vogel A.L., Hoffmann T.: “A new technique for the analysis of secondary organic aerosol using soft ionization mass spectrometry”. *Interdisziplinäres Doktorandenseminar der GDCH-Arbeitskreise DASp und A.M.S.El.*, Mainz, Germany

06/2012

Brüggemann M., Vogel A.L., Hoffmann T.: “Analysis of secondary organic aerosol using soft ionization mass spectrometry”. *International Max Planck Research School Days 2012*, Heidelberg/Mainz, Germany

Poster Presentations:

04/2015

Brüggemann M., Karu E. Laurent P., Held A.,, Hoffmann T.: "Real-time analysis of ambient aerosols using the AeroFAPA technique". *European Geoscience Union – General Assembly 2015*, Vienna, Austria

04/2014

Brüggemann M., Hoffmann T.: "Towards depth profiling of organic aerosols in real time using aerosol flowing atmospheric-pressure afterglow mass spectrometry (AeroFAPA–MS)". *European Geoscience Union – General Assembly 2014*, Vienna, Austria

09/2013

Brüggemann M., Hoffmann T.: "Direct analysis of secondary organic aerosol using atmospheric-pressure glow discharge mass spectrometry". *European Aerosol Conference*, Prague, Czech Republic

06/2013

Brüggemann M., Hoffmann T.: "Direct analysis of secondary organic aerosol using the flowing atmospheric-pressure afterglow (FAPA) ambient mass spectrometry source". *61st Annual Conference of the American Society for Mass Spectrometry (ASMS)*, Minneapolis, MN, USA

03/2013

Brüggemann M., Kunze L., Hoffmann T.: "Einsatz der flowing atmospheric-pressure afterglow-Technik zur massenspektrometrischen Analytik von sekundärem organischen Aerosol". *ANAKON 2013*, Essen, Germany

09/2012

Brüggemann M., Vogel A.L., Hoffmann T.: "A Micro-Orifice Volatilization Impactor (MOVI) coupled to an ion trap mass spectrometer with a soft ionization source (APCI-IT/MS) for the analysis of secondary organic aerosols". *European Aerosol Conference 2012*, Granada, Spain

04/2012

Brüggemann M., Vogel A.L., Hoffmann, T.: "Analysis of secondary organic aerosol using a Micro-Orifice Volatilization Impactor (MOVI) coupled to an ion trap mass spectrometer with atmospheric pressure chemical ionization (APCI-IT/MS)". *European Geoscience Union – General Assembly 2012*, Vienna, Austria

H. Acknowledgements

This part was removed from the electronic version of the document.

I. Curriculum Vitae

This part was removed from the electronic version of the document.